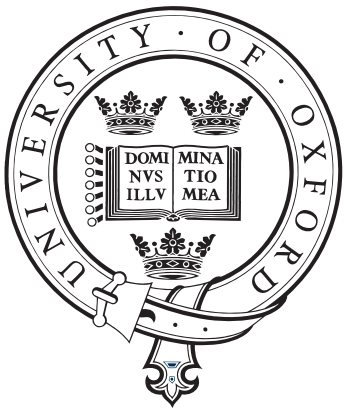
Towards Optical Raman Quantum Memories with Colour Centres in Diamond

Christian Weinzetl
Oriel College, Oxford



Submitted for the degree of Doctor of Philosophy
Trinity Term 2018

Supervised by
Dr. Joshua Nunn
&
Prof. Ian A. Walmsley

Clarendon Laboratory
University of Oxford
United Kingdom

Towards Optical Raman Quantum Memories with Colour Centres in Diamond

Christian Weinzetl
Oriel College, Oxford

Submitted for the degree of Doctor of Philosophy
Trinity Term 2018

Abstract

Quantum memories are a key technology enabling arbitrarily-scalable optical quantum information processing architectures via active synchronisation and multiplexing of quantum information. Optically active confined impurities, called colour centres, in a spin-free and highly transparent diamond host material are promising systems to realise such devices in the solid-state, suitable for integration in a scalable guided-wave on-chip photonic platform.

In this thesis, the transition from optical Raman quantum memories in atomic vapours to solid-state systems is prepared, exploring two diamond-based systems:

On the basis of ensembles of neutrally charged nitrogen vacancy centres, desirable properties and criteria of solid-state systems used for optical quantum memories are developed. These include non-vanishing off-resonant Raman coupling, variable acceptance bandwidth for broadband pulses and cross-linear polarised optical transitions to prevent the generation of noise during the Raman memory protocol, which have been realised experimentally by applying external uniaxial stress to the system. However, attempts to measure the very short orbital ground state lifetime affirmed unfavourable theoretical estimations, rendering this centre unsuitable for memory applications.

As a potential alternative, the negatively charged silicon vacancy centre has been investigated, which offers a large ground state splitting with extended life and coherence times and narrow inhomogeneous spectral lines due to its inversion symmetry. In an ensemble of silicon vacancy centres, the ground state lifetime is measured and coherent manipulation via resonant Ramsey interference and Hahn echo is demonstrated. In a second step, off-resonant two-photon transitions are achieved implementing stimulated Raman adiabatic passage between the orbital ground states. Finally, strong light-matter interaction of a weak signal field with the ensemble via phase-sensitive four-wave mixing is shown forming the basis for integrated Raman-based memories and single photon nonlinearities in ensembles of silicon vacancy centres and closely related defects.

To the ones I love

Acknowledgements

First, I would like to express my deepest gratitude to my supervisors Joshua Nunn and Ian Walmsley. Thank you for your intellectual curiosity, for extending the expertise of the group towards solid-state systems and making such a project as described in this thesis possible. Even though both of you are very busy, there was always time whenever support and guidance were needed.

I would like to thank Eilon Poem, my first mentor, who taught me the basics of working in the lab and the art of improvisation. You have always been there when needed and are a source of never-ending knowledge. Through the years, the memory group has seen many very talented post docs to which I am indebted, including Dylan, Patrick and Benni who where always helpful and open for discussions.

Special thanks to Christoph Becher for our collaboration and the support whenever I have been to Saarbrücken. This project would have not been possible without the hard work of Johannes and Jonas. It has been a great collaboration and a real pleasure working with you. Also thanks to Dirk R. Englund for providing a diamond sample for some experiments presented in this thesis.

I have been very lucky to be part of a highly motivated, supportive and sympathetic team during the four years of my DPhil studies. The Ultrafast group is made out of some incredible people I was happy to meet over the last years.

I am extremely thankful to my parents and my twin sister for the freedom they gave me to set my own goals, for their unwavering support from the very start, the love they show me every day and for being the best family I could have.

Author's Publications

Journal publications and manuscripts

1. E. Poem, C. Weinzetl, J. Klatzow, K. T. Kaczmarek, J. H. D. Munns, T. F. M. Champion, D. J. Saunders, J. Nunn and I. A. Walmsley. "**Broadband noise-free optical quantum memory with neutral nitrogen-vacancy centers in diamond**", *Physical Review B* **91**, 205108 (2015).

2. C. Weinzetl, J. Görlitz, J. N. Becker, I. A. Walmsley, E. Poem, J. Nunn and C. Becher. "**Coherent control and wave mixing in an ensemble of silicon-vacancy centers in diamond**", *Physical Review Letters* **122**, 063601 (2019).

3. J. Klatzow, J. N. Becker, P. M. Ledingham, C. Weinzetl, K. T. Kaczmarek, D. J. Saunders, J. Nunn, I. A. Walmsley, R. Uzdin and E. Poem. "**Experimental demonstration of quantum effects in the operation of microscopic heat engines**", *Physical Review Letters* **112**, 110601 (2019).

Conferences

Conference Talks

1. C. Weinzetl, E. Poem, J. Klatzow, K. T. Kaczmarek, J. H. D. Munns, D. J. Saunders, I. A. Walmsley and J. Nunn. "**Broadband Low-Noise Raman Quantum Optical Memory with Neutral NV Centres in Diamond**" *Quantum Light-Matter Interaction in Solid State Systems Conference (CIPRIS QLIMS)*, November 2015, Barcelona, Spain.

2. C. Weinzetl, J. Görlitz, E. Poem, J. N. Becker, I. A. Walmsley, C. Becher and J. Nunn. "**Coherent Population Transfer and Absorption in a thin Layer of Silicon-Vacancy Centers**" *Single Photons Single Spins Meeting (SPSS II)*, August/September 2017, Troyes, France.

Poster Presentations

1. C. Weinzetl, E. Poem, J. Klatzow, K. T. Kaczmarek, J. H. D. Munns, D. J. Saunders, I. A. Walmsley and J. Nunn. "**Proposed ultrafast quantum optical memories in diamond NV centres**" *Quantum Light-Matter Interaction in Solid State Systems Conference (CIPRIS QLIMS)*, November 2015, Barcelona, Spain.

2. C. Weinzetl, E. Poem, J. Klatzow, J. Nunn and I. A. Walmsley. "**Broadband Low-Noise Raman Quantum Optical Memory with Neutral NV Centres in Diamond**" *7^{th} NTT-BRL school jointly with ISNTT2015: International Symposium on Nanoscale Transport and Technology*, November 2015, Atsugi, Kanagawa, Japan.

3. C. Weinzetl, E. Poem, J. Klatzow, P. Ledingham, D. J. Saunders, I. A. Walmsley and J. Nunn. "**Localized Orbital Electronic States in Diamond for Strong and Fast Light-Matter Interactions**" *Royal Society Discussion Meetings: Quantum Technology for the 21^{st} Century*, May 2016, The Royal Society, London, United Kingdom.

4. C. Weinzetl, J. N. Becker, J. Görlitz, E. Poem, J. Klatzow, P. Ledingham, D. J. Saunders, I. A. Walmsley, C. Becher and J. Nunn. "**Localized Orbital Electronic States of Colour Centres in Diamond for Strong and Fast Light-Matter Interactions - Raman Memory in an Ensemble of Silicon-Vacancy Centres**" *CLEO/Europe-EQEC 2017*, June 2017, Munich, Germany.

5. C. Weinzetl, J. N. Becker, J. Görlitz, J. Klatzow, P. Ledingham, D. J. Saunders, E. Poem, J. Nunn, C. Becher and I. A. Walmsley. "**Colour Centres in Diamond for Strong and Fast Light-Matter Interactions**" *662. WE-Heraeus-Seminar on Quantum Networks - from building blocks to application*, February 2018, Bad Honnef, Germany.

Contents

Acknowledgements **v**

Author's Publications **vii**

List of Figures **xv**

List of Tables **xix**

List of Abbreviations **xxi**

1 Introduction **1**
1.1 Quantum memories . . . 3
1.2 Enhanced multiphoton rates . . . 4
1.3 Quantum computing . . . 5
1.4 Quantum communication . . . 8
1.5 Thesis outline . . . 11

2 Quantum memories **15**
2.1 Figures of merit . . . 16
2.2 Quantum memory protocols . . . 19
2.2.1 Non-light-matter quantum memories . . . 19
2.2.2 Echo memories . . . 20
2.2.3 Controlled reversible inhomogeneous broadening (CRIB) . . . 20
2.2.4 Atomic frequency comb (AFC) . . . 24
2.2.5 Electromagnetically induced transparency (EIT) . . . 26
2.2.6 The Raman memory . . . 29
2.3 Summary . . . 36

3 Colour centres in diamond **37**
3.1 Diamond as host material . . . 39
3.1.1 Types of diamond . . . 40
3.2 Colour centres . . . 40
3.2.1 Photoluminescence spectra . . . 41
3.2.2 Homogeneous and inhomogeneous optical linewidth . . . 44

3.2.3 Phonons . . . 45
3.2.4 Dynamic Jahn-Teller effect . . . 47
3.2.5 The nitrogen vacancy centre (NV^-/NV^0) . . . 50
3.2.6 The silicon vacancy centre (SiV^-) . . . 56
3.3 Summary . . . 62

4 Atomic light-matter interactions 65
4.1 Optical pumping . . . 66
4.2 Coherent control . . . 70
4.2.1 The Bloch sphere . . . 70
4.2.2 Ramsey interference . . . 73
4.2.3 Hahn echo . . . 75
4.2.4 Stimulated Raman adiabatic passage (STIRAP) . . . 78
4.3 Nonlinear processes – Four-wave mixing . . . 84
4.4 Summary . . . 87

5 Quantum memory with neutral nitrogen vacancy centres 89
5.1 Raman coupling strength . . . 90
5.1.1 Special characteristics of NV^- . . . 94
5.1.2 Special characteristics of NV^0 . . . 96
5.2 Optical transitions under an electric field or external stress . . . 97
5.2.1 The NV^0 Hamiltonian . . . 97
5.2.2 Application of external electric fields . . . 100
5.3 Cross-linear polarisation selection rules . . . 102
5.4 Relative noise intensity . . . 104
5.5 Raman coupling . . . 105
5.6 Memory in a (001) diamond sample . . . 106
5.6.1 Optical axis and electric field orientation . . . 106
5.6.2 Ground state level splitting . . . 107
5.6.3 Degree of polarisation . . . 108
5.6.4 Relative noise intensity . . . 110
5.6.5 Raman coupling . . . 111
5.6.6 Applicability as Raman memory . . . 111
5.6.7 Memory efficiency . . . 112
5.7 Storage time estimation . . . 114
5.7.1 Coherence time estimation . . . 114
5.7.2 Ground state lifetime . . . 118
5.8 Summary . . . 120

6 Engineering an ensemble of neutrally charged nitrogen vacancy centres 123
6.1 Diamond sample and experimental set-up . . . 124
6.1.1 Diamond sample . . . 124
6.1.2 Diamond clamp . . . 125
6.1.3 Laser fields . . . 127
6.1.4 Cryogenic set-up . . . 129
6.1.5 Spectral analysis . . . 130

6.1.6 Temporal resolution for lifetime measurements . . . 131
6.2 External control over an ensemble of nitrogen vacancy centres . . . 131
6.2.1 Ground state splitting by external uniaxial stress . . . 132
6.2.2 Imposing cross-linear polarisation selection rules . . . 134
6.3 Ground state lifetime measurement . . . 138
6.4 Summary . . . 141

7 Towards the silicon vacancy memory 143
7.1 Ground state coherence time estimation . . . 145
7.2 Diamond sample and experimental set-up . . . 148
7.2.1 Diamond sample . . . 148
7.2.2 Laser fields . . . 150
7.2.3 Cryogenic set-up . . . 156
7.2.4 Filter set-up . . . 158
7.3 Coherent control and wave mixing in ensembles of silicon vacancy centres . . . 160
7.3.1 SiV^- ground state lifetime . . . 160
7.3.2 Ramsey interference and Hahn echo measurements . . . 162
7.3.3 Stimulated Raman adiabatic passage (STIRAP) . . . 164
7.3.4 Phase-dependent strong light-matter interactions . . . 168
7.4 Numerical simulation . . . 173
7.4.1 Optical Bloch equations (Ramsey interference, Hahn echo, STIRAP) . . . 173
7.4.2 Linearised Maxwell-Bloch equations (phase-sensitive amplification and absorption) . . . 174
7.5 Summary . . . 184

8 Conclusion 187

9 Outlook 191
9.1 Storage of weak coherent pulses . . . 191
9.2 Noise suppression . . . 195
9.3 DLCZ memory . . . 197
9.4 Nonlinear interaction . . . 198
9.5 Further inversion symmetric defects in diamond . . . 199

Bibliography 203

A Optical pumping - Solutions to the rate equations 227

B Optical Bloch equations for four-level systems 231
B.1 Hamiltonian of a four-level system with four interacting electromagnetic fields in rotating wave approximation . . . 231
B.2 Temporal evolution of a quantum system: The master equation in Lindblad form . . . 241
B.3 Optical Bloch equations for a four-level system . . . 246

List of Figures

1.1 Temporal multiplexing, spatial multiplexing and hybrid multiplexing approach for enhanced multiphoton rates. . . . 6
1.2 Long-distance entanglement distribution via quantum repeaters and quantum repeater designs. . . . 10

2.1 Controlled reversible inhomogeneous broadening (CRIB/GEM) memory protocol. . . . 23
2.2 Atomic frequency comb (AFC) memory: Level scheme, spectral comb structure and pulse sequence. . . . 25
2.3 Electromagnetically induced transparency (EIT): Level scheme and linear susceptibility $\chi^{(1)}$. . . . 28
2.4 The Raman memory scheme. . . . 31
2.5 Four-wave mixing (FWM) during the Raman memory protocol. . . . 33

3.1 Zero-phonon line (ZPL) and phonon side bands (PSB). . . . 43
3.2 Phonon dispersion relation for diamond. . . . 46
3.3 Electron-phonon interaction on the example of the SiV^- ground state manifold ^2E_g. . . . 48
3.4 The $NV^{-/0}$ centre in a cubic diamond unit cell. . . . 51
3.5 Symmetry properties of the $NV^{-/0}$ and the SiV^- centre. . . . 52
3.6 Schematic electronic structure of the NV^- and the NV^0 centre. . . . 54
3.7 The SiV^- centre in a cubic diamond unit cell. . . . 57
3.8 SiV^- four-level structure and optical spectrum of the ZPL. . . . 59
3.9 Fluorescence spectrum including the ZPL and PSB of NV^- and SiV^- at room temperature, spectral resolution of the SiV^- ZPL for temperatures from 150 K to 6.4 K and photoluminescence polarisation of the optical transitions in a single SiV^- centre. . . . 60

4.1 Optical pumping in a three-level Λ-system. . . . 67
4.2 Bloch sphere and two-level system. . . . 71
4.3 Ramsey interference and Hahn echo: pulse sequences and level scheme. . . . 74
4.4 Bloch sphere representation of Ramsey interference and Hahn echo. . . . 77

4.5 Stimulated Raman adiabatic passage (STIRAP): Level scheme, pulse sequences and example simulations. 79

5.1 Level configuration and allowed optical transitions of NV^- and NV^0 centres. 94
5.2 Influence of an external electric field in x = $[\bar{1}\bar{1}2]$ direction on the ground state level splitting, the degree of polarisation of the optical transitions between the two ground states and the excited state, the relative probability of the control field in x-polarisation to couple to the higher ground state and the product of the Raman coupling coefficient and the detuning of the Raman transition from the excited state. 101
5.3 All possible NV orientations in a (001) diamond sample. 107
5.4 Influence of an external electric field in the [100]-direction on the ground state level splitting, the degree of polarisation of the optical transitions between the two ground states and the excited state, the relative probability of the control field in H-polarisation to couple to the higher ground state and the product of the Raman coupling coefficient and the detuning of the Raman transition from the excited state. 108
5.5 Optical transition coupling matrix given for the electric field and the intensity. 109
5.6 Raman memory scheme in an ensemble of NV^0 centres oriented along $\langle 111 \rangle$ with a strong electric field applied along [100]. 112

6.1 Berrylium copper anvil cell. 125
6.2 NV^0 experiment: Beam lines and cryogenic set-up. 128
6.3 Off-resonant fluorescence spectroscopy. 132
6.4 Spectrally resolved off-resonant fluorescence measurements into the ZPL as a function of the voltage applied to a piezo element varying the uniaxial pressure on the diamond. 133
6.5 Double Lorentzian fitting of the measured spectrum. 133
6.6 Engineering of the ensemble of NV^0 centres by external stress applied by a piezo element in direction [100]. 134
6.7 Stokes parameters. 136
6.8 Pulse sequence and level scheme for lifetime measurements. 138
6.9 Stimulated emission from the orbital excited state in the NV^0 level scheme (STED). 140

7.1 Diamond sample, optical zero-phonon line spectrum and SiV^- four-level structure. 149
7.2 Pulse sequence set-up for Ramsey interference and Hahn echo experiments. . 151
7.3 Generation and combination of all optical fields, phase stabilisation set-up. . 153
7.4 Optical field preparation. 154
7.5 Cryogenic set-up. 156
7.6 Grating-based filter set-up. 159
7.7 Ground state lifetime measurement. 161
7.8 Ramsey interference and Hahn echo measurements: Pulse sequence, level scheme and measurement results. 162
7.9 Stimulated Raman adiabatic passage (STIRAP) measurements. 165

7.10 Stimulated Raman adiabatic passage (STIRAP) temporal delay measurements and simulations. . . . 166
7.11 Phase-sensitive signal absorption and amplification: Time-resolved measurements, pulse sequence and interaction scheme. . . . 169
7.12 Signal absorption and amplification saturation measurements. . . . 170
7.13 Signal absorption and amplification in simulations. . . . 171
7.14 Temporal and spatial simulation of the interaction of signal, control and Stokes fields, as well as of the spin wave. . . . 178
7.15 Temporally resolved input and output of the Stokes and signal field, spatially resolved spin wave at the beginning and the end of the simulation and signal intensity, Stokes intensity and spin wave at the end of the interaction shown over the relative initial phase of the control field θ_C. . . . 180
7.16 Comparison between seeded and spontaneous Raman scattering and FWM processes. . . . 182
7.17 Influence of the strength of the Stokes field on the signal field. . . . 183

9.1 Measurement of the optical density (OD) of an ensemble of SiV^- centres in a layer of 120 µm. . . . 193
9.2 Double-monochromator for signal field separation. . . . 194
9.3 Magic-Λ scheme. . . . 196
9.4 DLCZ-memory in a three-level system. . . . 197

A.1 Optical pumping in a three-level Λ-system. . . . 228

B.1 Four-level system with four applied electromagnetic fields. . . . 233
B.2 Four-level system with decay rates Γ_i. . . . 246

List of Tables

9.1 Characteristics of Group-IV colour centres. 201

B.1 Four-level system: Definition of fields and transitions. 232

List of Abbreviations

APD	avalanche photo diode
bit	binary digit
BS	beam splitter
CCD	charge-coupled device
cF/fcc	face-centred cubic
cps	counts per second
CPT	coherent population trapping
Cs	caesium
CVD	chemical vapour deposition
CW	continuous-wave
DJT	dynamic Jahn-Teller
DLCZ	Duan-Lukin-Cirac-Zoller
DPSS	diode-pumped solid-state
EIT	electromagnetically induced transparency
EOM	electro-optical modulator
FORC	first-order Raman coupling
FPGA	field-programmable gate array
FSR	free spectral range
FWHM	full-width half-maximum
FWM	four-wave mixing
GeV	germanium vacancy
HPHT	high-pressure-high-temperature

HWP half-wave plate

IP interaction picture

JT Jahn-Teller

KLM Knill, Laflamme and Milburn

LOQC linear optical quantum computing

LP long pass

N nitrogen

NiV nickel vacancy

NV nitrogen vacancy

NV^0 neutral nitrogen vacancy centre

NV^- negative nitrogen vacancy centre

OD optical density

ODMR optically detected magnetic resonance

PBS polarising beam splitter

PID proportional-integral-derivative

PL photoluminescence

PLE photoluminescence excitation

PPKTP periodically poled potassium titanyl phosphate

ppm parts per million

PSB phonon sidebands

QIP quantum information processing

QKD quantum key distribution

QOM quantum optical memory

qubit quantum binary digit

QWP quater-wave plate

RK4 fourth-order Runge-Kutta

Rb rubidium

RCC Raman coupling coefficient

rf radio frequency

rms root mean square

RWA rotating wave approximation

Si silicon

SiC silicon carbide

SiV$^-$ negative silicon vacancy centre

SMI spin mixing interactions

SnV tin vacancy

SO spin-orbit

SP Schrödinger picture

SPDC spontaneous parametric down-conversion

std standard deviation

STED stimulated emission depletion

STIRAP stimulated Raman adiabatic passage

TBP time-bandwidth product

ZPL zero-phonon line

Chapter 1

Introduction

The comprehension of the nature of light and the knowledge of its properties has continuously changed and developed over millennia. At the turn of the 20$^{\text{th}}$ century, the development of quantum mechanics and a quantum model of matter led to flourishing research in the fields of light-matter interaction and information processing with light during the last century [1,2]. Concepts of superposition and the entanglement of states did not fit into the classical conception of the world and its local realism [3,4]. However, these new concepts gave way for the development of quantum technologies, summarised under the term "quantum information processing" (QIP) [5–9], outperforming their classical counterparts in many fields.

In classical applications and computers, information is encoded in binary digits (bits), the smallest unit of information. This notion can be extended to quantum bits (qubits) exploiting the laws of quantum mechanics. In contrast to a bit that can appear in either one of two distinct values only, for example 0 or 1, a qubit $|\psi\rangle$ can be in any linear combination

of two orthogonal states $|0\rangle$ and $|1\rangle$, a superposition [10]

$$|\psi\rangle = \alpha\,|0\rangle + \beta\,|1\rangle\,, \tag{1.1}$$

where α and β are complex numbers satisfying $|\alpha|^2 + |\beta|^2 = 1$. Orthogonality is ensured if the inner product of the two states, $\langle 0|1\rangle$, equals zero [11]. With qubits, instead of two values only, computation with a continuum of superpositions is possible [10]. At the end of the computation, performing a measurement on the qubit will either show the qubit in state $|0\rangle$ or state $|1\rangle$ as result. For example, for the qubit defined in equation (1.1), the probability to find the qubit in state $|0\rangle$ is $|\alpha|^2$, to find it in state $|1\rangle$ is $|\beta|^2$ [10].

Light can be considered as an ideal carrier of information, travelling at the fastest possible speed, showing low unintentional interaction with the environment and other electromagnetic waves, the possibility of guidance and confinement in structured materials like optical fibres and other waveguides and the wide range of optical, magneto- and electro-optical elements available for its manipulation.

In light, information can be encoded in the degrees of freedom of electromagnetic waves. These include single rail [12], dual rail [10,13], time bin [14], polarisation [13,15], narrowband frequency [16] and time-frequency encoding [17]. Conversion between different types of encoding is possible, for example time-bin to polarisation conversion [18] and time to frequency conversion [19,20].

However, travelling light requires active external intervention for synchronised operation in QIP. Therefore, in the following sections, basic concepts of quantum memories and their

areas of application are presented, before in a second step, QIP technologies are described in more detail and the benefits of quantum memories are highlighted.

1.1 Quantum memories

Optical quantum memories are devices to store and retrieve quantum states of light on demand. In the case of matter-based optical quantum memories, a coherent interface between light and matter is created, reversibly mapping quantum information between a photon travelling at the speed of light and a stationary medium, in an ideal case, without unintentionally altering, adulterating or destroying the information. Systems with long life and coherence times are used as storage media.

In order to increase the probability of a successful storage process, favourable conditions for strong light-matter interaction need to be created. Working with single systems, the interaction strength is intrinsically low, but can be enhanced by external optical cavities [21–23]. In the same way, the light-matter interaction can be strengthened for weakly absorbing ensembles like rare-earth systems [24–27]. However, also ensembles with high optical density (OD) exist, including elongated clouds of cold atoms [28–30] and hot vapour cells [31–33], which offer strong light-matter coupling and high robustness without any external resonators which reduces the experimental complexity.

An excellent solid-state platform for this purpose is diamond due to its optical properties and a wide band gap in which colour centres can generate advantageous electronic structures for quantum memory protocols. Furthermore, integration with other photonic structures like photonic crystal cavities and structured diamond waveguides is possible [34–36].

Quantum memories are essential components in QIP, including technologies as quantum computers and secure quantum communication (see Section 1.3 and Section 1.4) . Metrology applications, like magnetometry[37–40], electrometry[41,42] and thermometry[43–45], in addition to optical clocks[46–49], profit in their sensitivity from long coherence times in memories. The ability of quantum memories to store entangled states enables augmented sensing and precision metrology applications by squeezing quantum fluctuations[46,50,51]. Furthermore, memories offer the possibility of microwave-to-optical conversion[52,53], frequency shifting[54,55], enhanced nonlinear photon-photon interaction[56,57] and can operate as deterministic single-photon sources[58–61].

1.2 Enhanced multiphoton rates

Often, the system of choice for heralded single photons are sources based on spontaneous parametric down-conversion (SPDC)[62–64]. In this nonlinear process, strong pumping can easily lead to multiple photons generated per pulse. This can be avoided by low pump powers, at the expense of probabilities on the order of a few percent or less to generate single photons only[63,65]. Storing single photons in a memory whenever they are generated can turn a probabilistic into a deterministic source. This is particularly important when multiple photons are needed at the same time, for example in measurement-based one-way quantum computing with photonic cluster states[66,67].

Photonic cluster states can be created by entangling single photons performing probabilistic Bell measurements[6,68]. Here, memories can enhance their generation by reducing both the probabilistic aspect of photon pair generation and of entanglement schemes[69].

In particular, the Raman memory scheme can be used to create optical time-frequency multiplexed continuous variable cluster states [70,71].

Without quantum memories, the probabilistic photon pair generation quickly leads to low coincidence rates of generating multiple photons at the same time and, in consequence, to long measurement times. In an experiment entangling eight-photons, only ~ 9 eight-photon coincidence events per hour were obtained [72]. In a hybrid approach with quantum memories, temporal multiplexing using quantum memories [58,61] is combined with spatial multiplexing with several sources and active switching [73,74], so that N sources are combined with a quantum memory each [75]. The concepts of spatial and temporal multiplexing, as well as the hybrid approach are depicted in Fig. 1.1. Storing a single photon whenever it is emitted by the source reduces the waiting time till N photons are available by several orders of magnitude. For example, the average time to generate $N = 12$ photons at the same time can be reduced from ~ 3 years to $\sim 100\,\mu$s (pump pulse repetition rate: 1 GHz, heralding efficiency: 50 %, memory storage and retrieval effieciencies: 75 %, memory time bandwidth product: 1000, postselection) [75]. This enables multiphoton experiments at enhanced rates, necessary for single gates, complex computational operations or quantum networks in which operations can be synchronised by quantum memories as well [76].

1.3 Quantum computing

Quantum computers [77] are able to complete some tasks efficiently, which are computationally more expensive for classical computers [78]. For example, this includes the Shor algorithm for the prime factorisation of integers [79,80] and the Grover algorithm for the search through unstructured databases [81,82]. Furthermore, quantum computers enable efficient simulation

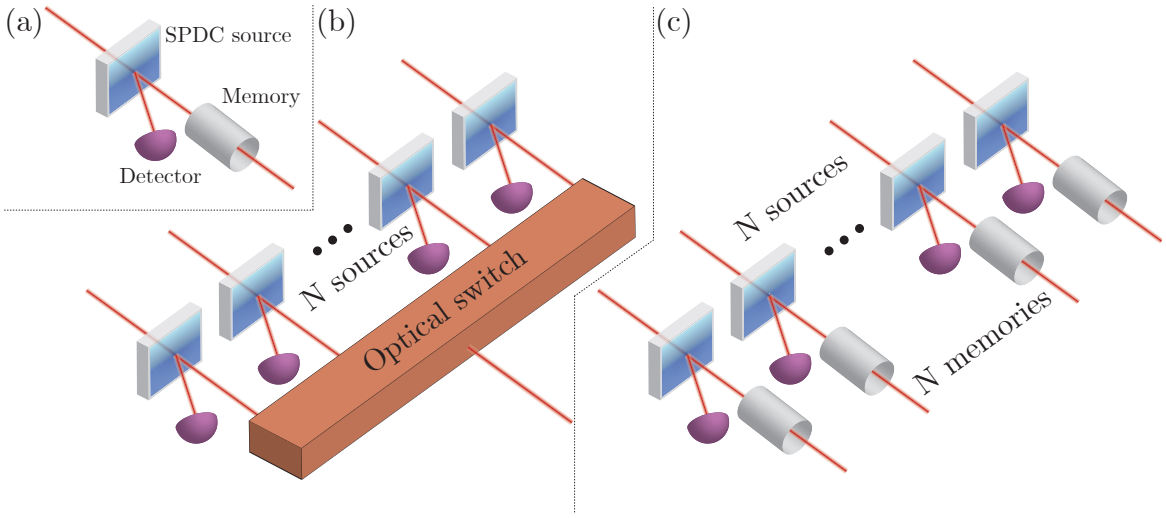


Figure 1.1: (a) Temporal multiplexing: The SPDC source is pumped repeatedly until a photon pair is generated. The heralding photon is measured by a detector, the signal photon is stored inside the memory and can be released for synchronisation with other events. (b) Spatial multiplexing: N sources are operated continuously in parallel. Whenever a photon pair is generated, the signal photon is sent into an optical switch, which is controlled by the detector signals of the heralding photons such that a successful channel can be selected. The single photon rate is enhanced at the output of the optical switch. (c) Hybrid multiplexing approach for enhanced multiphoton rates: N sources are operated continuously in parallel. Whenever a photon pair is generated, the signal photon is stored in the corresponding memory. The heralding photon indicates the emission of a signal photon and an attempted storage process. As soon as the number of photons already stored in a memory and the number of photons emitted from a source with an empty memory sum up to N, all photons are released and N photons are simultaneously available for further experiments. Subfigure (c) is adapted from [75].

of other quantum sytems [83,84].

In the same manner as in classical computing, logical gates can be defined as basic building blocks for more complicated calculations. Matter-based quantum computing includes systems as trapped ions [85–87], quantum dots [88,89], nuclear spins [90,91], superconductors [92–94] and colour centres in diamond [51,95–100]. In these systems, localised qubits can be coherently manipulated for computational operations on time scales limited by their life and coherence times. Information exchange between single localised qubits is realised by means of optical transmission of quantum signals.

An early pure photonic approach of quantum computing included nonlinear

photon-photon interactions to realise nondemolition measurements[101] and all-optical gates[13,102,103]. The nonlinear Kerr-effect[13,104–106] leads to phase-shifts depending on photon numbers in both optical fields and their interaction time. However, these are hard to realise on the single photon level and only small phase shifts on the order of 10^{-18} rad per photon are expected in nonlinear media due to the Kerr effect[107]. To overcome this limitation, highly excited Rydberg states in combination with electromagnetically induced transparency (EIT) can be used[108–111]. With this method, the nonlinear interaction in the medium is enhanced and phase shifts up to π rad have been reached[112]. However, it was shown that for single-photon Kerr nonlinearities high fideltities (low noise) and high phase shifts are mutually exclusive[113].

Another scheme of cross-phase modulation, bare of cavities and Rydberg atoms, is based on four-wave mixing (FWM) in a double-Λ system[114]. The phase shift and transmission of a signal field through the medium is governed by the total phase of all four interacting fields. Phase shifts of up to 3.6 ± 1 rad were measured between light pulses of only 8 photons in the double-Λ system formed by the D_2-line of cold ^{87}Rb[114].

In linear optical quantum computing (LOQC)[13], nonlinear photon-photon cross-phase modulation is omitted. Building blocks can be created using beam splitters and phase shifters. E. Knill, R. Laflamme and G. J. Milburn were able to show with their KLM-protocol, that on the basis of single photons, beam splitters, phase shifters and photon-detectors only, a universal quantum computer can be created[115]. The gates constructed from these elements are of probabilistic nature and, therefore, not successful at every attempt of operation. This requires quantum memories to store photons after successfully operated gates, waiting for other gates to succeed and to provide their signal for further operations

in a synchronised manner [76]. Unfortunately, LOQC requires a severe overhead of optical components in comparison to matter qubits [116].

1.4 Quantum communication

Distributing quantum information over long distances is necessary to establish quantum communication [117], secured by quantum cryptography [118], and to build large-scale quantum networks [119,120].

Secure quantum communication is enabled by quantum key distribution (QKD) which can be based on prepare-and-measure protocols, for example BB84 [121], or entanglement [122]. In the first case a secure key is established by exchanging quantum states. However, communication channels are not loss-free. Even at telecommunication wavelengths, optical signals experience losses of $\sim 0.2\,{}^{\mathrm{dB}}/_{\mathrm{km}}$ [117], quickly suppressing transmission rates to values that make the exchange of information impracticable. For example, transmission rates are reduced by ten orders of magnitude over a distance of 500 km [117]. Moreover, most qubits operate in the visible range of light, where higher losses of $\sim 1.8\,{}^{\mathrm{dB}}/_{\mathrm{km}}$ at 850 nm or more, towards shorter wavelengths, occur [123,124].

In classical signal processing signals are regularly amplified to ensure their full transmission. Unfortunately, for arbitrary quantum states, this is not possible due to the no-cloning theorem [10,125] and, as a consequence, prepare-and-measure protocols are hard to realise over long distances due to photon loss during signal transmission.

Loss can be circumvented in entanglement-based QKD by means of quantum repeaters [126], dividing the complete communication distance into $N-1$ stretches with N nodes. Smaller distances between nodes reduce losses and, thus, increase entangling probabilities

between adjacent nodes. As soon as entanglement is created between neighbouring nodes, the entanglement is extended over additional nodes by entanglement swapping [127] till the outermost nodes, which are separated by the full communication distance, are reached and entangled [117,128]. Quantum memories at each node store the entangled states till neighbouring entanglement operations have succeeded and the overall entangling scheme can proceed. Therefore, the memory lifetime is limiting the distance by which nodes can be separated. With the same entangling method, whole quantum networks can be generated.

The DLCZ protocol for long-distance quantum communication [129], developed by L.-M. Duan, M. D. Lukin, J. I. Cirac and P. Zoller in 2001, received a lot of attention and has been realised in many different systems [130]. Using the DLCZ memory protocol [129] (see Section 9.3), entanglement between two memory nodes is created by interference of single photons at beam splitters [131,132]. Independent of the memory protocol, quantum repeaters can also be created using photon pair sources [133] or single-photon sources and beam splitters [134]. The principle of long-distance entanglement via quantum repeaters as well as possible designs of quantum repeaters are shown in Fig. 1.2.

The previous sections have shown the importance of quantum memories for many emerging fields of research and applications. For practical use, memories need to be reliable, compatible with interacting photonic structures, compact and easily scalable.

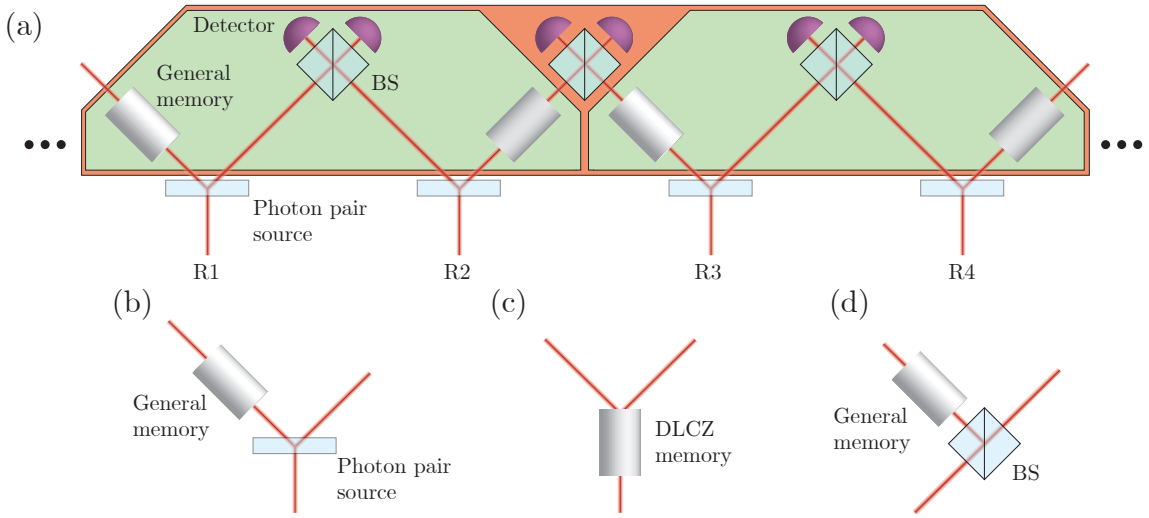


Figure 1.2: Long-distance entanglement distribution via quantum repeaters and quantum repeater designs: (a) Equidistant quantum repeaters R1 to R4 based on photon pair sources. Each photon pair source, for example a SPDC crystal, emits two entangled photons: one is stored in a memory, the other one interferes at a beamsplitter (BS) with a photon emitted from another source. If either one of the two detectors clicks, entanglement is established between the memory modes of two adjacent quantum repeaters. Entanglement between R1 and R2, and between R3 and R4, is depicted as green background. In a next step, photons are released from the memories of R2 and R3 creating entanglement between the memory modes of R1 and R4 by entanglement swapping with the same measurement-based entanglement scheme as in the first step (orange background). (b) Quantum repeater based on photon pair sources. A pair of photons are generated: one of which is sent to interfere with a photon from an adjacent node, while the other photon of the pair is stored (locally) in a quantum memory. Once entanglement has successfully been established across the first link, the second photon may then be released and used for entanglement swapping along another adjacent link. (c) Quantum repeater based on the DLCZ memory protocol. In each node, a single photon is scattered inside the interaction medium of the memory, emitting a scattered Stokes photon used for entanglement creation between the memory modes created during the scattering process. As soon as entanglement is heralded by the detectors, the memory mode is emitted as anti-Stokes photon in a second off-resonant scattering process and interacts at another BS for entanglement swapping. (d) Photons from a single-photon source are sent through a BS. The reflected mode is stored in a general quantum memory while the transmitted mode interferes at a beam splitter in order to create entanglement between the two memory modes of neighbouring nodes. Photon number entanglement can be created between the two outermost nodes by entanglement swapping.

1.5 Thesis outline

This thesis will discuss steps towards the realisation of optical Raman quantum memories with colour centres in diamond.

In Chapter 2, several quantum memory protocols are discussed and figures of merit for their evaluation are introduced. For the Raman memory scheme, previous experimental achievements, advantages and drawbacks are explained in greater detail.

Chapter 3 focusses on colour centres in diamond. The choice of diamond as host material, basic properties of photoluminescence spectra of colour centres and optical linewidths are addressed. Phonons and the dynamic Jahn-Teller effect are detrimental for life and coherence times but can be suppressed by several methods. The nitrogen vacancy centre and the silicon vacancy centre are introduced with special emphasis on their symmetry, their optical properties, the implications of their electronic structure and the life and coherence times of potential memory storage states. The neutrally charged nitrogen vacancy centre as well as the negatively charged silicon vacancy centre are going to be in the centre of theoretical and experimental investigations in later chapters.

Apart from long life and coherence times, the incoherent and coherent control of ensembles of atomic-like systems is necessary for the preparation and implementation of the Raman memory protocol. These techniques of atomic light-matter interaction are discussed in Chapter 4. Optical pumping in a three-level Λ-system is explained and limits of population transfer inside the system are highlighted. On the basis of the optical

Bloch sphere, coherent manipulation techniques are clarified which will be applied to ensembles of silicon vacancy centres in this thesis. The chapter concludes with a short introduction to four-wave mixing, a nonlinear effect that hampers noiseless memory operation.

In Chapter 5 the negatively charged nitrogen vacancy centre and its neutral counterpart are assessed for off-resonant Raman interaction. Thereupon, the impact of external electric fields on the neutral nitrogen vacancy centre with regard to the orbital level splitting of the ground states, the polarisation of the optical transitions, the Raman coupling in the limit of far off-resonant detuning and the relative noise intensity is examined for two different possible experimental configurations. In this way, criteria are developed for a noise-free Raman optical memory in the solid state. In a final step, the lifetime and coherence time of the memory state is estimated.

The experimental results presented in Chapter 6 support the theoretical investigations in the previous chapter. Applying external uniaxial stress, the orbital ground state levels of an ensemble of neutral nitrogen vacancy centres are split and cross-linear polarisation selection rules are strengthened. Resonant pumping measurements point towards the theoretical ground state lifetime.

The negative silicon vacancy centre is investigated in Chapter 7. Initially, an estimate of the ground state coherence time is made, then measurements of the ground state lifetime are presented, and coherent control and coherent population transfer within an ensemble of silicon vacancy centres are demonstrated. Moreover, phase-dependent light-matter

interactions based on four-wave mixing are shown. Both, the model for coherent control, used for the determination of coherence times and population transfer efficiencies, and the model for phase-sensitive interaction, breaking down the mechanisms involved, are explained at the end of the chapter.

Chapter 8 gives a conclusion of the results presented in this thesis, and finally in Chapter 9, further necessary steps towards the implementation of an optical Raman memory are discussed and the overall scope is extended beyond memory applications and towards other inversion symmetric colour centres in diamond.

Chapter 2

Quantum memories

QUANTUM memories carry the promise of a broad range of applications which led to an intensified research in this area over the last years.

In this chapter, a range of protocols for the implementation of the storage of classical and quantum fields of light are reviewed. First, in Section 2.1, the principal figures of merit used for the evaluation of memory protocols are discussed. Memory schemes are introduced in Section 2.2, starting with delay lines, optical cavities (§2.2.1) and photon echo techniques (§2.2.2). Then, more sophisticated methods are discussed, which include controlled reversible inhomogeneous broadening (CRIB) (§2.2.3), atomic frequency combs (AFC) (§2.2.4) and electromagnetically induced transparency (EIT) (§2.2.5). However, while these protocols require operation close to resonance, the Raman memory scheme offers ultrafast broadband storage by means of off-resonant two-photon transitions. This scheme, its previous results, the encountered problems as well as some possible ways forward for this platform will be elucidated in Subsection 2.2.6.

2.1 Figures of merit

In order to compare different types of quantum memories and to evaluate their performance several figures of merit are in common use. These include [60,128,135]

- ***Efficiency*** - The efficiency is defined as the intensity ratio between the stored (st.) and retrieved (ret.) optical field,

$$\eta = \frac{I_{\text{ret.}}}{I_{\text{st.}}}. \tag{2.1}$$

  This number can be easily adulterated by noise fields generated during the memory protocol (see Subsection 2.2.6). Storing single photons, the efficiency corresponds to the probability to re-emit a stored photon. In particular, the storage efficiency is important for a high entanglement distribution rate in quantum repeaters [117].

- ***Fidelity*** - The fidelity $\mathcal{F}$ describes the similarity between the quantum state read in and the quantum state read out of the memory and can be calculated by the overlap of the input and output density matrices, ρ_{i} and ρ_{o}, [136]

$$\mathcal{F} = \left[\text{Tr}\left(\sqrt{\sqrt{\rho_{\text{i}}}\rho_{\text{o}}\sqrt{\rho_{\text{i}}}}\right)\right]^2 \text{ (General case, mixed and pure states),} \tag{2.2}$$

$$\mathcal{F} = \text{Tr}(\rho_{\text{i}}\rho_{\text{o}}) = |\langle\psi_{\text{i}}|\psi_{\text{o}}\rangle|^2 \text{ (for two pure states, } \rho_{\text{i}} = |\psi_{\text{i}}\rangle\langle\psi_{\text{i}}| \text{ and } \rho_{\text{o}} = |\psi_{\text{o}}\rangle\langle\psi_{\text{o}}|), \tag{2.3}$$

  where $\mathcal{F}$ satisfies $\mathcal{F}(\rho_{\text{i}}, \rho_{\text{o}}) = \mathcal{F}(\rho_{\text{o}}, \rho_{\text{i}})$ and $0 \leq \mathcal{F}(\rho_{\text{i}}, \rho_{\text{o}}) \leq 1$ [136]. For single photons, the fidelity is conditional on successful retrieval from the memory with a classical bound of $\mathcal{F}^{\text{max}}_{\text{class.}} = \frac{2}{3}$ [137]. Higher values are only achievable in the quantum regime.

For coherent states the classical limit of the average fidelity approaches $\frac{1}{2}$ for large average photon numbers $\bar{n}$ [135,138,139].

- ***Storage Time*** The storage time is the time a signal field can be stored inside a memory and is in general limited by decoherence processes. Depending on the area of application, for example, long range quantum repeaters or local photon synchronisation and feed-forward, storage times of different orders of magnitude are required.

- ***Acceptance Bandwidth*** The acceptance bandwidth defines the maximum bandwidth which a single pulse can have for storage in the memory. The higher the acceptance bandwidth, the shorter pulses can be stored and the higher repetition rates can be achieved. Furthermore, the acceptance bandwidth is also important for spectral and temporal multiplexing. From the storage time τ and the acceptance bandwidth δ, one derives the time-bandwidth product TBP $= \delta\tau$ [75], which approximates how many operations with pulses of bandwidth δ could be possible during the storage time τ. For example, this is important for the generation of multiphoton states [75].

- ***Multimode Capacity*** - The multimode capacity relates to the number of temporal and spectral optical modes that can be stored inside an ensemble memory at the same time. For each memory scheme this scales differently with the resonant optical depth of the memory ensemble [140].

In [60] several types of quantum memories are evaluated against these criteria. As further figures of merit, the operating wavelength, the robustness and the ease of use can also be considered [128]. For quantum communication in optical fibres over long distances an operating wavelength in the low-loss window from 1260 nm to 1625 nm is desirable,

where, additionally, existing telecommunication infrastructure could be used. However, if memories at these wavelengths are not available, frequency conversion could be used to enable the storage and the long-distance transmission to occur at different wavelengths [141]. Furthermore, for the final application of quantum memories under non-laboratory conditions, systems should be resilient to outside influences and easy to operate. A small volume, operation at room temperature, a limited number of different laser sources, low technological and optical overheads as well as scalability are preferential.

2.2 Quantum memory protocols

Over the last two decades different quantum memory protocols have been developed, each trying to meet high figures of merit, and to be a versatile tool for the storage of single photons.

For single atomic-like systems, like single quantum dots or single colour centres, the interaction strength is typically small but can be enhanced by placing the system inside a cavity. Memories based on ensembles are often preferred as they are experimentally easier to implement and offer the advantage of increased light-matter interaction and higher memory efficiencies.

2.2.1 Non-light-matter quantum memories

Apart from storing light inside atomic-like systems it is also possible to bound light spatially in optical delay lines or cavities. Most fundamentally, light can be delayed by a fixed amount of time in optical fibres. However, limits are quickly reached, as confinement and guidance in optical fibres, even at telecommunication wavelength, involves losses so that only delay halftimes of $\sim 70\,\mu s$ can be achieved [142].

More flexibility is offered by high Q-factor cavities with fast electro-optical switching elements. Yet, the storage time needs to be an integer multiple of the round trip time and the memory time is limited by the loss per round trip and the switching loss. It has been shown that all optical storage loops with ultra-low loss optical elements can provide storage halftimes of $\sim 70\,ns$ for pulses of $1.7\,ns$ [76]. These cavities may find application in the synchronisation of single photon sources [143,144] or as part of a hybrid quantum memory enabled network [76].

2.2.2 Echo memories

Based on Erwin Hahn's experiments on the nuclear spin echo [145] (see Subsection 4.2.3), optical echo techniques have been developed, for example, the two-pulse optical echo used for the first time in [146]. Later, three pulse echo techniques were developed for the storage of classical light [147,148]. Unfortunately, these techniques cannot be extended to the single-photon level, as the application of π-pulses leads to population inversion which results in a signal-to-noise ratio (SNR) of 1 at the single-photon level and gain for coherent pulses [149,150].

The memory protocol using the controlled reversible inhomogeneous broadening (CRIB) of an optical transition presented in the next section is very similar to photon echo protocols, however, an echo is not generated by optical fields but by manipulation of the inhomogeneous broadening of an ensemble. In this way the detrimental effects of population inversion at the single-photon level are circumnavigated.

2.2.3 Controlled reversible inhomogeneous broadening (CRIB)

The fundamental idea of using the inhomogeneous broadening of an ensemble for photon echoes was presented by S. A. Moiseev and S. Kröll in 2001 [151]. Although their theory was based on the reversal of the inhomogeneous Doppler-broadening for counterpropagating fields in gases, their theory was soon applied in solid-state materials with external electric or magnetic fields [152–155].

Solid-state media, predominantly rare-earth-ion-doped (REID) crystals and glasses, are used. These offer narrow optical homogeneous linewidths due to reduced electron orbit-

lattice interactions[156] and fast, and sufficiently strong, manipulation by external electric and magnetic fields. Storage of weak coherent fields at telecommunication-wavelength could be realised[157]. However, as only a fraction of the inhomogeneously broadened ensemble is used as described in the following paragraph, only low optical depths and, therefore, low memory efficiencies are reached[154]. Furthermore, the acceptance bandwidth is limited by homogeneous linewidths in REID crystals in the kHz regime[156].

In the following, the protocol of the controlled reversible inhomogeneous broadening (CRIB) memory is described and shown in Fig. 2.1. In an ensemble of two-level systems with ground state $|g\rangle$ and excited state $|e\rangle$, the optical transition is inhomogeneously broadened ((a) (i)). This inhomogeneous broadening can be reduced using techniques such as spectral hole-burning[158] leaving only a narrow band at the central frequency of the inhomogeneous spectral distribution ((a) (ii)). An external magnetic or electric field is applied which broadens the spectral distribution again using the magnetic Zeeman[159–161] or the electric Stark effect[162] ((b) (i)). On the one hand the application of a static, spatially invariant, magnetic field can lift the degeneracy of spin levels. On the other hand fields can be applied which are changing linearly and symmetrically around zero over the length of the interaction medium, which leads to a symmetric response in frequency shift of the optical transition within the ensemble depending on its position ((b) (i) and (ii)). The latter is also known as gradient echo memory (GEM) and offers forward emission without re-absorption so that higher efficiencies than with the original CRIB protocol can be reached[155,163]. In both approaches the maximum frequency shift must be much larger than the inhomogeneous broadening after optical preparation. If now an optical pulse is absorbed, the ensemble

finds itself in a state [152]

$$|\psi\rangle = \alpha\,|g\rangle + \beta\,|e\rangle\,, \tag{2.4}$$

with photon absorption probability $|\beta|^2$. Depending on the detuning $\delta_j = \nu_j - \nu_0$ of each system in the ensemble, a phase of $\phi_j = \delta_j\tau$ is collected over a time τ. As soon as the gradient of the external field is inverted the detuning of each system changes sign, $\delta_j \to -\delta_j$ ((b) (i) and (ii)). Thus, the dephasing of the ensemble will have been reversed after another time τ and a photon echo can be measured. This can also be depicted with the use of the optical Bloch sphere (see Subsection 4.2.1). As soon as a superposition of ground and excited state is created each system precesses freely, collecting a phase proportional to its detuning from resonance ((b) (iii)). This process is reversed changing the sign but not the absolute value of detuning for each system ((c) (iii)).

The storage time is only limited by the inhomogeneous broadening of the narrow feature generated by spectral hole-burning. The memory efficiency both depends on the optical depth of the broadened absorption peak d and the spectral width (standard deviation) of the unbroadened absorption peak γ [157],

$$\eta(t) = d^2 e^{-d} e^{-t^2\gamma^2}. \tag{2.5}$$

For CRIB, backward emission is preferential for the memory efficiency [164]. The multimode capacity scales linearly with the optical depth [140].

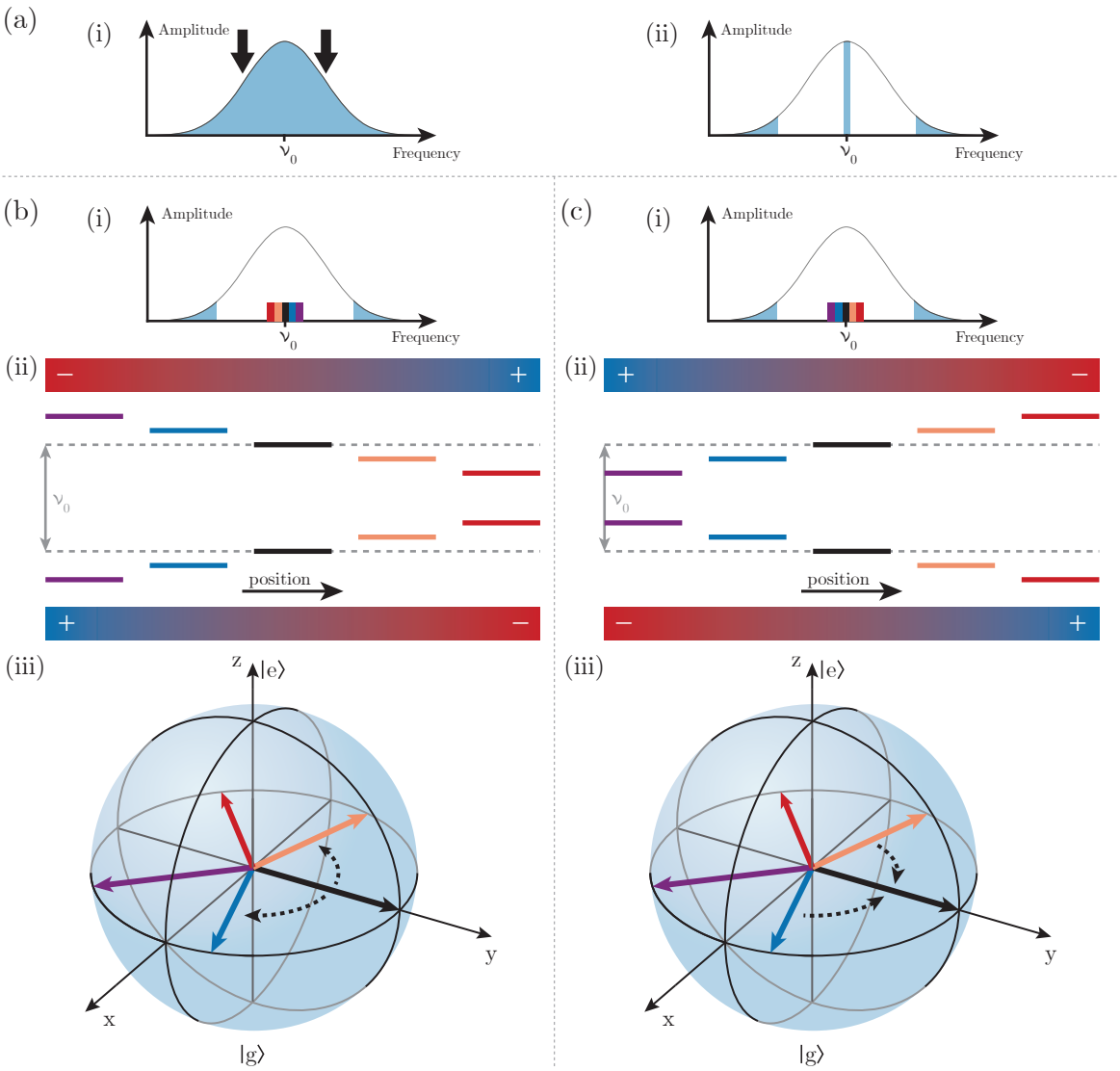


Figure 2.1: CRIB/GEM: (a) Inhomogeneous broadening of the optical transition $|g\rangle - |e\rangle$ before (i) and after (ii) spectral hole-burning. The central wavelength is indicated by ν_0, the areas of population removal by black arrows. (b) The systems at central frequency experience a frequency shift due to an external electric or magnetic field. The transition is inhomogeneously broadened in a controlled way (i). This may be realised by an external field gradient over the length of the ensemble (ii). Depending on the detuning of each system the states are dephasing on the Bloch sphere (iii). Arrows and energy levels show corresponding colours. (c) After a time τ the external field gradient is reversed leading to a reversed spectral distribution (i,ii) and a rephasing of all states on the Bloch sphere after a total time of 2τ (iii).

2.2.4 Atomic frequency comb (AFC)

Another way of shaping the inhomogeneous lineshape of an optical transition is the creation of a regularly structured atomic frequency comb (AFC) [165–167]. For this memory protocol, an ensemble with at least three atomic energy levels, a ground state $|g\rangle$, an excited state $|e\rangle$ and a metastable auxiliary state $|\text{aux}\rangle$, is necessary as can be seen in Fig. 2.2 (a). The optical transition between ground and excited state needs to be inhomogeneously broadened, with an inhomogeneous linewidth Γ_{inh} much larger than the homogeneous linewidth of each atomic system γ_{h}, $\Gamma_{\text{inh}} \gg \gamma_{\text{h}}$. This is necessary to create a regular structure of narrow peaks in the atomic density distribution of the inhomogeneous broadening as depicted in Fig. 2.2 (b). For each of the peaks, separated by Δ, the spectral width (FWHM) δ must exceed the homogeneous broadening of the transition, $\delta > \gamma_{\text{h}}$. The population removed from state $|g\rangle$ is transferred to the auxiliary level $|\text{aux}\rangle$ by means of optical pumping.

Even though a spectral comb structure in the optical density is created, due to the short pulse duration and the Heisenberg energy time uncertainty relation, resonant optical pulses can be completely absorbed if their spectral width δ_{p} is chosen much larger than the peak splitting, $\delta_{\text{p}} \gg \Delta$. The photon is stored as a Dicke state [168], an atomic excitation delocalised over the ensemble [166],

$$|\psi\rangle = \sum_{j=1}^{N} c_j e^{i\delta_j t} e^{-ikz_j} \, |g_1 \cdots e_j \cdots g_N\rangle \,, \tag{2.6}$$

where N is the total number of atomic-like systems in the ensemble, δ_j and z_j are the detuning from resonance of the optical transition and the position of system j respectively. The probability for storage in a specific excited state is given by $|c_j|^2$.

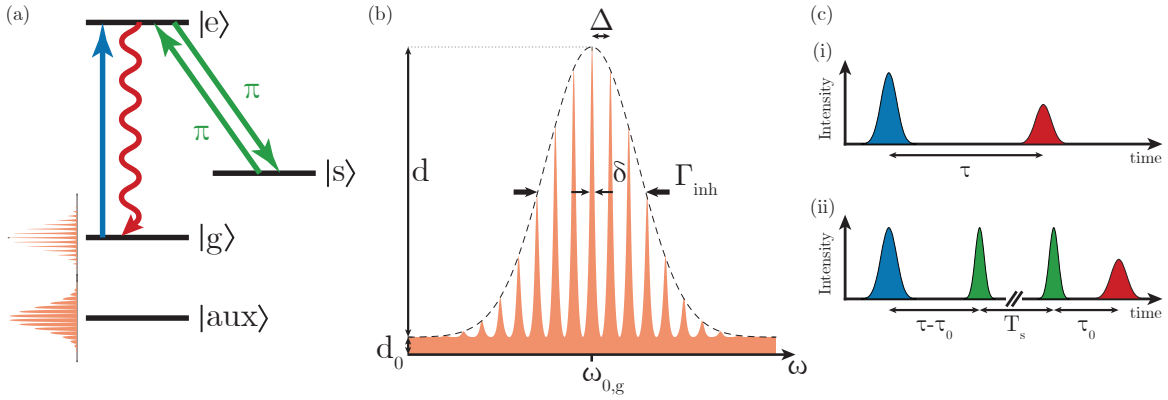


Figure 2.2: AFC: (a) Level scheme: A regular spectral frequency comb is prepared in the ground state $|g\rangle$. Excess population from the initial inhomogeneous distribution is removed to an auxiliary state $|\text{aux}\rangle$. A field to be stored (blue straight arrow) is applied resonantly to the optical transition $|g\rangle - |e\rangle$. For the transfer to a long-lived spin state $|s\rangle$, π-pulses can be applied (green straight arrows). After the full memory time τ an optical field via phonon echo is emitted (red sinusoidal arrow). (b) Spectral comb structure with the FWHM inhomogeneous broadening Γ_{inh} of the optical transition $|g\rangle - |e\rangle$, the FWHM spectral broadening of each peak δ, the peak separation in frequency Δ, the optical depth of the peak structure d and the residual optical depth d_0. The original inhomogeneous broadening is shown as black dashed line. (c) Pulse sequence: (i) After read-in the pulse is stored for a time $\tau = \frac{2\pi}{\Delta}$. (ii) After $\tau - \tau_0$ a π-pulse is applied transferring the population to a long-lived spin state $|s\rangle$. After a time T_s another π-pulse is applied and the stored field is emitted after the remaining AFC storage time τ_0. The colours of the pulses correspond to the fields in (a).

Due to the periodic structure of the population density distribution, the phase ϕ collected by the system is an integer multiple m_j of the peak splitting Δ, $\phi_i = m_j \Delta t$. After m_j full phase oscillations and a fixed memory time of[166]

$$\tau = \frac{2\pi}{\Delta}, \tag{2.7}$$

all systems are in phase again and the stored field is re-emitted by a coherent photon echo.

In order to extend this fixed memory time, the coherent excitation of the ensemble can be stored by an optical π-pulse (see Section 4.2) as a collective spin wave[169,170] in a long-living spin state $|s\rangle$ shown in Fig. 2.2 (a). A storage over a flexible time T_s in such a spin state is possible as the comb structure is not imprinted on the transition of the spin state. This is only true if the broadening of the $|g\rangle$-$|e\rangle$ and the $|e\rangle$-$|s\rangle$ transition are not correlated[166].

Therefore, the dephasing process is paused, but resumed when the population is transferred back into the excited state by another π-pulse. Pulse sequences for pure and extended AFC are presented in Fig. 2.2 (c). The memory efficiency for forward emission is given by [165]

$$\eta = \left(\frac{d}{F}\right)^2 e^{-\frac{7}{F^2}} e^{-\frac{d}{F}} e^{-d_0}, \tag{2.8}$$

where $F = \frac{\Delta}{\delta}$ is the finesse, d the optical depth of the comb and d_0 the residual optical depth as shown in Fig. 2.2 (b). The isolated write efficiency is defined as $\eta_{\mathrm{w}} = 1 - e^{-\frac{d}{F}}$ [165]. A particular strength of the AFC protocol is its multimode capacity [171]. The temporal and spectral multimode capacity is not limited by the optical depth [140,166], ultimately, it is linear in the number of comb teeth, which is only limited by the number of atoms in the ensemble as the number of modes stored can never exceed the number of atoms [140]. The number of teeth is also limited by the inhomogeneous linewidth, as it must be ensured that the teeth are well separated, which, in general, is true for $F \gtrsim 30$ [140].

2.2.5 Electromagnetically induced transparency (EIT)

In contrast to CRIB and AFC, electromagnetically induced transparency (EIT) [172] does not rely on photon echo but instead on changing intrinsic properties of the material in order to store light.

In an optical Λ-system, as shown in Fig. 2.3 (a) (i), a weak probe (P) and a strong control (C) field are applied to the transitions $|1\rangle - |3\rangle$ and $|2\rangle - |3\rangle$ respectively. For the special case of a resonant control field, the excited energy level is dressed and split by the Autler-Townes effect [173,174], leading to an energy shift of $\omega_{\pm} = \pm\Omega_C/2$ from the initial energy [108] (Fig. 2.3 (a) (ii)). Due to this splitting, the linear response, i.e. the polarisation of the

medium, to a weak probe field E_P, is altered [106]:

$$\tilde{P} = \tilde{P}_0 + \varepsilon_0 \chi^{(1)} E_P, \tag{2.9}$$

where the polarisation of the undisturbed system is given by $\tilde{P}_0$, ε_0 is the vacuum permittivity and $\chi^{(1)}$ the linear electric susceptibility.

For the case of a resonant control field ($\Delta_C = 0$) the linear susceptibility encountered by a probe field of detuning Δ_P behaves like [108]

$$\begin{aligned}\chi^{(1)}(\Delta_\mathrm{P}) \propto & \frac{4\delta(|\Omega_C|^2 - 4\delta\Delta) - 4\Delta\gamma_{21}^2}{||\Omega_C|^2 + (\gamma_{31} + i2\Delta)(\gamma_{21} + i2\delta)|^2} \\ & + i\frac{8\delta^2\gamma_{31} + 2\gamma_{21}(|\Omega_C|^2 + \gamma_{21}\gamma_{31})}{||\Omega_C|^2 + (\gamma_{31} + i2\Delta)(\gamma_{21} + i2\delta)|^2},\end{aligned} \tag{2.10}$$

depending on $\Delta = \Delta_P$, the two-photon detuning $\delta = \Delta_P - \Delta_C$, the Rabi-frequency of the control field $\Omega_C = -\frac{\vec{d}_{23}\vec{E}_C}{\hbar}$, where $\vec{d}_{23}$ is the electric dipole moment between state $|2\rangle$ and state $|3\rangle$ and $\vec{E}_C$ is the electric field of the control field, and the coherence decay rates $\gamma_{31} = \Gamma_3 + \gamma_{3,\mathrm{deph}}$, $\gamma_{32} = \Gamma_3 + \gamma_{3,\mathrm{deph}} + \gamma_{2,\mathrm{deph}}$ and $\gamma_{21} = \gamma_{2,\mathrm{deph}}$. The spontaneous emission rate from the excited state is given by $\Gamma_3 = \Gamma_{31} + \Gamma_{32}$ with pure dephasing rates $\gamma_{\{i,j\},\mathrm{deph}}$ of state $\{i, j\}$. A simulation of the susceptibility for the specific case of $\Delta_C = 0$ (so $\Delta = \delta$), $\gamma_{21} = 0$ and $\Omega_C/\gamma_{31} = 1$ is shown in Fig. 2.3 (b). The imaginary part is directly connected to the dissipation of the probe field; the real part determines the refractive index $n = \sqrt{1 + \mathrm{Re}[\chi^{(1)}]}$. It can be seen that instead of anomalous diserpsion when no control field is applied, there is normal dispersion ($\frac{dn}{d\omega} > 0$) and no absorption ($\mathrm{Im}[\chi^{(1)}] \approx 0$) in between the two dressed states $|+\rangle$ and $|-\rangle$.

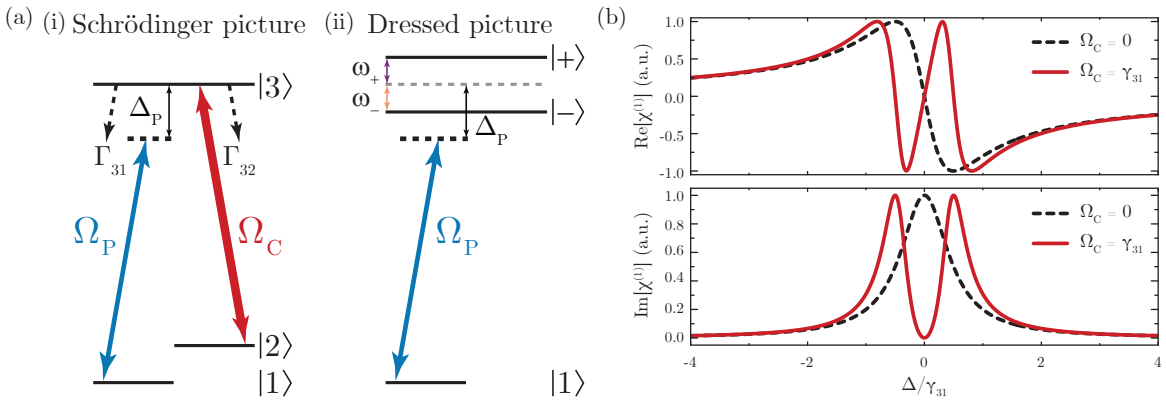


Figure 2.3: EIT: (a) Level scheme in (i) the Schrödinger and (ii) the dressed picture. (i) A probe field (Ω_P) and a control field (Ω_C) are applied on the optical transitions $|1\rangle - |3\rangle$ and $|2\rangle - |3\rangle$. While the control field is on resonance, the probe field is detuned by Δ_P. Spontaneous emission rates from state i to state j are given by Γ_{ij}. (ii) The dressed states $|\pm\rangle$ are shifted by $\omega_\pm$ from the resonant transition $|1\rangle - |3\rangle$. The probe field is detuned by Δ_P from the central frequency. (b) Real and imaginary part of the linear susceptibility $\chi^{(1)}$ (see equation (2.10)) for $\Omega_C = 0$ and $\Omega_C = \gamma_{31}$. Furthermore, γ_{21} is chosen to be zero.

In consequence, pulses travelling through the medium experience a reduced group velocity $v_{\mathrm{gr}} = \frac{d\omega}{dk} = \frac{c}{n+\omega\frac{dn}{d\omega}}$ [175,176]. Furthermore, the group velocity dispersion vanishes, $\frac{d^2n}{d\omega^2} = 0$ [175,176], leaving the pulse shape unchanged. The storage time within a medium of length L is given by [175]

$$\tau = L\left[\frac{1}{v_{\mathrm{gr}}} - \frac{1}{c}\right], \tag{2.11}$$

where c is the speed of light in the medium. This does not only lead to slowing down a pulse travelling through a medium but also to the complete reversible mapping onto a long-lived coherence of the medium by controlling the strength of the control field [177,178]. This process is very similar to the controlled adiabatic population transfer governed by a mixing angle described in Subsection 4.2.4.

EIT has been realised in various materials such as hot rubidium (Rb) vapour[178], ultracold atoms in optical lattices[48] and magneto-optical traps (MOT)[176], and REID crystals[179]. In all these systems long coherence times from microseconds to seconds were reached with storage times up to 1 minute with an optimised optical preparation and decoupling from decoherence effects in Pr^{3+}:Y_2SiO_5[180]. Moreover, high storage efficiencies have been shown in cold Rb (78%)[29] and multipass REID crystals (76%)[181]. However, in comparison to CRIB and AFC, the multimode capacity only scales with the square root of the optical depth $\sqrt{d}$[140]. Furthermore, the acceptance bandwidth is limited by the width of the transparent window, typically in the MHz regime[29,180]. The MHz-regime also cannot be overcome in memory protocols using larger dynamically controlled Autler-Towns splittings[182].

Resonant operation is avoided in the Raman memory scheme presented in the next subsection, offering larger acceptance bandwidths.

2.2.6 The Raman memory

The Raman memory is based on Raman scattering, the inelastic scattering on atomic excitations discovered by Adolf Smekal[183], Chandrasekhara Venkata Raman[184], and Grigory Landsberg and Leonid Mandelstam[185] in the 1920s. The scattered light with lower energy than the initial photons is called the Stokes field. If energy is gained, the scattered light is referred to as the anti-Stokes field. This effect can be observed for light resonant and off-resonant to atomic transitions.

For the Raman memory, in particular, the case of off-resonant Raman scattering is interesting, as off-resonant Raman interaction offers broadband and fast interaction without populating any excited state. First, the concept was developed in 2000 for efficient mapping and storage of a quantum state of light in atomic excitations[186] and has been further developed by Joshua Nunn[169] and Alexey Gorshkov[170,187,188] in 2007. The maximum memory efficiency only depends upon the resonant optical depth d[188,189], its multimode capacity scales with $\sqrt{d}$ only[140].

In Fig. 2.4 the full Raman memory scheme is depicted. In an optical Λ-system an ensemble is prepared in one of its ground states by optical pumping (a). The ground states are split in energy by δ_g. For the storage process, two optical fields are applied simultaneously in two-photon resonance. Both fields are detuned from the excited state $|3\rangle$ by Δ. To operate in the Raman regime, Δ must be large in comparison to the excited state linewidth[189]. The field coupling to transition $|1\rangle - |3\rangle$ is a strong coherent control field. The field on transition $|2\rangle - |3\rangle$ is a weak signal field to be stored inside the memory which can be treated either as a coherent or a quantised field. In a two-photon process, the signal field is absorbed and population is coherently transferred from state $|2\rangle$ to state $|1\rangle$. A spin wave (see equation (2.6)), a collective, delocalised, atomic excitation, is created (b). In order to retrieve the stored information, once more, the control field is applied, population is transferred back to state $|2\rangle$ and the stored signal field is emitted (c). For a full adiabatic transfer the two-photon detuning from resonance needs to be dominant over the maximum

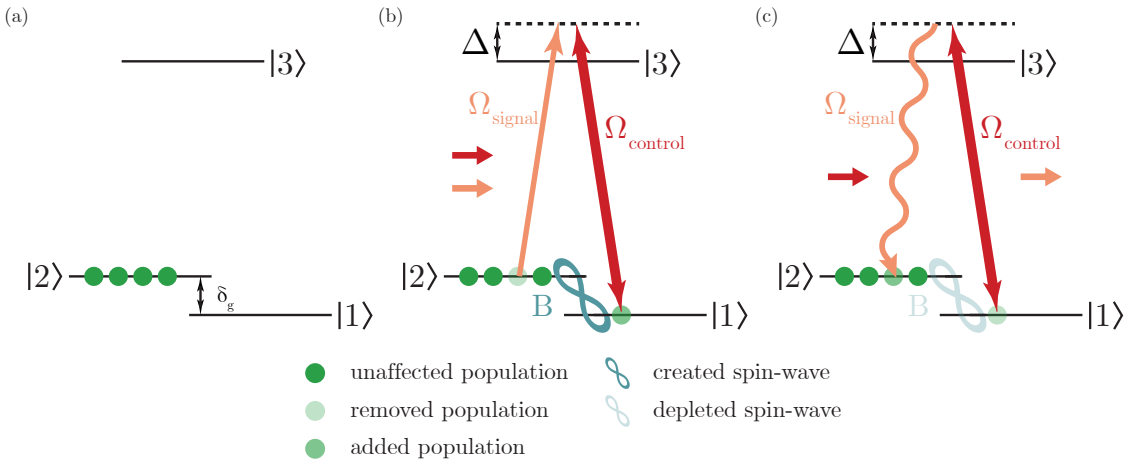


Figure 2.4: The Raman memory scheme. Optical fields entering (exiting) the ensemble are indicated by horizontal small arrows in the colour of the respective field on the right (left) side of each level scheme. (a) The three-level Λ-system with a ground state splitting of δ_g is prepared in ground state $|2\rangle$ by optical pumping. (b) Signal (Ω_{signal}) and control field (Ω_{control}) couple in two-photon resonance and singe-photon detuning Δ to the optical transition $|2\rangle - |3\rangle$ and $|3\rangle - |1\rangle$. In an off-resonant Raman transition, population is transferred from state $|2\rangle$ to state $|1\rangle$. The signal field is mapped onto the spin wave (B) created between the ground states. (c) In order to retrieve the stored signal field, the control field is applied again. The spin wave is read out, the signal is emitted and population is transferred back from state $|1\rangle$ to state $|2\rangle$.

Rabi frequency of the control field ($\Omega^{\text{max}}_{\text{control}}$) and the control field bandwidth (δ_{control})[189],

$$\Omega^{\text{max}}_{\text{control}} \ll |\Delta| \text{ and } \delta_{\text{control}} \ll |\Delta|. \tag{2.12}$$

As for EIT, adiabaticity is required to coherently transfer all properties of the signal field to the atomic system[108]. A full theoretical description of the Raman memory can be found in [189].

The bandwidth of the signal field is only limited by the detuning Δ from resonance, the bandwidth of the control field and, most fundamentally, by the ground state splitting of the ensemble, since the signal and control field must address the ground states separately. Ultrafast pulses can be stored with much higher TBP and clock rates than in resonant memory schemes. However, while the inhomogeneous broadening of the excited state requires further

off-resonant detuning only, inhomogeneous broadening of the ground state transition still limits the coherence time and, hence, the storage time.

Another advantage of the off-resonant interaction arises in cases of memory read-in efficiencies less than one. The share of the signal field not absorbed during the memory interaction can pass through the ensemble without further interaction in contrast to resonant techniques. Therefore, the Raman memory can be imagined as an array of beam splitters whose reflectivity equals the read-in or read-out efficiency of the memory [190].

The Raman memory was first realised in warm Cs vapour offering a ground state splitting between two hyperfine states ($6^2S_{1/2}$, $F = 3$ and 4) of 9.2 GHz [191]. Pulses of 1.5 GHz bandwidth have been stored for 12.5 ns with a total efficiency of 15 % and a TBP of 18.75. Nonetheless, as in this experiment the retrieval time was much less than the maximum coherence time of this transition, where coherence times can be expected to be of several hundred microseconds in hot vapour cells [192], time-bandwidth products of TBP $\approx 10^5$ appear achievable. Additionally, it has been confirmed that the read-in and the read-out process happen coherently [191]. In further experiments, polarisation storage in a dual-rail configuration for polarisation encoded information was shown with high fidelity (max. 97 ± 1 %) and with a storage time of 5×10^3 times the stored pulse duration [193]. The optical depth can be increased using waveguides such as hollow-core photonic crystal fibres [32,194] and suppression of radiation trapping [195]. Broadband heralded single photons have been stored in Cs vapour which identified four-wave mixing (FWM) processes as limiting factor for practical noise-free single-photon operation [31].

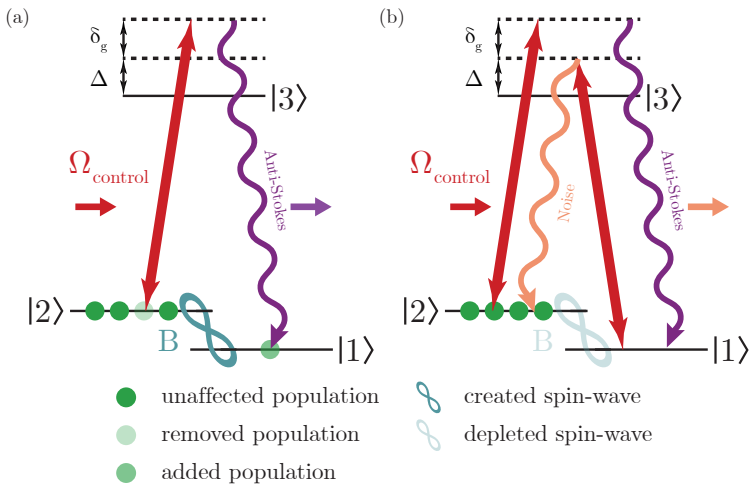


Figure 2.5: Four-wave mixing during the Raman memory protocol. (a) If not prevented, the strong control field (Ω_{control}) couples not only to state $|1\rangle$, as intended, but also to state $|2\rangle$. In a Raman scattering process in $(\Delta+\delta_g)$-detuning an anti-Stokes field is emitted, population is transferred from state $|2\rangle$ to state $|1\rangle$ and a spin wave is created. (b) In this situation the strong control field can scatter on state $|1\rangle$ emitting a noise field at the signal field frequency, transferring the population created in (a) back to state $|2\rangle$ and depleting the spin wave. After this FWM process the ensemble has returned to its initial configuration but the emitted noise field will be detected in addition to the stored signal field after the memory read-out.

Noise due to FWM can occur when the strong control field couples to both ground states as shown in Fig. 2.5. An anti-Stokes field is emitted when the strong control field couples to state $|2\rangle$. In this case, population is transferred from state $|2\rangle$ to state $|1\rangle$ and a spin wave is created (a). The control field can scatter on this newly populated state and emit a noise photon at the signal frequency (b). Population is transferred back to state $|2\rangle$ and the system returns into its initial state. Together, both scattering processes form a closed parametric contour in which noise is generated in a four-wave mixing process (see Section 4.3). This noise will be detected in addition to the stored signal field. A method to measure the strength of the noise process is applying the strong control field only during the read-in and read-out process. The light emitted at the signal field frequency is noise generated by FWM.

The FWM process can be suppressed by preventing the control field coupling to a second ground state via polarisation selection rules [55,196] (see Section 5.3). However, this method is ineffective for large detunings in alkali vapours [197]. Other methods include the evasion of phase-matching conditions by a large refractive index difference between the signal and anti-Stokes frequencies either through the use of a highly dispersive medium or through a large energy difference in the Stokes and anti-Stokes field [198].

Apart from alkali vapour cells, the Raman memory scheme has been successfully implemented in an ensemble of hydrogen molecules. Using the vibrational energy splitting ($\delta_g \approx 125\,\mathrm{THz}$), 100-fs pulses could be stored for 1 ns [199]. THz-bandwidth was also achieved in diamond using optical phonon modes ($\delta_g = 40\,\mathrm{THz}$ [200]) for storage at room temperature [198]. While lifetimes and coherence times are short ($\mathrm{T}_1 \approx 3.5\,\mathrm{ps}$, $\mathrm{T}_2 \approx 2\,\mathrm{T}_1$ [201]), FWM is suppressed due to high material dispersion [198]. Heralded photons were stored preserving the nonclassical photon statistics of single photons [202]. Furthermore, a photonic polarisation qubit of $\sim 250\,\mathrm{fs}$ duration was stored with high fidelity ($\mathcal{F} \approx 78\,\%$) and high memory efficiency ($\eta \approx 76\,\%$) for 1.3 ps [15].

Methods of noise suppression

In systems that cannot use dispersion for noise suppression, other approaches have to be chosen. An approach taken for alkali vapour cells is an external cavity [203,204]. Both storage interaction and noise suppression are enhanced. The FWM process is prevented by bringing the anti-Stokes field in anti-resonance and the control and signal field in resonance with a low-finesse birefringent cavity [203]. With this method, in theory, it is possible to suppress

noise sufficiently for nonclassical storage of single photons [204].

Optical memory mechanisms such as ORCA/FLAME [33,205] use another approach to suppress FWM processes. A ladder-type (Ξ) atomic system is employed using a highly excited state as storage level. Even though the strong control field can still couple to other energy levels, new fields generated by spontaneous Raman scattering can not couple to the storage state in a FWM process. Thus, noise is strongly suppressed in this memory scheme.

As already mentioned, polarisation selection rules on optical transitions for noise suppression are also favourable. Choosing cross-linear polarisations for signal and control field, the control field is hindered to couple to one out of two cross-polarised optical transitions and no FWM is initiated. In Chapter 5, this effect will be presented on the example of an ensemble of nitrogen vacancy centres (NV) in diamond. It is most effective if all colour centres are aligned along one axis and external fields, optical and polarisation axes can be chosen accordingly to maximise the effect. Recently, it was shown that through chemical vapour deposition (CVD) growth the orientation of NV centres can be efficiently controlled with high orientation probability ($> 90\%$) [206–208]. For the negative silicon vacancy centre (SiV^-), also treated in this thesis, no growth mechanism has been developed yet for a preferential orientation of its main symmetry axis. However, if necessary, single centres of a specific orientation can be preselected [209].

2.3 Summary

In this chapter, standard figures of merit have been introduced (§2.1) and, on this basis, different classes of memory schemes have been reviewed (§2.2). In particular, the Raman memory protocol is interesting (§2.2.6), as it offers the storage of ultrafast pulses in long-lived ground states with a high TBP. However, noise due to FWM is limiting storage at the single-photon level and needs to be suppressed. Next, the focus is laid on colour centres in diamond, which may be a promising platform for the implementation of the Raman memory protocol.

Chapter 3

Colour centres in diamond

A broad range of different quantum memory techniques, implemented in a wide selection of materials, have been presented in the previous chapter. For storage of temporally short pulses, the Raman quantum memory scheme is the most appropriate and has been demonstrated successully in hot alkali vapours[31,33,191,203,205] and in pure diamond[15,198,202] (see Subsection 2.2.6). Alkali vapours offer storage times in the nanosecond to microsecond regime and high TBP at room temperature. However, for storage in a ground state, they are still limited in their spectral bandwidth ($\delta_g < 10\,\mathrm{GHz}$ in Cs), require vapour cells of several centimetres length and are prone to FWM noise. Diamond phonon memories, despite their large bandwidth, compactness and noise suppression, suffer from short storage times of only some picoseconds, too short for many applications.

It is desirable to work with a solid-state system with a larger bandwidth than offered in alkali vapours, noise suppression, and longer storage times than phonons can offer, in order to store broadband single photons in a compact and scalable device, which is suitable for

integration with waveguides and on-chip photonic structures[210].

During the past decade, colour centres in diamond have emerged as valuable systems for quantum information processing (QIP), quantum sensing and metrology applications. Colour centres, also referred to as F-centres, are defects in crystals, which create localised energy structures within the electronic band structure of the host material. Therefore, these can be treated as atomic-like systems and may lead to new perspectives for Raman quantum memories.

While there is a multitude of colour centres, the neutral nitrogen vacancy centre (NV^0) offers some interesting properties and the negatively charged nitrogen vacancy centre (NV^-) has dominated the mentioned fields of research[211]. Furthermore, the negatively charged silicon vacancy centre (SiV^-) has emerged recently as a promising alternative system.

As a first step in this chapter, in Section 3.1, diamond and other crystalline systems will be examined, including a short classification of diamonds. In Section 3.2, colour centres in diamond are discussed in more detail, with a focus on photoluminescence spectra (§3.2.1), homogeneous and inhomogeneous linewidth broadening (§3.2.2), phonons in general (§3.2.3) and the dynamic Jahn-Teller effect in particular (§3.2.4). The chapter concludes with the description of nitrogen vacancy centres and silicon vacancy centres in Subsection 3.2.5 and Subsection 3.2.6, chosen as solid-state systems for theoretical considerations and experiments in Chapter 5, Chapter 6 and Chapter 7.

3.1 Diamond as host material

Diamonds are tetrahedrally bonded crystallised carbon atoms forming a face-centred cubic (cF/fcc) crystal lattice structure with FD$\bar{3}$m space group[212,213] (see Fig. 3.4 and Fig. 3.7). Apart from offering the highest hardness of all known bulk materials[214], they are as well suitable for experiments in the low Kelvin and millikelvin regime due to their high thermal conductivity[215]. Even though diamond offers high optical dispersion[216], dispersion effects can be neglected on typical optical bandwidths and distances light travels through diamond. An exception are Raman type memories in diamond storing light in optical phonons as seen in Section 2.2.6, where dispersion suppresses FWM noise.

Most important, diamond has the largest band gap of all semiconductors with approximately 5.5 eV[215], rendering it transparent for the complete visible spectrum up into the deep ultraviolet subrange (DUV, UV-C) down to $\approx 225\,\mathrm{nm}$[215]. Only for wavelengths between 2.6 and 6.2 µm multi-phonon effects lead to absorption[215].

Methods of diamond synthesis include synthesis at high pressure (7-10 GPa) and high temperature (1700-2000 K) (HPHT)[216–218] and the more recent chemical vapour deposition (CVD), which has larger engineering potential[215,216,218].

Even though other host materials exist, including silicon carbide (SiC) and silicon (Si), these are less rigid and offer a lower thermal conductivity than diamond[214,219,220]. Furthermore, with band gaps of $2.39 - 3.33\,\mathrm{eV}$[221] and 1.14 eV[222] respectively, the spectrum of optical transitions within their band gaps is narrower and, for silicon, also limited to the infrared regime. Still, colour centres in SiC and donor spins in Si are actively pursued for QIP applications[223–227].

3.1.1 Types of diamond

Diamonds are classified in different categories depending on the ratio of nitrogen (N) related impurities in the diamond lattice. Type I diamond offers a nitrogen concentration from 20 parts per million (ppm) to 3000 ppm and is further subdivided by the kind of nitrogen complexes that form predominantly [215]. Type II diamonds are nearly devoid of nitrogen related impurities with a nitrogen concentration below 20 ppm [215]. In the case that boron impurities are also present with a concentration of ~ 0.25 ppm in natural diamonds and up to 270 ppm in doped synthetic diamonds, the diamond is rated as IIb, otherwise as IIa [215].

To enable light-matter interaction within diamond, impurities can be added to the diamond lattice to form colour centres.

3.2 Colour centres

Colour centres are defects in the periodic atomic lattice of diamond. Single carbon atoms are replaced by other atoms, called dopants, or the lattice site is left empty, forming a vacancy. Dopants occurring in between lattice sites are referred to as interstitial defects. Often adjacent foreign atoms and vacancies combine to more complex and larger defects. These localised defects form energy bands within the band gap of the host material and can be considered as atomic- and molecule-like systems [228].

References [229] and [230] give a good overview of impurities creating optically active centres, which were known at the turn of the millennium. These impurities include H, He,

Li, B, N, O, Ne, Si, P, Ti, Cr, Co, Ni, Zn, As, Zr, Ag, Xe, Ta, W and Tl. On the other side, Be, F, Na, Al, S, Ar, V, Mn, Fe, Cu, Ga, Y, Nb, Mo, Pd, Cd, Sb, Pt, Au, and Er are said to form no optically active complexes in diamond. As well, other large atoms like europium (Eu)[231] and xenon (Xe)[232] have already been implanted in diamond creating optical centres. Methods to create colour centres include irradiation with focussed ion, neutron or electron beams[215,233,234], spatially localised ion implantation[235–237], spontaneous incorporation during CVD growth[215,238–240] and laser writing[241,242].

3.2.1 Photoluminescence spectra

Depending on their composition, symmetry and charge state, colour centres differ in their spectral properties and their robustness in respect to environmental imperfections. Important parameters include the wavelength of their zero-phonon line (ZPL) and the ratio of light emitted into the ZPL or the phonon-side bands (PSB).

If a colour centre is excited by light with a higher energy than the optical transition under consideration, photoluminescence (PL) in the form of fluorescence can be observed. Photons are absorbed and re-emitted, after possible non-radiative relaxation processes, at a wavelength directly at or close to the energy difference between the involved ground and excited state. In diamond, as it provides a rigid crystal lattice, vibrational excitations, phonons, need to be added to the energy spectrum of the defect as depicted in Fig. 3.1 (a). When a single colour centre is excited with blue-detuned light, it first relaxes via non-radiative decay from a level of vibrational excitation ($v_e \neq 0$) to an excited state of no

vibration ($v_e = 0$). From here, the centre can decay directly into the state of no vibration or into a vibrational state of the ground state energy level, emitting light into the ZPL or PSB respectively. The lattice modes, and, therefore, the phonon energy, is quantised with an energy difference of $\hbar\Omega_p$ between each mode. Regarding the Franck-Condon-principle[243–246], transitions between two vibrational modes are more likely the more the phonon wave functions overlap. Spectrally resolved fluorescence measurements of the ZPL and PSB of the neutral nitrogen vacancy centre (NV^0) and the negatively charged nitrogen vacancy centre (NV^-) are shown in Fig. 3.1 (b). For the PL spectrum of the NV^- centre, the ZPL and the four lowest transitions in the PSB are isolated by a multi-Gaussian fit.

The intensity distribution between the ZPL and the PSB can be characterised by the Huang-Rhys factor S and the Debye-Waller factor α, both related to each other via[247]

$$e^{-S} = \alpha = \frac{I_{\mathrm{ZPL}}}{I_{\mathrm{ZPL}} + I_{\mathrm{PSB}}}, \tag{3.1}$$

where $I_{\mathrm{ZPL\,(PSB)}}$ is the total intensity emitted into the ZPL (PSB). While the Debye-Waller factor directly reflects the share of fluorescence emitted into the ZPL, the Huang-Rhys factor is related to the average phonon number of a particular electronic transition, so that a distinction between weak ($S < 1$) and strong phonon coupling ($S > 1$) is possible[247].

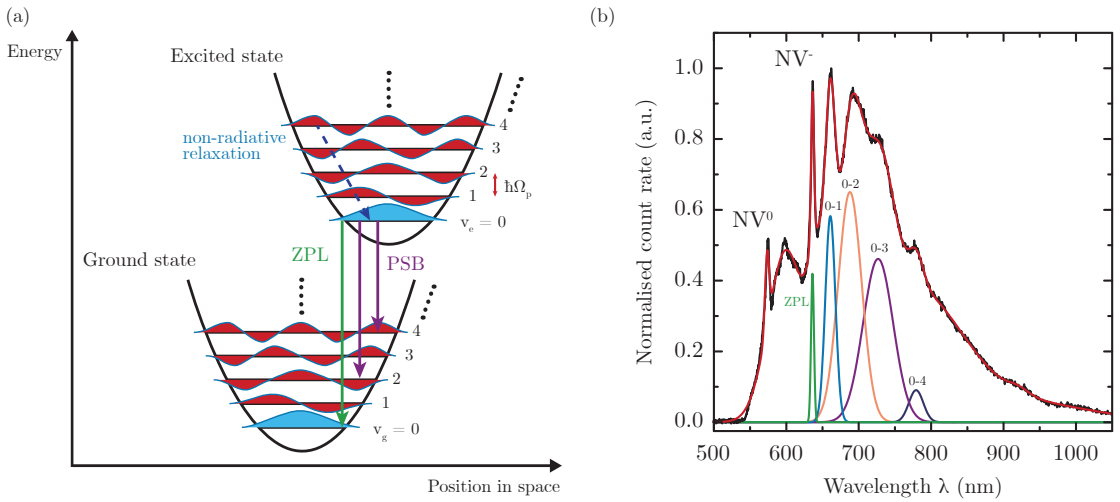


Figure 3.1: (a) Atomic-like system in two electronic configurations differing in energy and spatial distribution of the wavefunction. In the potential well of each state, phononic modes are separated by the phonon energy $\hbar\Omega_p$. v_g and v_e indicate the phonon mode of the ground and excited state respectively. Between the phonon modes, non-radiative relaxation processes are possible. Radiation emitted from the nonvibrational mode of the excited into the nonvibrational mode of the ground state forms the ZPL (green arrow between blue wavefunctions). All other transitions from the nonvibrational excited state into a phononic ground state form the PSB (purple arrows). The transition probability is defined by the Franck-Condon principle, hence the overlap of the wavefunctions of the initial and final state. (b) Fluorescence spectrum of NV^0 and NV^- at 8 K. The spectrum is fitted by a multi-Gaussian function shown as a red line in which the PSB of the NV^0 centre is only approximated by one Gauss function. For the NV^- centre, the ZPL as well as the four lowest optical transitions of the PSB are shown separately. The initial and final vibrational modes are indicated by the code 'v_e-v_g'. Be aware, that the spectra of NV^0 and NV^- are overlapping. Therefore, contributions of NV^0 in the NV^--dominated part of the spectrum ($\lambda > 637$ nm) cannot be isolated. The distilled ZPL and transitions into the PSB are only approximations but represent the optical transitions correctly.

3.2.2 Homogeneous and inhomogeneous optical linewidth

The homogeneous linewidth Γ_{hom} of an optical transition from an excited state to a ground state, is influenced by several factors. Apart from constant radiative (γ_{r}) and temperature-dependent non-radiative decay (γ_{nr}) of the excited state, phonon-mediated relaxation rates ($\gamma_{\pm}$) and pure dephasing (γ_{d}) contribute to the optical homogeneous linewidth,[248,249]

$$\Gamma_{\mathrm{hom}} = \gamma_{\mathrm{r}} + \gamma_{\mathrm{nr}} + \gamma_{\pm} + \gamma_{\mathrm{d}} \tag{3.2}$$

$$= \frac{1}{2\pi T_{\mathrm{r}}} + \frac{1}{2\pi T_{\mathrm{nr}}} + \frac{1}{2\pi T_{\pm}} + \frac{1}{\pi T_{\mathrm{d}}} = \frac{1}{\pi T_2}, \tag{3.3}$$

where T_1, $\frac{1}{T_1} = \frac{1}{T_{\mathrm{r}}} + \frac{1}{T_{\mathrm{nr}}} + \frac{1}{T_{\pm}}$, is the Fourier-limited lifetime and T_2 the homogeneous coherence time, which is ultimately restricted by the decay time T_1:

$$T_2 \leq 2\,T_1. \tag{3.4}$$

In the case of additional inhomogeneous broadening of the optical transition in ensembles, the inhomogeneous coherence time T_2^* is defined as

$$\frac{1}{T_2^*} = \frac{1}{T_2} + \frac{1}{T_{\mathrm{inhomd}}} = \Gamma_{\mathrm{inhom}}, \tag{3.5}$$

where $\frac{1}{T_{\mathrm{inhomd}}}$ is the rate of inhomogeneous dephasing and Γ_{inhom} the inhomogeneous optical linewidth.

For single colour centres, the term of inhomogeneous broadening can be used as well. In this context, the inhomogeneous distribution refers to the spectral distribution of single centres with respect to each other. Experiencing different local environments, single centres

can vary in the spectral position of their ZPL.

Effects of phonon-orbit coupling ($\gamma_{\pm}$) are particularly sensitive to the temperature[248] and can be detrimental to both life and coherence times, which are important for memory applications.

3.2.3 Phonons

Phonons in diamond can couple to the electronic orbital states of colour centres, reducing their orbital life and coherence times. Phonons are quantised vibrational modes in condensed matter, which include the vibrational oscillations of atoms in the rigid crystalline structure of diamond[250] (see Subsection 3.2.1). Every single atom is held in position by a potential well in which it can move. The strength of motion is determined by its temperature. As each potential well is determined by the interactions with the surrounding atoms, neighbouring atoms in the lattice can be imagined as connected by little springs. Therefore, the motion of one atom leads to a displacement of its direct neighbours and spreads out over the whole solid. As a definite energy $E(p) = \hbar\omega(k)$ and a quasi-momentum $p = \hbar k$ can be assigned to a phonon, which is spread over an ensemble of atoms, it is possible to talk about a collective excitation[251]. Here, $k = \frac{2\pi}{\lambda}$ is the wave number with wavelength λ. Due to boundary conditions, i.e. the limited extent of the diamond, only discrete quantised modes can form (see Subsection 3.2.1).

For these modes, it is necessary to distinguish between acoustic and optical phonons. In acoustic phonons neighbouring atoms are in phase. In optical phonons neighbouring atoms

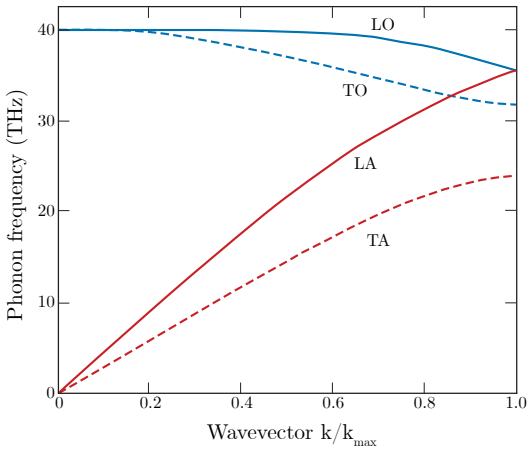


Figure 3.2: Phonon dispersion relation for diamond: Longitudinal (L, solid line) and transversal (T, dashed line) optical (O, blue) and acoustic (A, red) phonons can propagate through the diamond in [100] direction. Adapted from [252].

are out of phase, moving in opposite directions. In diamond, both manifestations can be observed. Optical phonons at high frequencies, acoustic phonons at low frequencies [251,252], for which the dispersion relations in diamond are depicted in Fig. 3.2 in [100] direction [252].

Looking at Raman scattering of optical fields in diamond, the first-order Raman line is observed 40 THz ($1332\,\mathrm{cm}^{-1}$) shifted to lower frequencies from the initial frequency of the incident field [200] (see Subsection 2.2.6). This is the upper energy bound for optical phonons, as it describes a phonon with zero quasi-momentum [215]. In the experiments described in this thesis, only acoustic phonons in the GHz regime need to be considered.

Phonons are bosons and, therefore, the occupation number n of phonon states with energy $\hbar\omega$ at temperature T obeys the Bose-Einstein statistics [253],

$$n(\omega) = \frac{1}{e^{\frac{\hbar\omega}{k_\mathrm{B}T}} - 1} \approx \frac{k_\mathrm{B}T}{\hbar\omega}. \tag{3.6}$$

For the approximation in equation (3.6), the Taylor expansion of the exponential function in first order was used. Phonons can couple to transitions between energy levels if their

energy corresponds to the level splitting Δ. It follows, that in order to suppress phonon effects, temperatures have to be chosen, so that

$$T \ll \frac{\hbar}{k_\mathrm{B}}\Delta. \tag{3.7}$$

3.2.4 Dynamic Jahn-Teller effect

The Jahn-Teller (JT) effect describes the phenomenon that three-dimensional structures, such as crystals, with spatially degenerate electronic states can deform in such a way as to reduce the geometrical symmetry, so that the degeneracy is lifted and an energetically lower, stable state is reached[254]. One can distinguish between the static JT effect, in which the system reaches the minimum of a deep potential well, and the dynamic JT (DJT) effect, where potential barriers between local minima are small enough to be overcome by the vibrational energies of phonons. This results in a constant change between these minima, visible as broadening of the state's linewidth. This broadening shows a strong temperature dependence, scaling with T^5 for $T < 100\,\mathrm{K}$[255].

Phonons, as well as optical fields, couple to the orbital part of a state only and are spin-preserving. Therefore, in terms of optical Λ-systems for Raman memories, the energetically close ground states, of which one is the storage state, should be of the same electronic orbital but have different spin, in order to avoid phonon coupling between them. However, as will be shown in Section 5.1, this has negative effects on the Raman coupling strength.

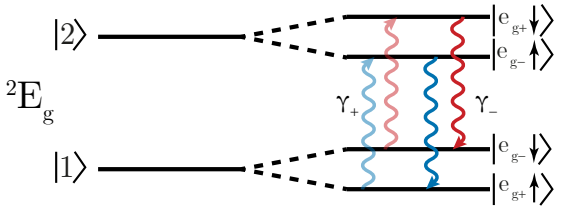


Figure 3.3: Electron-phonon interaction on the example of the SiV^- ground state manifold ^2E_g (see Subsection 3.2.6). Phonons are coupling to transitions of same spin but different orbital with rates γ_+ (up in energy) and γ_- (down in energy) ($\gamma_+ < \gamma_-$). Adapted from [248].

The phonon coupling between two electronic orbitals results in a population transfer between these states at rates γ_+ (up in energy) and γ_- (down in energy)[256], which had already been included in equation (3.2) and is shown on the example of silicon vacancy centres (SiV^-) in Fig. 3.3. In the SiV^- centre, E-symmetric acoustic phonon modes couple to E-symmetric orbital electronic states[248], as it is also the case for the E-symmetric excited state orbitals of the negatively charged nitrogen vacancy centre (NV^-)[255,257]. Both first-order and second-order phonon transitions are possible. First-order transitions are single-phonon transitions, while as second-order transitions, two-phonon Raman scattering and elastic scattering processes can occur[248]. Due to the opposite parity of the ground and excited states (^2E_g, ^2E_u) (see Fig. 3.8 (a)), no optical phonons can couple to the optical transitions between them.

Using equation (3.7), phonons are efficiently suppressed in SiV^- for $T \ll 2.4\,\mathrm{K} \approx \frac{\hbar}{k_B}\delta_g$, where δ_g is the SiV^- ground state splitting (see Subsection 3.2.6). For higher temperatures ($2.4\,\mathrm{K} < T < 20\,\mathrm{K}$), first-order transitions dominate, which scale linearly with temperature, $\gamma_\pm^{1^{st}} \propto T$[248]. In general, in this regime, the strength of the phonon induced interaction depends on the phonon density of states $\rho(\Delta)$, which is proportional to Δ^2 in the Debye approximation[255], where Δ is the level splitting, and $n(\Delta, T)$ the occupation of states (see

equation (3.6)),[248]

$$\gamma_{\pm} \propto \rho(\Delta)\{2n(\Delta, T) + 1 \mp 1\}. \tag{3.8}$$

Be aware, that $\gamma_+ < \gamma_-$ is always the case and, therefore, no complete suppression of phonon transitions to lower energy levels is possible. For higher temperatures ($T > 20\,\mathrm{K}$, $T \gg \frac{\hbar}{k_\mathrm{B}}\delta_g$), second-order transitions take over, scaling with the cube of the temperature, $\gamma_{\pm}^{2\mathrm{nd}} \propto T^3$ [248].

In consequence, experiments at low cryogenic temperature are necessary to circumvent the negative effects of electron-phonon interactions. Dynamical decoupling from the phonon bath is not possible due to the Markovian nature of the interaction between the bath and the SiV^- level structure[248]. Further methods of phonon suppression include phonon band gap suppression in nanodiamonds[248] and in nanoscale optomechanical structures and cavities[258,259]. Another approach focusses on the level splitting the phonons need to match, which is the second parameter in equation (3.8) apart from the temperature, setting the phonon-induced transition rates $\gamma_{\pm}$. After a first increase of phonon processes, for ground state splittings of more then 120 GHz at 4 K, the phonon interaction decreases[260,261]. While the phonon density of states still increases, the decrease in phonon occupation prevails and leads to the suppression of phonon processes. Such large ground state level splittings can be found in ensembles of strain engineered colour centres[260,261] and, without any external control, in some Group-IV colour centres (see Section 9.5).

Colour centres used for theoretical and experimental investigations in this thesis are the neutrally charged nitrogen vacancy centre (NV^0) and the negatively charged silicon vacancy centre (SiV^-), which will be described in the following sections.

3.2.5 The nitrogen vacancy centre (NV^-/NV^0)

Since their first description in 1976 [262] nitrogen-vacancy (NV) centres, which occur in a neutral (NV^0), a positive (NV^+) and a negative charge state (NV^-) [263,264], have been a promising area of research [211]. The full potential of the centre was revealed when photostability and the feasability of optically detected magnetic resonance (ODMR) measurements at room-temperature were shown on single NV^- centres [265], and the energy structure of the centre was explored [266,267]. Ensembles of NV centres implemented in diamond can be used as identical, optically accessible and controllable atomic-like systems in the solid state. While the negatively charged version of the centre stood in the focus of research in both metrology [38,40,45] and quantum applications [268–270], the neutral and positive state got much less attention.

An all-encompassing account of the research on the nitrogen vacancy centre is beyond the scope of this thesis. For detailed information on the electronic structure, the reader is referred to [211], [266] and [267].

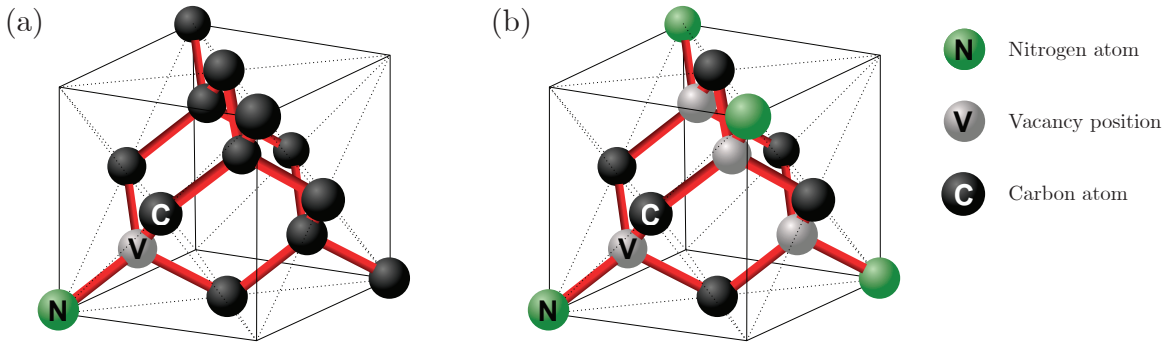


Figure 3.4: The $NV^{-/0}$ centre in a cubic diamond unit cell. (a) In one possible orientation. (b) In four possible orientations. For each of the four orientations shown, the nitrogen atom and the vacancy can swap position, which results in a total of eight possible configurations. For reasons of clarity, carbon atoms at the edges of each unit cell, which have no direct bounds into the cell, are omitted.

The NV centre shows C_{3v} symmetry with a nitrogen-vacancy pair replacing two carbon atoms in the diamond lattice (Figure 3.4)[266,267,271]. Following the Schönflies symmetry notation, crystallographic point groups with C_{3v} symmetry are trigonal and identical by rotation around the z-axis by 120° (C_3^1), rotation around the z-axis by 240° (C_3^2), rotation around the z-axis by 360°, which is the same as the identity transformation ($C_3^3 = E$), and reflection through three vertical (v) planes containing the z-axis (σ_1, σ_2, σ_3)[272–274], as shown in Fig. 3.5 (a).

Embedded into a diamond unit cell depicted in Fig. 3.4, the main symmetry axis (C_3) of the NV centre can point into eight different directions $\langle 111 \rangle$.

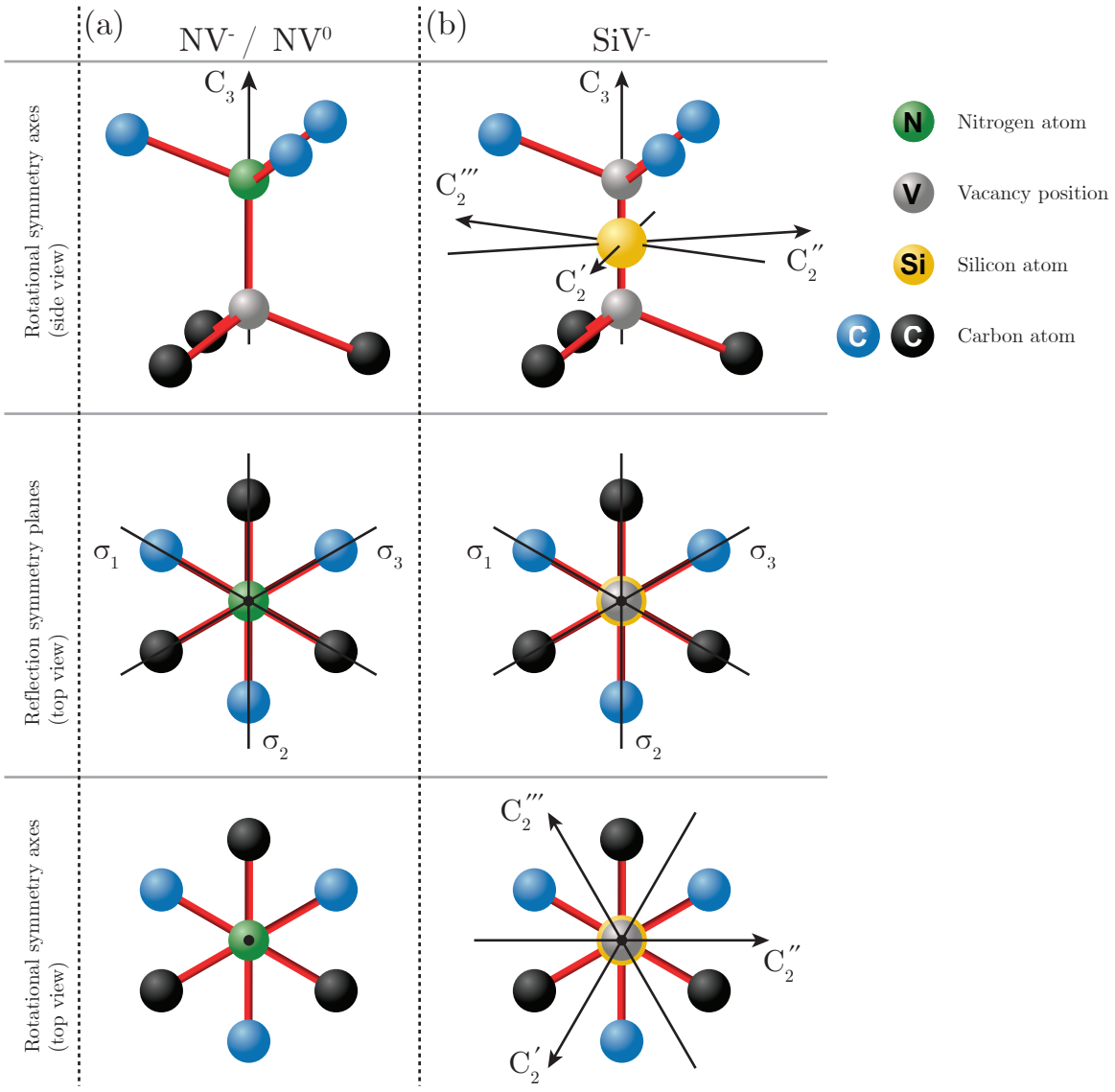


Figure 3.5: Symmetry properties of the $NV^{-/0}$ and the SiV^{-} centre. (a) C_{3v} symmetry of the NV^{-} and NV^{0} centre, with C_3 rotational axis along the connection of the vacancy position and the nitrogen atom (z-axis) and three vertical mirror planes (σ_1, σ_2, σ_3). (b) D_{3d} symmetry of the SiV^{-} centre, with C_3 rotational axis along the connection of the vacancy positions and the silicon atom (z-axis), three vertical mirror planes (σ_1, σ_2, σ_3) and additional C_2 rotational axes (C_2', C_2'', C_2'''), perpendicular to the main-symmetry axis (C_3) and through the silicon atom. In parts adapted from [275].

The negatively charged nitrogen vacancy centre (NV^-)

The NV^- centre possesses a ZPL line at 637 nm (1.945 eV)[211,262] between a spin-triplet, orbital-singlet ground state manifold $^3A_2$ and a spin-triplet, orbital-doublet excited state manifold ^3E[257], depicted in Fig. 3.6 (a). Within the ground state manifold, the spin states $|\pm1\rangle$ and $|0\rangle$ are split by 2.87 GHz[265]. Additionally, the spin-singlet states $^1A_1$ and $^1E_{1,2}$ are separated by 1042 nm (1.190 eV)[211,276], which play an important role in decay mechanisms from the excited states, including intersystem crossing[277] and spin-flipping. In combination, the spin-triplet states $^3A_2$, ^3E_x and ^3E_y form three V-systems of different spin[278] (see Section 5.1, Fig. 5.1 (a)). Optical Λ-systems, needed in the Raman memory scheme (see Subsection 2.2.6), can only be created by spin mixing in the excited states.

However, this level structure also offers many advantages, which contributed to the success and intense research on the NV^- centre. These include the possibility of optical read-out of the ground state spin[279–281] and the long life and coherence times of the $^3A_2$ spin states. While an excited state lifetime of $T_1^e = 25$ ns of a single centre in a nanodiamond and of $T_1^e = 11.6$ ns in bulk diamond was measured at room temperature[282], life and coherence times are several orders of magnitude longer in the ground state. The ground state spin relaxation time was detemined to $T_1^g = 7.7$ ms (room temperature, $B = 8$ T, ensemble, Type Ib diamond)[283], $T_1^g = 265$ ms ($T = 78$ K, ensemble, Type Ib diamond)[284] and even $T_1^g = 3.8$ s ($T = 40$ K, $B = 8$ T, ensemble, Type Ib diamond)[283]. The ground state spin dephasing time T_2^g is on the order of microseconds at room and cryogenic temperatures[211]. However, in an impressive experiment, the coherence time was extended to $T_2^g = 1.8$ s at room temperature, measured in a single centre in isotopically

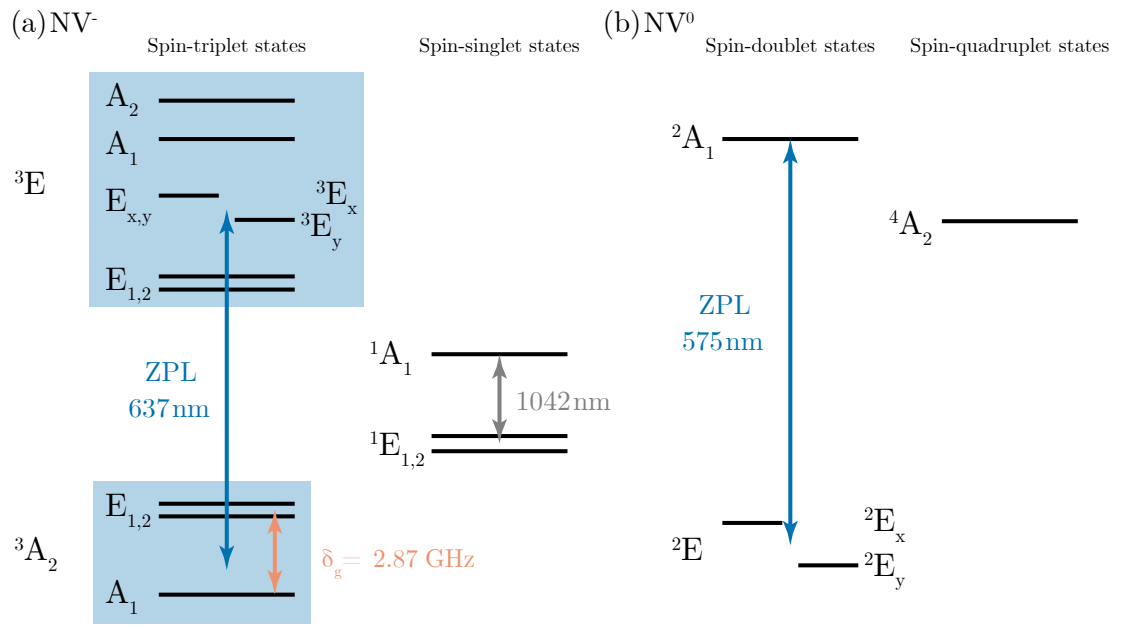


Figure 3.6: Schematic electronic structure of (a) the NV^- centre and (b) the NV^0 centre. (a) NV^- energy diagram with a spin-triplet, orbital-singlet ground state manifold $^3A_2$ and a spin-triplet, orbital-doublet excited state manifold ^3E separated by the 637 nm ZPL. The $^3A_2$ manifold shows a splitting of $\delta_g = 2.87$ GHz. The spin-singlet states $^1A_1$ and $^1E_{1,2}$ are separated by 1042 nm. (b) NV^0 energy diagram with ZPL at 575 nm between the spin-doublet states ^2E and $^2A_1$, and with the spin-quadruplet state $^4A_2$.

pure, spin-free, IIa diamond [40]. A comprehensive list of ground state life and coherence times is given in [211]. In less pure diamonds than the diamond used in [40], dynamical decoupling sequences can be employed to increase coherence times by decoupling from the spin bath in diamond and fluctuations of applied external magnetic fields [285–289].

These long coherence times are interesting for many applications, including magnetometry [40,290], sensing in life sciences [291], QIP and quantum networks [100,292], for testing the foundations of quantum mechanics [293], quantum thermodynamics [294], as well as diamond lasers and masers at room temperature [295,296]. Moreover, the NV^- centre has been suggested as a platform for Raman memories with high TBP of the order of 10^7 but small bandwidth (110 MHz) [297].

On the downside, without the use of optical cavities, its intense phonon sidebands (Debye-Waller factor, $\alpha \approx 0.04$)[298] strongly limit achievable rates in probabilistic entanglement schemes and hence its applicability in QIP[293]. Other negative aspects include intentional and unintentional charge transitions and fluctuations between NV^- and NV^0[299–302], as well as spectral diffusion in the low to high GHz-regime, observed in off-resonant fluorescence measurements in bulk and nanodiamonds due to electrostatic fluctuations in the environment and charged impurities in the diamond lattice[301,303–305].

The neutrally charged nitrogen vacancy centre (NV^0)

The neutral NV^0 centre experiences the same problems of charge state fluctuations and spectral diffusion. Still, in comparison to the NV^- centre, the electronic structure is very different and proved to be much harder to identify. The identification of a spin-doublet ($m_s = \pm\frac{1}{2}$) ^2E to $^2A_1$ transition[306,307] as ZPL at 575 nm (2.156 eV)[306] and of an additional spin-quadruplet excited state $^4A_2$[277], finally led to the electronic structure shown in Fig. 3.6 (b)[271,301,307].

This level structure directly enables two same-spin Λ-systems for which no spin mixing in the excited states is necessary (see Section 5.1, Fig. 5.1 (b)). However, as the two ground states belong to different electronic orbitals, phonons can couple to the transitions between them, quenching life and coherence times (see Subsection 5.7.2).

Independent of phonon processes, the lifetime of the excited state was determined in experiments for the usage of NV^0 as a single photon source by photon antibunching measurements to $T_1 \approx 13\,\mathrm{ns}$[308]. In luminescence lifetime measurements the radiative lifetime was measured to be slightly larger with $T_1 \approx 19\,\mathrm{ns}$[309]. Just like in NV^-, from the excited state, most light is emitted into the PSB with a Huang-Rhys factor of $S \approx 3.3$[230], equivalent to a Debye-Waller factor of $\alpha \approx 0.04$.

A similar E-symmetric spin-doublet ground state, as in NV^0, is found in the negatively charged silicon vacancy centre (SiV^-), which has recently emerged as a promising alternative system to the negative NV^- centre.

3.2.6 The silicon vacancy centre (SiV^-)

The SiV^- centre is a trigonal-antiprismatic complex featuring a silicon atom in a split-vacancy configuration in between two empty carbon lattice sites and six nearest-neighbour carbon atoms[310,311]. The resulting inversion symmetry renders the system insensitive to first-order Stark shifts[312,313], enabling narrow spectral distributions of centres even in non-ideal crystal environments due to reduced spectral diffusion. For the trigonal D_{3d} symmetry, in comparison to the NV centre, three C_2 rotational axes (C_2', C_2'' and C_2'''), perpendicular to the main-symmetry axis (C_3), are added in Fig. 3.5 (b). This also leads to a reduction of possible orientations within the diamond lattice. Due to its centro-symmetry, only four orientations are distinct as illustrated in Fig. 3.7.

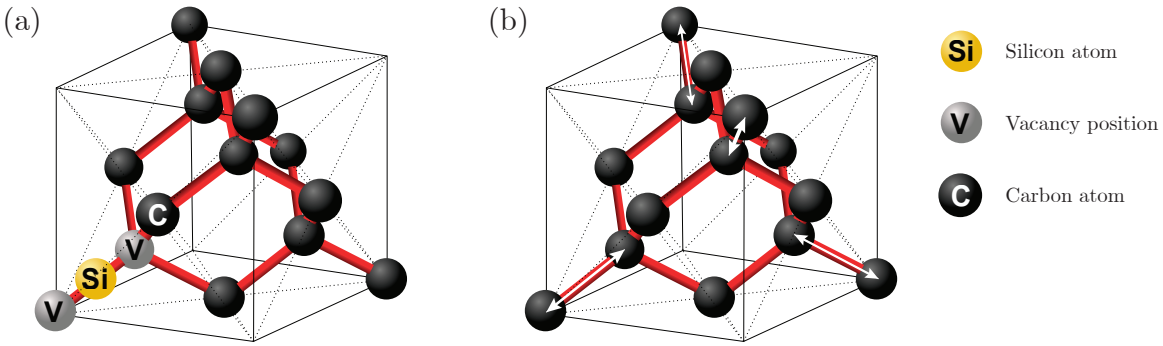


Figure 3.7: The SiV^- centre in a cubic diamond unit cell. (a) In one possible orientation. (b) The four possible orientations of the main symmetry z-axis (V-Si-V) are indicated by arrows. Contrary to the $NV^{-/0}$ centre, the D_{3d} symmetry prevents further distinguishable orientations. For reasons of clarity, carbon atoms at the edges of each unit cell, which have no direct bounds into the cell, are omitted.

Even in dense ensembles, the inversion symmetry of SiV^- centres offers an inhomogeneous broadening in the low GHz regime ($\sim 10\,\mathrm{GHz}$)[314], smaller than the separation of its ground states. This is a unique feature amongst other solid-state quantum systems such as NV^- centres[39,315], quantum dots[316] or rare-earth-doped crystals[317]. An exception are non-doped stoichiometric rare-earth crystals, where the hyperfine structure of ^{153}Eu can be resolved, while a high optical depth is still achieved[318].

In low density SiV^- ensembles, inhomogeneous broadenings down to 300 MHz are reached[319]. Even for high densities, this allows for fundamental studies and applications in the fields of strong coherent light-matter interactions and single photon nonlinearities, which so far have been reserved for systems such as single atoms coupled to optical cavities[22], ultra-cold Rydberg-atoms[320] or atomic vapors[321]. In contrast, SiV^- ensembles offer high photon interaction cross-sections even in small sample volumes and thus allow for the implementation of similar effects in compact and scalable devices in the solid state.

The electronic structure of the centre is displayed in Fig. 3.8 (a) and consists of two-fold spin-degenerate orbital-doublet ground and excited states, ^2E_g and ^2E_u, in which the orbital components are split apart by strong spin-orbit (SO) interactions, leading to splittings of δ_g=48 GHz in the ground and δ_e=259 GHz in the excited state[311,313]. The four optical transitions A, B, C and D connect the orbital ground states $|1\rangle$ and $|2\rangle$ with the orbital excited states $|3\rangle$ and $|4\rangle$, where A is the largest and D the smallest energy transition, in a ZPL at 737 nm (1.68 eV)[311]. A comprehensive analysis of the SiV^- level structure can be found in [275], [311] and [313]. Apart from SiV^-, the silicon vacancy centre also occures in a potentially promising neutral charge state, SiV^0, with a ZPL at 946 nm (1.31 eV)[322–327], which is not further treated in the context of this thesis.

At zero magnetic field and at cryogenic temperatures the SiV^- level structure results in a characteristic four-line fine structure of the ZPL[240], as shown in Fig. 3.8 (b) and Fig. 3.9 (b), forming an optically accessible double-Λ-type system, enabling a multitude of optical coherent control schemes. In single SiV^- centres, nearly lifetime-limited optical linewidths (A: 352 MHz, B: 409 MHz, C: 136 MHz, D: 119 MHz) have been observed[329]. At room temperature the ZPL linewidth is less than 1 nm[330,331].

As most photons are emitted into the ZPL ($\alpha \approx 0.8$, S = 0.08)[330] (in contrast to NV^- in Fig. 3.9 (a)) and thanks to narrow inhomogeneous distributions of the SiV^- resonance, photon emission rates in the high MHz range for samples containing single emitters have been realised[312]. Further, single emitters can be efficiently coupled to nanostructures[333,334]. This makes the SiV^- centre a strong candidate as source of

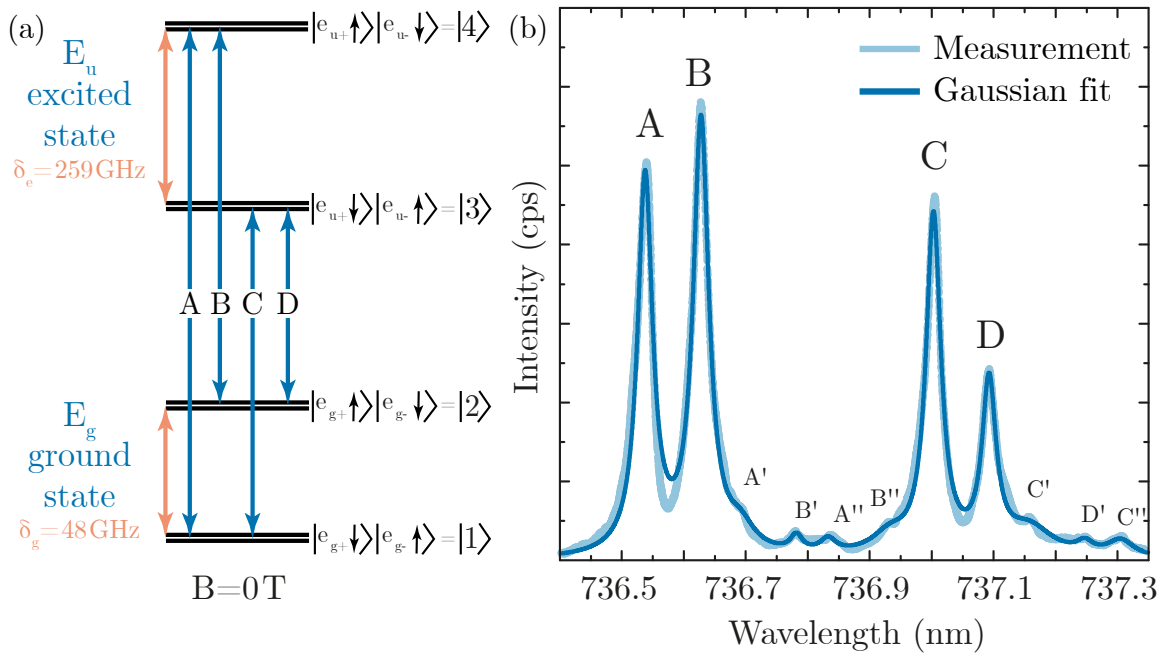


Figure 3.8: SiV^- four-level structure and optical spectrum of the ZPL at 737 nm. (a) The four optical transitions A, B, C, D between the four orbital states $|1...4\rangle$ form a double-Λ system. (b) Photoluminescence excitation spectrum at T= 5 K of the SiV^- ensemble used throughout this work (light blue). A Gaussian fit indicates an inhomogeneous broadening of $\approx$ 10 GHz of the transitions A, B, C, D (dark blue). The sample displays twelve optical transitions as it has been grown with a natural silicon isotope distribution. The D" transition is not included in the measurement. Subfigure (b) adapted from [328].

indistinguishable single photons in QIP [333,335,336]. Moreover, as its single photon count rates surpass rates in NV^- by one order of magnitude [298,325].

The ZPL transitions of a single centre are polarised with matching polarisations of the inner (B,C: linear polarised (z)) and outer transitions (A,D: elliptically polarised (xy)) [313,337]. When projected onto a (001) diamond surface, this results in two orbital Λ-systems with cross-linear polarisation selection rules as shown in Fig. 3.9 (c) [313]. Unfortunately, these selection rules do not apply for ensembles of all possible orientations of the main SiV^- symmetry axis.

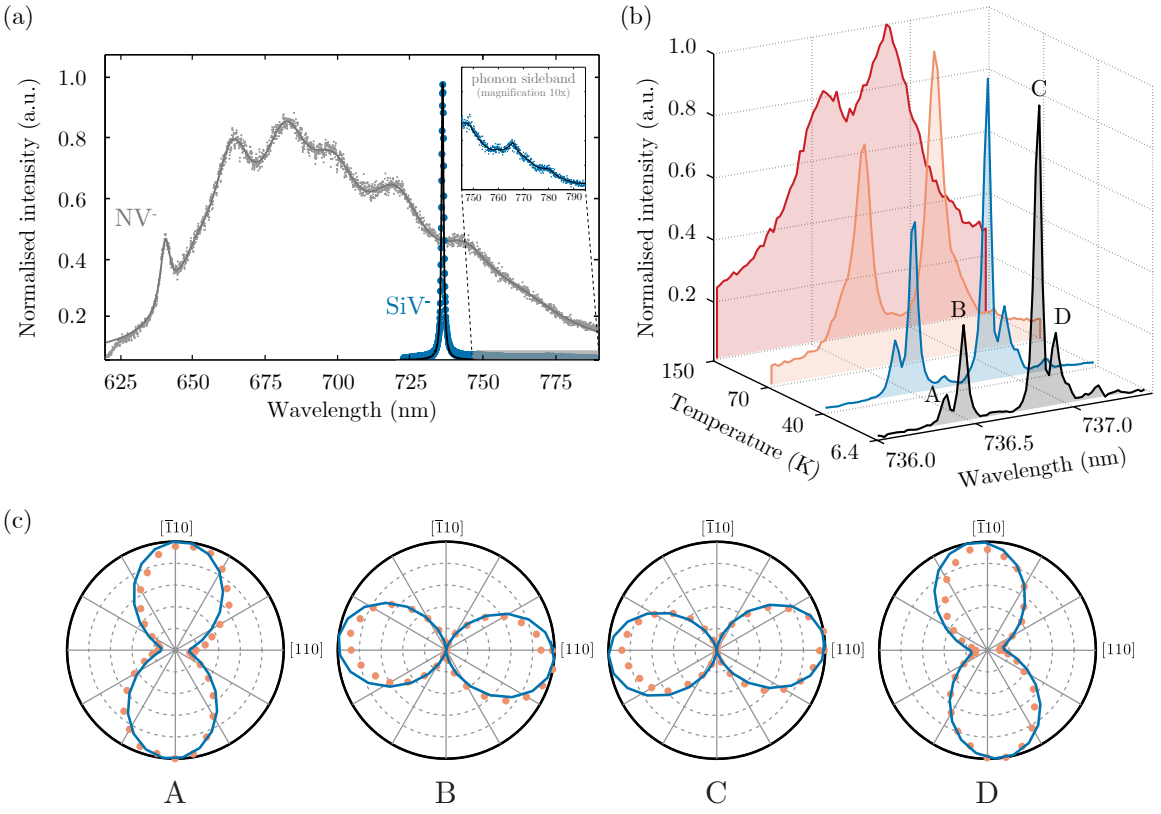


Figure 3.9: (a) Fluorescence spectrum including the ZPL and PSB of NV^- and SiV^- at room temperature. The inset shows the enlarged SiV^- PSB. (b) Spectral resolution of the SiV^- ZPL for temperatures from 150 K to 6.4 K. Cooling down, the four optical transitions A, B, C and D emerge. (c) Photoluminescence polarisation of the optical transitions A, B, C and D in a single SiV^- centre. Measurement points are given by orange dots, simulated values by blue lines. Subfigures (a) and (b) adapted from [332], subfigure (c) adapted from [313].

Both in the ground and excited state, acoustic phonons couple states $|1\rangle$ and $|2\rangle$, and states $|3\rangle$ and $|4\rangle$ respectively. Within the ground states, first-order phonon transitions limit the orbital relaxation time to $T_1^{\text{orbit},g} = 38\,\text{ns}$ at 4.5 K [338]. As these transitions are spin-preserving, single spins are less affected with spin relaxation times of $T_1^{\text{spin},g} = 2.4\,\text{ms}$ for magnetic fields aligned along the centre's C_3 symmetry axis [338]. In experiments of coherent population trapping (CPT), the spin coherence time (free induction decay time) T_2^* has been determined to 35-45 ns at 4-5 K [338,339]. Ramsey measurements using microwave pulses even led to electronic spin dephasing times of 115 ns, where the better result is traced

back to noise from the optical driving fields, slightly higher temperatures and strain splitting of the orbital levels in the CPT measurements just mentioned [340]. Nonetheless, this is several orders of magnitude smaller than in the NV^- centre (see Subsection 3.2.5) and is assigned to phonon processes between the ground state orbitals. Following equation (3.7), temperatures far less than 2.4 K would be needed to freeze out phonon transitions in the ground state. However, recent experiments with single SiV^- centres at millikelvin temperature have shown that spin coherence times are limited to $T_{2,echo} = 138$ ns at 40 mK by the interaction with a spin bath of substitutional nitrogen within the diamond lattice [283,341,342].

Notwithstanding, these life and coherence times are long enough for the SiV^- centre to be suggested as a qubit, which can be manipulated by coherent control [332,343–345]. In single centres, microwave control of the spin ground states [340], resonant all-optical spin control [342], as well as ultrafast off-resonant sub-cycle optical control of the orbital states [343] have been demonstrated successfully. Using microwave fields for dynamical decoupling of states of opposite spin, spin coherence times of $T_2 = 13$ ms were reached for the realisation of long-lived qubits [346].

The experiments described in Chapter 7 of this thesis will go beyond the coherent manipulation of single centres, describing coherent manipulation, the first demonstration of coherent population transfer, as well as strong light-matter interaction in ensembles of colour centres.

3.3 Summary

Diamond outperforms other materials like SiC and Si as a host material for dopants in terms of band gap, hardness and thermal conductivity (§3.1). A multitude of different optically active colour centres can be created with a well defined electronic level structure within the band gap (§3.2). For their assessment regarding light-matter interactions, memory schemes and QIP, parameters as the Huang-Rhys and Debye-Waller factor (§3.2.1) along with life and coherence times (§3.2.2) are of the utmost importance. Temperature sensitive phonon-orbit coupling reduces life and coherence times, requiring operation at cryogenic temperatures to suppress acoustic phonons and first-order transitions between orbital states. Among several alternatives, large splittings of orbital states can support suppression of phonon mediated decay (§3.2.3 and §3.2.4). Even though both NV^- and NV^0 show C_{3v} symmetry, they differ strongly in their electronic structure. In NV^- a spin-triplet, orbital-singlet ground state offers outstanding coherence times appreciated in a large variety of applications. Yet, for Raman type memories the level structure of NV^0 is more suitable (§3.2.5). A similar level structure is present in SiV^-, which offers low inhomogeneous broadening in ensembles thanks to its D_{3d} symmetry. In a double-Λ-type system with large ground state splitting and cross-linear polarised transitions in (001) projection, microwave and all-optical control of electronic spin and orbital states have been demonstrated on single centres (§3.2.6).

In Chapter 5, the NV^0 centre will be used as model system to explore the prospects and requirements for a colour centre based Raman memory. Basic theoretical findings will be confirmed in Chapter 6. In the next chapter, atomic light-matter interactions will be

discussed, which will be applied for the coherent and incoherent manipulation of ensembles of SiV^- centres in Chapter 7.

Chapter 4

Atomic light-matter interactions

In this chapter the theoretical basis of atomic light-matter interactions encountered in later chapters is presented. Starting with incoherent processes, optical pumping in a three-level system is described in Section 4.1. This is followed by coherent manipulation techniques in Section 4.2, illustrated with the help of the Bloch sphere (§4.2.1). First, coherent control by Ramsey interference (§4.2.2) and the Hahn echo rephasing sequence (§4.2.3) is explained. In a second step, stimulated Raman adiabatic passage (STIRAP) is introduced in Subsection 4.2.4, which offers the possibility of off-resonant coherent manipulation of ensembles of atomic systems using two distinct optical fields in two-photon resonance. The chapter concludes in Section 4.3 with the description of four-wave mixing (FWM), a nonlinear effect encountered in Raman memories (see Subsection 2.2.6).

4.1 Optical pumping

Optical pumping[347] can be understood as the interaction of electromagnetic fields with an ensemble of identical atomic multilevel systems with the aim to create some particular population distribution within this ensemble, which does not correspond to its thermal population distribution. In the ideal case, all systems are transferred into the same state. However, this transfer is limited by the decay rates of the involved states.

The temporal evolution of the populations in the three states of the Λ-system shown in Fig. 4.1 (a) can be described by the rate equations

$$\frac{\mathrm{d}N_1(t)}{\mathrm{d}t} = \dot{N}_1(t) = -\Gamma_{12}\,N_1(t) + \Gamma_{21}\,N_2(t) + \Gamma_{31}\,N_3(t), \tag{4.1}$$

$$\frac{\mathrm{d}N_2(t)}{\mathrm{d}t} = \dot{N}_2(t) = \Gamma_{12}\,N_1(t) - (\Gamma_{21} + R)\,N_2(t) + (\Gamma_{32} + R)\,N_3(t), \tag{4.2}$$

$$\frac{\mathrm{d}N_3(t)}{\mathrm{d}t} = \dot{N}_3(t) = R\,N_2(t) - (\Gamma_{31} + \Gamma_{32} + R)\,N_3(t), \tag{4.3}$$

where N_i is the share of systems in state $|i\rangle$, also referred to as population, and $N_1 + N_2 + N_3 = 1$ has to be fulfilled for all times t. A pumping laser field is applied in resonance to transition $|2\rangle - |3\rangle$ with the aim to transfer as much population as possible into state $|1\rangle$. The spontaneous decay rates from state $|i\rangle$ to state $|j\rangle$ are given by Γ_{ij} and R is the laser induced bi-directional transition rate of stimulated emission and stimulated absorption between state $|2\rangle$ and state $|3\rangle$. In thermal equilibrium, before optical pumping ($t = 0$), populations between the energetically close ground states $|1\rangle$ and $|2\rangle$, split by δ_g,

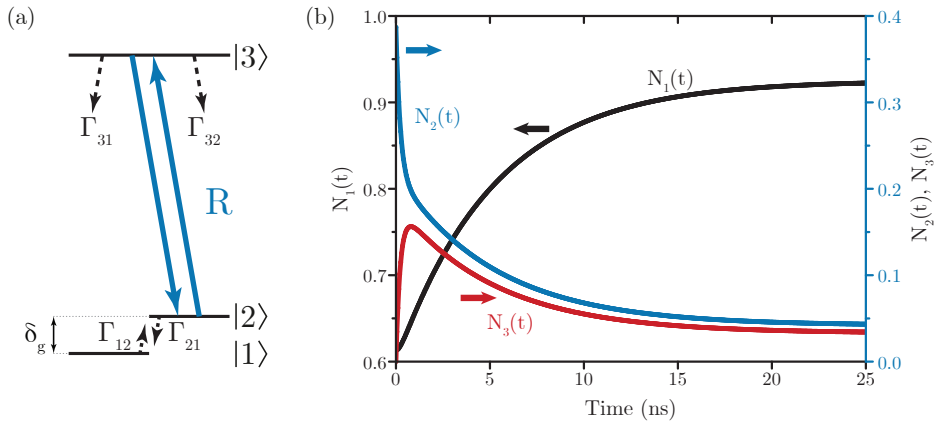


Figure 4.1: (a) Optical pumping in a three-level Λ-system with a ground state splitting of δ_g. A coherent laser field is applied resonantly to transition $|2\rangle - |3\rangle$ generating rates of stimulated absorption ($|2\rangle \rightarrow |3\rangle$) and stimulated emission ($|2\rangle \leftarrow |3\rangle$) of equal amount R. Decay rates Γ_{ij} from state $|i\rangle$ to state $|j\rangle$ are indicated as dashed arrows. (b) Simulation of optical pumping of an ensemble of SiV^- centres using the full analytical solution of the coupled rate equations (4.1)-(4.3). Population is transferred from state $|2\rangle$ to state $|1\rangle$. Parameters are set to $R = 2\,\mathrm{GHz}$, $\Gamma_{12} = 13.8\,\mathrm{MHz}$, $\Gamma_{21} = 21.9\,\mathrm{MHz}$, $\Gamma_3 = \Gamma_{31} + \Gamma_{32} = 540\,\mathrm{MHz}$ with a branching ratio of $\frac{\Gamma_{31}}{\Gamma_{32}} = 2$, $N_1(0) = 0.61$, $N_2(0) = 0.39$ and $N_3(0) = 0$ at a temperature of 5 K.

are Boltzmann distributed,

$$\frac{N_2(0)}{N_1(0)} = e^{-\frac{\hbar\delta_g}{k_B T}}. \tag{4.4}$$

In consequence, to establish this thermal Boltzmann distribution, the decay rates between these two states must also show the same ratio, so that

$$\frac{\Gamma_{12}}{\Gamma_{21}} = e^{-\frac{\hbar\delta_g}{k_B T}}. \tag{4.5}$$

The system of coupled linear first-order differential equations ((4.1)-(4.3)) can be solved using the Laplace transform. In the Laplace space the system of differential equations is simplified to a system of coupled linear algebraic equations and can be solved. The inverse Laplace transform of the solution finally leads to the full temporal analytical description of

the population development in time. These results are given in Appendix A. Alternatively, the optical Bloch equations can be used for the simulation of the full temporal development (see Appendix B.3). These enable not only the temporal description of the population distribution but also of the coherence generated in the system.

Without the analysis of the full temporal development, the final steady-state population distribution can be determined by the examination of the system in a state of no further changes ($\dot{N}_1(t) = \dot{N}_2(t) = \dot{N}_3(t) = 0$), here, denoted as $t \to \infty$. In this case, the population distribution reads,

$$N_1(t \to \infty) = \frac{\Gamma_{21}(\Gamma_{31} + \Gamma_{32} + R) + \Gamma_{31}R}{\mathcal{G}}, \tag{4.6}$$

$$N_2(t \to \infty) = \frac{\Gamma_{12}(\Gamma_{31} + \Gamma_{32} + R)}{\mathcal{G}}, \tag{4.7}$$

$$N_3(t \to \infty) = \frac{\Gamma_{12}R}{\mathcal{G}}, \tag{4.8}$$

with $\mathcal{G} = \Gamma_{12}(\Gamma_{31} + \Gamma_{32} + 2R) + \Gamma_{21}(\Gamma_{31} + \Gamma_{32} + R) + \Gamma_{31}R$.

The limit of population redistribution by optical pumping becomes obvious for infinite strong pumping rates R. Under this condition, the populations tend to

$$N_1(\{R,t\} \to \infty) = \frac{\Gamma_{21} + \Gamma_{31}}{2\Gamma_{12} + \Gamma_{21} + \Gamma_{31}} = 1 - \frac{2\Gamma_{12}}{2\Gamma_{12} + \Gamma_{21} + \Gamma_{31}}, \tag{4.9}$$

$$N_2(\{R,t\} \to \infty) = N_3(\{R,t\} \to \infty) = \frac{\Gamma_{12}}{2\Gamma_{12} + \Gamma_{21} + \Gamma_{31}}. \tag{4.10}$$

In terms of optical pumping, inspecting equation (4.9), a full population transfer is limited

by the decay rate Γ_{12} of state $|1\rangle$, which should be minimised, while a high decay rate Γ_{31} is favourable. The decay rate Γ_{21} of state $|2\rangle$ is constrained by equation (4.5). It is noteworthy that in the regime of strong pumping rates, state $|2\rangle$ and $|3\rangle$ show the same behaviour as an isolated two-level system with a maximum population ratio $\frac{N_{\text{excited}}}{N_{\text{ground}}} = 1$.

As an example, optical pumping of an ensemble of silicon vacancy centres (SiV^-) in diamond (see Subsection 3.2.6), using the analytical solution of the population development, is shown in Fig. 4.1 (b) . Population is transferred from the upper ground state $|2\rangle$ via the lower excited state $|3\rangle$ into the lower ground state $|1\rangle$ as done during optical pumping in the experiments described in Chapter 7. It can be seen, that the excited state $|3\rangle$ quickly gains population when the pump field sets in and that state $|2\rangle$ and state $|3\rangle$ tend to an equal population distribution $\frac{N_2(t)}{N_3(t)} \approx 1$ within 0.7 ns. In the further course of evolution more and more population leaves the two-level system formed by state $|2\rangle$ and state $|3\rangle$ towards state $|1\rangle$ until a steady-state distribution is reached. Following equation (4.9) the population in state $|1\rangle$ is limited to $\approx$ 93 %. In experiments, the fluorescence from the excited state $|3\rangle$, which is proportional to its population N_3, can be measured and allows to draw conclusions about the population distribution in state $|1\rangle$ and state $|2\rangle$ (see Subsection 7.3.3).

4.2 Coherent control

4.2.1 The Bloch sphere

Two-level systems can be treated and visualised efficiently using the Bloch sphere[10,348]. The Bloch sphere is a visual representation of the pure state of a two-level system,

$$|\psi\rangle = \alpha\,|1\rangle + \beta\,|2\rangle\,, \tag{4.11}$$

where $|1\rangle$ and $|2\rangle$ form an orthonormal basis of the Hilbert space, and $\alpha = |\alpha|e^{i\phi_\alpha}$ and $\beta = |\beta|e^{i\phi_\beta}$ are complex numbers for which $|\alpha|^2 + |\beta|^2 = 1$, so that $|\psi\rangle$ is normalised. Using the polar decomposition of the complex numbers, eliminating the global phase ϕ_α and defining $|\alpha| = \cos\left(\frac{\theta}{2}\right)$ and $|\beta| = \sin\left(\frac{\theta}{2}\right)$, the state vector can be written as

$$|\psi\rangle = \cos\left(\frac{\theta}{2}\right)|1\rangle + \sin\left(\frac{\theta}{2}\right)e^{i\phi}\,|2\rangle\,, \tag{4.12}$$

with the definition of $\phi = \phi_\beta - \phi_\alpha$. The angles θ and ϕ can be interpreted as the polar and azimuthal angle in a spherical coordinate system. Therefore, and due to the normalisation condition, any pure state $|\psi\rangle$ can be visualised as a unit vector as shown in Fig. 4.2 (a). All possible orientations of the vector form the surface of the Bloch sphere. This definition needs to be generalised for mixed states, which are a statistical ensemble of pure states. For pure states the density matrix is defined as $\rho = |\psi\rangle\langle\psi|$ (see Appendix B.2), while for mixed states the density matrix is given by $\rho = \sum_n p_n\,|\psi_n\rangle\langle\psi_n|$ with the real probabilities p_n and pure states $|\psi_n\rangle$. It follows that the trace, $\mathrm{Tr}(A) = \sum_i a_{ii}$, of pure states is $\mathrm{Tr}(\rho) = \mathrm{Tr}(\rho^2) = 1$. For mixed states $\mathrm{Tr}(\rho^2) < 1$ always holds[349]. Any 2×2 density matrix can be written in

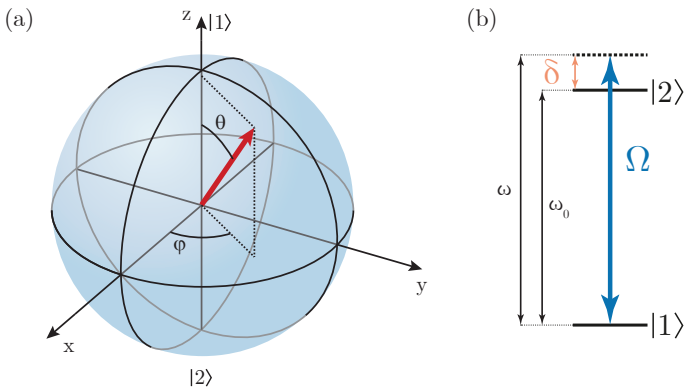


Figure 4.2: (a) Bloch sphere with polar angle θ and azimuthal angle ϕ unambiguously defining the direction of the Bloch vector (red arrow). (b) Two-level system with ground state $|1\rangle$ and excited state $|2\rangle$, separated by an energy of $\hbar\omega_0$. An optical field of angular frequency ω and Rabi frequency Ω is applied, detuned from resonance by $\delta = \omega - \omega_0$.

the basis of the identity matrix I and the Pauli matrices[348],

$$I = \begin{pmatrix} 1 & 0 \\ 0 & 1 \end{pmatrix}, \quad \sigma_x = \begin{pmatrix} 0 & 1 \\ 1 & 0 \end{pmatrix}, \quad \sigma_y = \begin{pmatrix} 0 & -i \\ i & 0 \end{pmatrix}, \quad \sigma_z = \begin{pmatrix} 1 & 0 \\ 0 & -1 \end{pmatrix}, \tag{4.13}$$

which obey the commutation relations ($[A, B] = AB - BA$)

$$[\sigma_i, \sigma_j] = i\, 2\, \varepsilon_{ijk}\, \sigma_k, \tag{4.14}$$

where ε_{ijk} is the Levi-Civita symbol. With this, any 2×2 density matrix can be written as[350]

$$\rho = \frac{1}{2}\left(I + x\,\sigma_x + y\,\sigma_y + z\,\sigma_z\right) = \frac{1}{2}\left(I + \vec{r}\,\vec{\sigma}\right). \tag{4.15}$$

Here, $\vec{r}$ is the Bloch vector within the Bloch sphere as shown in Fig. 4.2 (a) and defined by the elements ρ_{ij} of the density matrix according to

$$\vec{r} = \begin{pmatrix} x \\ y \\ z \end{pmatrix} = \begin{pmatrix} \rho_{12} + \rho_{21} \\ i(\rho_{12} - \rho_{21}) \\ \rho_{11} - \rho_{22} \end{pmatrix}. \tag{4.16}$$

The temporal evolution of the density operator is governed by the Liouville-von Neumann equation in the interaction picture[349],

$$\partial_t \rho = -i[\rho, \mathcal{H}], \tag{4.17}$$

where $\mathcal{H}$ is the interaction Hamiltonian in rotating-wave approximation (RWA) and rotational frame[350],

$$\mathcal{H} = \begin{pmatrix} \delta & \Omega \\ \Omega & 0 \end{pmatrix}, \tag{4.18}$$

of an electromagnetic field with Rabi frequency Ω (see Appendix B.1) applied to a two-level system with a detuning $\delta = \omega - \omega_0$ from resonance of the two-level transition ω_0. This configuration is depicted in Fig. 4.2 (b). Equation (4.17) simplifies to[350]

$$\partial_t \vec{r} = \vec{\Omega}_G \times \vec{r} = \frac{1}{\Omega_G^2} \begin{pmatrix} \Omega^2 + \delta^2 \cos(\Omega_G t) & -\delta\Omega_G \sin(\Omega_G t) & \delta\Omega\left[\cos(\Omega_G t) - 1\right] \\ \delta\Omega_G \sin(\Omega_G t) & \Omega_G^2 \cos(\Omega_G t) & \Omega\Omega_G \sin(\Omega_G t) \\ \delta\Omega\left[\cos(\Omega_G t) - 1\right] & -\Omega\Omega_G \sin(\Omega_G t) & \Omega^2 \cos(\Omega_G t) + \delta^2 \end{pmatrix} \vec{r}, \tag{4.19}$$

where '×' indicates the cross product of two vectors, describing the temporal evolution of the Bloch vector precessing around the vector of the generalised Rabi frequency, Ω_G, defined as [350]

$$\vec{\Omega}_G = \begin{pmatrix} -\Omega \\ 0 \\ \delta \end{pmatrix}, \tag{4.20}$$

with frequency $\Omega_G = \sqrt{\Omega^2 + \delta^2}$. In the case that no electromagnetic field is applied ($\Omega = 0$), this corresponds to a free oscillation around the z-axis at frequency δ. For fields applied satisfying $\Omega \gg \delta$, the Bloch vector rotates around the x-axis with a frequency of $\Omega_G \approx \Omega$. Choosing the interaction time τ of a laser field with a two-level system carefully, angles, also referred to as pulse areas, of $\Omega\tau = \frac{\pi}{2}$ and π can be used for coherent manipulation of ensembles of atomic-like systems for coherence time measurements. Methods of coherent control will be described in the following subsections of this chapter. Experimental results are presented in Subsection 7.3.2 and Subsection 7.3.3.

4.2.2 Ramsey interference

The method of Ramsey interference was first described by Norman Ramsey in 1950. In an experiment molecular beams passed through two spatially separated optical fields, subject to a strong homogeneous magnetic field in between the light-molecule interactions [351]. By measuring resonance curves, he discovered that if pulse areas of $\frac{\pi}{2}$ each are applied when passing through the optical fields, oscillations as a function of the applied laser frequency become visible in the absorption spectrum of the optical transitions. These oscillations are

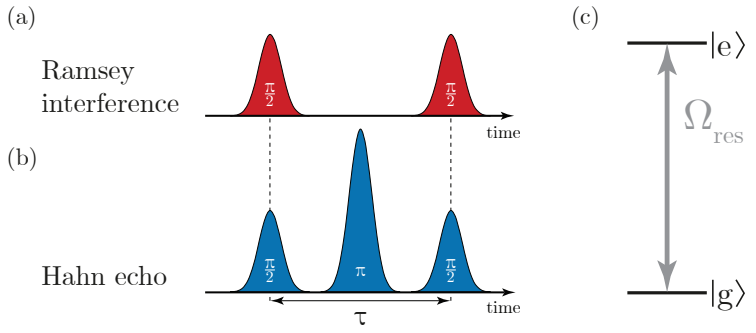


Figure 4.3: (a) Ramsey interference pulse sequence: two $\frac{\pi}{2}$-pulses are applied separated by a temporal delay τ. (b) Hahn echo pulse sequence: two $\frac{\pi}{2}$-pulses are applied with a π-pulse in between. π- and $\frac{\pi}{2}$-pulses are separated by a delay of $\frac{\tau}{2}$ each. (c) Level scheme: A resonant field (Ω_{res}) is applied to a two-level system with ground state $|g\rangle$ and excited state $|e\rangle$.

also called Ramsey fringes.

This method can be used for the measurement of the inhomogeneous coherence time of ensembles of atomic-like systems. The pulse sequence as well as the resonant coupling of an optical field to a two-level system are shown in Fig. 4.3 (a) and (c). Two $\frac{\pi}{2}$-pulses are applied separated by a temporal delay τ. The complete Ramsey scheme is illustrated on the basis of the Bloch sphere in Fig. 4.4 (a) to (d). At first, with all population prepared in the ground state (Fig. 4.4 (a)), a $\frac{\pi}{2}$-pulse is applied transferring the system into a coherent superposition of ground and excited state (Fig. 4.4 (b)). During the pulse delay time τ the system evolves freely within the equatorial plane (Fig. 4.4 (c)). For an inhomogeneously broadened ensemble, different parts of the ensemble experience slightly differing detunings from the resonant field and precess at different angular velocities. Only states with a positive detuning are depicted. Finally, when the second $\frac{\pi}{2}$-pulse is applied, the states are transferred into the x-z-plane. Projections onto the z-axis ($z = \rho_{22} - \rho_{11}$) give the population in the excited state (Fig. 4.4 (d)). The final population in the excited state depends on the time of free evolution τ. As states of different subensembles precess at different speeds during the free evolution process, different phases ϕ are accumulated and the states dephase with

respect to each other. Coherence is lost and less light can be emitted from the excited state. This process becomes all the more visible the longer the free precession time τ. Measuring this decay in fluorescence amplitude the inhomogeneous coherence time can be determined.

4.2.3 Hahn echo

This decoherence can be counteracted by adding a π-pulse to the Ramsey scheme ($\frac{\pi}{2} - \frac{\pi}{2}$) symmetrically in between the two $\frac{\pi}{2}$-pulses. The new pulse scheme ($\frac{\pi}{2} - \pi - \frac{\pi}{2}$) can be seen in Fig. 4.3 (b). Still, the optical field is applied in resonance as it is shown in subfigure (c).

The scheme is named after Erwin Hahn who was first to describe nuclear magnetic spin echos[145]. Dephasing due to inhomogeneous broadening is removed by coherent resonant radio-frequency (rf) control resulting in a rephasing process, the constructive interference of magnetic moments and the spontaneous emission of a nuclear spin signal. As inhomogeneous effects are removed, this method is suited for the measurement of homogeneous coherence times.

Whilst today, most often a pulse sequence of $\frac{\pi}{2} - \pi - \frac{\pi}{2}$ is referred to when speaking of the Hahn echo sequence[352], the echos reported in the original work [145] are generated by $\frac{\pi}{2}$ fields only. After two rf pulses and a first echo, Hahn was also able to observe secondary spin echoes evoked by a third rf pulse[145]. Optical photon echoes were first reported in a ruby crystal[146].

The full Hahn echo method on the Bloch sphere is depicted in Fig. 4.4 (a) to (c) and (e) to (h). The first three steps shown in subfigures (a) to (c) correspond exactly to the Ramsey

scheme described in Subsection 4.2.2. However, already after a free precession time of $\frac{\tau}{2}$ a π-pulse is applied and the Bloch vectors are rotated around the x-axis (e). Afterwards, these continue precessing for another time of $\frac{\tau}{2}$ (f). Again, the angular velocity depends upon the initial detuning from resonance of each subensemble within the inhomogeneous linewidth. As the order of Bloch vectors was reversed by the application of the π-pulse, all vectors will rephase and overlap again after a free evolution of time $\frac{\tau}{2}$ (g). All vectors have accumulated the same phase and interfere constructively. Applying a last $\frac{\pi}{2}$-pulse, the ensemble is transferred back into the ground state (h). If the applied resonant optical fields are not completely symmetrically centred with respect to the inhomogeneous broadening this leads to oscillations of the final population between the ground and excited state. The population in the excited state can be determined in fluorescence measurements. As in the Ramsey scheme, a decay in fluorescence amplitude can be observed extending the time of free evolution τ. As the detrimental effects of inhomogeneous broadening are eliminated, this decay can be attributed to homogeneous disruptive factors fundamentally limiting the coherence time.

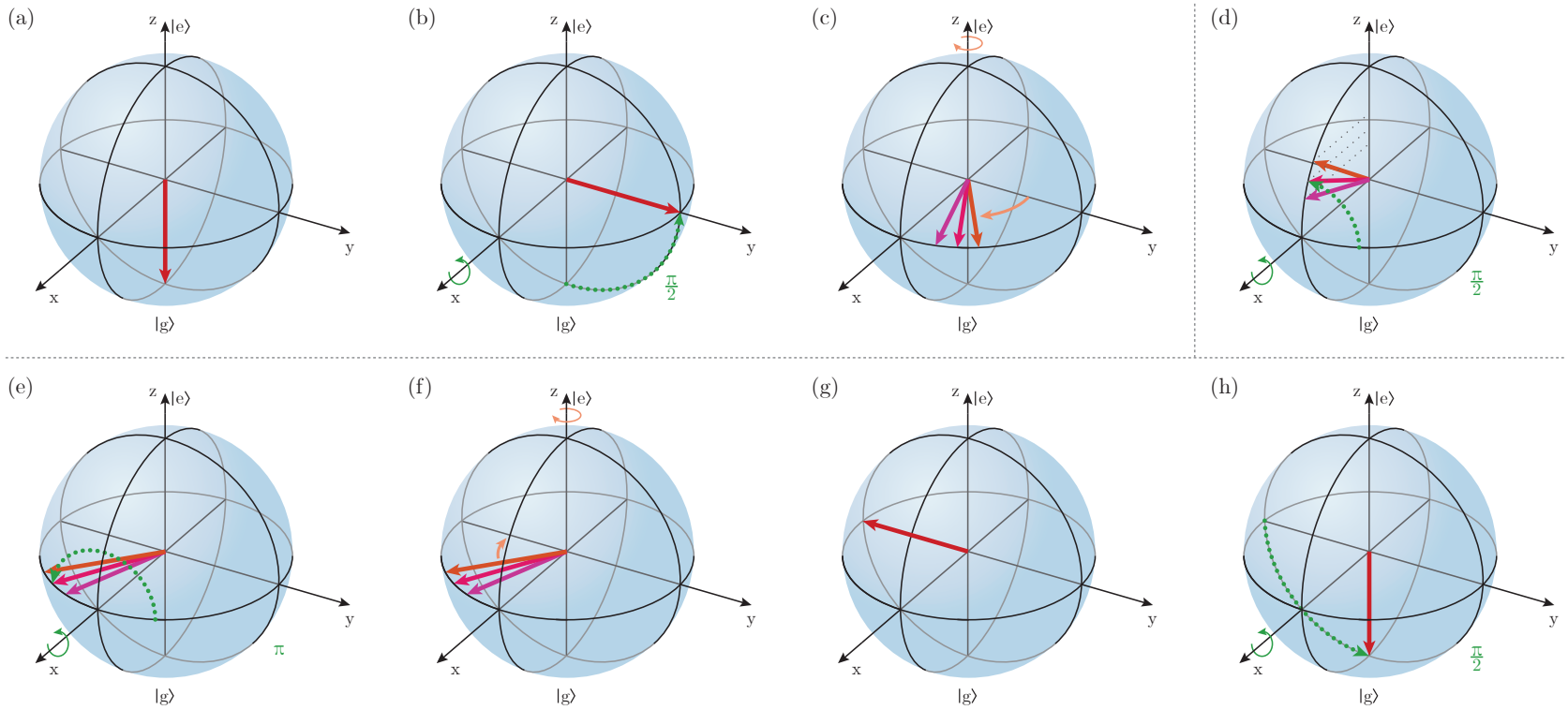


Figure 4.4: Bloch sphere representation of Ramsey interference ((a)-(d)) and Hahn echo ((a)-(c), (e)-(h)). Bloch vectors are shown as straight arrows. Rotations around the x-axis by angles of $\frac{\pi}{2}$ and π are indicated by green dotted arrows, free evolution around the z-axis by orange curved arrows within the equatorial plane. Only states with positive detuning from resonance are depicted.

4.2.4 Stimulated Raman adiabatic passage (STIRAP)

These control schemes can be extended to coherent control by two-step transitions. This enables the coherent manipulation of energetically close ground states with two distinct optical fields. Usually ground states offer longer coherence times than excited states. Therefore, these techniques play an important role in optical memories (see Subsection 2.2.5 and Subsection 2.2.6).

Stimulated Raman adiabatic passage (STIRAP) is a robust technique for lossless population transfer between two non-degenerate quantum states[353]. Detailed reviews of STIRAP can be found in [354] and [355].

For transferring population between two ground states, two optical fields need to be applied to the system on or close to resonance to an excited state and coupling to one ground state each as shown in Fig. 4.5 (a)(i). In the case that population is to be transferred from state $|1\rangle$ to $|2\rangle$, a pump field (P) couples to $|1\rangle$, another field called Stokes field (S) couples to $|2\rangle$ with a detuning $\Delta_P = \omega_{31} - \omega_P$ and $\Delta_S = \omega_{32} - \omega_S$ from the excited state $|3\rangle$ respectively. In fact, the field coupling to state $|2\rangle$ could be a Stokes or an anti-Stokes field, depending on the energy configuration of state $|1\rangle$ and state $|2\rangle$ to each other.

The Hamiltonian, in the rotating-wave approximation (RWA)[356,357], for a three-level system is given by[108,354]

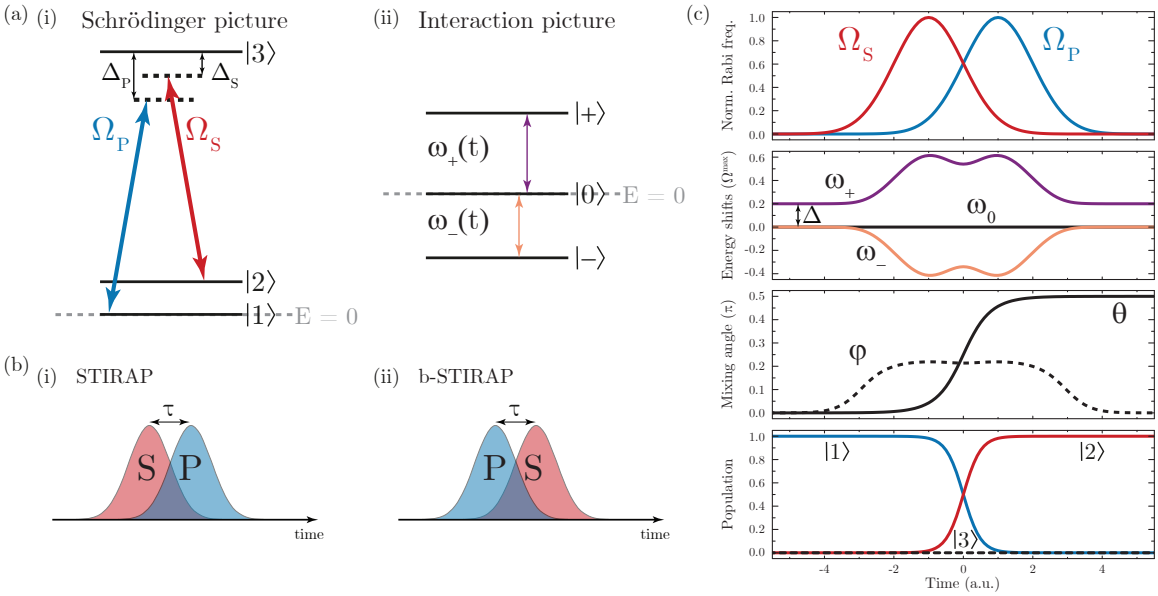


Figure 4.5: STIRAP: (a) Level scheme in (i) the Schrödinger picture and (ii) the interaction picture. (i) Pump field (Ω_P) and Stokes field (Ω_S) are applied with detunings of Δ_P and Δ_S. (ii) While the dark state $|0\rangle$ always remains at zero energy, the energy shift $\omega_\pm$ of the bright states $|\pm\rangle$ is time-dependent. (b) Pulse sequence for (i) STIRAP and (ii) b-STIRAP. The Stokes (S) and the pump pulse (P) are separated by a delay τ. (c) Simulations of the energy shifts, the mixing angles and the population distribution for $\Delta = 0.2\,\Omega_{S,P}^{\max}$. The applied pulse shapes are presented in the upmost figure.

$$\mathcal{H} = \frac{\hbar}{2}\begin{pmatrix} 0 & \Omega_P(t) & 0 \\ \Omega_P(t) & 2\Delta_P & \Omega_S(t) \\ 0 & \Omega_S(t) & 2(\Delta_P - \Delta_S) \end{pmatrix}, \tag{4.21}$$

with the Rabi frequencies

$$\Omega_P = -\frac{d_{13}E_P(t)}{\hbar} \quad \text{and} \quad \Omega_S = -\frac{d_{23}E_S(t)}{\hbar}. \tag{4.22}$$

The transition electronic dipole moments between states $|i\rangle$ and $|j\rangle$ are given by d_{ij}, $E_{P(S)}$ is the electric field amplitude of the pump (Stokes) field. In two-photon resonance ($\Delta = \Delta_P = \Delta_S$) the eigenstates can be evaluated as[354]

$$|0(t)\rangle = \cos(\theta(t))\ |1\rangle - \sin(\theta(t))\ |2\rangle\,, \tag{4.23}$$

$$|+(t)\rangle = \sin(\theta(t))\ \sin(\varphi(t))\ |1\rangle + \cos(\theta(t))\ \sin(\varphi(t))\ |2\rangle + \cos(\varphi(t))\ |3\rangle\,, \tag{4.24}$$

$$|-(t)\rangle = \sin(\theta(t))\ \cos(\varphi(t))\ |1\rangle + \cos(\theta(t))\ \cos(\varphi(t))\ |2\rangle - \sin(\varphi(t))\ |3\rangle\,, \tag{4.25}$$

with time-dependent mixing angles[354]

$$\tan(\theta(t)) = \frac{\Omega_P(t)}{\Omega_S(t)} \quad \text{and} \quad \tan(2\varphi(t)) = \frac{\sqrt{\Omega_P^2(t) + \Omega_S^2(t)}}{\Delta}. \tag{4.26}$$

State $|0\rangle$ is referred to as a dark state because only ground states are involved assumed to be long-lived and not fluorescing. The states $|+\rangle$ and $|-\rangle$ may include the short-lived excited state $|3\rangle$ and, therefore, are referred to as bright. The corresponding eigenenergies evaluate to[354]

$$\omega_0 = 0, \tag{4.27}$$

$$\omega_\pm = \frac{1}{2}\left(\Delta \pm \sqrt{\Delta^2 + \Omega_P^2(t) + \Omega_S^2(t)}\right). \tag{4.28}$$

Both, states and energies in the interaction picture are presented in Fig. 4.5 (a) (ii). A full analytical solution for all possible detuning configurations is given in [358].

For a full, lossless population transfer between the two ground states, the properties of the dark state can be exploited. This is possible by using a counter-intuitive pulse sequence (S-P), as shown in Fig. 4.5 (b) (i), in which the Stokes field is applied first before the pump field interacts with the system. If the intial state $|\psi(t = -\infty)\rangle$ is prepared solely in state $|1\rangle$ only the dark state $|0\rangle$ is populated ($\theta = 0$, $\varphi = 0$). A full simulation of the eigenenergies, the mixing angles and the population transfer is shown in Fig. 4.5 (c). It can be seen that the mixing angle θ is changing slowly from 0 to $\frac{\pi}{2}$ over the whole interaction. In the same way, population is transferred from state $|1\rangle$ to state $|2\rangle$, i.e. the dark state slowly transforms from $|0(t = -\infty)\rangle = |1\rangle$ to $|0(t = +\infty)\rangle = |2\rangle$. For this pulse order, the mixing angle φ has no direct influence on the population transfer.

Adiabatic condition

During the transfer process of population from state $|1\rangle$ to $|2\rangle$, the dark state must change sufficiently slowly such that the state vector of the system, $|\psi\rangle = |1\rangle$ at $t = -\infty$, is able to smoothly follow and to adapt. This adiabaticity ensures that the dark state remains dark and no population is lost during the transfer.

• *Local adiabatic condition*

Population is lost by nonadiabatic coupling of the dark state $|0\rangle$ to one of the bright states $|\pm\rangle$, given by $\langle\pm|\dot{0}\rangle$ [355,359], where

$$\langle +|\dot{0}\rangle = -\dot{\theta}\sin(\varphi) \leqslant |\dot{\theta}\sin(\varphi)| \leqslant |\dot{\theta}| \tag{4.29}$$

$$\text{and } \langle -|\dot{0}\rangle = -\dot{\theta}\cos(\varphi) \leqslant |\dot{\theta}\cos(\varphi)| \leqslant |\dot{\theta}|. \tag{4.30}$$

The dot above variables indicates the temporal derivative. Therefore, nonadiabatic coupling can be assumed to be negligible if it is small in comparison to the energy shift [108,355],

$$\langle\pm|\dot{0}\rangle < |\dot{\theta}| \ll |\omega^{\pm}|. \tag{4.31}$$

A similar chain of arguments starting from the Hamiltonian (4.21), transformed into the basis of $\{|+\rangle, |0\rangle, |-\rangle\}$ is presented in [108] leading to the same condition (4.31). Using equation (4.26), equation (4.31) reads,

$$\left|\frac{\Omega_S\dot{\Omega}_P - \Omega_P\dot{\Omega}_S}{\Omega_S^2 + \Omega_P^2}\right| \ll |\omega^{\pm}|, \tag{4.32}$$

first derived in [360]. This condition must be fulfilled at any moment t during the STIRAP interaction and, therefore, is called the "local" adiabaticity condition.

• *Global adiabatic condition*

For global adiabaticity various criteria have been developed [108,354,355,361] . Integrating both sides of equation (4.31), defining a pulse area [354]

$$\mathcal{A} = \int_{-\infty}^{+\infty} |\omega^{\pm}(t)| dt \tag{4.33}$$

and with

$$\int_{-\infty}^{+\infty} |\dot{\theta}(t)| dt = \frac{\pi}{2} \tag{4.34}$$

as visible in Fig. 4.5 (c), the condition for global adiabaticity reads,

$$\mathcal{A} \gg \frac{\pi}{2}. \tag{4.35}$$

Other global conditions based on experience and numerical simulations suggest $|\omega^{\pm}_{\max}|\,\tau > 10$, where τ is the time the pulses overlap, as a sufficient condition [354,355].

Bright STIRAP

An inverted pulse order (P-S) can also lead to complete coherent population transfer for a non-zero detuning ($\Delta \neq 0$). While the dark state $|0\rangle$ is empty at the beginning of the interaction ($\theta(t = -\infty) = \pi/2$), only $|-\rangle$ ($\varphi(t = -\infty) = 0$) enables an adiabatic transfer from state $|1\rangle$ to $|2\rangle$. However, population is lost by decay from the bright state $|3\rangle$, and as such this scheme is called (bright) b-STIRAP [362,363].

For no detuning from the excited state ($\Delta = 0$) a full population transfer is not always possible. As $\varphi(t) = \pi/4$ over the whole interaction, both bright states $|\pm\rangle$ are populated at the beginning of the interaction and Rabi-oscillations in the transfer efficiency are observed [364].

4.3 Nonlinear processes – Four-wave mixing

In contrast to linear light-matter interactions as described in the previous sections, in nonlinear optics the induced polarisation $\tilde{P}$ at time t and position $\vec{r}$ within the material also depends on higher order terms of the power series in the electric field E [106],

$$\tilde{P}(\vec{r},t) = \varepsilon_0 \left[\chi^{(1)}E(\vec{r},t) + \chi^{(2)}E^2(\vec{r},t) + \chi^{(3)}E^3(\vec{r},t) + \cdots\right] \tag{4.36}$$

$$= \tilde{P}^{(1)}(\vec{r},t) + \tilde{P}^{(2)}(\vec{r},t) + \tilde{P}^{(3)}(\vec{r},t) + \cdots, \tag{4.37}$$

where ε_0 is the permittivity of free space. Four-wave mixing (FWM) is a third-order nonlinear process ($\chi^{(3)}$-process) in which a fourth field is generated by the interaction of three other fields. The nonlinear polarisation generating this field is given by [106]

$$\tilde{P}^{(3)}(\vec{r},t) = \varepsilon_0 \chi^{(3)} E^3(\vec{r},t), \tag{4.38}$$

with the total applied electric field [106]

$$E(\vec{r},t) = A_1(\vec{r})e^{i(\vec{k}_1\vec{r}-\omega_1 t)} + A_2(\vec{r})e^{i(\vec{k}_2\vec{r}-\omega_2 t)} + A_3(\vec{r})e^{i(\vec{k}_3\vec{r}-\omega_3 t)} + c.c., \tag{4.39}$$

where $\hbar\omega_j$ is the energy of field E_j and $A_j(\vec{r})$ the slowly varying field amplitude. The angular wave vector $\vec{k}_j = \frac{2\pi n(\lambda_j)}{\lambda_j}$, where n is the refractive index of the medium, depends both on the wavelength λ_j and the dispersion of the medium ($\frac{\mathrm{d}n}{\mathrm{d}\lambda}$). Substituting equation (4.39) in equation (4.38), the third-order polarisation can be expressed as the sum of all possible frequencies ω_n generated with amplitudes $P(\omega_n)$ [106],

$$\tilde{P}^{(3)}(t) = \sum_n P(\omega_n) e^{i\omega_n t}. \tag{4.40}$$

In total, 44 different frequency components (with distinction between positive and negative frequencies), for example [106]

$$P_n = P(\omega_n = \omega_1 - \omega_2 + \omega_3) = 6\varepsilon_0 \chi^{(3)} A_1 A_2^* A_3 e^{i\left(\vec{k_1} - \vec{k_2} + \vec{k_3}\right)\vec{r}}, \tag{4.41}$$

can be generated. The asterisk indicates the complex conjugate of the field. FWM is a parametric process which means that the quantum state of the material is unaltered by the process. In the case that not all applied fields have a frequency different from each other, the process is called degenerate FWM [365].

The wave propagation through the medium is described by the nonlinear driven wave equation [106,365,366]

$$\nabla^2 \vec{E} - \frac{n^2}{c^2} \frac{\partial^2}{\partial t^2} \vec{E} = \frac{1}{\varepsilon_0 c^2} \frac{\partial^2}{\partial t^2} \vec{P}^{\mathrm{NL}}, \tag{4.42}$$

where n is the refractive index of the medium, c the speed of light, ε_0 the permittivity of free space and $\vec{P}^{\mathrm{NL}}$ the nonlinear polarisation driving a wave with electric field vector $\vec{E}$.

For the case of plane waves travelling in the z-direction, this reduces to[366]

$$\frac{\partial A_n}{\partial z} = -i\frac{\omega_n}{2cn_n\varepsilon_0}P_n, \tag{4.43}$$

which describes the spatial evolution of the newly generated field amplitude A_n by the FWM process polarisation P_n. The polarisation may only drive the field effectively if the wave vector mismatch between the driving fields and the generated field in the direction of propagation $\hat{\vec{r}}$,

$$\Delta k = \Delta\vec{k}\cdot\hat{\vec{r}} = \left(\vec{k_1} - \vec{k_2} + \vec{k_3} - \vec{k_4}\right)\cdot\hat{\vec{r}}, \tag{4.44}$$

is small[106]. Perfect phase matching is reached if $\Delta k = 0$.

4.4 Summary

Important concepts of incoherent and coherent manipulation of ensembles of atomic-like systems were discussed in this chapter. To a limited degree, ensembles of identical atomic-like systems can be prepared in the same state by optical pumping (§4.1). Their inhomogeneous and homogeneous coherence times can be determined by Ramsey interference (§4.2.2) and Hahn echo measurements (§4.2.3) respectively. STIRAP, introduced in Subsection 4.2.4, allows for coherent adiabatic population transfer between the two ground states of a Λ-system and can be seen as preliminary stage for the Raman memory scheme. The Raman memory scheme is prone to noise generated in FWM processes also shown in this chapter (§4.3). Furthermore, seeded phase-dependent FWM processes play an important role in the absorption and amplification of weak signal fields as will be discussed in Subsection 7.3.4 and Subsection 7.4.2.

Before these coherent and incoherent manipulation techniques are implemented experimentally with an ensemble of silicon vacancy centres (SiV^-) described in Chapter 7, the requirements of a solid-state Raman quantum memory and the possible ways of engineering its properties by external electric fields or stress are examined in the following chapter.

Chapter 5

Quantum memory with neutral nitrogen vacancy centres

Ensembles of colour centres in diamond may offer exceptional properties for the implementation of broadband Raman memories. In this chapter the theoretical background of the usage of the neutrally charged NV^0 centre ground-state manifold as a two-level quantum system in a solid-state Raman-type memory is elaborated, first proposed by Eilon Poem et al. in [315]. All additional information, explanations, changes and figures as well as all simulations shown here have been added, were made or carried out by Christian Weinzetl. At the centre of this proposal is the use of the same-spin Λ-system created between the A_1 orbital excited state and the two $E_{x/y}$ orbital ground states of the NV^0 centre for mapping optical pulses onto orbital material excitations. The main findings will be explained and discussed in this chapter.

First, the Raman coupling strength is described and it is demonstrated under which

conditions favourable Raman coupling is achieved (§5.1). In particular, in systems in which the ground states of a Λ-system belong to the same orbital but have different spin projections, only weak Raman coupling can be established for detunings larger than the spin-orbit interaction in the excited states. These findings will have consequences on the prospects of different charge states of the nitrogen vacancy centre to be used as optical Raman quantum memories (§5.1.1, §5.1.2). Second, the effects of an external electric field or uniaxial stress are discussed regarding the orbital ground state splitting in energy (§5.2), the degree of cross-linear polarisation of the optical transitions (§5.3), the relative noise intensity during the Raman memory scheme (§5.4) and the Raman coupling strength (§5.5). For this analysis an ideal case (§5.2.2 - §5.5) and a case commonly found in diamond samples are considered (§5.6). Furthermore, a potential configuration for the experimental realisation of a Raman memory with nitrogen vacancy centres (§5.6.6) as well as the expected memory efficiency are discussed for the common case (§5.6.7). In a final section, lifetimes and coherence times for the orbital ground states of an ensemble of NV^0 centres are estimated (§5.7).

5.1 Raman coupling strength

Calculating the Raman coupling strength between two different ground states i and f, mediated by more than one excited state, for a detuning from the excited states much larger than their bandwidth (to avoid resonant coupling), the Raman coupling coefficient (RCC) is given by [367,368]

$$R_{fi}^{\beta\alpha} = \sum_k \frac{D_{fk}^{\beta} D_{ik}^{\alpha *}}{\Delta_k} \approx \underbrace{\frac{\sum_k D_{fk}^{\beta} D_{ik}^{\alpha *}}{\bar{\Delta}}}_{\text{FORC}} - \frac{\sum_k D_{fk}^{\beta} D_{ik}^{\alpha *} \varsigma_k}{\bar{\Delta}^2}. \tag{5.1}$$

In this equation $D^{\{\alpha,\beta\}}_{\{f,i\}k}$ stands for the transition dipole moment between the ground state $\{f,i\}$ and the excited state k in polarisation $\{\alpha,\beta\}$, Δ_k is the detuning of the signal and control frequencies from the excited state k in two-photon resonance, $\bar{\Delta}$ is the mean detuning from all excited states and $\varsigma_k = \Delta_k - \bar{\Delta}$ is a weight factor taking into account the difference between the mean detuning and the detuning from the excited state k. For the approximation in equation (5.1) second-order perturbation theory has been used [315]. This approximation is only possible for detunings larger than all values of ς_k for which $D^{\beta}_{fk}D^{\alpha*}_{ik} \neq 0$, i.e. for transitions and excited states participating in the optical Raman transition. At the same time, for large detunings, the first term of the approximation, the first-order Raman coupling (FORC), prevails over the second term. In particular this is the case if the second term vanishes for a system with a single excited state. In this case $\varsigma_k = 0$.

The cases in which the FORC term vanishes are by far more problematic, when considering the probability for a Raman transition. In these cases, the Raman coupling decreases rapidly with the square of the detuning. This is the case if all products $D^{\beta}_{fk}D^{\alpha*}_{ik}$, for $i \neq j$, are zero for all polarisations, either if at least one of the dipole vectors is of length zero or if the two dipole moments are orthogonal to each other. For the case where all non-zero terms $(i = f)$ are equal, this can be written in a compact way for a polarisation pair $\{\beta,\alpha\}$, using the complete dipole matrices as

$$D^{\beta}D^{\alpha\dagger} = a_{\beta,\alpha}I. \tag{5.2}$$

Here, $a_{\beta,\alpha}$ is a constant and I the identity matrix. It can be seen that all off-diagonal

elements, which are the only matrix elements appearing in equation (5.1), are zero. For this reason, the FORC vanishes identically.

If the FORC vanishes identically for a specific pair of polarisations and basis of states, this is also true for any pair of polarisations and choice of bases. Dipole moments for a given polarisation can be understood as projections of transitional dipole moments onto the vector of polarisation, $D^{\beta'} D^{\alpha'\dagger} = \vec{\beta'} D D^\dagger \vec{\alpha'}^\dagger$. Defining the polarisations $\vec{\alpha'}$ and $\vec{\beta'}$ as rotated initial polarisations $\vec{\alpha}$ and $\vec{\beta}$, $\vec{\alpha'} = R_\alpha^{\alpha'} \vec{\alpha}$ and $\vec{\beta'} = R_\beta^{\beta'} \vec{\beta}$ with the rotation matrix $R_\alpha^{\alpha'}$ ($R_\beta^{\beta'}$), equation (5.2) is satisfied by $D^{\beta'} D^{\alpha'\dagger} = \vec{\beta'} D D^\dagger \vec{\alpha'}^\dagger = R_\beta^{\beta'} \vec{\beta} D D^\dagger \vec{\alpha}^\dagger R_\alpha^{\alpha'\dagger} = R_\beta^{\beta'} a_{\beta,\alpha} R_\alpha^{\alpha'\dagger} I = a'_{\beta',\alpha'} I$. Furthermore, equation (5.2) also holds for any unitary basis transformation in the ground and excited states. For the basis transformation

$$\widetilde{D}^{\alpha(\beta)} = U\, D^{\alpha(\beta)}\, V^\dagger, \tag{5.3}$$

where U and V are unitary transformation matrices transforming between bases in the ground and excited state respectively, equation (5.2) holds as well. Equivalently, it is $\widetilde{D}^\beta \widetilde{D}^{\alpha\dagger} = U\, D^\beta\, V^\dagger V\, D^{\alpha\dagger}\, U^\dagger = U\, D^\beta\, D^{\alpha\dagger}\, U^\dagger = U\, a_{\beta,\alpha}\, I\, U^\dagger = a_{\beta,\alpha} I$ with the same constant $a_{\beta,\alpha}$. Note that the derivation above does not include the case where the transformation mixes ground and excited states. However, mixing of ground and excited states only happens for fields stronger than the energy difference between ground and excited states.

It can be shown that for systems in which the ground states show different spins but the same orbital, and in which the ground and excited state as well as the transition dipole

moment can be decomposed into spin-orbit (SO) products, the first-order Raman coupling (FORC) vanishes identically. The proof is as follows: In the spin-orbit basis the dipole moment can be written as the product of an orbital function d and a spin δ function

$$D^{\alpha(\beta)}_{i(f)k} = d^{\alpha(\beta)}_{\mathrm{o}_g\mathrm{o}_k}\delta_{\mathrm{s}_{i(f)}\mathrm{s}_k}. \tag{5.4}$$

For the initial (i) and final (f) state the orbital o_g is the same. The orbital of the excited state is given by o_k. Spins of the initial, final and transitional excited state are denoted by s_i, s_f and s_k. In this case the numerator of the FORC term reads,

$$\sum_k D^{\beta}_{fk} D^{\alpha*}_{ik} = \left(\sum_{\mathrm{o}_k} d^{\beta}_{\mathrm{o}_g\mathrm{o}_k} d^{\alpha*}_{\mathrm{o}_g\mathrm{o}_k}\right)\delta_{\mathrm{s}_i\mathrm{s}_f} = a_{\beta,\alpha}\delta_{if}, \tag{5.5}$$

where $\delta_{ik}\delta_{kf} = \delta_{if}$ has been used and $a_{\beta,\alpha}$ is a constant. Owing to this relation, condition (5.2) is fulfilled and the FORC term vanishes identically.

As discussed above, this is also true for any other choice of polarisation and basis representation of the states. However, the decomposition into the product of the spin and orbit basis of equation (5.4) and, in consequence, equation (5.5) do not hold for SO mixing of the excited states. In order to avoid SO mixing, the detuning from the excited states taking part in the Raman interaction needs to be larger than the energy splitting between those states of different spin induced by SO mixing itself.

In conclusion, only spin mixing interactions (SMI) mixing spin-orbit products of excited states with different spins, can prevent the FORC from vanishing in Λ-systems with ground states of different spin but same orbital degree of freedom. For average detunings $\bar{\Delta}$ larger

than the SMI energy, the FORC vanishes and the relative Raman coupling strength, $\mathcal{R}$, decreases with the square of the average detuning.

5.1.1 Special characteristics of NV^-

Regarding the level structure and the allowed optical transitions between the ground and excited states under an external electric field or stress, the fundamental differences between the negatively and neutrally charged NV centre with respect to the Raman coupling strength can be explained using Fig. (5.1).

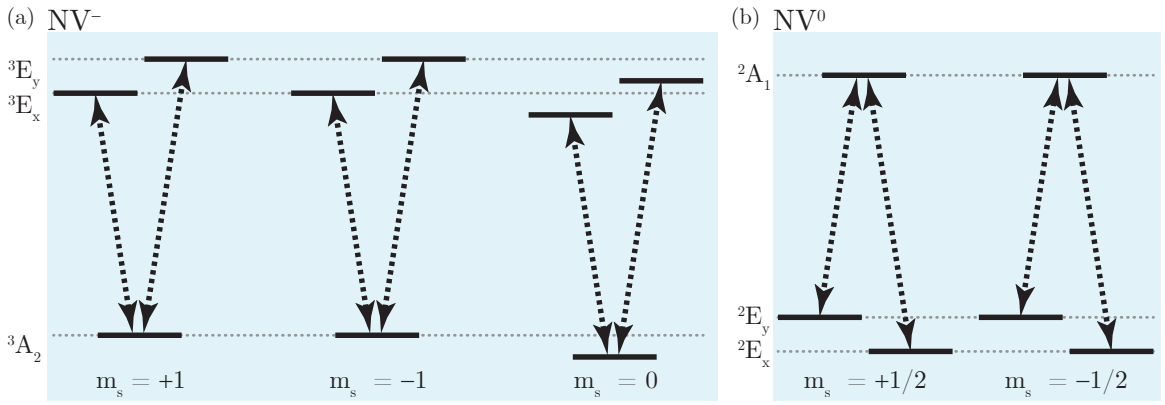


Figure 5.1: Level configuration of NV^- (a) and NV^0 centres (b) for strong electric fields applied along the x-axis in the NV basis. For each level the orbital and the spin m_s is given. Dotted arrows indicated allowed optical transitions between ground and excited states of same spin. (a) For NV^-, three V-level systems, each of different spin, can be distinguished. In order to create a Λ-system between the ground states, SMI of the excited states of different spin is necessary in order to establish a two photon transition between two ground states of different spin but the same electronic orbital. (b) For NV^0, two Λ-systems with ground states of same spin but different orbital can be observed. No SMIs are required.

The level structure of NV^- (see Subsection 3.2.5) can be divided in three different independent spin systems with spins $m_s = +1$, -1 and 0, allowing only spin preserving transitions between the ground and excited state manifolds which is shown in Fig. 5.1 (a). In the ground state manifold all states have the same orbital ($^3A_2$) but a different spin. For

each spin a V-system between ground and excited states is created. For the purpose of a Raman quantum optical memory (QOM), a Λ-system needs to be constructed. This is only possible using two ground states with the same orbital but a different spin.

Therefore, as derived beforehand in Section 5.1, a Raman QOM in this system with different spin ground states, can only be realised by SMIs that enable Raman coupling between the different ground states via two mixed excited states. In general, these SMIs can occur as transverse spin-orbit, or transverse spin-spin interactions. Transverse spin-orbit interactions only mix triplet and singlet states of different electronic configurations [267] and have no contribution to the SMI in the excited states of the NV^-. Excited state mixing by spin-spin interaction occurs when those levels are energetically shifted close to each other by external magnetic [369] or electric fields [370], or external stress [371]. Nonetheless, in all these cases the SMI in NV^- is of the order of 1.5 GHz or less [369]. For detunings larger than the SMI the FORC vanishes and the RCC decreases quadratically with the mean detuning $\bar{\Delta}$. Raman coupling becomes inefficient for detunings larger than the relevant excited state splittings.

Low Raman coupling is the main limiting factor for this centre to be used as Raman QOM. This problem can be circumvented, for example, by increasing the coupling by a cavity design [27,372] or spectral hole-burning techniques [158,373]. Spectral hole-burning may allow a closer-to-resonance operation, and therefore, a higher coupling efficiency.

Furthermore, using microwave fields to drive the excited states of the NV^- centre, a memory scheme would be conceivable. This would include addressing two same spin trans-

itions between ground and excited states resonantly by the signal and control field. Microwave field π-pulses need to be applied between the addressed spin states in the excited manifold. However, in this resonant memory scheme, the bandwidth of the signal field stored would be limited by the inhomogeneous broadening of the resonant and microwave transitions, unlike in the off-resonant Raman memory scheme.

5.1.2 Special characteristics of NV^0

In comparison to the NV^- system, the NV^0 presents a different level and energy structure (see Subsection 3.2.5), presented in Fig. 5.1 (b). Again, only spin-preserving transitions are allowed but in this case, a Λ-system is created immediately, comprising two ground levels with the same spin but occupying different orbitals. Hence, condition (5.5) for vanishing FORC does not apply and no SMIs are needed to establish a Raman scheme. The FORC does not vanish and, in fact, is the only term in equation (5.1) as each possible Raman transition is only via one excited state. The coupling only decreases by $1/\bar{\Delta}$ and is, for example, given the same pair of polarisations $\{\alpha, \beta\}$ and dipole moments of the same order of magnitude, approximately two orders of magnitude higher for a detuning of $\sim 30\,\mathrm{GHz}$ than for the NV^- centre.

This makes the neutral NV centre a plausible candidate for a solid-state Raman QOM. Further properties of the NV^0 centre, especially under the influence of an external electric field are discussed below in the following sections.

5.2 Optical transitions under an electric field or external stress

5.2.1 The NV^0 Hamiltonian

The full Hamiltonian of the NV^0 centre, excluding internal random strain, can be given as[266,267,315]

$$\hat{\mathcal{H}} = \hat{\mathcal{H}}_0 + \hat{\mathcal{H}}_{\mathrm{SO}} + \hat{\mathcal{H}}_{\mathrm{DJT}} + \hat{\mathcal{H}}_{\mathrm{EF}} \tag{5.6}$$

$$= \hat{\mathcal{H}}_0 + \lambda_{\parallel}\hat{L}_z\hat{S}_z + \lambda_{\perp}(\hat{L}_x\hat{S}_x + \hat{L}_y\hat{S}_y) + \hat{\mathcal{H}}_{\mathrm{DJT}} - \hat{\vec{d}}\cdot\vec{F}. \tag{5.7}$$

$\hat{\mathcal{H}}_0$ includes the kinetic energy of the electrons and the Coulomb interaction of the electrons of the centre with the electrons and nuclei of the diamond lattice[266], $\lambda_{\parallel\,(\perp)}$ is the longitudinal (transverse) spin-orbit (SO) coupling energy in $\hat{\mathcal{H}}_{\mathrm{SO}}$, $\hat{\mathcal{H}}_{\mathrm{DJT}}$ is the Hamiltonian of dynamic Jahn-Teller (DJT) interactions[313], $\hat{\vec{d}}$ is the electric dipole vector operator[266,267] and $\vec{F}$ is the electric field vector within the interaction Hamiltonian $\hat{\mathcal{H}}_{\mathrm{EF}}$ describing the interaction with an external electric field[315]. Unlike in Hamiltonians for the negatively charged NV centre[266,267], there are no spin-spin interactions due to one electron only in the outmost orbital[211,266,277]. As shown in Fig. 3.5, the z-axis is chosen along the connection between the nitrogen atom and the vacancy position, the x-axis is defined to lie within one of the three nitrogen vacancy symmetry reflection planes. Thus, the y-axis is normal to the chosen reflection plane.

The Hamiltonian of the excited and ground states can be examined separately. For the excited states, only the energy of the mean ZPL energy at zero external field, $\varepsilon_e = 521.4\,\mathrm{THz}$, and longitudinal external fields have to be considered. The excited states are not affected by

DJT coupling and show no angular momentum. In the basis of $\{A_{1,\uparrow}, A_{1,\downarrow}\}$ (see Fig. 3.6 (b)) their Hamiltonian reads

$$\mathcal{H}_e = (\varepsilon_e - d_{\parallel} F_z) \begin{pmatrix} 1 & 0 \\ 0 & 1 \end{pmatrix}, \tag{5.8}$$

where F_z is the z-component of the electric field. However, this field dependence is very weak and does not lift the degeneracy of the states[306]. Therefore, the excited states can be considered constant in energy.

With vanishing transverse SO interactions[371,374] the ground state Hamiltonian simplifies to[266,267]

$$\mathcal{H}_g = \mathcal{H}_{0,g} + \mathcal{H}_{SO,g} + \mathcal{H}_{DJT+EF,g}, \tag{5.9}$$

with

$$\mathcal{H}_{0,g} = \varepsilon_g \begin{pmatrix} 1 & 0 & 0 & 0 \\ 0 & 1 & 0 & 0 \\ 0 & 0 & 1 & 0 \\ 0 & 0 & 0 & 1 \end{pmatrix}, \tag{5.10}$$

$$\mathcal{H}_{SO,g} = \frac{\lambda_{\parallel}}{2} \begin{pmatrix} 0 & 0 & -i & 0 \\ 0 & 0 & 0 & i \\ i & 0 & 0 & 0 \\ 0 & -i & 0 & 0 \end{pmatrix}, \tag{5.11}$$

$$\mathcal{H}_{DJT+EF,g} = (\Upsilon_x - d_\perp F_x)\begin{pmatrix} 1 & 0 & 0 & 0 \\ 0 & 1 & 0 & 0 \\ 0 & 0 & -1 & 0 \\ 0 & 0 & 0 & -1 \end{pmatrix} + (\Upsilon_y - d_\perp F_y)\begin{pmatrix} 0 & 0 & 1 & 0 \\ 0 & 0 & 0 & 1 \\ 1 & 0 & 0 & 0 \\ 0 & 1 & 0 & 0 \end{pmatrix}, \qquad (5.12)$$

in the basis of $\{E_{x,\uparrow}, E_{x,\downarrow}, E_{y,\uparrow}, E_{y,\downarrow}\}$ (see Fig. 3.6 (b)). The electric field components in y and z direction are given by F_y and F_z, Υ_x and Υ_y are the components of the vibronic DJT energy with $\Upsilon = \sqrt{\Upsilon_x^2 + \Upsilon_y^2}$ [313], and the mean ground state energy ε_g is set to zero. All directional components are given in the basis of the NV^0 centre. The transverse electric dipole moment and the longitudinal SO interaction energy have been estimated to $d_\perp \approx 5\,\mathrm{GHz\,\mu m/V}$ and $\lambda_\parallel \approx 4.3\,\mathrm{GHz}$. The estimation is based on the values for the E-symmetric excited state manifold of the NV^- centre [371,375] corrected by the ratio of the measured strain energy coefficients of both NV charge states [262,306].

In ensembles of NV^0 centres, the ground state splitting with no external fields applied amounts to $S_0 = \sqrt{\lambda_\parallel^2 + 4\Upsilon^2}$ [313]. In [315] the stress-free ground state splitting S_0 was measured by off-resonant fluorescence spectroscopy and estimated by fitting the ZPL to a double Gaussian function to $S_0 \lesssim 24\,\mathrm{GHz}$, leaving the DJT energy estimate at $\Upsilon \lesssim 12\,\mathrm{GHz}$ as an upper bound [315]. This value will be used in the following analysis.

5.2.2 Application of external electric fields

As the Hamiltonian and all necessary variables are defined, the ground state splitting due to external fields or pressure can be examined. The effects of external electric fields and uniaxial stress are equivalent [376]. The energy splitting, as well as the alignment of dipole moments, the Raman coupling efficiency and the level of unwanted coupling depend on the orientation of the NV^0 centre, the direction of the applied electric field and the strength of the DJT components.

For an NV^0 centre with a z-axis aligned along [111] and an external field in $[\bar{1}\bar{1}2]$, in parallel to the centres x-axis, the energy splitting of the ground states is depicted in Fig. 5.2 (a). Simulations are carried out for $\Upsilon = 0\,\mathrm{GHz}$, as well as for $\Upsilon = 12\,\mathrm{GHz}$ with directionality $\alpha = \arctan(\Upsilon_y/\Upsilon_x) = 0°, \pm 90°$ and 180°. These represent different possibilities for how the DJT effect could affect the results. In all simulations presented in Fig. 5.2 the curves for $\alpha = +90°$ and $\alpha = -90°$ overlap completely. In all cases, SO and DJT interactions are quickly overcome by the applied external field manifesting itself in a linear energy shift with a slope corresponding to the transverse electric dipole moment $d_\perp$. As mentioned above, the energy of the excited states does only weakly depend on the applied electric field and can be assumed to be constant. In particular, this is valid when $F_z = 0$ for fields applied in the centres x direction only.

With no external fields applied, the orbital ground states E_x and E_y are split and mixed by the SO and DJT interactions. Given no DJT effects, the eigenstates are the total angular momentum projection states, $E_{\pm\frac{1}{2}} = \frac{1}{\sqrt{2}}(E_{x,\uparrow(\downarrow)} \mp iE_{y,\uparrow(\downarrow)})$ and

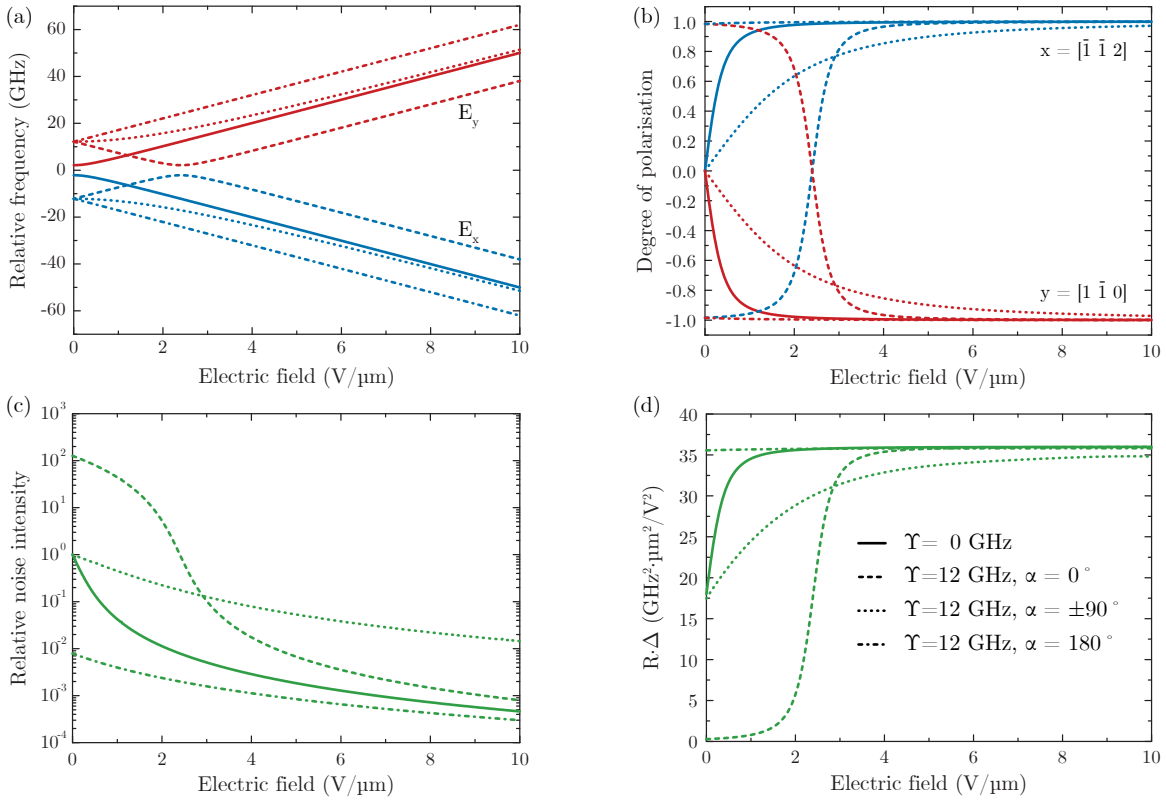


Figure 5.2: Influence of an external electric field in x = $[\bar{1}\bar{1}2]$ direction on the ground state level splitting (a), the degree of polarisation of the optical transitions between the two ground states and the excited state (b), the relative probability of the control field in x-polarisation to couple to the higher ground state (c) and the product of the Raman coupling coefficient and the detuning of the Raman transition from the excited state (d). All simulations have been conducted for no DJT effects ($\Upsilon = 0$) (solid lines), as well as for a DJT energy of $\Upsilon = 12\,\mathrm{GHz}$ for $\alpha = \tan^{-1}(\Upsilon_y/\Upsilon_x) = 0°$, ±90° and 180° (broken lines). The linestyle for each setting is indicated as inset in subfigure (d). All NV^0 centres are aligned with their symmetry axis in z = [111] direction. In (b), a degree of polarisation of 1 (-1) corresponds to a complete polarisation in x = $[\bar{1}\bar{1}2]$ (y = $[1\bar{1}0]$) direction. In (d), the Raman coupling strength detuning product is independent of the detuning in the large detuning regime. The Raman coupling coefficient has been calculated for x-polarised light coupling to the lower ground state, while y-polarised light coupling to the higher ground state. For the simulation, (a) the equations (5.9) - (5.12), (b) the equations (5.13) - (5.15), (c) the equations (5.13), (5.14) and (5.16), and (d) equation (5.1) were used.

$E_{\pm\frac{3}{2}} = \frac{1}{\sqrt{2}}(E_{x,\uparrow(\downarrow)} \pm iE_{y,\uparrow(\downarrow)})$, caused by the SO interactions. In more general cases, the share of each orbital ground state depends upon the strength of Υ_x, Υ_y and $\lambda_{\|}$. In all cases, the application of an external electric field eventually leads to the complete transformation of the states to $\{E_{x,\uparrow}, E_{x,\downarrow}, E_{y,\uparrow}, E_{y,\downarrow}\}$.

For memory applications a splitting of 50 GHz or more could be achieved with fields of $\sim 5\,\mathrm{V/\mu m}$ (Fig. 5.2 (a)) or equivalently external pressure of $\sim 50\,\mathrm{MPa}$[306], both already applied in other experiments to NV^0 or NV^- centres[306,370]. A splitting of this order of magnitude is necessary to clearly separate the inhomogeneously broadened optical transitions and to store short pulses of large bandwidth which is limited by the ground state splitting. Furthermore, this splitting in energy can be used for spectral separation of signal and control field by dispersive optical elements. Still, often, especially for pulse bandwidths at the same order of magnitude as the ground state splitting, this is not enough to suppress the control field tails at signal frequency sufficiently, especially when working with signal fields at the single photon level. For this reason, different directions of polarisation of these two fields are desirable, both for signal field filtering as well as to avoid noise generation by FWM (see Subsection 2.2.6). Namely, this is possible by imposing cross-linear polarisation selection rules on the two optical transitions between the two orbital ground and the single orbital excited state.

5.3 Cross-linear polarisation selection rules

Applying uniaxial stress or an electric field, cross-linear polarisation selection rules can be imposed on the atomic-like system to suppress noise encountered in Raman memories (see Subsection 2.2.6). In consequence, orthogonally-polarised control and signal fields couple only to mutually different ground states. Without this effect previous implementations of the Raman protocol in alkali vapours with successful storage of $\sim 300\,\mathrm{ps}$ pulses for more than $1\,\mu\mathrm{s}$ suffered from relatively high noise levels[31,191,377]. A further advantage of the external stress or electric field induced ground state splitting is that the acceptance

bandwidth of the memory can be actively controlled. By separating the ground state levels in energy large pulse bandwidths can be stored coupling only to one of the ground state levels as discussed in the previous section.

In the ground state and excited state basis $\{E_{x,\uparrow}, E_{x,\downarrow}, E_{y,\uparrow}, E_{y,\downarrow}\}$ and $\{A_{1,\uparrow}, A_{1,\downarrow}\}$ the components of the dipole transition moments can be expressed as

$$D^x = \frac{d_{ge}}{\sqrt{2}} \begin{pmatrix} 1 & 0 \\ 0 & 1 \\ 0 & 0 \\ 0 & 0 \end{pmatrix}, \quad D^y = \frac{d_{ge}}{\sqrt{2}} \begin{pmatrix} 0 & 0 \\ 0 & 0 \\ 1 & 0 \\ 0 & 1 \end{pmatrix}, \quad D^z = \frac{d_{ge}}{\sqrt{2}} \begin{pmatrix} 0 & 0 \\ 0 & 0 \\ 0 & 0 \\ 0 & 0 \end{pmatrix}, \tag{5.13}$$

where d_{ge} is the dipole strength between the ground and excited states. Only spin-conserving transitions are allowed. The transitional dipole moment can be estimated using [297]

$$d_{ge} = \sqrt{\frac{3\pi^2 \epsilon_0 \hbar c^3 \gamma_{\mathrm{ZPL}}}{n_d \nu_0^3}} \approx 6 \, \frac{\mathrm{GHz\,\mu m}}{\mathrm{V}}, \text{ where } \gamma_{\mathrm{ZPL}} = 0.035\,\gamma. \tag{5.14}$$

For this estimation, the NV^0 excited state radiative decay rate $\gamma \approx {}^1\!/_{20}\,\mathrm{ns}^{-1}$ [309], the refractive index of diamond n_d [378] and the ZPL frequency of the NV^0 centre ν_0 have been used (see Subsection 3.2.5).

The degree of polarisation of the optical transitions with respect to x and y directions (as defined in the NV basis) can be calculated using the coupling strength $P_{\{x,y\}}^{\{(1),(2)\}}$ of $\{x, y\}$-polarised light to the optical transitions {1: $E_x \leftrightarrow A_1$} and {2: $E_y \leftrightarrow A_1$} (high

stress/electric field notation). The full degree of polarisation, also called "visibility", is defined as

$$\mathcal{P}^{\{(1),(2)\}} = \frac{P_x^{\{(1),(2)\}} - P_y^{\{(1),(2)\}}}{P_x^{\{(1),(2)\}} + P_y^{\{(1),(2)\}}}. \tag{5.15}$$

It is worth noting that $P_{\{x,y\}}^{\{(1),(2)\}} \propto |E|^2$ and, in consequence, the same formula (5.15) for the degree of polarisation can be used for experimental measurements of the emitted fluorescence intensity in different orientations of polarisation (see Section 6.2.2).

The change of polarisation degree depending on the applied electric field is shown in Fig. 5.2 (b). For all cases of DJT energies and directions, both optical transitions develop perfect coupling to x- or y-polarised light. Transition 1 couples only to x-polarised light, transition 2 solely to y-polarised light.

5.4 Relative noise intensity

For Λ-transitions in Raman memories, this has the great advantage of suppressing accidental coupling of signal and control field to other transitions than those they should be applied to, in the end reducing the intensity of noise generated. In particular, an unintentional material excitation is created when the strong control field couples to both transitions transferring populations between the ground states. Defining the relative noise intensity as

$$\mathcal{N} = \frac{P_x^{(2)}}{P_x^{(1)}}, \tag{5.16}$$

$\mathcal{N}$ represents the probability of x-polarised light to couple to the energetically higher ground state on transition 2, divided by the probability of x-polarised light coupling to the intended transition 1 connecting the lower ground state with the excited states. This value reflects to which extent a control photon couples to the wrong optical transition whenever a control photon couples to the correct optical transition. When this is the case, a noise excitation is created within the memory or a FWM process is enabled. As presented in Fig. 5.2 (c), at a level splitting of $S \approx 50\,\mathrm{GHz}$ a relative noise intensity of $\sim 1/550$ is reached for $\Upsilon = 0\,\mathrm{GHz}$. In the most unfavourable conditions shown here, for $\Upsilon = 12\,\mathrm{GHz}$ and $\alpha = \pm 90°$, still a suppression factor of $\sim 1/15$ is reached.

5.5 Raman coupling

In the same way the degree of polarisation increases with the electric field, the Raman coupling between the two ground states rises. The Raman coupling coefficient as described in Section 5.1 equation (5.1) has been calculated in the large detuning approximation for which only the FORC term needs to be considered. The Raman coupling and detuning product $R^{x\,y}_{E_1\,E_2} \cdot \bar{\Delta}$, shown in Fig. 5.2 (d) is independent of the detuning and includes both spin-conserving transitions between the two orbital ground state with a x-polarised field applied to transition 1 and a y-polarised field applied to transition 2. Both Λ-systems contribute equally to the total Raman coupling. Again, independent of DJT effects, all systems asymptotically approach a common value.

To sum up, this leaves the NV^0 centre as a valuable system with a variable ground state splitting by external stress or applied electric fields, highly cross-linear polarised op-

tical transitions which prevent spurious coupling and noise generation during the memory protocol, as well as with two same-spin optical Λ-systems connecting both ground states.

5.6 Memory in a (001) diamond sample

The configuration presented in the previous section with the symmetry axis of the NV^0 centre aligned in [111] and an electric field applied in $[\bar{1}\bar{1}2]$ direction can be seen as an ideal configuration. Maybe the most compelling argument is the complete cross-linear polarisation of the optical transition and, consequently, the low probability of noise in Raman memory schemes. However, ensembles of NV^0 centres with unique orientation are rare, even though the fabrication of diamond samples with uniform alignment has seen progress recently [206–208]. In experiments described in Chapter 6, a (001)-faceted ensemble with all possible NV orientations is used. For this reason, theoretical predictions and differences to ensembles with single NV orientation are worked out in this section. Furthermore, the applicability of such ensembles as Raman memory will be discussed.

5.6.1 Optical axis and electric field orientation

In a (001)-faceted diamond sample the axis of the NV^0 centre can be aligned in eight different directions in $\langle 111 \rangle$, as shown in Fig. 5.3. The external electric field is applied in [100] direction with an optical access axis along [001]. In the same basis, linear polarisation directions are defined as horizontal, H = [100], and vertical, V = [010].

Due to the symmetry of this configuration, the projection of the electric field onto the x, y and z axis of each centre is the same for each NV^0 orientation.

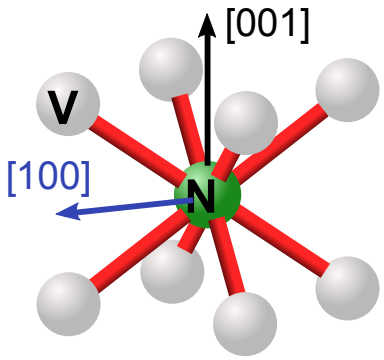


Figure 5.3: All possible NV orientations in a (001) diamond sample. From the central green nitrogen atom "N" the white vacancies "V" are pointing in ⟨111⟩ direction. Uniaxial stress or electric fields are applied to the centres in [100] direction (blue arrow); the optical axis is parallel to [001] (black arrow).

5.6.2 Ground state level splitting

The shift in energy when an external electric field is applied is shown in Fig. 5.4 (a), again, for no DJT and for DJT energies of 12 GHz absolute value and different directionalities α. For electric fields stronger than 5 $\mathrm{V/\mu m}$, the absolute value of the slope of 4.08 $\mathrm{GHz\,\mu m/V}$ is smaller in comparison to an ideal alignment of the electric field and corresponds to the projection of the electric field onto the x-y-plane of the NV^0 basis. In consequence, higher electric fields (than for the ideal scenario described earlier) in [100] direction are needed to reach a ground state splitting of 50 GHz. Furthermore, for $\Upsilon = 12\,\mathrm{GHz}$ the energy shift differs for $\alpha = +90°$ and $\alpha = -90°$. The same switching is observed for the degree of polarisation, the relative noise intensity and the Raman coupling-detuning product presented later in this section. For half of the possible NV^0 orientations the effects are inverted according to the sign of α. For no DJT energies involved, or when $\alpha = 0°$ or 180° for which $\Upsilon_y = 0\,\mathrm{GHz}$, all orientations of the NV^0 symmetry axis experience the same energy shifts.

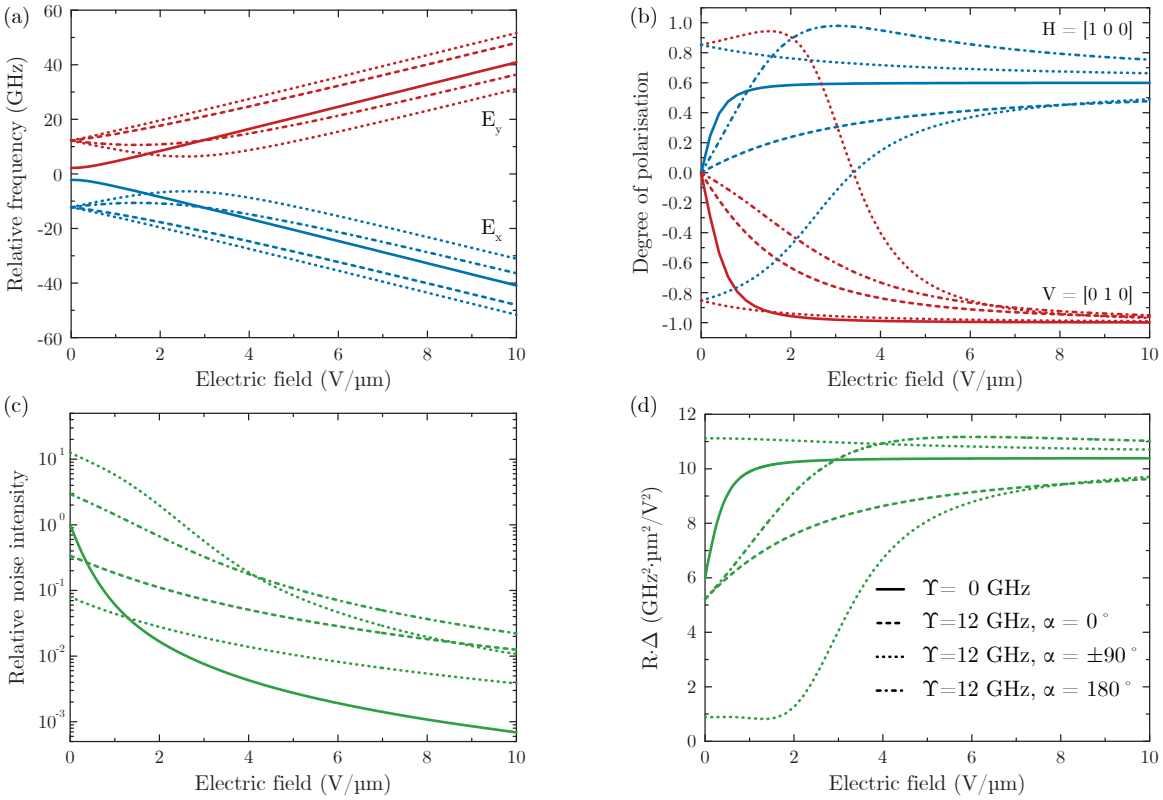


Figure 5.4: Influence of an external electric field in the [100]-direction on the ground state level splitting (a), the degree of polarisation of the optical transitions between the two ground states and the excited state (b), the relative probability of the control field in H-polarisation to couple to the higher ground state (c) and the product of the Raman coupling coefficient and the detuning of the Raman transition from the excited state (d). All simulations have been conducted for no DJT effects ($\Upsilon = 0\,\mathrm{GHz}$) (solid lines), as well as for a DJT energy of $\Upsilon = 12\,\mathrm{GHz}$ for $\alpha = \tan^{-1}(\Upsilon_y/\Upsilon_x) = 0°$, $\pm 90°$ and $180°$ (broken lines). The linestyle for each setting is indicated as inset in subfigure (d). All NV^0 centres are aligned with their symmetry axis along one of the eight directions $\langle 111 \rangle$. For all possible orientations the results are the same. Only for $\alpha = \pm 90°$ results depend on the sign of α and switch between the orientation of the centre. In (b), a degree of polarisation of 1 (-1) corresponds to a complete polarisation in H = [100] (V = [010]) direction. In (d), the Raman coupling strength detuning product is independent of the detuning in the large detuning regime. The Raman coupling coefficient has been calculated for H-polarised light coupling to the lower ground state, while V-polarised light coupling to the higher ground state. For the simulation, (a) the equations (5.9) - (5.12), (b) the equations (5.13), (5.14) and (5.17), (c) the equations (5.13), (5.14) and (5.18), and (d) equation (5.1) were used.

5.6.3 Degree of polarisation

With increasing external electric field the transition dipole moments align asymptotically in directions defined by the direction of the electric field. For transition 1 the dipole moment aligns along the projection of the electric field onto the x-y plane (NV basis) of the centre

parallel to ⟨211⟩. The dipole moment of transition 2 aligns perpendicular to this projection in the x-y plane along ⟨011⟩. Projection of these dipole moments onto the (001)-facet of the diamond (1:⟨210⟩, 2:⟨010⟩) predicts a polarisation degree of $\mathcal{P}^{(1)} = 0.6$ for transition 1 and perfect vertical polarisation, $\mathcal{P}^{(2)} = -1$, for transition 2. For the calculation of these values a modified equation (5.15),

$$\mathcal{P}^{\{(1),(2)\}} = \frac{P_H^{\{(1),(2)\}} - P_V^{\{(1),(2)\}}}{P_H^{\{(1),(2)\}} + P_V^{\{(1),(2)\}}}, \tag{5.17}$$

has been used. The degree of polarisation of both transitions over the applied electric field is depicted in Fig. 5.4 (b). Another way of representing the orientation and strength of polarisation is the coupling matrix shown in Fig. 5.5. For the electric field coupling, ratios of $\{E_{1,H} : E_{1,V} : E_{2,H} : E_{2,V}\} = \{2 : 1 : 0 : \sqrt{3}\}$, for the field intensity emission, ratios of $\{I_{1,H} : I_{1,V} : I_{2,H} : I_{2,V}\} = \{4 : 1 : 0 : 3\}$ are expected.

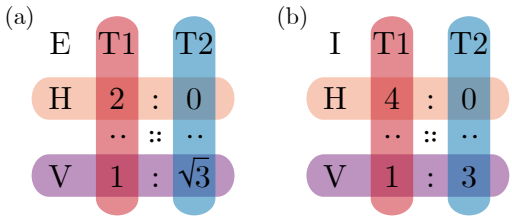


Figure 5.5: Coupling matrix given for (a) the electric field and (b) the intensity. Ratios are given for horizontal (H) and vertical (V) polarisation of transitions 1 ($E_x \leftrightarrow A_1$) (T1) and 2 ($E_y \leftrightarrow A_1$) (T2) (large strain/field notation).

5.6.4 Relative noise intensity

As seen in the previous subsection, unlike when an electric field is applied in the x-direction with NV^0 centres only aligned in the z = [111] direction, the cross-linear polarisation of the two optical transitions is not perfect. Nonetheless, noise can be suppressed efficiently. For the purpose of a low noise level in a potential Raman memory, the strong control field should couple to transition 1 with horizontal polarisation. In consequence, simultaneous coupling to transition 2 should be low, as this transition asymptotically tends to complete vertical polarisation. In Fig. 5.4 (c) the relative noise intensity

$$\mathcal{N}_{\mathcal{C}} = \frac{P_H^{(2)}}{P_H^{(1)}}, \tag{5.18}$$

for unwanted control field coupling is presented. Comparing these results to the simulations in Section 5.4 the relative noise intensity encountered is increased for the same electric field strengths. However, as higher electric field strengths are necessary to reach a ground state splitting of $S \approx 50\,\mathrm{GHz}$, still, as in the case of unidirectional NV^0 alignment, a relative noise level of $\sim 1/550$ for $\Upsilon = 0\,\mathrm{GHz}$ is reached for this ground state splitting. The most inconvenient case of $\Upsilon = 12\,\mathrm{GHz}$ and $\alpha = 180°$ even exhibits a slightly lower relative noise intensity of $\sim 1/20$.

The downside of applying the strong control field to transition 1 is that the vertically polarised signal field needs to be applied to transition 2. In this case the signal field will also couple unintentionally to transition 1 with a probability of

$$\frac{P_V^{(1)}}{P_V^{(1)} + P_V^{(2)}} = 25\%. \tag{5.19}$$

However, this does not introduce any noise and is far preferable to having a quarter of the control field coupling to the optical transition of the signal field with a relative noise intensity of $\mathcal{N}_\mathcal{C} \approx 1/3$.

5.6.5 Raman coupling

The Raman coupling detuning product in the large detuning approximation $R^{H\,V}_{E_1\,E_2} \cdot \bar{\Delta}$, as can be seen in Fig. 5.4 (d), is reduced in comparison to the configuration with unidirectional NV^0 centres as described above. This is due to the orientation of the optical axis with respect to the z-axis of the NV^0 centres and the projection of the dipole moments onto the (001) diamond facet.

5.6.6 Applicability as Raman memory

After these considerations, it is clear that in a potential memory application the strong control field is applied to transition 1, the weak signal field to transition 2. A full memory scheme is shown in Fig. 5.6. Here, the ensemble can be prepared in the upper ground state with a horizontally polarised pump field, only coupling to transition 1. In subfigure (a) the population distribution is shown during and after the pumping process. In a second step (subfigure (b)), both vertical signal and horizontal control field are applied, the signal field

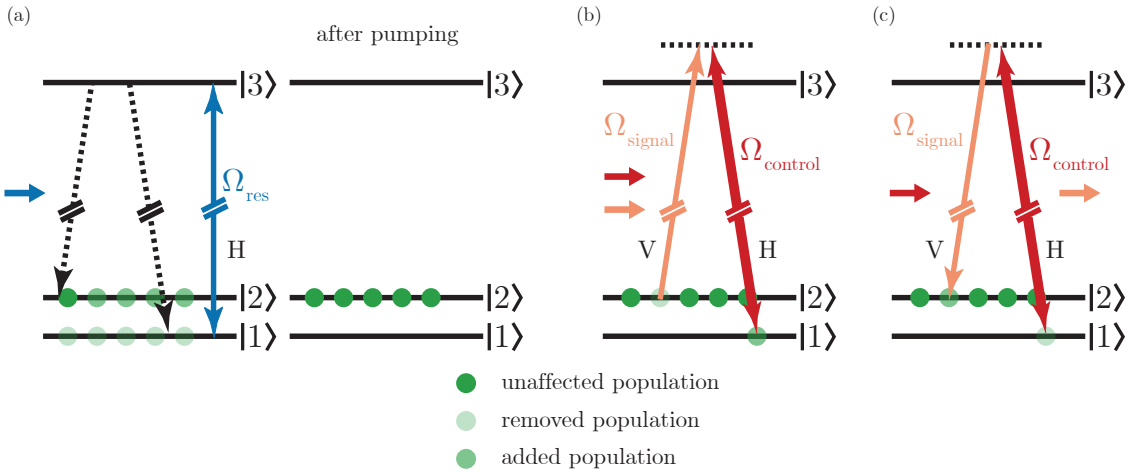


Figure 5.6: Raman memory scheme in an ensemble of NV^0 centres oriented along $\langle 111 \rangle$ with a strong electric field applied along [100]. Optical fields entering (exiting) the ensemble are indicated by horizontal small arrows in the colour of the respective field on the right (left) side of each level scheme. (a) Population is transferred from the lower ground state $|1\rangle$ by resonant optical pumping in horizontal (H) polarisation and by spontaneous emission (dashed arrows) to the upper ground state $|2\rangle$. On the right, the population distribution after pumping is shown. (b) Read-in of a weak vertically (V) polarised signal field via a two-photon Raman transition coupling to a strong horizontally polarised control field. Population is transferred from state $|2\rangle$ to state $|1\rangle$. (c) Read-out of the previously stored weak signal field. The strong control field couples again to the lower ground state. Population is transferred back to state $|2\rangle$ and the signal field is emitted.

is absorbed, transferring population to the lower ground state and generating a spin wave in the ensemble. After a variable storage time a second control field is applied and the stored signal field is retrieved as can be seen in subfigure (c).

5.6.7 Memory efficiency

Besides a successful implementation of optical pumping and the Raman memory scheme, the memory efficiency is crucial for the applicability as memory. The memory efficiency can be estimated using the relative Raman coupling strength [169,170,189]

$$\eta \approx \sqrt{\frac{\pi^2 h}{\varepsilon_0^2 c}} \sqrt{n E_C} \frac{\mathcal{R} \cdot \Delta}{\lambda_C \Delta} \tag{5.20}$$

In this equation h is the Planck constant, c the speed of light in vacuum, n the number density of NV^0 centres, E_C the control field energy, $\mathcal{R} \cdot \Delta$ the detuning-independent Raman coupling strength and off-resonant detuning product, λ_C the wavelength of the control field and Δ the two-photon detuning from the excited state. Assuming a control field energy $E_C = 10\,\mathrm{nJ}$, a NV^0 density of $10^{16}\,\mathrm{cm}^{-3}$ and a detuning $\Delta = 100\,\mathrm{GHz}$, in the large detuning regime, if the inhomogeneous broadening of the optical tranisitions $\delta\varepsilon$ is far smaller than the detuning, $\delta\varepsilon \ll \Delta$, the relative Raman coupling strength amounts to $\eta \sim 1$. This corresponds to a total memory efficiency of $\sim 25\,\%$ [169,170,189].

The total efficiency can be increased using waveguides offering an extended interaction length of signal and control field and a higher field confinement [379]. The wavelength λ_C as spatial scaling factor in equation (5.20) can be replaced by the ratio d^2/L, where d is the width and L the length of the waveguide. For a waveguide of dimensions $1\,\mu\mathrm{m} \times 1\,\mu\mathrm{m} \times 1\,\mathrm{mm}$, the relative Raman coupling strength increases to $\eta > 50$ implying a memory efficiency larger than 99 % even for control field energies of $0.1\,\mathrm{nJ}$ [169,170,189]. These dimensions are only given as an example to demonstrate that high memory efficiencies can be realised in compact waveguides. However, due to the high refractive index of diamond ($n = 2.4$ at $800\,\mathrm{nm}$ [215]) this specific waveguide might also guide higher optical modes at $575\,\mathrm{nm}$.

5.7 Storage time estimation

Solid-state same-spin-different-orbital systems, as used here, are prone to lattice distortions and vibrations compared to same-orbital-different-spin systems, decreasing the life and coherence time of the NV^0 ground-state manifold with respect to that of the NV^- centre. In the following, dominant effects are discussed limiting life and coherence times in ensembels of NV^0 centres.

5.7.1 Coherence time estimation

Random local strain leads to a shift in energy of single NV^0 centres and, hence, an inhomogeneous broadening of the energy transitions of the ZPL. The inhomogeneous broadening of the two-photon energy transition between the ground states is to be estimated to determine the ground state coherence time of the ensemble. Yet, this inhomogeneous dephasing can be counteracted by spin-echo techniques increasing the ensemble coherence time again [380]. Even though random local strain is predominant, spin fluctuations due to transverse spin-orbit interactions can lead to spatial fluctuations of the energy splitting between the memory ground states. However, these fluctuations are only a few GHz [266,267] and can be counteracted the same way as inhomogeneous effects by local strain described at the end of this subsection. The focus will be laid on the estimation of the coherence time limited by spatial random local strain.

The linear strain Hamiltonian of the ground states reads [306,315]

$$\mathcal{H}_{St,g} = (\epsilon_{1,E} e_{1,E_x} + \epsilon_{2,E} e_{2,E_x}) \begin{pmatrix} 1 & 0 & 0 & 0 \\ 0 & 1 & 0 & 0 \\ 0 & 0 & -1 & 0 \\ 0 & 0 & 0 & -1 \end{pmatrix} \tag{5.21}$$

$$+ (\epsilon_{1,E} e_{1,E_y} + \epsilon_{2,E} e_{2,E_y}) \begin{pmatrix} 0 & 0 & 1 & 0 \\ 0 & 0 & 0 & 1 \\ 1 & 0 & 0 & 0 \\ 0 & 1 & 0 & 0 \end{pmatrix}, \tag{5.22}$$

with the two linear deformation-mode pairs of the E symmetric orbitals $\{e_{1,E_x}, e_{2,E_x}\} = \{e_{xx} - e_{yy}, 2e_{xy}\}$ and $\{e_{1,E_y}, e_{2,E_y}\} = \{2e_{xz}, 2e_{yz}\}$ with the strain tensor components e_{ij} [306,315]. The strain energies are given by $\epsilon_{1,E} \approx -600\,\mathrm{THz}$ and $\epsilon_{2,E} \approx 360\,\mathrm{THz}$ [306]. Adding this strain component to the ground state Hamiltonian (5.9) and by diagonalisation, the ground state energies are determined to be [306,315]

$$\varepsilon_{1,2} = A \pm \sqrt{B^2 + C^2 + D^2}, \tag{5.23}$$

where[315]

$$A = -\varepsilon_{es} + d_{\parallel}F_z - \epsilon_{1,A_1}e_{1,A_1} - \epsilon_{2,A_1}e_{2,A_1}, \tag{5.24}$$

$$B = \Upsilon_x - d_{\perp}F_x - \epsilon_{1,E_x}e_{1,E_x} - \epsilon_{2,E_x}e_{2,E_x}, \tag{5.25}$$

$$C = \Upsilon_y - d_{\perp}F_y - \epsilon_{1,E_x}e_{1,E_y} - \epsilon_{2,E_x}e_{2,E_y}, \tag{5.26}$$

$$D = \frac{\lambda_{\parallel}}{2}. \tag{5.27}$$

For large stress fields applied in x direction, E_x-type strains prevail reducing the ground state energies to $\varepsilon_{1,2} \approx A \pm B$, with $B \approx -\epsilon_{1,E_x}e_{1,E_x} - \epsilon_{2,E_x}e_{2,E_x}$. Therefore, the ground state splitting can be approximated to

$$S = \varepsilon_2 - \varepsilon_1 \approx 2B \approx -2(\epsilon_{1,E_x}e_{1,E_x} + \epsilon_{2,E_x}e_{2,E_x}). \tag{5.28}$$

Considering isotropic random strain with a standard deviation of $\delta e = \delta e_{1,E_x} = \delta e_{2,E_x}$, with a Gaussian error propagation the uncertainty of the ground state splitting amounts to

$$\delta S \approx 2\delta e\sqrt{(\epsilon_{1,E_x})^2 + (\epsilon_{2,E_x})^2}. \tag{5.29}$$

The standard deviation in strain δe can be estimated from measurements of the optical linewidth of the ensemble at cryogenic temperatures and no external strain. Starting from equation (5.23) and still neglecting SO coupling the linewidth adds up to[315]

$$\delta\varepsilon \approx \delta e\sqrt{\epsilon_{1,A_1}^2 + \epsilon_{2,A_1}^2 + (\epsilon_{1,E_x}^2 + \epsilon_{2,E_x}^2)\frac{8\Upsilon^2}{4\Upsilon^2 + \lambda_{\parallel}^2}}. \tag{5.30}$$

When equation (5.30) is solved for δe and substituted in equation (5.29), the standard deviation of the ground state splitting is found to be [315]

$$\delta S \approx \frac{\kappa}{\sqrt{1+\frac{8\kappa^2\Upsilon^2}{4\Upsilon^2+\lambda_\parallel^2}}}\delta\varepsilon \tag{5.31}$$

$$\approx \frac{\kappa}{\sqrt{1+2\kappa^2}}\delta\varepsilon, \text{ for } 4\Upsilon^2 \gg \lambda_\parallel^2. \tag{5.32}$$

where $\kappa = \sqrt{(\epsilon_{1,E_x}^2+\epsilon_{2,E_x}^2)/(\epsilon_{1,A_1}^2+\epsilon_{2,A_1}^2)} \approx 1.34$ with $\epsilon_{1,A_1} \approx 192\,\text{THz}$ and $\epsilon_{2,A_1} \approx -483\,\text{THz}$ [306,315].

Gaussian fitting of off-resonant fluorescence spectra of the ZPL and deconvolution with the spectrometer response function, the standard deviation has been determined to $\delta\varepsilon \approx 16\,\text{GHz}$ at $5.7\,\text{K}$ [315]. The measurement presented in [315] without any external stress applied is close to linewidths presented in the next chapter, using a different diamond and exerting pressure on the diamond surface. Therefore, 16 GHz can be regarded as a good approximation for further considerations, leading to $\delta S \approx 10\,\text{GHz}$. This corresponds to a FWHM deviation of $\delta S_{\text{FWHM}} = 2\sqrt{2\ln 2}\cdot\delta S = 23.55\,\text{GHz}$.

As a result, the coherence time can be approximated to

$$T_2^* = \frac{1}{2\pi\cdot 23.55\,\text{GHz}} \approx 7\,\text{ps}, \tag{5.33}$$

following the Heisenberg uncertainty principle [381].

Even though this coherence time is very short, the inhomogeneous broadening can be reduced by rephasing techniques such as spin echo techniques via millimetre-wave pulses [382] or two-photon transitions [383]. Therefore, above all, the ground state lifetime will be of higher significance in determining the storage time in an ensemble of NV^0 centres with counteracted inhomogeneous broadening.

5.7.2 Ground state lifetime

At cyrogenic temperatures, the ground state lifetime is primarily affected by vibrational perturbations coupling to the strain Hamiltonian. These dynamic distortions of the diamond lattice are dominated by first-order electron-phonon transitions [248] (see Subsection 3.2.4). For temperatures in the low Kelvin regime, the phononic decay rate between two orbital states is given by [248]

$$\gamma_+ = 2\pi\chi\rho\Delta^3\, n(\Delta, T) \tag{5.34}$$

$$\text{and} \quad \gamma_- = 2\pi\chi\rho\Delta^3\, [n(\Delta, T) + 1]. \tag{5.35}$$

Here, γ_+ indicates the transition rate from the lower to the higher state, while γ_- is the decay rate from the energetically higher to the lower orbital state. These rates can be approximated to [248]

$$\gamma_+ \approx \gamma_- \approx 2\pi\chi\rho\Delta^3\, n(\Delta, T) \approx \frac{2\pi}{\hbar}\chi\rho\Delta^2 k_B T, \tag{5.36}$$

where $n(\Delta, T) = {}^{1}/_{(\exp({}^{\hbar\Delta}/_{k_B T})-1)}$ is the average phonon number at an energy splitting Δ and temperature T. In the last step, equation (5.36) is approximated by a Taylor expansion

of the exponential function. For $T > {}^{\hbar\Delta}/_{k_B}$ sufficient accuracy of this approximation is given. The density of phonon modes in the host material, diamond, is given by ρ. χ is related to the interaction frequency [248]. The total transfer rate

$$ {}^{1}/_{\gamma_{\text{total}}} = {}^{1}/_{\gamma_{+}} + {}^{1}/_{\gamma_{-}} \tag{5.37} $$

is connected to the ground state lifetime τ by

$$ \tau = \frac{1}{\gamma_{\text{total}}} \approx \frac{2}{\gamma_{\pm}}. \tag{5.38} $$

By comparison to the phonon-induced mixing rate between the E_x and E_y state within the orbital doublet excited state ${}^3E$ of NV^-, a lower bound of the lifetime of the E-symmetric NV^0 ground states can be determined. In [257] the decay rate between these E-symmetric states at $T_{\text{NV}^-} = 5.8\,\text{K}$ and a state splitting of $\Delta_{\text{NV}^-} = 3.9\,\text{GHz}$ was measured to $\gamma_{\pm} = 2\pi \cdot (-0.34 \pm 1.87)\,\text{MHz}$ (error given for a 95% confidence interval). The maximum value in this interval, $\gamma_{\pm}^{\text{max}} = 2\pi \cdot 1.53\,\text{MHz}$, yields a minimum lifetime of $\tau_{\text{NV}^-}^{\text{min}} \approx 0.21\,\mu\text{s}$ using equation (5.38). In consequence, the ground state lifetime of NV^0 centres can be bounded to

$$ \tau_{\text{NV}^0} > \tau_{\text{NV}^-}^{\text{min}} \frac{\chi_{\text{NV}^-} \Delta_{\text{NV}^-}^3 \left[\frac{n(\Delta_{\text{NV}^-}, T_{\text{NV}^-})^2 + n(\Delta_{\text{NV}^-}, T_{\text{NV}^-})}{2n(\Delta_{\text{NV}^-}, T_{\text{NV}^-})+1}\right]}{\chi_{\text{NV}^0} \Delta_{\text{NV}^0}^3 \left[\frac{n(\Delta_{\text{NV}^0}, T_{\text{NV}^0})^2 + n(\Delta_{\text{NV}^0}, T_{\text{NV}^0})}{2n(\Delta_{\text{NV}^0}, T_{\text{NV}^0})+1}\right]} \tag{5.39} $$

$$ \approx \tau_{\text{NV}^-}^{\text{min}} \frac{\chi_{\text{NV}^-} \Delta_{\text{NV}^-}^3 \, n(\Delta_{\text{NV}^-}, T_{\text{NV}^-})}{\chi_{\text{NV}^0} \Delta_{\text{NV}^0}^3 \, n(\Delta_{\text{NV}^0}, T_{\text{NV}^0})}. \tag{5.40} $$

With the coefficient ${}^{\chi_{\text{NV}^-}}/_{\chi_{\text{NV}^0}}$ estimated to 0.5 [262,306,315] and a stress induced ground state splitting $\Delta_{\text{NV}^0} = 50\,\text{GHz}$ a lower bound for the NV^0 ground state lifetime is $\tau_{\text{NV}^0} > 1\,\text{ns}$ at

$T_{\mathrm{NV}^0} = 3.7\,\mathrm{K}$ and $\tau_{\mathrm{NV}^0} > 370\,\mathrm{ps}$ at $T_{\mathrm{NV}^0} = 10\,\mathrm{K}$, using equation (5.39). Equation (5.40) is the Taylor approximation in n up to the second term.

5.8 Summary

In this chapter, ensembles of neutrally charged nitrogen vacancy centres (NV^0) have been considered theoretically as optical Raman quantum memories. The Raman coupling strength for single centres was defined and conditions were worked out under which favourable Raman coupling in an optical Λ-system can be expected (§5.1). In case the off-resonant Raman transition connects two ground states of same orbital but different electron spin, the first-order Raman coupling vanishes identically and effective Raman coupling is only experienced for detunings less than the spin-orbit mixing interactions in the excited states. For larger detunings, the Raman coupling strength decreases quadratically with the average detuning from the excited states. In consequence the negatively charged nitrogen vacancy centre only experiences good Raman coupling for average detunings of 1.5 GHz or less, whereas the neutrally charged nitrogen vacancy centre offers spin conserving Λ-systems with a first-order Raman coupling decreasing linearly with the mean detuning only. This is why the neutrally charged nitrogen vacancy centre is chosen for further theoretical considerations and examinations regarding desirable characteristics of solid-state systems for Raman quantum memories.

For this centre the full system Hamiltonian including spin-orbit interactions, dynamic Jahn-Teller interactions and the interaction with an external electric field is given for the excited and ground states (§5.2.1). An upper limit for the dynamic Jahn-Teller interactions was estimated to at most 12 GHz. For an external uniaxial electric field the orbital ground

state splitting (§5.2.2), the cross-linear polarisation of the optical transitions (§5.3), the relative noise intensity of a strong control field (§5.4) as well as the Raman coupling strength in the far detuning regime (§5.5) were simulated and discussed. Dynamic Jahn-Teller energies of 0 GHz and 12 GHz with several decompositions in their x and y components were considered.

For an ensemble of neutral nitrogen vacancy centres all aligned along [111] and an electric field in $x = [\bar{1}\bar{1}2]$, an energy shift of the amount of the transverse electric dipole moment, $\sim 5\,{}^{\mathrm{GHz}}/_{\mathrm{V}}$, for fields $F_x > \frac{1}{d_\perp}\sqrt{\Upsilon^2 + \frac{\lambda_\parallel^2}{4}} \approx 2.5\,{}^{\mathrm{V}}/_{\mu\mathrm{m}}$, can be seen. Splittings of 50 GHz, enabling the storage of pulses of ~ 30 GHz can be reached with reasonable electric fields. Even though larger splittings are easily reachable, these and larger pulse bandwidths would require larger detunings from the excited states to avoid resonant coupling and would lead to weaker Raman coupling. The optical transitions between the orbital states are almost completely cross-linear polarised under electric fields also reducing the relative noise intensity to $\sim {}^{1}/_{550}$ for a ground state splitting of ~ 50 GHz and no dynamic Jahn-Teller interactions. All simulations tend towards the same strength of Raman coupling.

For an ensemble of neutrally charged nitrogen vacancy centres equally distributed among the eight possible orientations within the diamond lattice, the axes of the electric field and the optical axis are chosen symmetrically for all orientations along [100] and [001] respectively (§5.6). Due to projections onto the NV basis, slightly higher electric fields are needed for the same ground state splittings. Cross-linear polarisation selection rules can only partially be implemented and the Raman coupling for horizontally and vertically polarised fields is reduced due to projection of the dipole moments of the optical transitions onto the (001) diamond facet. However, by choosing fields and polarisations deliberately a

Raman memory scheme with the same low relative noise intensity as in the ideal case and high memory efficiency, in particular in waveguides, can be realised.

Albeit important properties of a solid-state system for Raman memories have been identified, unfortunately, estimations of the inhomogeneous coherence time and lifetime of an ensemble of neutral nitrogen vacancy centre lead to values of $T_2^* \approx 7\,\mathrm{ps}$ and $\tau > 370\,\mathrm{ps}$ at 10 Kelvin (§5.7). This is too short to be used for memory applications and another solid-state system should be chosen. Moreover, as the lifetime of the upper ground state is shorter than the lifetime of the excited state, optical pumping based on the spontaneous emission of the excited state is prevented (see section 4.1). Nonetheless, the engineering of ensembles of NV^0 centres by the application of external stress can be explored experimentally in order to confirm theoretical predictions made in this chapter.

Chapter 6

Engineering an ensemble of neutrally charged nitrogen vacancy centres

THE nitrogen vacancy experiments were carried out by Christian Weinzetl under supervision of Dr. Eilon Poem in the Clarendon Laboratory at the University of Oxford.

In this chapter experiments with the neutral nitrogen vacancy centre (NV^0) are described. In a first section, detailed information is given on the experimental set-up as well as on the diamond sample in use (§6.1). In a second step, orbital ground state level splitting by external uniaxial stress is presented and the degree of polarization of the optical transitions is determined (§6.2). This chapter concludes with the description of lifetime measurements of the orbital ground states (§6.3) and a summary of the results (§6.4).

6.1 Diamond sample and experimental set-up

The experimental set-up used for the experiments presented in this chapter shall allow off-resonant and resonant confocal pumping and read-out of the NV^0 optical ZPL transition and the PSB.

6.1.1 Diamond sample

The diamond sample used in the experiments presented in this chapter was kindly provided by the research group of Professor Dirk R. Englund (Quantum Photonics Laboratory, Massachusetts Institute of Technology, Cambridge, Massachusetts, USA). The diamond sample is a type IIa electron-irradiated, optical grade (001) CVD diamond with dimensions of $(3 \times 3 \times 0.3)\,\mathrm{mm}^3$ and a volume of $2.7 \times 10^{-3}\,\mathrm{cm}^3$. It is not identical to but prepared in the same way as the diamond sample used in [45] for broadband magnetometry and temperature sensing in which the diamond is used as a light-trapping waveguide. There the absorption constant of the sample was measured for single pass beam transmission from the front to the back surface, $\alpha \approx 0.45\,\mathrm{cm}^{-1}$. With a single NV^- absorption cross section of $\sim 2 \times 10^{-17}\,\mathrm{cm}^2$ [384], an NV^- density of $2.3 \times 10^{16}\,\mathrm{cm}^{-3}$ is found within the sample. No further information on the ratio between NV^- and NV^0 is given. However, while the NV^0 concentration is not known, it can be expected within one order of magnitude [39,304]. All sides of the diamond have been polished. Only the sides of $(3 \times 0.3)\,\mathrm{mm}^2$ were addressed with a confocal microscope for the experiments described here.

As shown in Fig. 5.3, there are eight possible orientations of the NV^0 centre within the diamond lattice. Its symmetry axis along the connection between the nitrogen atom and the vacancy position is pointing along $\langle 111 \rangle$.

6.1.2 Diamond clamp

In order to apply external uniaxial stress to the diamond sample, an anvil cell made out of a beryllium-copper alloy (Alloy 3) was designed, milled and precipitation-hardened. The front and rear view of the clamp is shown in Fig. 6.1. Beryllium-copper was chosen as it offers both high thermal conductivity and high strength. Therefore, high pressure can be applied to the diamond sample without the deformation of parts of the clamp, while it can be assured that the diamond is cooled down to the same temperatures as the clamp itself which is directly connected to the cold finger of the cryostat. The temperature was

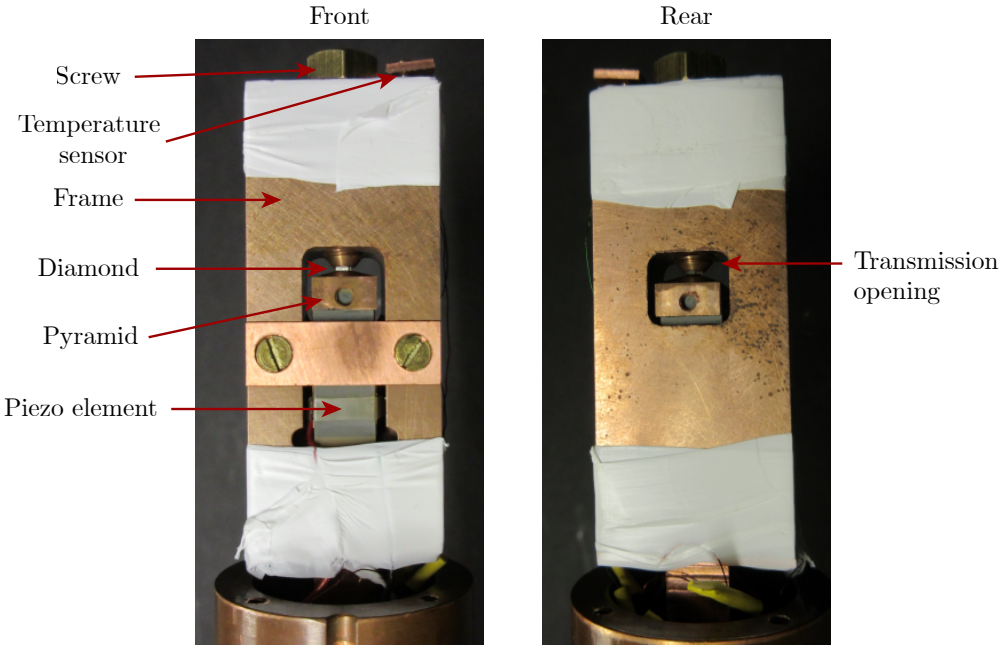


Figure 6.1: Berrylium copper anvil cell. Uniaxial stress can be applied to the diamond sample by a mechanical screw and a piezoelectric element.

monitored by a temperature sensor mounted at the top of the clamp. The diamond is fixed between a pyramidal-shaped cap, placed on top of the piezoelectric element, and the tip of the screw of the clamp. One of the four narrow sides of the diamond sample is optically accessible from the front. The opening at the rear can be used for transmission experiments or the application of additional counter-propagating fields.

The pressure on the diamond can be adjusted both by the screw and the piezoelectric element. When the diamond is mounted in the clamp, uniaxial stress is applied in the [100] direction. While a coarse adjustment of the screw is only possible at room temperature, with the cryostat open, the length of the piezo element can be finely adjusted by varying the applied voltage even with a closed cryostat and at cryogenic temperatures. With the screw, only a coarse adjustment is possible as the change of temperature during the cooling process leads to a contraction of the frame, the screw and the piezo element. In cycles of cooling down and warming up the cryostat, it was observed that the pressure induced by the screw of the anvil cell on the diamond slightly diminishes due to possible mechanical relaxation processes in the structure of the cell. These changes can be counteracted by the piezo element or by manually tightening the screw. Voltage from -20 to 150 V can be applied to the piezo element which contracts when negative voltage is applied.

6.1.3 Laser fields

Ground state splitting by external uniaxial stress

As shown in Fig. 6.2 a diode-pumped continuous wave (CW) solid-state laser at 532 nm (Coherent, Verdi V8) can be applied directly to the diamond sample. A telescope (magnification, M=5) is used in order to enlarge the beam to the size of the aperture of the objective. A dichroic mirror (long pass (LP) for $\lambda > 572$ nm) is used for its deflection into the objective, transmitting light at the NV^0 ZPL and into the phonon sidebands. Power control is realised by both a HWP-PBS combination or an additional polariser.

Lifetime measurement

The diode-pumped CW solid-state laser can also be used for pumping a dye laser at 575 nm (Coherent, CR-599, CW, 3-plate birefringent filter, 40 GHz effective linewidth). After power control by a HWP and a polariser and polarisation control via a HWP, a fast switching Pockels cell (Leysop LTD, model number: ds11b, 10kHz repetition rate, 3-4 ns rising time) is used for temporal shaping of the 575 nm CW radiation. Two rectangular pulses of 100 ns length with temporally tunable delay between them are created. A dichroic mirror (LP for $\lambda > 593$ nm) is used separating resonant laser light from fluorescence into the PSB. For off-resonant experiments (see Section 6.2.1 and Section 6.2.2) this dichroic mirror is removed to enable detection of the ZPL.

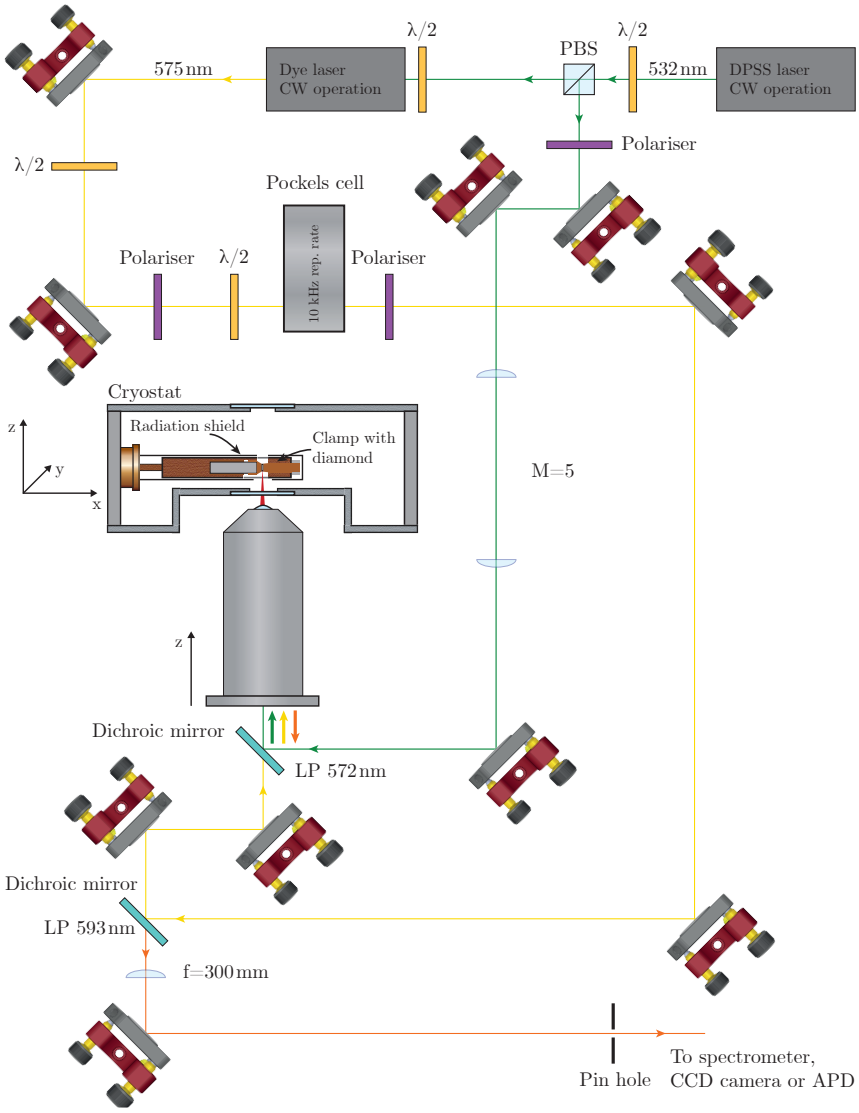


Figure 6.2: Beam lines and cryogenic set-up. A green diode pumped solid-state laser and a yellow dye laser are directed onto the diamond sample inside the cryostat via an objective. Both laser beams can be changed in power and polarisation. Two dichroic mirrors (LP 572 nm, LP 593 nm) allow usage of both lasers while fluorescence into the phonon sidebands can be measured by a spectrometer, a CCD camera or an APD. For measurements of the ZPL, the long-pass filter cutting at 593 nm is removed. A plano-convex lens (f = 300 mm) and a pin hole are used for imaging of the diamond surface and for spatial filtering of the fluorescence enhancing the effects of confocal microscopy. The objective can be moved in the z-direction, while the flow cryostat can be moved in all directions of space. For lifetime measurements of the ground states, a Pockels cell is used in the arm of the yellow laser. Inside the cryostat, the diamond is mounted in the beryllium copper clamp and additionally protected by a radiation shield.

6.1.4 Cryogenic set-up

The diamond sample is placed inside a helium-flow cooled cryostat (Oxford Instruments LTD). Under vacuum down to $4 \cdot 10^{-7}$ mbar, temperatures between 5.7 and 7 K are reached. For both, focusing the pump beam and collecting the fluorescence, a $\times 20$, NA $= 0.29$, long working-distance objective lens (Sigma Koki PAL-20-L) is used. Using this objective in vacuum, a Gaussian FWHM focal spot size of $\approx 1.1\,\mu$m with a Rayleigh length of $\approx 8.7\,\mu$m is expected. However, the change in refractive index between vacuum and diamond leads to a distortion of the focal spot size reducing the peak intensities. The focal spot is elongated in the direction of the optical axis and reduced in its width [332].

The microscope is operated in confocal geometry. Fluorescence is collected and collimated by the same objective as used for the exciting laser light. Fluorescence and laser fields are separated by dichroic mirrors. The front plate of the cryostat was redesigned and the access window was placed closer to the diamond clamp to focus directly onto the diamond surface.

For analysis, after the cryogenic set-up, the fluorescence quality is increased by spatial filtering, imaging the diamond surface onto a pin hole of variable size (25 µm, 50 µm, 100 µm) using a 30 cm optical lens, which completes the confocal microscope. Furthermore, the diamond surface can be imaged onto a charge-coupled device (CCD) camera in order to ensure focal overlap of the optical fields in operation.

6.1.5 Spectral analysis

For the spectral analysis of the zero-phonon line (ZPL) a 0.48 m long spectrometer in Czerny-Turner design (Digikröm DK480) equipped with a 1200 $^{\text{lines}}/_{\text{mm}}$ diffraction grating and a thermoelectrically cooled CCD camera (Andor, iXon$^{\text{EM}}$+, model number: DU-885K-CS0-#VP, 4.8 $^{\text{GHz}}/_{\text{pixel}}$ resolution) are used. For resonant excitation into the ZPL, this spectrometer is replaced by a home-made spectrometer with a 300 $^{\text{lines}}/_{\text{mm}}$ diffraction grating to measure the fluorescence into the PSB as well.

A problem encountered in the experiments is the spatial variation of the orientation of the crystal lattice, even though a single crystal is used. Many different growth sectors with distinct ensemble orientations were detected leading to various spectroscopic results. These can be found in diamond due to stacking faults[385,386]. Furthermore, these different NV orientation can be a result of amorphisation of the diamond lattice caused by polishing[387]. This can be misleading in case fluorescence from different sub-ensembles is detected at the same time. For the experiments it was crucial to locate a diamond subspace with (001) orientation large enough to avoid excitation and fluorescence collection from misaligned NV^0 centres. Here, the confocal detection geometry is advantageous. For potential future experiments, especially if working in transmission configuration, it might be necessary to use another diamond sample with higher orientation uniformity and, in consequence, higher probability to excite centres with the desired orientation.

6.1.6 Temporal resolution for lifetime measurements

During measurements of the ground state lifetime, fluorescence into the PSB was detected by an avalanche photo diode (APD). The measured signal was temporally resolved by a field programmable gate array (FPGA) used as a time-tagging device. For further information on the FPGA, please refer to [388].

6.2 External control over an ensemble of nitrogen vacancy centres

In the experiment, a (001) diamond sample with NVs of all possible orientations is used as presented in Fig. 5.3. On this sample uniaxial stress in the [100] direction is applied, optical fields are directed along the [001] axis. In these experiments, both the ground state splitting by external stress as well as the degree of linear polarisation was measured using off-resonant fluorescence spectroscopy. The schematic fields and radiative decay is shown in Fig. 6.3. The fluorescence into the ZPL is collected and spectrally resolved by the high resolution spectrometer in four polarisation configurations defining the direction of the applied stress as horizontal as shown in Fig. 6.4 (e). Polarisation filtering is realised by a combination of HWP and Glan-Taylor prism. The spectrally resolved fluorescence measurements are presented in Fig. 6.4 (a)-(d). These measurements have been used for an analysis of the ground state splitting and the imposed cross-linear polarisation selection rules by external uniaxial stress.

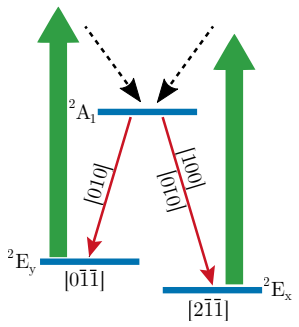


Figure 6.3: Off-resonant fluorescence spectroscopy: A green strong off-resonant pump laser (532 nm, thick green arrows) excites the NV centre to the phonon sidebands of the excited state from where the centre decays non-radiatively to the excited state (black dashed arrows). Corresponding to the orientation of the dipole moments, the fluorescence (red arrows) of the low energy transition is vertically polarised, whereas a mixed linear polarisation is expected for the high energy transition. As an example, the situation is depicted for a NV^0 centre in [111] orientation. The orientation of the dipole moments is given beneath the ground state levels.

6.2.1 Ground state splitting by external uniaxial stress

For data analysis the measured spectrum for each voltage setting and selected polarisation was fitted with a double Lorentzian function (Fig. 6.5). This ensures that both energy transitions can be treated separately as well as this eliminates any weak background from incorrectly oriented diamond subspaces. The analysis of the ground state splitting is based on the anti-diagonal (A) fluorescence measurement (Fig. 6.4 (d)).

Using a piezo element the ground state splitting in energy can be varied linearly from 69(8) GHz by 144(14) GHz up to 213(11) GHz, which corresponds to an applied pressure of ≈ 0.25 GPa [306]. The large minimum splitting is caused by a tight screw so that strain is applied even for the lowest piezo voltage. Fig. 6.6 shows the relative frequency of the optical transition as well as the total energy splitting between the two ground states. An overall slope of 0.842(17) GHz/V is achieved with an increased incline of 0.916(12) GHz/V for an applied voltage ≥ 40 V. These values have been determined by linear fits to the data presented in Fig. 6.6 (b).

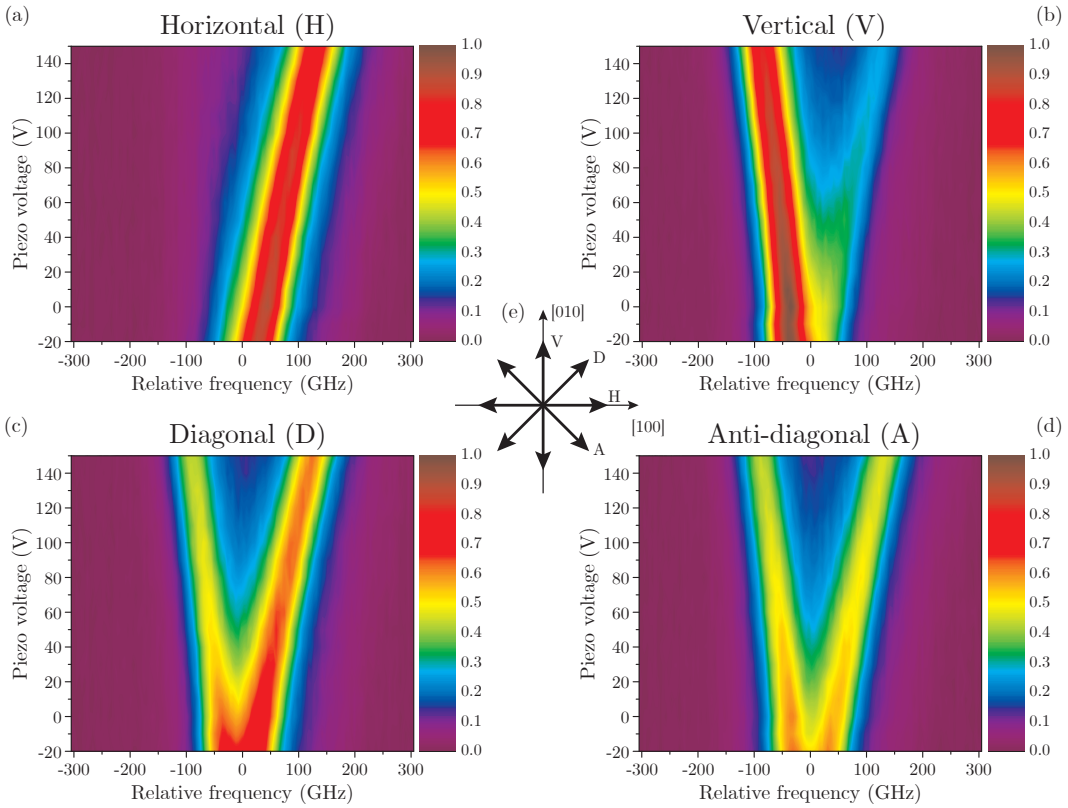


Figure 6.4: Spectrally resolved off-resonant fluorescence measurements into the ZPL as a function of the voltage applied to a piezo element varying the uniaxial pressure on the diamond. The signal is polarisation filtered in (a) horizontal, (b) vertical, (c) diagonal and (d) anti-diagonal direction as depicted in subfigure (e). All measurements are normalised with respect to the maximum overall measured intensity.

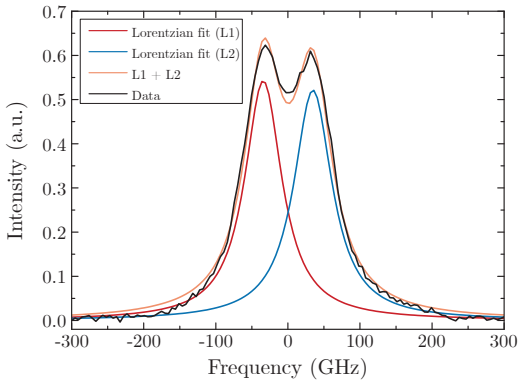


Figure 6.5: Double Lorentzian fitting of the measured spectrum in anti-diagonal (A) measurement configuration for U = −20 V applied to the Piezo element.

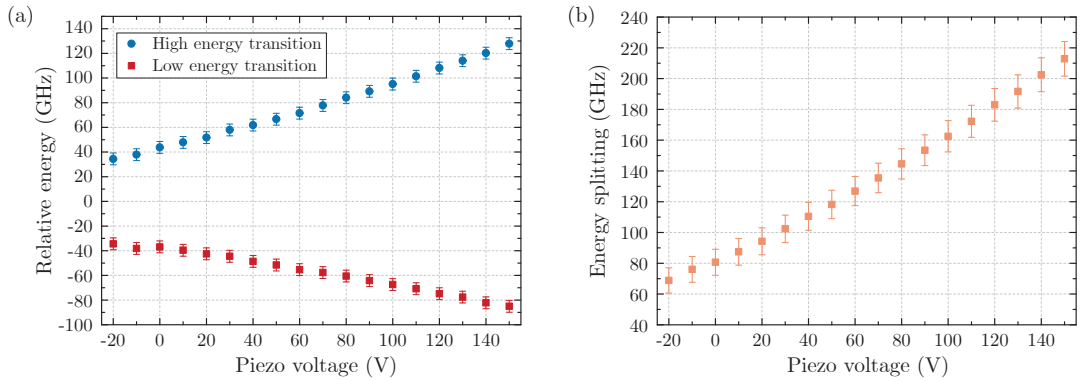


Figure 6.6: Engineering of the ensemble of NV^0 centres by external stress applied by a piezo element in [100]-direction. (a) Relative energy of the low (red squares) and high energy transition (blue circles). (b) Energy splitting between the two orbital ground states.

With an estimated transverse permanent electric dipole moment projected onto the x-y-plane of the NV^0 centres of $4.08\,^{\mathrm{GHz\,\mu m}}/_{\mathrm{V}}$ (see Subsection 5.6.2), the applied stress induces an internal electric field over a range of $\approx 35\ ^{\mathrm{V}}/_{\mu\mathrm{m}}$.

For a memory application, ground state splittings of $\sim 50\,\mathrm{GHz}$ are aimed for, even though higher energy splittings are easily possible. Increasing the signal bandwidth to be stored requires a higher detuning from the excited state which is decreasing the Raman coupling. Moreover, the lifetime of the ground state will be shorter for higher splittings. In this regime ($T > {}^{\hbar\Delta}/_{k_B}$), the spontaneous phonon emission rate increases quadratically with the splitting[248] (see Subsection 3.2.4).

6.2.2 Imposing cross-linear polarisation selection rules

Employing the same measurement data, the cross-linear polarisation selection rules, external electric fields or stress can introduce to the system, can be examined. For this, the nature of linear polarisation can be analysed using linear Stokes parameters[389]. Expressed in the two Cartesian measurement bases ($\hat{h}$,$\hat{v}$) and ($\hat{d}$,$\hat{a}$) the Stokes parameters read,

$$S_0 = \langle E^2_{\hat{h}} \rangle + \langle E^2_{\hat{v}} \rangle = \langle E^2_{\hat{d}} \rangle + \langle E^2_{\hat{a}} \rangle, \tag{6.1}$$

$$S_1 = \langle E^2_{\hat{h}} \rangle - \langle E^2_{\hat{v}} \rangle, \tag{6.2}$$

$$S_2 = \langle E^2_{\hat{d}} \rangle - \langle E^2_{\hat{a}} \rangle, \tag{6.3}$$

where the delimiters $\langle \dots \rangle$ indicate averages of intensities. The basis ($\hat{d}$,$\hat{a}$) is rotated anticlockwise by 45° with respect to the basis ($\hat{h}$,$\hat{v}$). The basis vectors translate to horizontal ($\hat{h}$), vertical ($\hat{v}$), diagonal ($\hat{d}$) and anti-diagonal ($\hat{a}$). S_0 is the total intensity, S_1 the difference between horizontally and vertically polarised light and S_2 indicates the difference between light polarised in diagonal and anti-diagonal direction.

These parameters are calculated and depicted in Fig. 6.7 (a)-(c). As guidance for the eye, the 50% level contour of total intensity is superimposed as black lines. While these parameters are not normalised yet, from parameter S_1 shown in Fig. 6.7 (b), it is already obvious that the low energy transition is predominantly vertically polarised, the high energy transition horizontally polarised. In Fig. 6.7 (c) values close to zero of the S_2-parameter suggest, that the low energy transition is emitting fluorescence of only one linear polarisation, while for the negative values of the high energy transition, two linear components of different strength are anticipated.

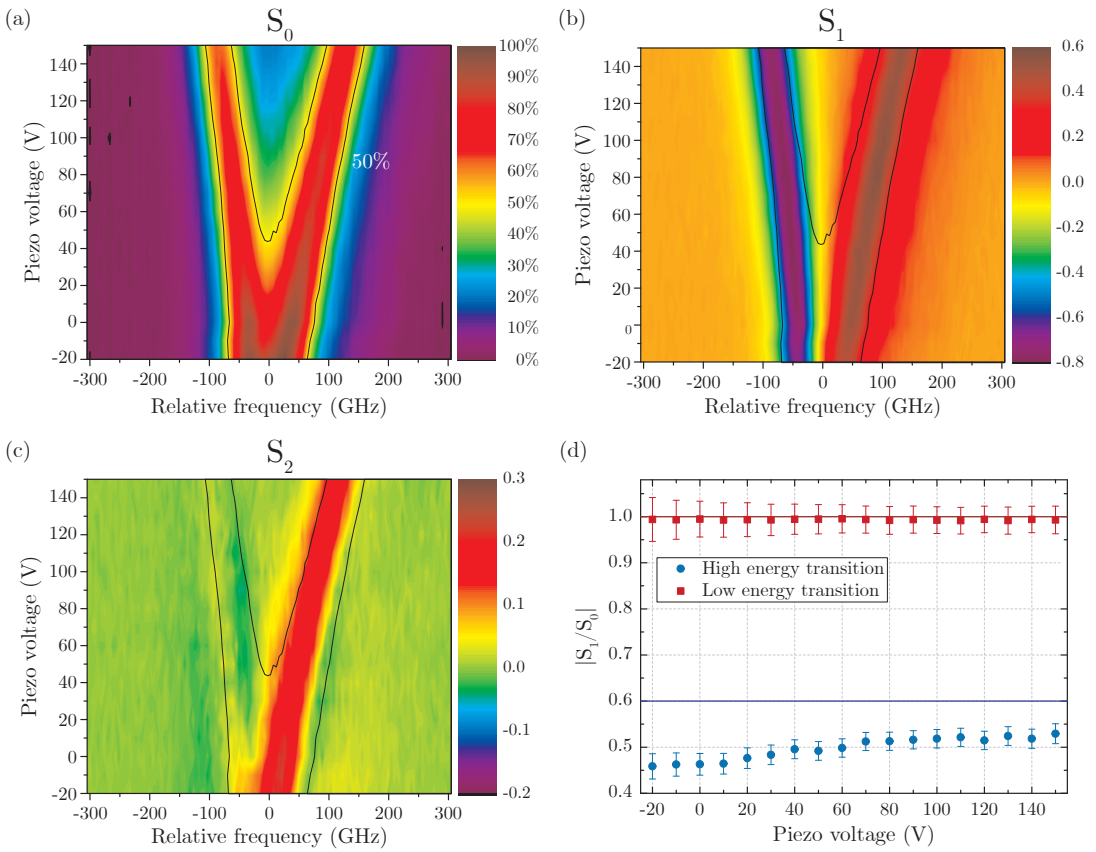


Figure 6.7: Stokes parameter (a) S_0, (b) S_1 and (c) S_2. Engineering of the ensemble of NV^0 centres by external stress applied by a piezo element in [100]-direction. (d) Normalised S_1-Stokes parameter (S_1^N) for the low (red squares) and high energy transition (blue circles). Theoretical limits of the degree of polarisation, as presented in Fig. 5.4 (b), are shown as solid lines. The maximum polarisation for the high energy transition was not reached which may be related to non-zero DJT effects as shown in Fig. 5.4 (b). However, as the total electric field applied and the strength as well as the direction of the DJT effects is not known, the conditions within the diamond cannot be determined more precisely.

Defining a normalised S_1-Stokes parameter as

$$S_1^N = \frac{S_1}{S_0}, \tag{6.4}$$

the degree of horizontal and vertical polarisation alignment can be determined equivalently to the simulations shown in Fig. 5.4 (b). Again, the experimental data were fitted to a model of two superimposed Lorentzian functions in order to separate the transitions from

each other. The amplitudes of the separated Lorentz curves were used to calculate the polarisation parameters for each transition independently.

For the low energy transition S_1^{N} is negative, for the high energy transition positive. Whereas the low energy transition shows nearly perfect horizontal polarisation, the high energy transition does not reach the theoretical value of 0.6 (see Subsection 5.6.3) as shown in Fig. 6.7 (d), but only a maximum value of $S_1^{\mathrm{N,max}} = 0.53(2)$. However, this deviation can be explained by the DJT energy. Looking at Fig. 5.4 (b) it can be seen that for $\Upsilon = 12\,\mathrm{GHz}$ and some strain orientations α, the asymptotic value of 0.6 for the high energy transition is approached slower than it is the case for the low energy transition. Additionally, the measured intensity ratios between the two spectral lines are verified by this analysis. The low energy to high energy transition coupling ratios of $0:4$, and $3:1$ in horizontal and vertical polarisation respectively, as it had been shown in (Fig. 5.5) (b), confirm the correct set-up configuration and theory.

6.3 Ground state lifetime measurement

Having shown external control over the NV^0 centre, further properties of this colour centre have to be explored. One fundamental and central quantity is the ground state lifetime for which lower bounds have been estimated in Subsection 5.7.2 to hundreds of picoseconds.

In resonant fluorescence measurements the ensemble was addressed by CW light of 575 nm temporally shaped by a Pockels cell as described in Subsection 6.1.3 and tuned to the low energy transition at a temperature of $T = 8\,\mathrm{K}$. The orbital ground states were split by $> 40\,\mathrm{GHz}$, the effective linewidth of the dye laser. The fluorescence into the PSB was measured and temporally resolved. The pulse sequence as well as the applied fields to the level scheme are shown in Fig. 6.8. The resonant fields (pump and readout) can be approximated by super-Gaussian pulses with rise times of 3-4 ns and a variable temporal delay τ between them.

When a resonant field is applied to state $|2\rangle$ the ensemble is pumped to state $|3\rangle$ from which the system decays radiatively into the ground states $|1\rangle$ and $|2\rangle$. The amount of fluorescence emitted into the PSB is correlated to the share of centres of the ensemble in

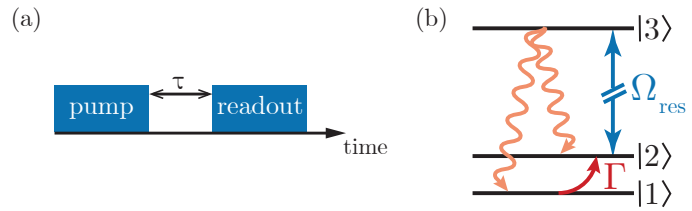


Figure 6.8: (a) Pulse sequence: Two identical fields (pump and readout) of 100 ns duration are applied to the diamond sample with a temporal delay of τ. (b) Level scheme: The pump and readout field couple resonantly to the optical transition between state $|2\rangle$ and $|3\rangle$. Centres brought into state $|3\rangle$ decay into states $|1\rangle$ and $|2\rangle$. The lifetime can be determined from the transition rate Γ between the orbital ground states $|1\rangle$ and $|2\rangle$.

state $|2\rangle$. At the inset of resonant pumping the amount of fluorescence should be increased and represent the thermal Boltzmann distribution of centres between the two ground states of different energy. Resonant pumping brings the three-level system in a new equilibrium determined by the pumping rate, the decay rate and the branching ratio from the excited state $|3\rangle$ into states $|1\rangle$ and $|2\rangle$, and the rethermalisation rate between the two ground states (see section 4.1). In this equilibrium the fluorescence into the PSB is lower due to a decrease of population in state $|2\rangle$.

When the resonant field is turned off, the ensemble returns into the state of thermal equilibrium. Applying the resonant field again, the amount of population transferred back into state $|2\rangle$ can be monitored. Increasing the temporal delay τ between the two resonant fields, the ground state lifetime can be determined. The same kind of experiment is presented in Subsection 7.3.1 determining the ground state lifetime of an ensemble of negatively charged silicon vacancy centres.

However, in this experiment with NV^0 centres, no increased fluorescence at the inset of resonant pumping could be observed. This is possible if the rising time of the resonant fields is longer than the lifetime of the upper ground state and also if the decay of the excited state is slower than the decay of the ground states. Therefore, the rising time of the fields generated by the Pockels cell of 3-4 ns can be assumed as upper bound for the centres lifetime supporting theoretical predictions of the lower bound of the lifetime in the regime of hundreds of picoseconds (see Subsection 5.7.2).

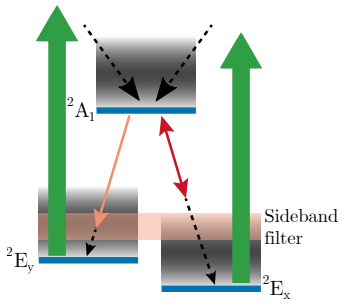


Figure 6.9: Stimulated emission from the orbital excited state in the NV^0 level scheme (STED). Off-resonant excitation (green), the field which is stimulating fluorescence emission (red) and fluorescence (orange) are given as solid arrows. Non-radiative decay is indicated by dashed arrows. Phonon levels are presented as shaded grey areas. A change in fluorescence can be detected using a sideband filter detuned from the stimulating laser field.

A possible way for measuring the ground state lifetime, apart from employing faster switching rates for the resonant pump field, is stimulated emission depletion (STED) [390,391]. With this technique the fluorescence into the phonon sidebands is increased by stimulated emission as shown in Fig. 6.9. A strong laser field with a Rabi frequency comparable to the fast phononic decay rate and with a wavelength within the fluorescence phonon sideband dresses the excited state with phononic states. This removes population from the excited state and a clear dip in fluorescence into the ZPL and parts of the phonon sidebands, different from the laser field stimulating the emission, can be observed. In consequence, this technique increases the decay rate of the excited state $|3\rangle$ leading to more comparable lifetimes of the ground and excited states which may simplify the measurement of the ground state lifetime. Recently, stimulated emission has been reported for an ensemble of negatively charged nitrogen vacancy centres in diamond [295].

6.4 Summary

In this chapter, the results of experiments with an ensemble of neutrally charged nitrogen vacancy centres were described. In an experimental set-up built for resonant and off-resonant fluorescence spectroscopy the diamond sample was mounted in a clamp inside a flow cryostat enabling the exertion of uniaxial stress on the diamond by a mechanical screw and a piezoelectric element (§6.1). In off-resonant fluorescence measurements, fluorescence into the zero-phonon line has been spectrally resolved for filtered horizontal, vertical, diagonal and anti-diagonal polarisation. Increasing the voltage applied to the piezoelectric element, and therefore the uniaxial stress onto the diamond, the orbital ground state energies could be changed over a range of 144(14) GHz and split up to 213(11) GHz (§6.2). Stokes parameters have been defined to describe the degree of polarisation of the emitted fluorescence. Calculation of the Stokes parameters for the whole fluorescence signal provided first insights into the degree of linear polarisation and the ratio of their components in the $\{H, V\}$ basis. An in-depth analysis separating the two optical transitions from each other and removing background fluorescence shows a nearly complete horizontal polarisation of the low energy transition. The high energy transition with $S_1^{N,\max} = 0.53(2)$ does not reach the theoretical limit of 0.6 which can be traced back to dynamic Jahn-Teller coupling (§6.2.2). In total, the theoretical predictions made in the previous chapter on the ground state level splitting and the degree of linear polarisation were confirmed.

The measurement of the orbital ground state lifetime remained without result, suggesting lifetimes shorter than the rising times of a resonant pump field of 3-4 ns (§6.3), which is confirming the theoretical estimations presented in the previous chapter. Notwithstanding

that the lifetime could not be determined exactly, external control over the neutrally charged nitrogen vacancy centre regarding the orbital ground state splitting and the possibility of engineering the degree of polarisation of the optical transitions could be shown.

Facing short lifetimes and even smaller ground state coherence times, the neutrally charged nitrogen vacancy centre, while it has given deep insight into the control and the desired properties of orbital Λ-systems in the solid state, needs to be abandoned in favour of a colour centre of better fundamental properties.

Chapter 7

Towards the silicon vacancy memory

THE silicon vacancy experiments were carried out in the research laboratory of Prof. Dr. Christoph Becher at Saarland University (Naturwissenschaftlich-Technische Fakultät, Fachbereich Physik, Universität des Saarlandes, Campus E 2.6, 66123 Saarbrücken, Germany). Experiments were undertaken by Johannes Görlitz (MSc student, Saarbrücken), Jonas Nils Becker (PhD student, Saarbrücken) and Christian Weinzetl. Christian Weinzetl built the set-up, participated in and carried out all measurements in Chapter 7, performed theoretical simulations for STIRAP (see Subsection 7.4.1 and Appendix B) and phase-dependent amplification and absorption (see Subsection 7.4.2). The STIRAP simulations shown in this thesis were performed by Jonas Nils Becker, Johannes Görlitz and Christian Weinzetl. The simulations for Ramsey and Hahn Echo measurements have been carried out by Jonas Nils Becker. The ground state coherence time was estimated by Jonas Nils Becker and Eilon Poem.

Due to their inversion symmetry, silicon vacancy centres (SiV^-) in diamond feature narrow inhomogeneous distributions, a rare property in solid-state systems, enabling fabrication of dense SiV^- ensembles with optical linewidths well below the centre's ground state splitting, providing an optically-resolved Λ-system (see Subsection 3.2.6).

In previous works, all-optical ultrafast coherent control of single SiV^- centres has been demonstrated[342–344]. In this chapter, a suite of coherent manipulations along with strong, collectively enhanced light-matter coupling in a mesoscopic SiV^- ensemble is presented (§7.3). The ground state splitting due to the spin-orbit interaction allows for fast manipulation even at zero magnetic fields[315]. Specifically, the orbital ground state lifetime was measured (§7.3.1) and all-optical coherent manipulation via resonant Ramsey interference, optical Hahn echo (§7.3.2) and stimulated Raman adiabatic passage (STIRAP) (§7.3.3), as well as strong light-matter interactions in the form of Raman absorption and amplification of weak coherent fields by four-wave mixing (FWM) (§7.3.4) are demonstrated and supported by numerical simulations (§7.4).

Before the experimental results are presented, the theoretical ground state coherence time is determined (§7.1). Afterwards, the diamond sample and the experimental set-up are described (§7.2). The experimental set-up can be divided in three stages: laser field preparation (§7.2.2), cryogenic set-up (§7.2.3) and filter set-up (§7.2.4). For the Ramsey and Hahn echo experiments the laser field preparation set-up as well as the set-up around the cryogenic system differ from the STIRAP and phase-sensitive experiments. The filter set-up is only used for the latter.

7.1 Ground state coherence time estimation

Apart from setting an upper limit for the ground state coherence time by measuring the ground state lifetime as done in Subsection 7.3.1, the ground state coherence time can be estimated from the inhomogeneous broadening of the single-photon transitions of the ensemble. As the ground states can be used as memory states, their coherence time is of crucial importance.

For an assessment, it is necessary to estimate the inhomogeneous broadening of the two-photon transition between the two ground states. According to [313] (SO, JT) and [306] (S) the full Hamiltonian of the ensemble can be written as $\mathcal{H} = \mathcal{H}_{\mathrm{SO}} + \mathcal{H}_{\mathrm{JT}} + \mathcal{H}_{\mathrm{S}}$ taking into account contributions from spin-orbit (SO) and Jahn-Teller (JT) interactions, as well as from local strain (S), where[275]

$$\mathcal{H}_{SO} = \frac{\lambda_{\{g,e\}}}{2} \begin{pmatrix} 0 & 0 & -i & 0 \\ 0 & 0 & 0 & i \\ i & 0 & 0 & 0 \\ 0 & -i & 0 & 0 \end{pmatrix}, \tag{7.1}$$

$$\mathcal{H}_{JT} = \frac{\Upsilon_{x,\{g,e\}}}{2} \begin{pmatrix} 1 & 0 & 0 & 0 \\ 0 & 1 & 0 & 0 \\ 0 & 0 & -1 & 0 \\ 0 & 0 & 0 & -1 \end{pmatrix} + \frac{\Upsilon_{y,\{g,e\}}}{2} \begin{pmatrix} 0 & 0 & 1 & 0 \\ 0 & 0 & 0 & 1 \\ 1 & 0 & 0 & 0 \\ 0 & 1 & 0 & 0 \end{pmatrix}, \tag{7.2}$$

$$\mathcal{H}_S = \epsilon_{\{g,e\}} e_x + \epsilon_{\{g,e\}} e_y, \tag{7.3}$$

in the ground state and excited state bases $\{|e_{gx}\uparrow\rangle, |e_{gx}\downarrow\rangle, |e_{gy}\uparrow\rangle, |e_{gy}\downarrow\rangle\}$ and $\{|e_{ux}\uparrow\rangle, |e_{ux}\downarrow\rangle, |e_{uy}\uparrow\rangle, |e_{uy}\downarrow\rangle\}$ [275]. Here, e_i are strain tensor components in direction $i \in \{x, y\}$, $\epsilon_{\{g,e\}}$ are the strain energies, $\Upsilon_{i,\{g,e\}}$ are the dynamic JT energies and $\lambda_{\{g,e\}}$ is the SO interaction energy for the ground (g) and excited (e) states. Neglecting global energy shifts for the ground and excited states, the eigenenergies of the ground states $|1\rangle$ and $|2\rangle$ (see Subsection 3.2.6) read

$$\epsilon_{1,2} = \pm\sqrt{\frac{\lambda_g^2}{4} + (\Upsilon_{x,g} + \epsilon_g e_x)^2 + (\Upsilon_{y,g} + \epsilon_g e_y)^2}, \tag{7.4}$$

so that the two-photon transition of the ground states is of an energy of

$$S = \epsilon_2 - \epsilon_1 = 2\sqrt{\frac{\lambda_g^2}{4} + (\Upsilon_{x,g} + \epsilon_g e_x)^2 + (\Upsilon_{y,g} + \epsilon_g e_y)^2}. \tag{7.5}$$

The width of the distribution of the two-photon transition frequencies δS is calculated by performing a Gaussian error propagation up to the second order in $\delta e_{\{x,y\}}$. Assuming $\delta e_x = \delta e_y = \delta e$, the variance of the distribution of the two-photon transition between the ground states is given by

$$\begin{aligned}(\delta S)^2 \;=\; & \left(\frac{4\epsilon_g \Upsilon_{x,g}\delta e + \epsilon_g^2 (\delta e)^2}{\sqrt{\Upsilon_{x,g}^2 + \Upsilon_{y,g}^2 + \frac{\lambda_g^2}{4}}} - \frac{\epsilon_g^2 \Upsilon_{x,g}^2 (\delta e)^2}{\left(\Upsilon_{x,g}^2 + \Upsilon_{y,g}^2 + \frac{\lambda_g^2}{4}\right)^{\frac{3}{2}}} \right)^2 \\ & + \left(\frac{4\epsilon_g \Upsilon_{y,g}\delta e + \epsilon_g^2 (\delta e)^2}{\sqrt{\Upsilon_{x,g}^2 + \Upsilon_{y,g}^2 + \frac{\lambda_g^2}{4}}} - \frac{\epsilon_g^2 \Upsilon_{y,g}^2 (\delta e)^2}{\left(\Upsilon_{x,g}^2 + \Upsilon_{y,g}^2 + \frac{\lambda_g^2}{4}\right)^{\frac{3}{2}}} \right)^2 .\end{aligned} \tag{7.6}$$

The standard deviation (std) of the strain distribution δe can be set in relation to the std of the optical linewidth $\delta\nu$ via $\delta e = \delta\nu/\epsilon_e$. Analysing the PLE measurement from Subsection 7.2.1, Fig. 7.1, $\delta\nu$ has been determined to be $\frac{10\,\mathrm{GHz}}{2\sqrt{2\ln(2)}} \approx 4.25\,\mathrm{GHz}$.

Using the strain energies $\epsilon_g = 484\,\mathrm{GHz/GPa}$ and $\epsilon_e = 630\,\mathrm{GHz/GPa}$ determined in [392], the ratio $\kappa = \epsilon_g/\epsilon_e = 0.77$ can be introduced. Assuming small JT contributions ($\Upsilon_{\{x,y\},g} \approx 0$) and that the ground state splitting is predominantly given by SO coupling ($S = \lambda_g = 48\,\mathrm{GHz}$) equation (7.6) simplifies to

$$\delta S = 2\sqrt{2}\kappa^2 \frac{(\delta\nu)^2}{S} = 0.63\,\mathrm{GHz}. \tag{7.7}$$

This corresponds to a FWHM inhomogeneous broadening of the orbital ground state two-photon transition of $\delta S_{\mathrm{FWHM}} = 2\sqrt{2\ln 2}\cdot\delta S = 1.48\,\mathrm{GHz}$. This is in good accordance with CPT measurements on this diamond sample, determining the ground state coherence time directly to about 1.6 GHz [328]. Therefore, the coherence time T_2^* is approximated to

$$\tau_S = \frac{1}{2\pi\cdot 1.48\,\mathrm{GHz}} \approx 100\,\mathrm{ps}, \tag{7.8}$$

following the Heisenberg uncertainty principle [381].

On this timescale, effects of orbital coherence will be observable. Therefore, this assessment serves as an estimate of the memory time in an ensemble of SiV^- centres. With Gaussian pulses of 6.7 GHz bandwidth (TBP = 0.67), this is $\approx$1.5 times the stored pulse duration. With Lorentzian-shaped pulses of identical bandwidth (see Subsection 7.2.2) $\approx$25 times is realistic. With this coherence time and the SiV^- ground state splitting of 48 GHz, the TBP is limited to 4.8.

Even though the memory time is not very long in comparison to the temporal duration of the pulses stored, successful storage and retrieval of weak coherent fields would be a first proof-of-principle of memory applications with colour centres in diamond potentially enabling compact and scalable devices that can be integrated on photonic chips. Furthermore, the well understood SiV^- centre can serve as a model system for other colour centres in diamond which may offer more favourable properties for memory applications (see Subsection 9.5).

7.2 Diamond sample and experimental set-up

7.2.1 Diamond sample

For all experiments discussed in this chapter, an ensemble of SiV^- centres in a 300 nm thick diamond layer fabricated by homoepitaxial chemical vapor deposition (CVD) growth on top of a pre-selected Ib low strain, high-pressure-high-temperature (HPHT) diamond substrate with (001) main surfaces was used (Fig. 7.1 (a)). Due to a growth process with low methane concentrations, resulting in low diamond deposition rates of about 10 nm/h, the ensemble experiences only low inhomogeneous broadening in a low strain environment. Further details on the sample's spectroscopic properties and growth conditions can be found in the references [240], [313] and [328].

In Fig. 7.1(b) a photoluminescence excitation (PLE) measurement of the SiV^- ensemble used for experiments in this thesis is shown. The SiV^--doped layer was grown using a silicon source with a natural isotope distribution resulting in an ensemble displaying twelve

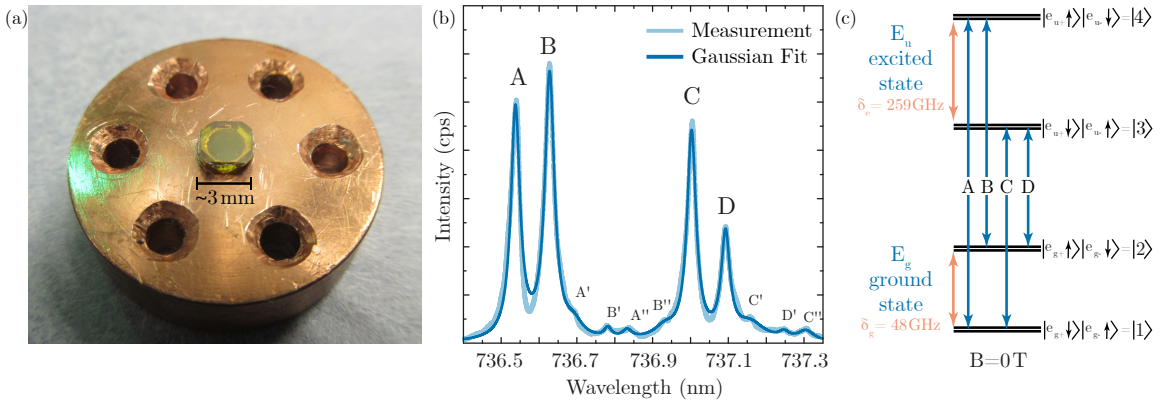


Figure 7.1: Diamond sample, optical zero-phonon line spectrum and SiV^- four-level structure. (a) Diamond sample of $\sim (3 \times 3 \times 1)$ mm on a copper mount. The SiV^- ensemble is spatially located in a 300 nm thick horizontal diamond layer at the upper surface. (b) Photoluminescence excitation spectrum at T = 5 K of the SiV^- ensemble used throughout this work (light blue) [328]. A fit of the spectrum to a set of Gaussian spectral lines indicates an inhomogeneous broadening of ≈ 10 GHz of transitions A, B, C, D (dark blue). The sample displays twelve optical transitions as it has been grown with a natural silicon isotope distribution. The D" transition is not included in the measurement. (c) The four optical transitions A, B, C, D between the four orbital states $|1...4\rangle$ form a double-Λ system. The orbital ground states $|1\rangle$ and $|2\rangle$ are separated by $\delta_g = 48$ GHz, the orbital excited states $|3\rangle$ and $|4\rangle$ by $\delta_e = 259$ GHz. Subfigures (b) and (c) from Fig. 3.8 are shown again, as the PLE measurement and the SiV^- level structure are particularly important for the discussions within this chapter. Subfigure (b) adapted from [328].

optical transitions [314,328]. The main lines A-D correspond to SiV^- centres containing ^{28}Si, while energetically shifted transitions correspond to centres containing ^{29}Si (A'-D') and ^{30}Si (A"-D") with intensity ratios matching the natural isotope abundances [314,393]. The Gaussian inhomogenous linewidth of each main optical transition of this sample is $\approx$10 GHz, only about a factor of 25 (B) to 85 (D) larger than the natural linewidth of single SiV^- centres [329] and smaller than the ground state splitting $\delta_g = 48$ GHz (Fig. 7.1 (c)), allowing for ultrafast manipulation of individual optical transitions even without the application of strong electric or magnetic fields.

As mentioned in subsection 3.2.6, the optical transitions of the SiV^- centre are cross-polarised. In consequence, for single SiV^- centres the polarisation of signal and control field

can be chosen such that they couple only to a single orbital ground state each. Nevertheless, this property is not sufficient in ensembles to suppress noise, as the ensemble consists of centres in all possible, i.e. four, spatial directions within the diamond lattice. Therefore, even though a complete FWM process is not possible in a single centre, the full FWM process takes place in the ensemble as a whole.

7.2.2 Laser fields

Ramsey interference and Hahn echo

For the Ramsey and Hahn echo measurements presented in Subsection 7.3.2, an ultrafast mode-locked Ti:Sapphire laser (Spectra-Physics, TSUNAMI, X1BB) with 80 MHz repetition rate and a fundamental pulse length of 1 ps is operated as the only light source. A solid one-piece Fabry-Pérot etalon (Thickness: 100 µm, FWHM = 20 GHz, FSR = 1000 GHz) was used to reduce the spectral bandwidth in order to address only the optical transition C resonantly. The complete pulse sequences are generated from this single laser source as shown in Fig. 7.2.

After the total power is regulated by a combination of a half-wave plate (HWP) and a polarising beam splitter (PBS), up to three 12 ps long pulses of different pulse areas are generated. These can be delayed with respect to each other with the help of a retro-reflector delay stage. While the first pulse is fixed in time, the second and third pulse are delayed by $\tau/2$ and τ respectively. Due to different polarisations, finally, a beam splitter (BS) has to combine all pulses. In all experimental steps described in this thesis an autocorellator was used for the calibration of temporal delays.

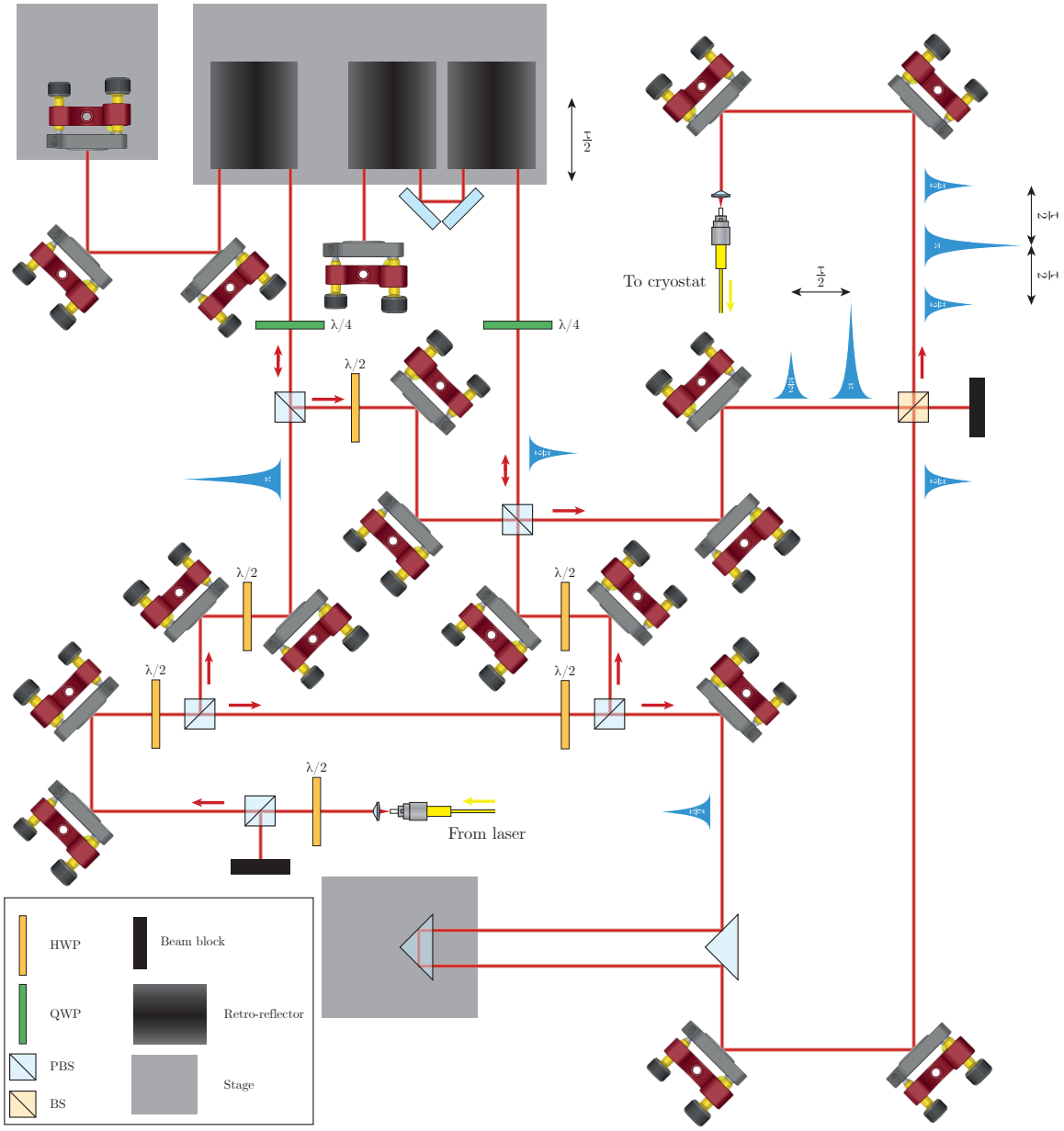


Figure 7.2: Pulse sequence set-up for Ramsey interference and Hahn echo experiments: After spectral shaping and a reduction of the pulse repetition rate by a Pockels cell, the laser power is divided in up to three pulses with pulse areas of $\frac{\pi}{2}$, π and $\frac{\pi}{2}$. For the generation of temporal delay, a stage with retroreflectors is used. Employing two retroreflectors in one of the beam arms, the temporal delay is doubled. The QWPs are placed before the retro-reflectors turning linear into circular polarisation. This ensures that the polarisation is not altered by the retro-reflectors and that the beam is reflected when returning to the PBS. Double-passing the retro-reflectors makes sure that the returning beam is not affected by shifts of the translation stage perpendicular to its direction of travel. This renders the set-up passively stable. The additional stages with a mirror or a prism serve for general temporal adjustments of path lengths. All pulses are recombined via a BS taking into account their different polarisation planes, before they are coupled to a fibre and sent to the cryogenic set-up.

STIRAP and phase-sensitive experiments

For the experiments of stimulated Raman adiabatic passage (STIRAP) as well as for the experiments of absorption and amplification of a weak signal field, both control and signal field are generated by an ultrafast mode-locked Ti:Sapphire laser (Spectra-Physics, TSUNAMI, X1BB) with 80 MHz repetition rate and a fundamental pulse length of 1 ps. The repetition rate is reduced to 1 MHz by a Pockels cell (Leysop Ltd. & Bergmann Messgeräte Entwicklung (BME) KG). The full laser field preparation set-up is given in Fig. 7.3.

The total power is split up by a PBS into two beamlines. With identical solid one-piece Fabry-Pérot etalons (Thickness: 300 µm, FWHM = 6.7 GHz, FSR = 333 GHz) in each arm, different spectral domains are carved out of the TSUNAMI pulses as shown in Fig. 7.4 (a). Control and signal field are separated in their central frequency by the ground state splitting δ_g. At the frequency of the Stokes transition, red-shifted by the ground state splitting from the control field frequency, $\nu_{Stokes} = \nu_C - \delta_g$, the etalon of the control field has not reached its maximum suppression yet. Additionally, the Stokes frequency is still close to the central frequency of the TSUNAMI pulses. Therefore, the field transmitted at the Stokes frequency can influence dynamics within the SiV^- level structure.

The temporal shape of control and signal field changes from squared hyperbolic secant to double-sided exponential when passing through the etalon. In the temporal domain a pulse width of $t^{\mathrm{E}}_{\mathrm{FWHM}} \approx 9.5\,\mathrm{ps}$ for the electric field and $t^{\mathrm{I}}_{\mathrm{FWHM}} \approx 4\,\mathrm{ps}$ in intensity are achieved as depicted in Fig. 7.4 (b) [1]. The bandwidth of the applied laser pulses is limited by the

[1] Be aware that the time-bandwidth product for Lorentzian pulses $\Delta\tau \cdot \Delta\nu \approx 0.142$ cannot be applied here. In this equation the electromagnetic field is assumed to be Lorentzian. However, etalons create Lorentzian-shaped intensity profiles. The Fourier transform of electric fields created in this way has no analytical solution. Numerically it can be approximated in this simulation to $\Delta\tau \cdot \Delta\nu \approx 0.027$, where $\Delta\tau$ and $\Delta\nu$ are the FWHM of the intensity of pulses in time and frequency space. The temporal pulse profile was confirmed by calculating its autocorrelation and comparing it to experimental measurements.

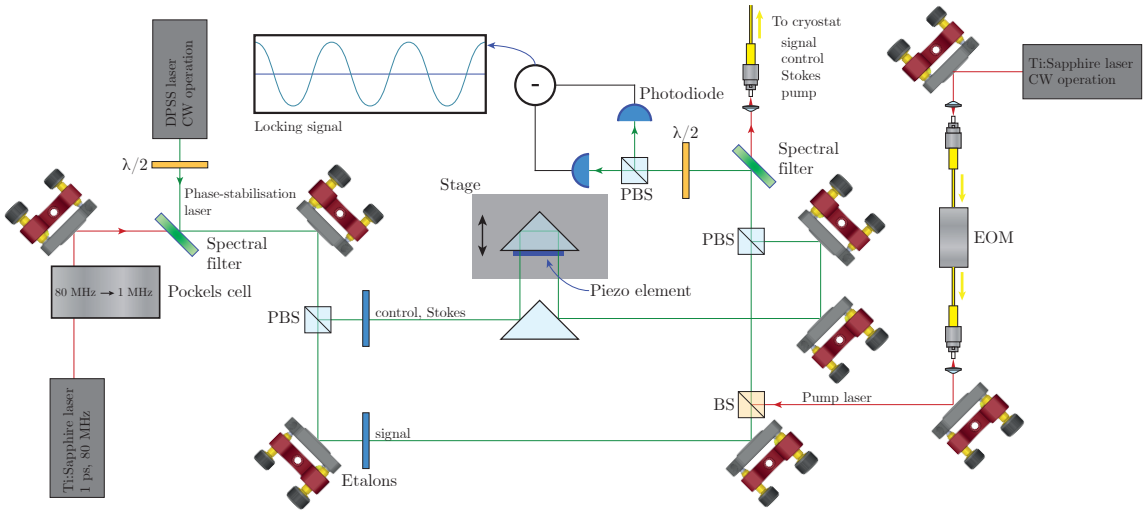


Figure 7.3: Generation and combination of all optical fields, phase stabilisation set-up: Control/Stokes and signal field are generated on different beam lines by spectral shaping out of a broad pulse spectrum using identical etalons. An interferometer is created by the two beam lines. This interferometer is stabilised by an additional green laser and a piezo element, locking control/Stokes and signal field in their relative phase. While control, Stokes, signal and pump field proceed to the cryostat, the interference pattern of the green laser is used for phase-locking.

ground state splitting δ_g, as the spectral width has to be chosen appropriately to address only one optical transition at once. This is ensured by the etalons chosen. Both fields can be delayed with respect to each other by a double-prism delay line in the control field arm before they are overlapped again by a PBS (Fig. 7.3). At this point, the signal and control fields are cross-polarised. Later, in the cryogenic set-up, this is used for suppression of the control and Stokes fields after passing through the diamond sample.

During the spectral shaping process, while control/Stokes and signal field are spatially separated, density fluctuations of the air and vibrations of the optics change the relative optical path length and, therefore, the relative phase between those fields. The two optical pathways create an interferometer which needs to be actively stabilised. For this purpose, an additional laser beam is sent through both arms of the interferometer formed by the two beam lines (Fig. 7.3). A wavelength of 532 nm is chosen to which the etalons are mostly

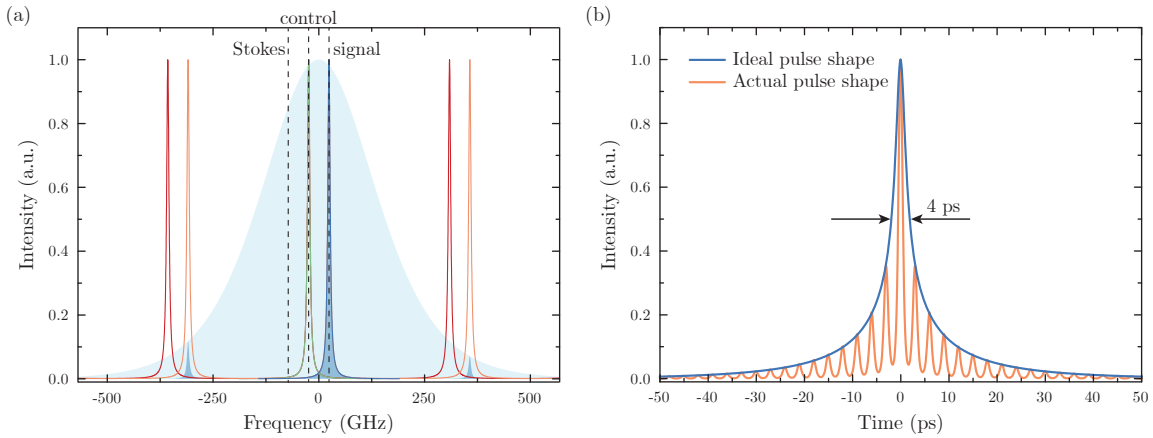


Figure 7.4: Spectral shaping: (a) From the $\Delta\nu_{\mathrm{FWHM}} = 315\,\mathrm{GHz}$ pulses generated by the Ti:Sapphire laser (light blue-shaded area) the signal and control field are created. The Lorentzian-shaped etalon combs of the two etalons are shown, as well as the transmitted intensities by the signal etalon (dark blue-shaded area). The etalon transmission lines at signal and control frequency are indicated in light green (control) and blue (signal). The relative frequencies of signal, control and Stokes field are shown by dashed vertical lines. (b) Temporal intensity profile of the generated signal field. While in blue the ideal pulse shape taking only the central transmission peak into account is shown, the actual pulse shape is modulated by the transmitted frequencies of higher order transmission peaks (orange). The generated pulses have a temporal width of $t^{\mathrm{I}}_{\mathrm{FWHM}} \approx 4\,\mathrm{ps}$.

transmissive. Here, a CW diode-pumped solid-state (DPSS) laser (Spectra-Physics, Millennia) is in use. Spectral filters are used to combine and isolate the green laser from the laser fields at 737 nm before these are separated for spectral shaping and after they are recombined. Since the two arms of this interferometer are cross-polarised, this is also the case for the two arms of the green laser recombined. Therefore, a HWP can be used to adjust their intensity on two photodiodes after a PBS in order to create an error signal. The relative intensity in the interferometer arms is controlled by a HWP in the green laser beampath before combination with the red laser. The interference signals detected by the two photodiodes are subtracted one from the other in order to eliminate laser fluctuations common to both arms. Their difference is used as a reference signal to lock on with a proportional-integral-derivative (PID) controller (LaseLock, TEM Messtechnik GmbH). As an active and controllable component, a piezo element is added to the delay stage of the control arm. The

high voltage is adjusted to keep the relative optical length of both arms equal over time. No additional changes in the relative phase can occur as the control, Stokes and signal fields are spatially overlapped for the rest of the set-up till the spectral filter set-up is reached. Phase stabilisation is only necessary for the phase-sensitive experiments with a weak signal field. For STIRAP experiments with strong control and signal fields the weak Stokes leakage is negligible and the population transfer phase-insensitive.

An additional pump field on resonance with transition D of the SiV^- ensemble is generated by a Ti:Sapphire laser (Spectra-Physics, TSUNAMI, X1BB) modified to work in continuous-wave (CW) mode with a bandwidth of $5 - 7$ GHz. For CW operation, all mode-locking and all frequency selective elements except for the birefringent filter were removed from the linear cavity. Instead, an additional monolithic Fabry-Pérot etalon (FSR = 250 GHz, Finesse = 48.67) is installed inside the cavity for frequency fine-tuning. In this way, most of the inhomogeneously broadened ensemble is prepared simultaneously. Temporal shaping of the CW laser is ensured by a fibre-coupled Mach-Zehnder-based electro-optical modulator (EOM, Jenoptik, AM705b) cutting out 100 ns pulses for pumping and probing the SiV^- ensemble. This temporally shaped CW field is combined with the signal field using a BS as both fields are applied to the diamond sample with the same linear polarisation.

7.2.3 Cryogenic set-up

The core of the cryogenic set-up is a liquid helium flow cryostat (Janis Research Company, ST-500) with a base temperature of 5 K (Fig. 7.5). A microscope objective (Olympus, LMPLFLN, 100×, NA = 0.9) inside the cryostat allows for highly-efficient confocal microscopy in reflection geometry. In this geometry a dichroic element is used for reflecting the exciting laser beams while transmitting the fluorescence emitted into the phonon sidebands. All laser fields applied to the diamond sample are coupled to the same fibre arriving at the cryogenic set-up. This ensures spatial overlap of all fields on the sample.

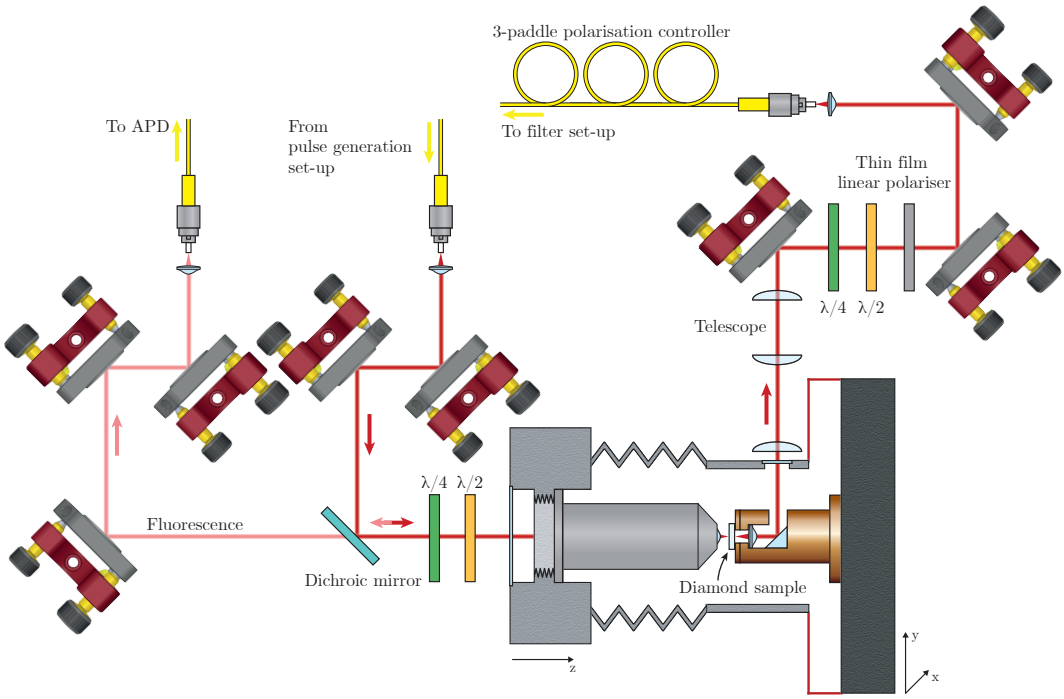


Figure 7.5: Cryogenic set-up: The cryogenic set-up can be operated in reflection and transmission mode. In reflection, the fluorescence into the phononic sidebands is collected behind the dichroic mirror. In transmission geometry, the transmitted laser fields as well as fluorescence can be analysed.

Ramsey interference and Hahn echo

For the Ramsey interference and Hahn echo experiments, after the fibre coupler from the pulse generation set-up, a HWP at 45 degrees to the cross-polarised beams and a PBS are added in order to have all pulses polarised in the same plane (not included in Fig. 7.5). For these experiments the confocal set-up is used only in reflection geometry as described so far.

STIRAP and phase-sensitive experiments

For STIRAP and phase-sensitive experiments, changes in polarisation induced by the fibre, as well as by the dichroic mirror, are counteracted by a quarter-wave plate (QWP) and a half-wave plate (HWP) between the dichroic mirror and the objective.

Additionally to working in reflection, by mounting the sample on a holder with a hole, the set-up can be used in transmission geometry using the same objective lens on the front side of the sample. For light collection on the back side of the sample an aspheric lens ($f = 3.1\,mm$) at a fixed distance from the diamond sample is used. All elements are thermally conductively connected. Outside the cryostat an additional lens and a telescope are used for beam collimation and size adjustment of the transmitted radiation.

Fluorescence detection is carried out using a single avalanche photo diode (APD, Excelitas SPCM-AQRH-14) with a dark count rate of about 100 cps and a jitter time of 350 ps. For photon counting and time-resolved measurements, the APD is connected to time-tagging electronics (PicoQuant, PicoHarp 300) with a jitter time of 4 ps.

7.2.4 Filter set-up

For absorption and amplification measurements it is important to separate the signal from the control and Stokes fields after passing through the diamond sample, in order to detect any changes in the signal field.

Suppression of the control and Stokes field is realised by a grating-based filter set-up (Fig. 7.6 (a)). Additional suppression of the control field is carried out by a nanoparticle linear film polariser and the polarisation-selectivity of the diffraction grating itself. The electromagnetic fields transmitted through the diamond are coupled to a single-mode fibre to send them into the filter set-up. Both diamond sample and fibre change the polarisation of the two cross-polarised fields differently. Because of this, corrective optical elements can only be used to optimise the polarisation of one of these fields. Hereby, the priority is laid on maximising the power-ratio of signal to control field $P_{\mathrm{S}}/P_{\mathrm{C}}$ detected after the filter set-up. In a first step, before the fibre, a combination of QWP, HWP and nanoparticle linear film polariser are used. In a second stage, a 3-paddles fibre polarisation controller and a HWP are employed to exploit the polarisation-dependence of the diffraction grating in order to suppress the control and Stokes field (Fig. 7.6 (a)).

The filter set-up was characterised with a narrowband ($<$ 10 MHz rms) Ti:Sapphire ring laser (Sirah, Matisse TX) which was frequency-tuned across the wavelength of the signal field. The Gaussian acceptance bandwidth of the filter set-up was measured to be $\Delta\nu_{\mathrm{FWHM}} = 6.1(1)\,\mathrm{GHz}$ (Fig. 7.6 (b)). This leads to a resolution-based suppression of the control field by a factor of $4.8 \cdot 10^{-4}$ at its central frequency. With an additional suppression of $10^{-3} - 10^{-4}$ by the film polariser in use, the total suppression of the control field can be assumed to be at least on the order of 10^{-7}. The resolution of the full set-up is limited to a

lower bound of $\Delta\nu_{\mathrm{DG}} = 3.32\,\mathrm{GHz}$ set by the resolution of the diffraction grating. The full resolution is not reached in the experiment due to partial illumination of the diffraction grating and imperfections of optical elements.

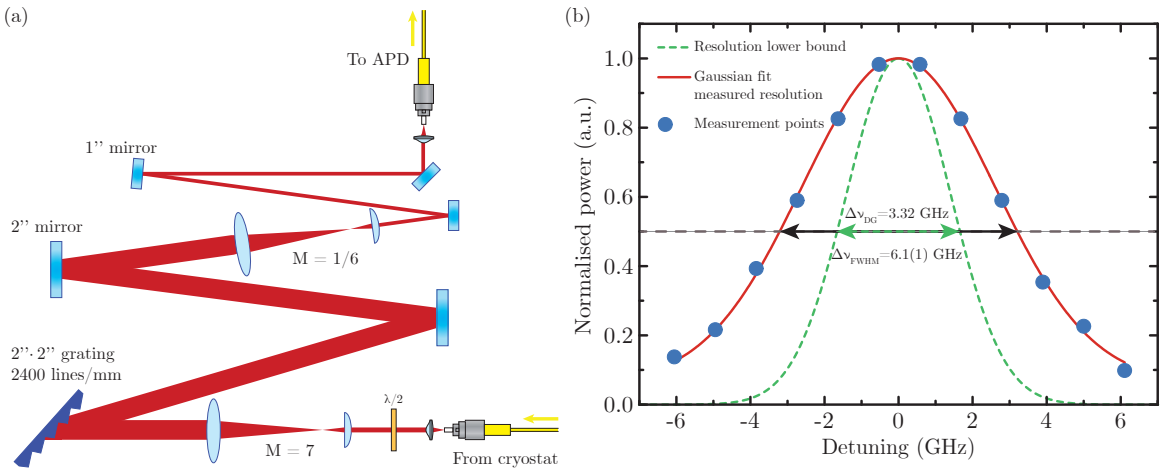


Figure 7.6: Grating-based filter set-up: (a) Schematic structure: The entrance of the filter set-up is fibre-coupled to maintain a fixed beam path through the set-up. In order to maximise the resolving power of the set-up, an optical telescope (magnification $M = 7$) widens the transverse beam diameter to illuminate most of the diffraction grating (2" · 2", $2400\,^{\mathrm{lines}}/_{\mathrm{mm}}$). After a propagation distance of $\sim 1\,\mathrm{m}$ the width of the ray is reduced by an inverse telescope (magnification $M = 1/6$) and coupled to a fibre. The fibre operates as a pinhole that provides frequency selectivity (mode field diameter MFD = (3.6 - 5.3) µm at 633 nm). (b) The power coupled to the single mode fibre at the end of the filter set-up is measured sweeping a narrowband laser over the frequency of the signal field (blue dots). The spectral resolution is determined by a Gaussian fit to $\Delta\nu_{\mathrm{FWHM}} = 6.1(1)\,\mathrm{GHz}$ (red line). For comparison the maximum optical resolution of the diffraction grating with $\Delta\nu_{\mathrm{DG}} = 3.32\,\mathrm{GHz}$ is shown as well (green dashed line).

7.3 Coherent control and wave mixing in ensembles of silicon vacancy centres

In the following section, the main experimental results working with an ensemble of SiV^- centres is laid out. These reach from the measurement of the ground state lifetime, via the coherent manipulation of the ensemble by Ramsey interference and Hahn echo measurements, to coherent ground state population transfer by STIRAP and strong light-matter interaction of the ensemble with a signal field. These results have been published in [394]. At the end of this section, the simulation models describing the coherent control of the ensemble and the phase-sensitive strong light-matter interaction are clarified.

7.3.1 SiV^- ground state lifetime

For memory applications, the limiting factor for storage times is given by the coherence time of the ensemble as theoretically estimated in Section 7.1. Measuring the lifetime of the storage state is another good way for estimating the maximum coherence time of this state, as both parameters are connected by $T_2 \leq 2\,T_1$ (see Subsection 3.2.2). The final coherence time of the SiV^- ensemble under consideration is expected to be much shorter than $2\,T_1$ due to homogeneous and inhomogeneous effects.

In the SiV^- centre, phononic decay and excitation rates lead to a stable temperature-dependent population distribution between the two ground states $|1\rangle$ and $|2\rangle$ [248]. The same effects are also responsible for a rethermalisation when the ground states are brought out of their equilibrium population distribution. For the ensemble of SiV^- centres under consideration, the lifetime of the orbital ground states has been measured to be $T_1^{\text{orbit}} = 27(8)\,\text{ns}$ at a temperature of 5 K. For this, resonant CW light is applied on transition D for 100 ns. This

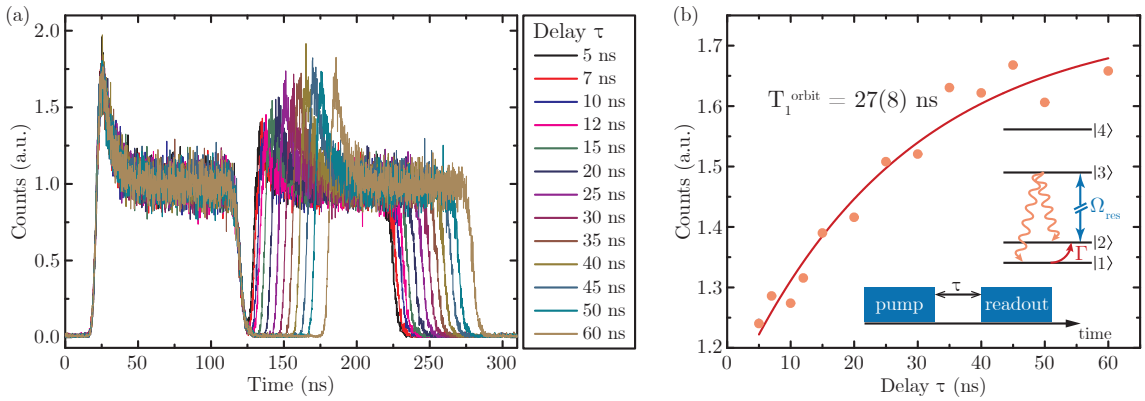


Figure 7.7: Ground state lifetime measurement: (a) For various temporal delays between the pump pulse and the readout pulse the time-resolved fluorescence into the phonon sidebands is recorded. After the end of the pump pulse, the population distribution of the ground states returns to thermal equilibrium. The height of the peak during the readout pulse is a measure of the population in the probed state $|2\rangle$. (b) The exponential change of the peak height (measurements: orange dots, fit: red line) determines the ground state lifetime to be $T_1^{\text{orbit}} = 1/\Gamma = 27(8)$ ns. Insets show the pulse sequence and the optical field configuration.

is long enough to bring the ensemble into a new steady state. When the pump field is turned off the system returns into its initial equilibrium state. The progress of rethermalisation is probed with a readout pulse identical to the pump pulse. During both pulses the fluorescence into the phonon sidebands is measured. The amount of fluorescence is proportional to the population in state $|2\rangle$. Increasing the delay between the end of the first and the beginning of the second pulse, the population in the resonantly coupled ground state $|2\rangle$ increases. This is reflected by the growth of the fluorescence peak when the readout field is applied (Fig. 7.7 (a)). The change of peak height is fitted by an exponential function to determine the lifetime T_1^{orbit} of the ground states as shown in Fig. 7.7 (b).

7.3.2 Ramsey interference and Hahn echo measurements

In order to demonstrate coherent control over the ensemble, resonant Ramsey interference measurements (see Subsection 4.2.2) were performed using a sequence of two 12 ps-long optical pulses with variable delay τ resonantly applied to transition C of the ensemble, preparing a coherence between the lower ground state $|1\rangle$ and the lower excited state $|3\rangle$ of the ensemble. The pulse sequence and the addressed optical transitions are given in Fig. 7.8 (a) and (b). The fluorescence intensity as a function of the delay τ is measured, which reflects the upper state population after the pulse sequence. In Fig. 7.8 (c) individual fringes oscillating at optical frequencies were not resolved and only the upper and lower envelopes are shown for both measurements. A model of optical Bloch equations (OBE) for the ensemble was developed and is explained in detail in Subsection 7.4.1. With an inhomogen-

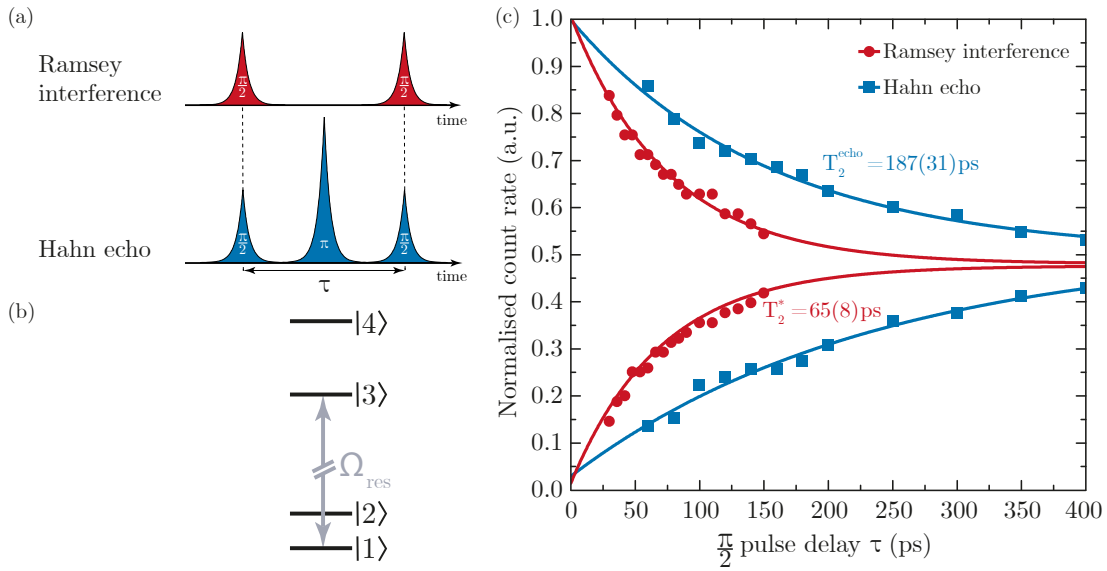


Figure 7.8: (a) Pulse sequence of 12 ps long optical pulses for Ramsey interference (red, upper) and Hahn echo (blue, lower) measurements. (b) SiV^- level system with a resonant optical field on transition C, identical for both Ramsey interference and Hahn echo measurements. (c) Optical Ramsey interference (red circles, inner) and Hahn echo measurement (blue squares, outer). Measured envelopes (dots and squares) and simulations (solid lines) using a four-level optical Bloch equation model assuming an ensemble of 10 emitters with a 10 GHz broad Gaussian distribution are shown (T=5 K, $P_{\frac{\pi}{2}} = 0.5(2)$ µW, $P_{\pi} = 1.8(3)$ µW). The pulse areas were experimentally optimised.

eous broadening of 10 GHz inferred from Fig. 3.8 (b) and the transition rates measured for a single emitter in [343] as input parameters, the OBE ensemble model appropriately describes the resulting Ramsey fringe decay, averaging over only a small number of ten emitters in the model and thus limiting its numerical complexity while still providing exact results for dense ensembles. The observed fringe decay indicates an inhomogenous coherence time of $T_2^* = 65(8)$ ps, about a factor of 15 lower than what has been observed for single centres [343]. This is caused by a relative dephasing of individual emitters in the ensemble with different Larmor frequencies due to their varying detuning relative to the applied optical field.

Using an optical Hahn echo sequence (see Subsection 4.2.3 and Fig. 7.8 (a)), the possibility of counteracting this dephasing, which is caused by local variations of the static strain field in the sample, was explored. The measured Hahn echo envelopes, shown in Fig. 7.8 (c), result in an improved coherence time of T_2^{echo}=187(31) ps. While the theoretical model indicates that, in principle, values equivalent to the single-emitter coherence time can be reached with this technique, an excitation-induced dephasing of about 900 MHz, most-likely related to phonon broadening by the applied π laser pulses, has to be added to match the observed coherence decay. Similar effects have already been observed for single SiV^- centres using ultrafast laser pulses [343]. Albeit this can be improved further by optimising thermal management, the observed increase in coherence time outlines the great potential of similar echo sequences in future experiments to mitigate the effects of the remaining inhomogeneous broadening.

The aforementioned resonant experiments demonstrate the coherent manipulation of the ensemble involving its excited state, however, for many applications it is desirable to

access the longer-lived and more narrowband ground state coherence. This coherence can be addressed optically using off-resonant two-photon Raman transitions for which the ground state coherence time of the ensemble can be estimated to $T^*_{2,g} \approx 100\,\text{ps}$ (see Section 7.1), in conformity with coherent population transfer (CPT) measurements [328].

7.3.3 Stimulated Raman adiabatic passage (STIRAP)

The feasability of ensemble Raman transitions is demonstrated by inducing a coherent population transfer between the two ground states $|1\rangle$ and $|2\rangle$ of the ensemble by implementing a stimulated Raman adiabatic passage (STIRAP) using ultrafast off-resonant signal and control pulses [353,354] (see Subsection 4.2.4). For this, initialisation of the system in $|1\rangle$ and readout of the resulting population of $|2\rangle$ is realised by means of optical pumping, resonantly driving transition D with two subsequent 100 ns long pulses as displayed in Fig. 7.9 (a). This is reducing the population ρ_{22} in $|2\rangle$ from its thermal equilibrium value of ρ_{22}=37% at 5 K to a minimum of ρ_{22}=19%, 6 ns after the end of the pump pulse, limited by the competition between optical pumping and relaxation between the ground states with a time constant of $T_1^{\text{orbit}} = 27(8)\,\text{ns}$ as measured in Subsection 7.3.1. The fluorescence from state $|3\rangle$ into the phonon sidebands is measured.

For population transfer, with the same delay from the pump pulse, in between the two resonant fields, the two Raman pulses are then applied, leading to a coherent population transfer from $|1\rangle$ to $|2\rangle$ as indicated by the strong increase of the readout pulse rising edge fluorescence in Fig. 7.9 (b). Employing the OBE model, this peak corresponds to a population in state $|2\rangle$ of $\rho_{22} = 49\%$. The population transfer in the limit of ultrashort pulses and zero relative pulse delay is assumed to be bidirectional between $|1\rangle$ and $|2\rangle$ with

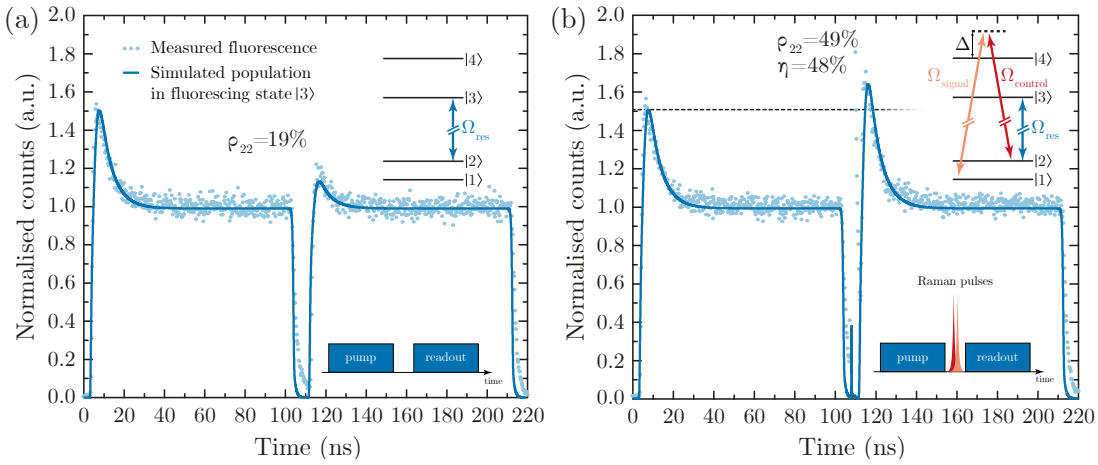


Figure 7.9: Stimulated Raman adiabatic passage. The fluorescence into the phononic sidebands is measured both (a) without and (b) with the Raman pulses between the pump and readout pulses (light blue dots). For simulations, the OBE model described in the main text is used (blue line). (a) Optical pumping and readout of the ground orbital state $|2\rangle$ using resonant illumination of transition D. The OBE model indicates a population in $|2\rangle$ of $\rho_{22} = 19\%$ in between both resonant pulses. (b) Sequence from (a) including the Raman signal and control field applied in between the resonant pulses with zero temporal delay to each other. Both fields are blue-detuned by $\Delta = 70\,\mathrm{GHz}$ from the upper excited state $|4\rangle$ while in two-photon resonance. A population of $\rho_{22} = 49\%$, equivalent to a transfer efficiency of $\eta = 48\%$, is reached directly after the Raman pulses have been applied. Inserts show optical field configurations and pulse sequences. The power of the resonant, signal and control fields are $\mathrm{P_{res}} = 30\,\mu\mathrm{W}$, $\mathrm{P_{signal}} = 33\,\mu\mathrm{W}$, and $\mathrm{P_{control}} = 27\,\mu\mathrm{W}$ respectively.

the same transfer efficiency η. This is also indicated by the simulation. In the case of perfect efficiency, the populations in the ground states are swapped. Therefore, the final population ρ_{22}^f after STIRAP is limited by the initial population ρ_{22}^i in $|2\rangle$ after imperfect initialisation. In the experiment, a transfer efficiency of $\eta = (\rho_{22}^f - \rho_{22}^i)/(1-2\rho_{22}^i) = 48\%$ is reached. This is about a factor of two below the simulated transfer efficiency maximum (see Fig. 7.10). According to the model, this is mainly limited by the available power in the Raman pulses.

In order to investigate the power regime worked in and to verify that population is transferred by means of STIRAP, a temporal delay scan between the control and signal pulse was carried out. As can be seen in Fig. 7.10 (a) the delay between signal and control pulse was changed over a range of 140 ps. Around zero delay, the transfer efficiency reaches

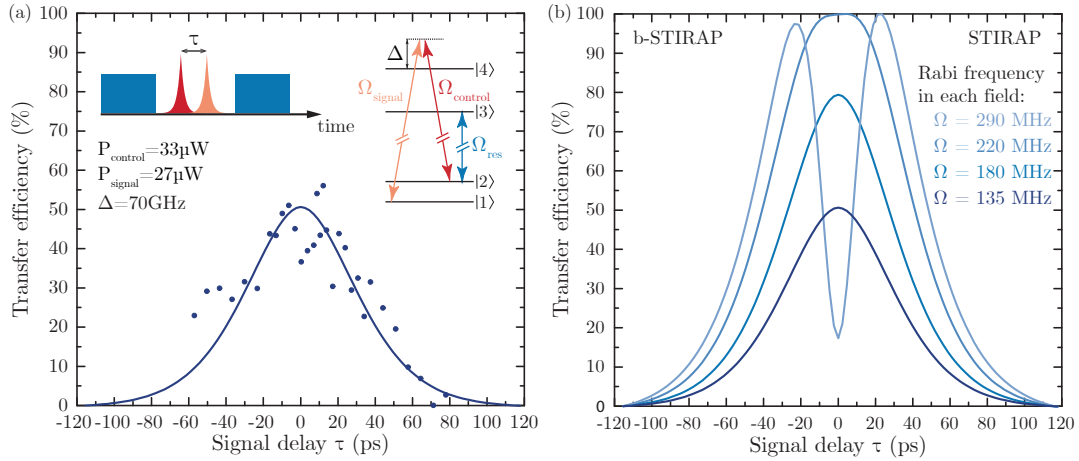


Figure 7.10: STIRAP varying the temporal delay between control and signal pulse: For $\tau > 0$: Control pulse preceding, for $\tau < 0$: Signal pulse preceding. (a) Temporal delay scan between control ($P_{control} = 33\,\mu W$) and signal field ($P_{signal} = 27\,\mu W$) in two-photon resonance detuned by $\Delta = 70\,GHz$ from the upper excited state $|4\rangle$. The measured transfer efficiencies (dots) correspond to a theoretical relative Rabi frequency of $\Omega = 135\,MHz$ in both pulses used in the OBE model (solid line). Insets show the pulse sequence and the applied optical fields. The experimental transfer efficiencies were determined using the OBE model. The corresponding curve of theoretical transfer efficiencies was determined by fitting to the right side ($\tau > 0$) of the experimental data with the identical Rabi frequencies of the two pulses as free parameter, while leaving the maximum transfer efficiency centred at $\tau = 0$. (b) With the same spectral detuning, simulations of the OBE model over a pulse delay from -120 to 120 ps are shown. For low Rabi frequencies ($\Omega < 220\,MHz$) in both pulses the maximum transfer efficiency is reached at zero delay between the pulses. Increasing these frequencies, the characteristic STIRAP ($\tau > 0$) and b-STIRAP ($\tau < 0$) lobes emerge.

its maximum, while it vanishes for large delays. Around the maximum, the transfer efficiency exhibits a nearly Gaussian distribution. This corresponds to a STIRAP regime of low powers which is confirmed by the OBE simulations. Only for higher pulse powers ($\Omega > 220\,MHz$) in both signal and control field, the delay curve develops its characteristic shape with a classical STIRAP and a b-STIRAP peak at delays different than zero [362,363] (Fig. 7.10 (b)). In the simulations, Rabi frequencies are used as scaling parameters only. It can be seen that in the experiment the transfer efficiency is limited by the maximum available laser power in the two STIRAP pulses. Therefore, in this delay scan with a theoretical relative Rabi frequency of $\Omega = 135\,MHz$ in both fields, only a transfer efficiency of $\approx 50\%$ can be reached.

The transfer efficiency vanishes when the signal and control fields are brought out of

two-photon resonance. Furthermore, when the signal or control field is applied separately, no population transfer is observed by such single pulses. This confirms that population has been transferred by an off-resonant two-photon process.

In the low power regime, in which experiments are carried out in this thesis, there is no physical distinction between STIRAP and two-photon Raman transitions. However, the STIRAP description appears to be more common in ensembles. Moreover, the STIRAP description and label has been chosen to better capture the transition to the high power regimes which should be aimed at for full population transfer. The transition from the low to the high power regime has been shown in Fig. 7.10 (b).

Within the low power regime the data may also be fitted to a $\sin^2(\Omega^2 T/\Delta)$ function for some effective pulse width T. However, in addition to a relative Rabi frequency as scaling parameter, an effective pulse width would have to be introduced. Furthermore, this effective pulse width would differ for every temporal delay between the two pulses introducing a higher level of arbitrariness. Therefore, an analysis with the OBE model, verified earlier by Ramsey and Hahn echo measurements (see Subsection 7.3.2), is preferred.

The experiments shown are adiabatic, fulfilling equation (4.32) which is valid both in the low and high power regime. Due to identical signal and control fields, their strong temporal overlap and their weak Rabi frequencies in comparison to the off-resonant detuning, the population transfer can be assumed adiabatic. In the case of a non-adiabatic two-photon process, the excited state $|4\rangle$ would have to be involved and signal and control field would

need to couple resonantly with their frequency tails to the optical transitions between ground and excited states.

7.3.4 Phase-dependent strong light-matter interactions

In a final experiment, the strength of one of the laser fields was reduced, using it as a signal field, while the other, strong field, is used as a control field. Then, the signal's gain and absorption induced by its interaction with the SiV^- ensemble, driven by the control field, was directly measured. With the same blue detuning of $\Delta = 70\,\mathrm{GHz}$ as in the STIRAP experiments, here, in contrast to those experiments, the signal field is measured after transmission through the diamond sample. In order to measure the weak signal field, all other wavelengths are suppressed by a polariser and a fibre-coupled grating filter set-up (see Subsection 7.2.4). Both absorption and amplification were observed for the weak signal field, depending on the relative phase between the signal and control arm of the set-up. By fine-tuning using a piezoelectric element in the control arm, the delay between the pulses near the point of full temporal overlap, and therefore the relative phase between them, could be adjusted without significant change of the overlap itself. A maximum of $\approx 80\%$ absorption and $\approx 60\%$ amplification were reached after subtraction of the residual control field. All measured fields after filtering are shown in Fig. 7.11 (a).

In the measurements, saturation of absorption and amplification was reached when increasing the power of the control field (Fig. 7.12). Saturation powers of the control field have been determined to $P^{\mathrm{amp}}_{\mathrm{control}} = 7(5)\,\mu\mathrm{W}$ and $P^{\mathrm{abs}}_{\mathrm{control}} = 21(10)\,\mu\mathrm{W}$ respectively. Therefore, for the given detuning, both effects are most likely limited by the number of SiV^-

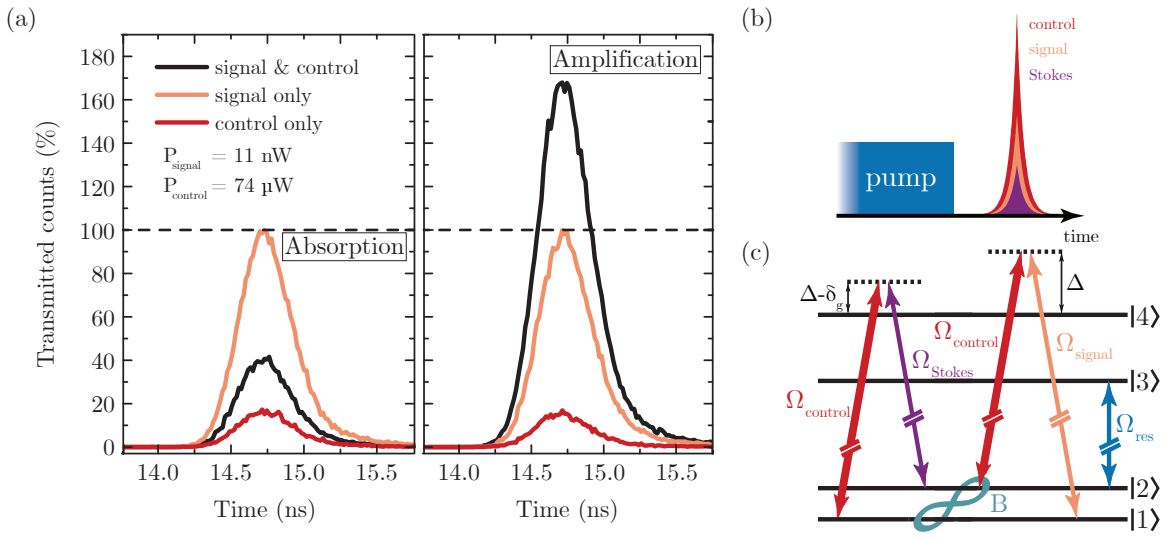


Figure 7.11: Phase-sensitive signal absorption and amplification. (a) Time-resolved measurement of optical fields sent through the ensemble. The filter set-up is set to maximum transmission for the signal wavelength. The fields are normalised in amplitude to the counts measured when only the signal field is sent through the diamond. After subtracting the background control field, which could not be suppressed by the filter set-up, $\approx 80\%$ absorption (left) and $\approx 60\%$ amplification (right) of the signal field were measured, depending on the relative phases of the fields (see main text). (b) Pulse sequence. After preparing the ensemble by resonant optical pumping, control, signal and Stokes field are applied at the same time. (c) The strong control field couples to both ground states creating two Λ-systems with different detuning from the excited states. Stokes and signal field, which are also applied to the sample, together with the control field, create a parametric scattering route of optical transitions. Between the orbital ground states $|1\rangle$ and $|2\rangle$ a coherent excitation B (spin wave) is created.

centres addressed, i.e. by the optical density of the sample for a given focal spot size of the applied fields.

Absorption and amplification can be explained by an off-resonant FWM process with an additional Stokes field. The signal and control field are generated in separate beam paths by etalons of the same type from the same laser pulse. As well as preparing the control field, this configuration unintentionally produces an additional field at the Stokes frequency by means of leakage through the low-energy tail of the control field etalon (see Subsection 7.2.2). The Stokes, control and signal pulses arrive at the same time after the

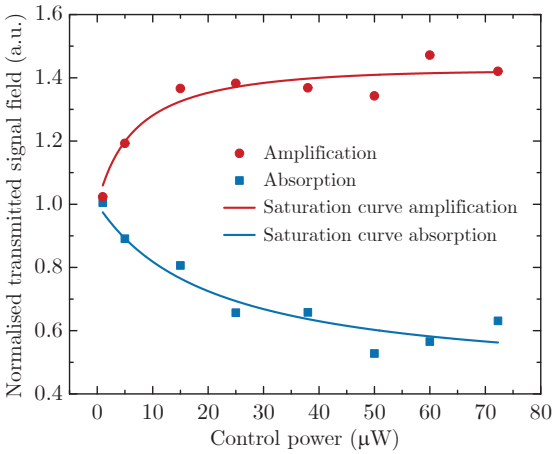


Figure 7.12: Signal absorption and amplification saturation measurements: Increasing the power of the control field, saturation in both amplification (red circles) and absorption (blue squares) can be observed. In this measurement, saturation values of $I_{inf}^{amp} = 1.5(2)$ and $I_{inf}^{abs} = 0.4(1)$ are reached, where I is the normalised transmitted signal field, i.e. $I_0 = 1$.

pump pulse and with a fixed phase relation at the ensemble, as can be seen in the schematic pulse scheme of Fig. 7.11 (b). Within the SiV^- ensemble, FWM takes place because the control field couples to both ground states, generating a double-Λ system via two virtual excited states and, together with signal and Stokes fields, creates a parametric scattering route as indicated in Fig. 7.11 (c). Both Λ-systems interact via the ground state coherence B (spin wave) [2]. The third-order susceptibility is enhanced by the parametric scattering route, increasing the FWM process in this thin ensemble of low optical density [172].

The interaction of the fields can be described by the linearised Maxwell-Bloch equations in the adiabatic approximation [395]. These equations have been modified to account for the initial population distribution set by the limited pumping power and the rethermalisation of the ground states (see Subsection 7.4.2).

[2] Here, the term 'spin wave' is used for a coherent superposition of an excitation over an ensemble of atomic systems. In this experiment the ground state coherence is not created between spin levels, but orbital states.

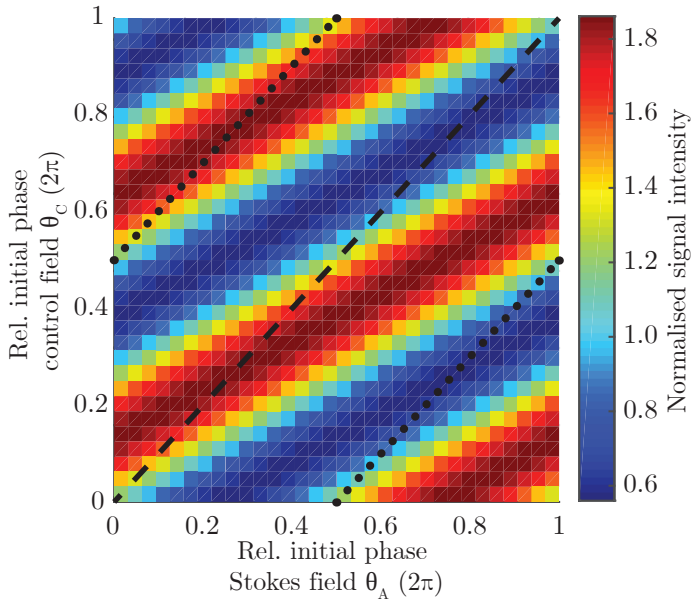


Figure 7.13: Signal absorption and amplification in simulations. Phase dependence of the transmitted signal field intensity on the relative initial phases of control (θ_C) and Stokes field (θ_A) in respect to the initial phase of the signal field. The colour bar encodes the total intensity of the signal field after the diamond, normalised to the total intensity of the signal field before interaction. In this specific qualitative simulation, the signal field varies between $\approx 80\%$ amplification and $\approx 40\%$ absorption. Examples of two possible paths in phase-space with 2π-periodicity, accessible in the experiment, are given by the dashed and dotted lines. All possible paths are parallel to each other and of the same total length.

The relative phases of the signal, control and Stokes fields determines whether the signal field will be absorbed or amplified, as can be seen in Fig. 7.13. The phase dependence arises from seeded Raman scattering where the phase of each field is set as an initial condition [396,397]. Simulations show that the signal and Stokes fields are both amplified or absorbed under the same phase conditions (see Subsection 7.4.2). Therefore, an energy transfer between these two fields can be excluded and energy is only transferred between them and the control field.

By applying active phase stabilisation fixing the relative phase between the signal field and the arm containing the control and Stokes fields, as described in Subsection 7.2.2, it was

possible to switch between absorption and gain in a controlled way. As shown in Fig. 7.13, for a fixed phase relationship between control and Stokes field, all possible intensities of the signal field lie on a line in phase-space, where all possible paths are parallel to each other.

In the experiment, this relationship is fixed since the control and Stokes field propagate along the same beam path. Therefore, it is possible to move along one of these lines by changing the relative phase between the signal field and the arm containing control and Stokes field and, thus, varying the intensity of the transmitted signal. Similar phase-sensitive effects involving resonant coherent population trapping in warm helium cells[398,399], as well as off-resonant FWM interactions in a double-Λ system in warm rubidium vapour[400], have been observed recently.

7.4 Numerical simulation

In this section, the sets of mathematical equations as well as the numerical simulation models used to analyse the effects observed in the experiments described in Section 7.3, are explained in further detail.

7.4.1 Optical Bloch equations (Ramsey interference, Hahn echo, STIRAP)

To model coherent light-matter interactions in an ensemble of SiV^- centres, a model of optical Bloch equations (OBE) was developed. With this model, light-matter interactions for Ramsey interference, Hahn echo and STIRAP experiments were simulated.

The temporal evolution of the population distribution within the SiV^- four-level system is governed by the master equation in Lindblad form,

$$\dot{\rho} = -\frac{i}{\hbar}\left[\mathcal{H}, \rho\right] + \sum_{i,j=1}^{4} \Gamma_{ij}(\rho_{ii}\left|j\right\rangle\!\left\langle j\right| - \frac{1}{2}\{\left|i\right\rangle\!\left\langle i\right|, \rho\}), \tag{7.9}$$

where $\mathcal{H}$ is the orbital four-level interaction Hamiltonian in rotating wave approximation and ρ is the density matrix of the system. The spontaneous decay rates Γ_{ij} $(i \neq j)$ and the pure dephasing rates Γ_{ii} are introduced following [343]. Square and curly brackets are used to denote commutators and anticommutators respectively.

The coherent evolution of the ensemble was described by solving the OBE of Eq. (7.9) using the fourth-order Runge-Kutta method (RK4) [401–403] for ten individual SiV^- centres, each with a different resonance frequency, i.e. off-resonant detuning relative to the applied electromagnetic fields, to account for the inhomogeneous broadening defined by a Gaussian

distribution. The solutions for the individual emitters are then weighted by the amplitude of the Gaussian at the respective detuning and averaged. For the full derivation of the optical Bloch equations, refer to Appendix B.

7.4.2 Linearised Maxwell-Bloch equations (phase-sensitive amplification and absorption)

For the phase-sensitive amplification and absorption of a weak coherent signal field, the interaction of the signal (E_S), the Stokes (E_A) and the control field (Ω_C) with the ground state orbital coherence (B, spin wave) is governed by the linearised Maxwell-Bloch equations in the adiabatic approximation, as described in reference [395],

$$(c\partial_z + \partial_t)E_S = ic\sqrt{\frac{d\gamma}{L}}\frac{\Omega_C}{\Gamma_S}B - \kappa_S E_S, \tag{7.10}$$

$$(c\partial_z + \partial_t)E_A = ic\sqrt{\frac{d\gamma}{L}}\frac{\Omega_C}{\Gamma_A}B^* - \kappa_A E_A, \tag{7.11}$$

$$\begin{aligned}\partial_t B = {} & (p_1 - p_2) \times \left(-i\sqrt{\frac{d\gamma}{L}}\frac{\Omega_C^*}{\Gamma_S}E_S + i\sqrt{\frac{d\gamma}{L}}\frac{\Omega_C}{\Gamma_A}E_A^*\right) \\ & - \left[\frac{1}{\Gamma_S} + \frac{1}{\Gamma_A^*}\right]|\Omega_C|B.\end{aligned} \tag{7.12}$$

Equation (7.12) has been complemented by the initial population distribution between the ground states. Using the same pumping scheme as described for STIRAP in Subsection 7.3.3, the population in the lower ground state is $p_1 = 0.8$, while in the upper ground state a population share of $p_2 = 0.2$ is remaining.

As initial conditions $\forall\{t,z\} \in (\{t=0, z\in\mathbb{R}\} \vee \{t\in\mathbb{R}, z=0\})$, the incoming fields are defined as:

$$E_S(t,z) = |E_S(t,z)|\, e^{i\theta_S}, \tag{7.13}$$

$$E_A(t,z) = |E_A(t,z)|\, e^{i\theta_A}, \tag{7.14}$$

$$\Omega_C(t,z) = |\Omega_C(t,z)|\, e^{i\theta_C}, \tag{7.15}$$

$$B(t,z) = 0\, e^{i\theta_B} = 0. \tag{7.16}$$

The signal and Stokes fields interact with the ensemble and its spin wave B in the presence of a strong control field with Rabi frequency Ω_C propagating through the medium in the z-direction. All phases (θ_C, θ_A and θ_B) are set relatively to the initial phase of the signal field (θ_S) which is always chosen to be zero as a starting condition. It is assumed that there is no coherent spin wave existent inside the interaction medium at the beginning of the interaction. The incident fields form a closed parametric scattering route of optical transitions. Therefore, their initial phase has a direct influence on the dynamics inside the ensemble of SiV^- centres. For every possible phase combination of Stokes and control field an appropriate phase of the signal field can be found in order to achieve maximum amplification or absorption of the signal field.

Simulations have been conducted implementing the set of differential equations (7.10) to (7.12) with the initial conditions (7.13) to (7.16). The differential equations are given in their explicit form calculating a variable y at a future time $t+\Delta t$, where Δt is a small step in time. The future value of the variable y only depends upon the variables current

value and other variables u, v, ... at the current time t, $y(t + \Delta t) = f[y(t), u(t), v(t), ...]$. A method for solving this kind of explicit set of differential equations is the fourth-order Runge-Kutta method (RK4), discretising the temporal evolution. It turns out that the present differential equations can become stiff under demanding conditions. This means that the differential equations are only solvable when step sizes are taken to be very small, otherwise, solutions become numerically unstable.

In diamond layers on the scale of hundreds of nanometres and for pulses in the pico-second regime, a mismatch between the sample thickness and the pulse length in space is experienced. The layer is very short in comparison to the total pulse length. For Gaussian-shaped pulses of 6.7 GHz bandwidth the ratio between the sample length of 300 nm and the FWHM pulse length in space is of the order of 1 : 66,000. Therefore, the number of steps in time over the pulse width is very large in comparison to the number of steps through the medium in space. Still, as strong light-matter interactions within the diamond layer need to be modelled, a high number of steps is already necessary over the length of the medium rendering a simulation over the full length of the pulses even more demanding in terms of discretisation.

As significant effects of absorption and gain have been observed in this diamond layer of 300 nm, high gradients in the fields are expected, quickly leading to numerical instabilities if the step size in time and space is chosen too large. These numerical issues were avoided in the simulations by choosing an interaction length, field strengths and pulse durations with a more favourable quotient of pulse and interaction length and smaller gradients of the involved fields. Nonetheless, this approach is valid to show and analyse the effects

observed in the experiment as only a qualitative analysis is performed and the set of partial differential equations (PDE) as well as the initial conditions remain the same.

In space, a Chebyshev grid[404] is used. The k nodes of the grid are so-called Chebyshev points, which are the roots of the Chebyshev polynomial of the first kind of degree k[405]. The Chebyshev grid offers a higher node density at the simulation boundaries than found in grids with equally distributed nodes. This supports the interpolation accuracy at the boundaries of the medium and, hereinafter, the accuracy over the rest of the medium.

In Fig. 7.14, the full interaction of signal, control and Stokes field as well as of the spin wave is shown as a representative example. The evolution of the control field was included in the simulation, where its amplitude was held constant over the full interaction. Therefore, the control field can be interpreted as an infinite energy bath and the total energy of the system is not conserved. As initial conditions, the phases of the control and Stokes field, relative to the signal field, are chosen as $\theta_A = \frac{\pi}{4}$ and $\theta_C = -\frac{\pi}{4}$.

In this simulation the signal field is absorbed by $\approx 40\,\%$. It can be seen that the maximum absorption is reached at about $z = 12\,\mathrm{mm}$. The Stokes field only experiences small changes during the interaction. The control field is chosen to be strong in comparison to the signal and Stokes field. Both its intensity and phase stay stable over the course of the simulation. The changes in phase are only numerical inaccuracies on the order of $2\pi \cdot 10^{-17}$. Signal and Stokes field adapt in their phase while propagating through the medium.

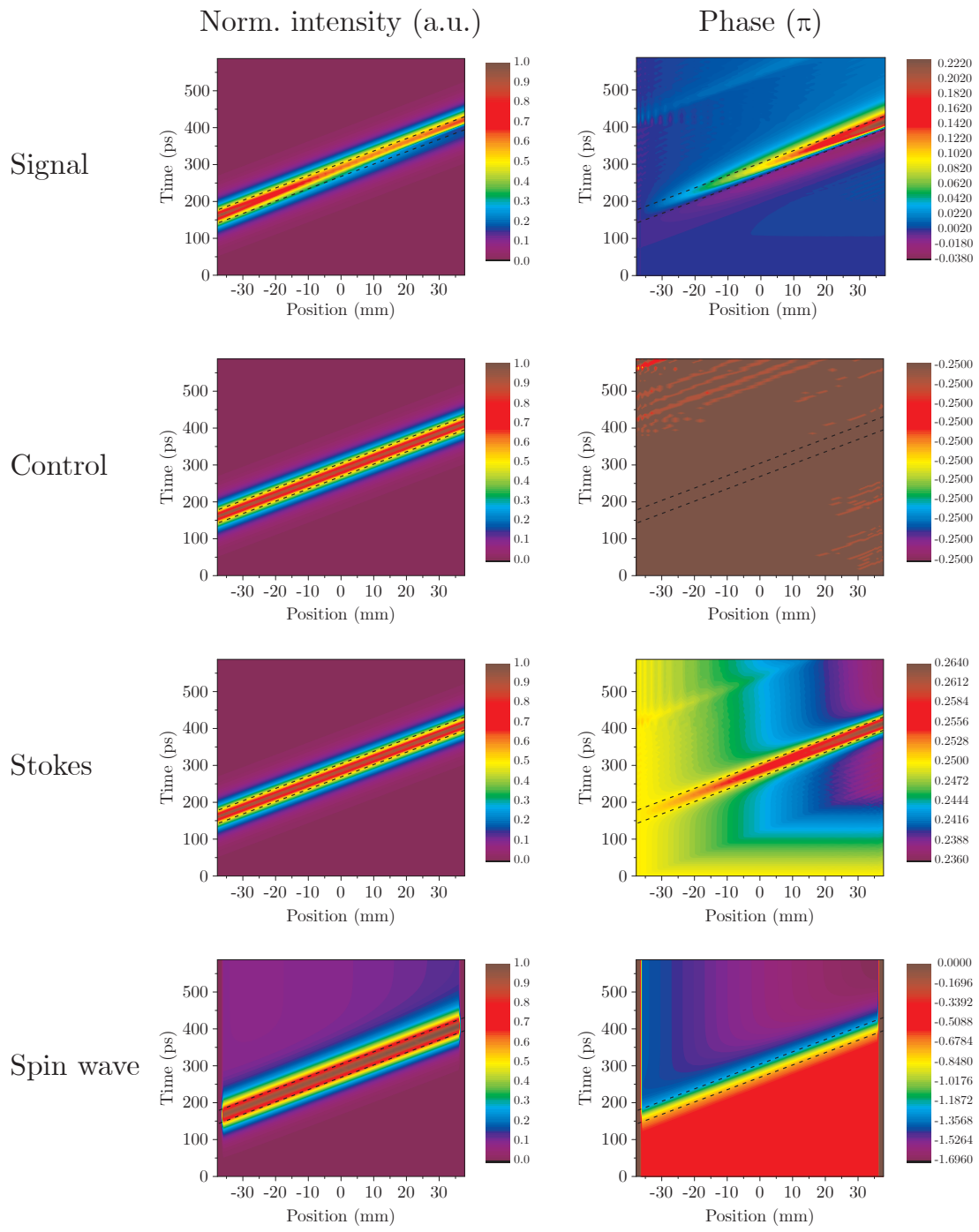


Figure 7.14: Simulation of the interaction of signal, control and Stokes fields, as well as of the spin wave. The propagation within and outside the medium is shown, resolved in time and space. All fields are normalised to their maximum initial intensity whereas the spin wave is normalised to its maximum value during the full simulation (left column). In the right column the phase of the fields and of the spin wave is shown. For easier interpretation, the course of the control field in space and time is indicated in every subfigure by two dashed lines separated by the control's FWHM width. The full simulation distance spans 7.56 cm in length including free propagation in air symmetrically surrounding the medium of 7.2 cm length.

In contrast to the propagating fields, the spin wave is stationary and only develops in time for any given point in space. It only builds up in the limits of the interaction medium and reaches its maximum during the interaction of all fields. That's why the spin wave can be interpreted as a mediator between the two Λ-systems involved in the simulation. After the interaction, only a residual fraction of $\approx 10\,\%$ of the maximum amplitude of the ground state excitation remains in the medium. In a memory application, a stable plateau of excitation would have built up. In this example, in phase space, the spin wave experiences a phase shift of nearly $1.7\,\pi$.

In Fig. 7.15 (a) and (b) the signal and Stokes input and output fields, as well as the spin wave at the beginning and the end of the FWM process, are given. In its uppermost graph, Fig. 7.15 (c) shows the sinusoidal switching between absorption and amplification of the signal field by scanning the relative phase between control and signal field while keeping all other initial phases fixed. Below, the simultaneous development of the Stokes intensity and the total integrated amplitude of the spin wave left in the ensemble at the end of the simulation are plotted. It is striking that the behaviour of signal and Stokes field are in phase while the oscillations of the spin wave are shifted by $\frac{1}{4}\pi$. This shows that no energy is transferred between the signal and Stokes field, but only between the control field and the signal or Stokes field each. Comparing the final population in the spin wave to the phase-sensitive change of signal and Stokes field, it can be seen that the spin wave is at its mean value for maximum absorption and amplification of the signal and Stokes fields (solid vertical lines). The population in the spin wave reaches its extreme values when no energy is transferred in or out the signal and Stokes fields by seeded FWM (dashed vertical lines). This is confirming its role as mediator and transitional state between the two Λ-systems.

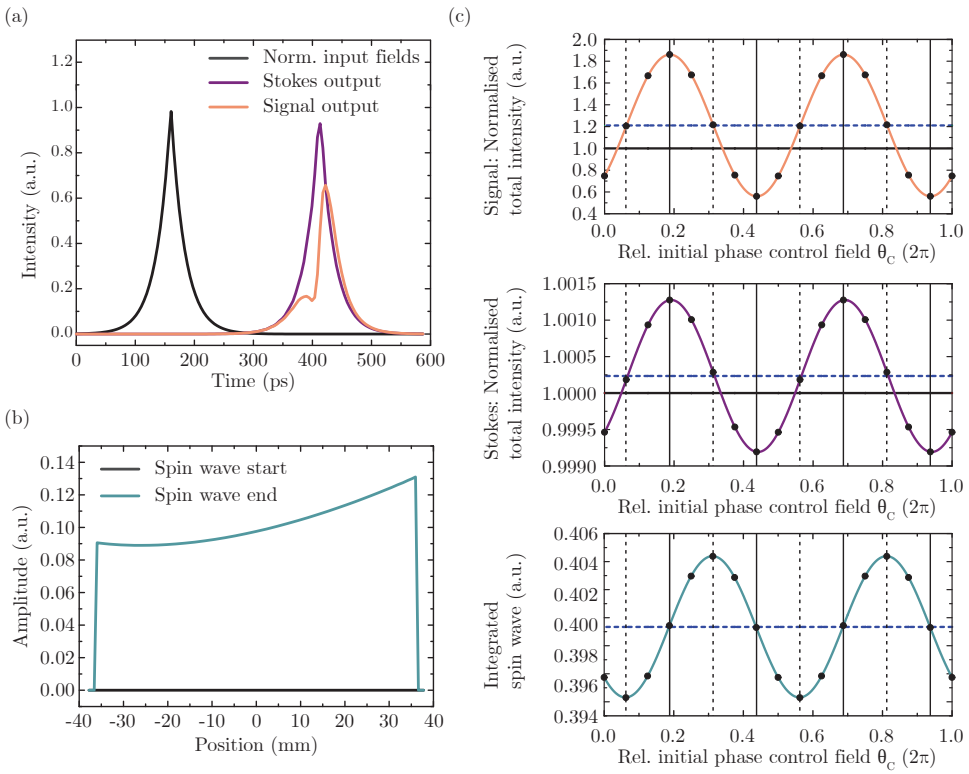


Figure 7.15: (a) Temporally resolved input and output of the Stokes and signal field, normalised to their input field respectively. (b) Spatially resolved spin wave at the beginning and the end of the simulation, normalised to its maximum value during the whole interaction. (c) Signal intensity, Stokes intensity and spin wave at the end of the interaction shown over the relative initial phase of the control field θ_C. Mean values of the oscillations are shown as horizontal dotted blue lines. Phase values corresponding to extrema in the signal and Stokes intensity are indicated by vertical solid black lines, whereas vertical dashed black lines mark phases of mean signal and Stokes intensities and extreme values for the spin wave.

Signal and Stokes fields are proportional to the derivative of the spin wave trajectory over the relative phase of the control field θ_C.

It might be surprising that the mean values of the signal and Stokes field (horizontal blue dotted line) as well as the minimum value of the integrated spin wave differ from 1 and 0 respectively. Seeded FWM can only explain phase-sensitive oscillations but not constant, e.g. phase-insensitive, total amplification of the signal and Stokes field, as well as a phase-insensitive increase of the ground state excitation. Apart from the phase-sensitive

FWM, where a closed parametric scattering route is entirely created by the fields sent into the diamond, the strong control field generates additional radiation at the Stokes and signal frequency by spontaneous Raman scattering on states $|1\rangle$ and $|2\rangle$. Both scattering processes combined form again a closed parametric scattering route. However, as the process is initially not seeded, the phases of the Stokes and signal field adapt automatically for a maximum field generation in this cascaded Raman scattering process[406]. In consequence, a spin wave is always generated in both scattering processes. In Fig. 7.16 the seeded (a) and spontaneous (b) Raman scattering and a mixed FWM process (c) are compared.

Another important aspect to consider in these simulations is the influence of the strength of Stokes and control field on the amount of absorption and amplification of the weak signal field. Fig. 7.17 depicts how the intensity of the signal field depends upon the strength of the Stokes field for two different energies of the control field. The stronger the Stokes field, the stronger the phase-dependent change in intensity between the maximum and minimum intensity of the transmitted signal field and the higher its mean oscillating intensity value. When the seeding Stokes field intensity is increased, a regime can be reached in which the input signal is always amplified. In this regime the spontaneous Raman scattering exceeds the phase-sensitive seeded FWM process. Here, the dependence of spontaneous Raman scattering on the Stokes field arises from a mixture of the pure seeded and pure spontaneous Raman scattering as shown in Fig. 7.16 (c). Only the less detuned scattering process is seeded while the field at the signal wavelength is still generated by spontaneous Raman scattering. The same dependence can be observed for increasing the optical density of the medium, hence increasing the interaction cross section of the Stokes field. Reducing

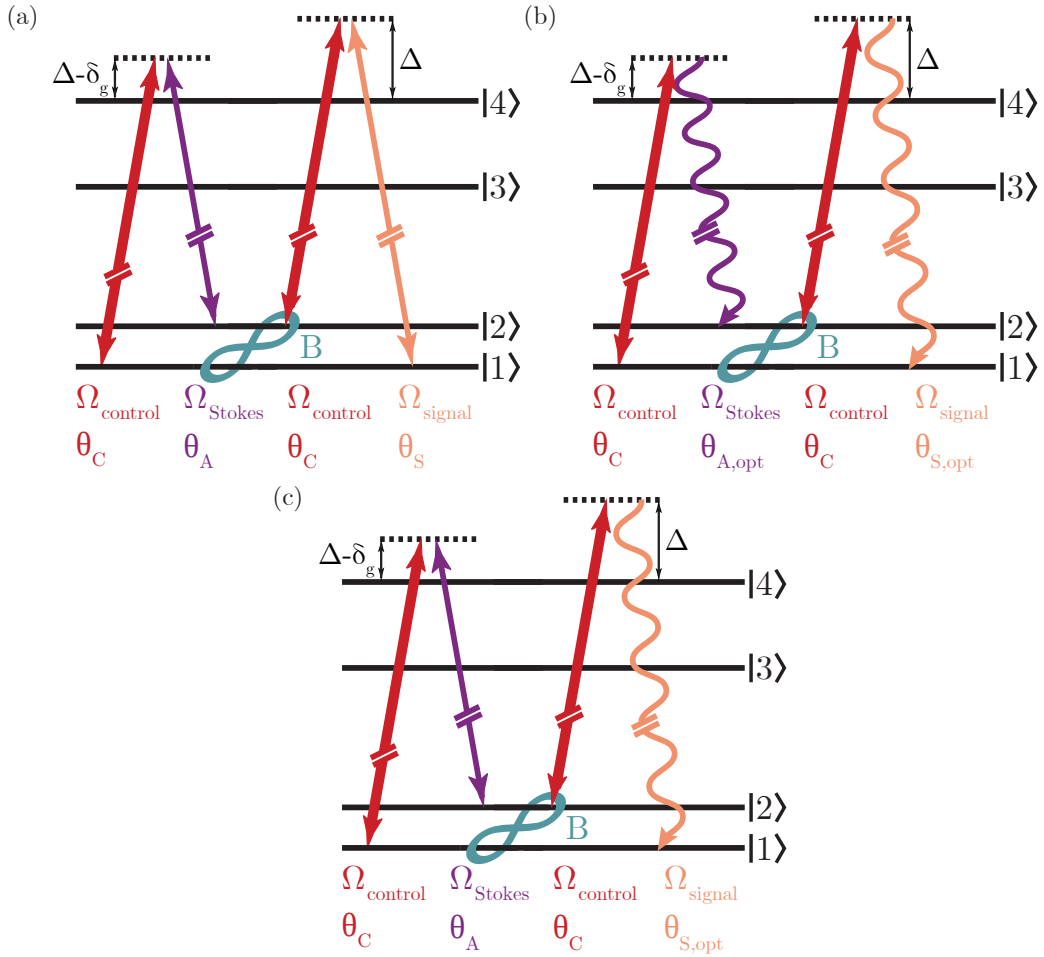


Figure 7.16: Comparison between seeded (a) and spontaneous (b) Raman scattering and (c) FWM processes. (a) The initial phases of all fields (θ_C, θ_A and θ_S) are well defined. A parametric scattering route is created by stimulated Raman scattering. (b) Only the initial phase of the control field θ_C is set. By spontaneous Raman scattering coupling to the ground states $|1\rangle$ and $|2\rangle$ fields at the Stokes and signal wavelength are generated. The phases of those fields ($\theta_{A,\mathrm{opt}}$ and $\theta_{S,\mathrm{opt}}$) adapt automatically for maximum field generation. (c) Mixed double Raman scattering. Only the less detuned Raman scattering process is seeded while radiation at signal frequency is still generated by a spontaneous phase-independent scattering process where its phase adapts automatically.

the energy of the control field diminishes both Raman processes and, in total, stronger absorption can be achieved before a regime of sole amplification is reached again.

Strong absorption and amplification only occurs when the system is seeded by the Stokes field. Excluding the Stokes field from the simulations, no considerable interaction of

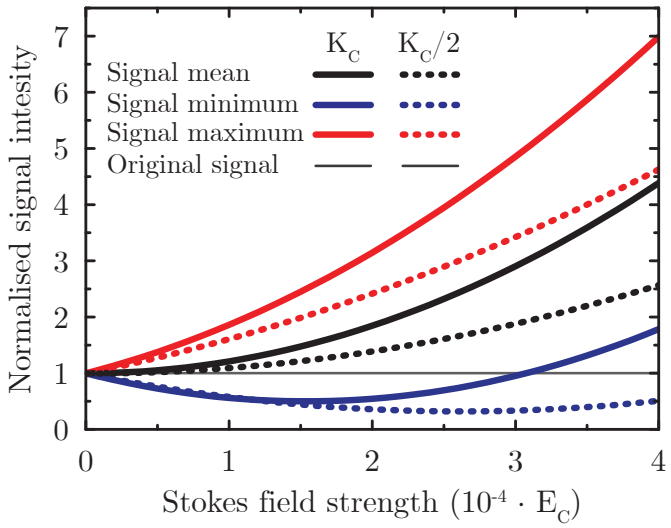


Figure 7.17: Influence of the strength of the Stokes field on the signal field for two different energies of the control field, K_C and $K_C/2$. The strength of the Stokes field is given in multiples of the strength of the control field $E_C \propto \sqrt{K_C}$. While the mean intensity of the signal field increases quadratically the difference between signal minimum and maximum only increases linearly with the strength of the Stokes field. For strong Stokes fields, a regime of sole amplification of the signal field is reached. Reducing the energy of the control field, seeded and spontaneous Raman scattering are reduced. However, a lower signal minimum, i.e. a higher total absorption, can be reached as spontaneous Raman scattering is reduced.

the signal and control fields is observed. This effect is closely related to strong coherent light amplification by electromagnetically induced transparency (EIT) and coherent population trapping (CPT). Rendering an optical transition transparent by applying a strong resonant field resulting in an Autler-Townes splitting and a strong dispersion at the central frequency, the third-order susceptibility $\chi^{(3)}$ is enhanced at the same time and is dominating linear light-matter interactions[172]. This effect has been observed in double-Λ systems of various vapour systems, including helium[398,399], rubidium[407,408], sodium[409] and caesium[410].

For memory experiments, the seeding Stokes field needs to be suppressed to avoid FWM. The resulting loss in interaction strength can be counteracted by increasing the strength of the control field and the optical density of the ensemble (see Section 9.1).

7.5 Summary

In this chapter the negatively charged silicon vacancy centre has been examined in terms of suitability for coherent control, wave mixing and the Raman memory scheme.

An estimation of the ground state coherence time including spin-orbit and Jahn-Teller interactions as well as local strain, based on photoluminescence excitation measurements of the optical linewidth in an ensemble of silicon vacancy centres, led to coherence times of $T_2^* \approx 100\,\mathrm{ps}$ (§7.1). This is two orders of magnitude larger than the coherence time estimated for the neutrally charged nitrogen vacancy centre (§5.7.1) and may be extended by rephasing techniques on the one hand and further by cooling to lower temperatures on the other hand.

For all experiments a Ib low strain, high-pressure-high-temperature diamond substrate with (001) main surfaces was used with a 300 nm thick diamond layer containing an ensemble of negatively charged silicon vacancy centres on top. The sample offers narrow inhomogeneous optical linewidths of $\approx 10\,\mathrm{GHz}$, smaller than the ground state splitting, allowing for ultrafast manipulation of individual optical transitions even without the application of external electric or magnetic fields (§7.2.1).

Inside a cryostat, the ensemble of silicon vacancy centres can be addressed using a confocal set-up. Fluorescence into the phonon sidebands is measured in reflection, laser fields in transmission geometry (§7.2.3). For filtering in the frequency domain a grating based filter set-up with a resolution of $\Delta\nu_{\mathrm{FWHM}} = 6.1(1)\,\mathrm{GHz}$ is used (§7.2.4).

In time-resolved fluorescence measurements the orbital ground state lifetime at a temperature of 5 K has been measured to be $T_1^{orbit} = 27(8)$ ns, setting an upper limit for the coherence time of the ensemble (§7.3.1).

In further experiments, coherent control over the ensemble was demonstrated. The inhomogeneous coherence time between the lower ground and the lower excited state was determined to $T_2^* = 65(8)$ ps by resonant Ramsey interference measurements. This inhomogeneous coherence time was improved to $T_2^{echo} = 187(31)$ ps using an optical Hahn echo sequence (§7.3.2). A model of optical Bloch equations was developed and validated appropriately describing these two measurements (§7.4.1).

As it is more desirable to access the longer-lived ground state coherence for memory applications, the off-resonant two-photon Raman transition was demonstrated by inducing a coherent population transfer between the two orbital ground states of the ensemble (§7.3.3). Implementing a stimulated Raman adiabatic passage, a bidirectional transfer efficiency of $\eta = 48\,\%$ is reached. The transfer efficiency was determined employing the previously validated set of optical Bloch equations.

Having confirmed the possibility of two-photon transitions between the two orbital ground states, the strength of one of the laser fields was reduced, using it as a signal field. A phase-sensitive absorption and amplification of this weak signal field is observed, where the phase-sensitivity arises from off-resonant four-wave mixing processes within the ensemble (§7.3.4). These observations are supported by simulations of seeded four-wave mixing processes using linearised Maxwell-Bloch equations (§7.4.2). A signal, Stokes and control field interact with each other and with a spin wave between the ground states. Underlying processes are identified as seeded and spontaneous Raman scattering.

Chapter 8

Conclusion

In this thesis, the transition from optical Raman quantum memories in vapours towards the realisation of Raman memories in solid-state systems, i.e. in colour centres in diamond, has been prepared and presented.

Colour centres in diamond have been identified as a promising and versatile platform of atomic-like systems in a transparent host material offering a large band gap. As defects, the neutrally charged nitrogen vacancy centre (NV^0) and the negatively charged silicon vacancy centre (SiV^-) were chosen for the implementation of linear and nonlinear light-matter interactions.

On the basis of the neutrally charged nitrogen vacancy centre it was shown that in optical Λ-systems with ground states of same spin but different orbital, strong Raman coupling and high memory efficiencies can be reached even for far off-resonant two-photon transitions. This enables the storage of broadband pulses with a spectral width only limited by the orbital ground state splitting. It was shown, both theoretically and experimentally, that

this memory acceptance bandwidth can be changed as well as that cross-linear polarisation selection rules can be forced upon the system when uniaxial electric fields or stress are applied. The cross-linear polarisation selection rules strongly reduce four-wave mixing processes and limit noise disturbing the storage of signals at the single-photon level. Therefore, a variable acceptance bandwidth and cross-linear polarisation selection rules were identified as further properties a solid-state system for Raman memory applications should offer. Unfortunately, due to short life and coherence times of $T_1 > 370\,\mathrm{ps}$ at $10\,\mathrm{K}$ and $T_2^* \approx 7\,\mathrm{ps}$ at $5.7\,\mathrm{K}$, ensembles of neutrally charged nitrogen vacancy centres are not suitable for memory applications.

Applying external uniaxial stress, the orbital ground state levels were split up to $213(11)\,\mathrm{GHz}$, the theoretically predicted degrees of polarisation for the two optical transitions were confirmed and it was shown that the cross-linear polarisation of the two transition strengthens when the stress is increased. The inability to measure the orbital ground state lifetime in optical pumping experiments suggests an upper bound of 3-4 ns.

A system where a ground state splitting of $\approx 50\,\mathrm{GHz}$ evoked by spin-orbit interactions is present without the application of any additional electric or magnetic fields, is found in the negatively charged silicon vacancy centre. Yet, this splitting of the orbital ground states could be further increased applying external stress. Furthermore, this centre offers well-defined polarisation selection rules for its optical transitions connecting ground states of same spin, but different orbital.

Initially, the orbital ground state lifetime was measured to be $\mathrm{T}_1^{\mathrm{orbit}} = 27(8)\,\mathrm{ns}$. Then, step-by-step, coherent control was gained over an ensemble of silicon vacancy centres. First, the inhomogeneous coherence time between ground and excited states was determined to

be $T_2^* = 65(8)$ ps by Ramsey interference, before, with the Hahn echo sequence, a rephasing technique was implemented, increasing the coherence time by a factor of three and proving the general possibility of reducing inhomogeneous effects of the ensemble. Then, after these single-photon processes, two-photon coherent manipulation was demonstrated targeting the two orbital ground states which will finally serve as the storage states of a Raman memory. Strong two-photon light-matter interaction in an only 300 nm thick ensemble was demonstrated by stimulated Raman adiabatic passage. Transfer efficiencies between the ground states up to $\eta = 48\,\%$ were reached. This presenting a preliminary stage of Raman memory experiments, the laser fields were adapted in power and efficient phase-sensitive absorption and amplification of weak coherent states by strong seeded off-resonant four-wave mixing processes were shown and supported by simulations. Weak coherent signal fields were amplified by $\approx 60\,\%$ and absorbed by $\approx 80\,\%$ dependent on the relative phase between the interacting fields.

Even though the lifetime and inhomogeneous coherence time ($T_2^* \approx 100$ ps) are not very long in comparison to the temporal duration of the pulses applied, successful storage and retrieval of weak coherent fields would be a first proof-of-principle of memory applications with colour centres in diamond potentially enabling compact and scalable devices that can be integrated on photonic chips.

Furthermore, the well understood silicon vacancy centre can serve as model system for other colour centres in diamond which may offer more favourable properties for memory applications (see Section 9.5)). In the following chapter, an outlook on possible ways forward

including the storage of weak coherent pulses, optional memory schemes for noise suppression and other applications of the system are given, before attention is paid to the prospects of other inversion symmetric defects in diamond.

Chapter 9

Outlook

9.1 Storage of weak coherent pulses

Up to now, only strong light-matter interactions via FWM processes were demonstrated. In these mechanisms, when the signal field is absorbed, the energy of this field is largely transferred to the control field. Only a small fraction of the signal field is transferred to the spin wave. In the same way, the Stokes field is partially transferred to the spin wave creating a storage state which contains shares of both signal and Stokes field. Arguing from a memory perspective, the Stokes field is adding noise to the storage state.

Therefore, for a quantum memory, the Stokes field needs to be suppressed for several reasons. First, FWM, seeded by the Stokes field, is a phase-sensitive process. A phase-independent process is to be desired for reducing experimental complexity and ensuring maximum transfer efficiencies for all phase combinations. Second, the main effect of FWM is transferring energy between the participating fields while creation of a spin wave is only a by-product. Most of the signal field is not stored inside the medium but is in direct energy exchange with the control field. Third, when a spin wave is created, it contains parts of the

signal as well as the Stokes field. Stokes and signal field are in direct "rivalry", competing for storage by a limited amount of SiV^- centres. If the stored spin wave was retrieved, the emitted field at the signal frequency would contain energy from both the initial signal and Stokes field. Storage with high fidelity at the single-photon level is not possible under these conditions.

In a future memory experiment, the Stokes field can be suppressed by generating signal and control fields from two distinct laser sources. For this, two synchronously pumped tunable dye lasers (Sirah Lasertechnik, Gropius) are available in the laboratories at Oxford. In comparison to Lorentzian-shaped spectral intensity profiles of pulses generated by etalons, pulses with a spectral intensity shape of a squared hyperbolic secant suppress frequencies in their tails more efficiently. Therefore, the seeded FWM process should be strongly reduced.

Furthermore, simulations have shown that suppressing the Stokes field also diminishes the strength of light-matter interactions as the interaction-enhancing advantages of a seeded closed parametric scattering route described in Subsection 7.4.2 are lost. In order to increase light-matter interactions again, the SiV^- diamond sample used in Chapter 7 is going to be replaced by a diamond sample with dimensions of $(1.4 \times 0.8 \times 0.3)$ mm with a thicker layer of SiV^- centres of about 120 µm FWHM and higher optical density (OD) of the centres. While it was not possible to measure the low OD of the thin ensemble used in Chapter 7, the OD of the thick ensemble was determined to be up to $OD \approx 5$ for the C transition as shown in Fig. 9.1. For OD measurements a narrowband (< 10 MHz rms) Ti:Sapphire ring laser (Sirah Lasertechnik, Matisse TX) was used and frequency tuned over the optical tranisitions A to D. Additionally, this measurement showed an inhomogeneous broadening of ≈ 10 GHz as seen in the PLE measurement of the thin ensemble (Fig. 7.1 (b)).

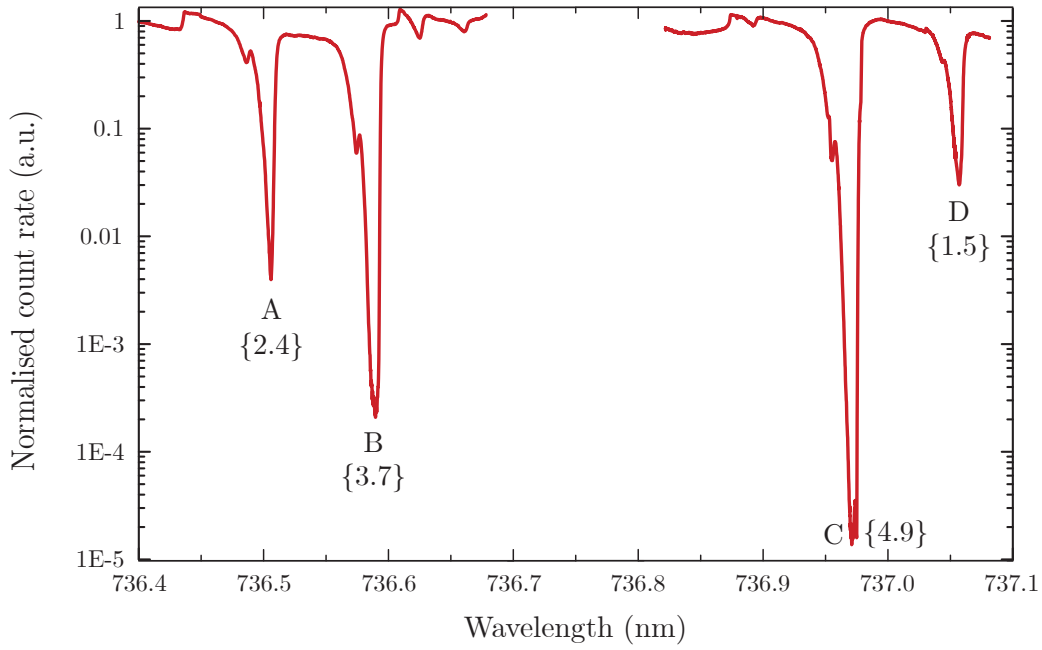


Figure 9.1: Measurement of the optical density (OD) of an ensemble of SiV^- centres in a layer of 120 µm. The full dimensions of the sample are $(1.4 \times 0.8 \times 0.3)$ mm. For each of the optical transitions A to D, its optical density is given in curly brackets.

This can be attributed to a similarly low strain environment in the thick ensemble.

For better suppression of the control field when the signal field is read out, a double-monochromator will be used as filter set-up as shown in Fig. 9.2. While not increasing the resolution of the filter set-up, passing two gratings and a slit in the Fourier plane is suppressing residuals of the control field more efficiently.

The usage of APDs and nanowire detectors, able to deal with the challenging timescale of 100 ps memory lifetimes (see Section 7.1), will enable the temporal resolution of the signal pulse retrieved from the memory.

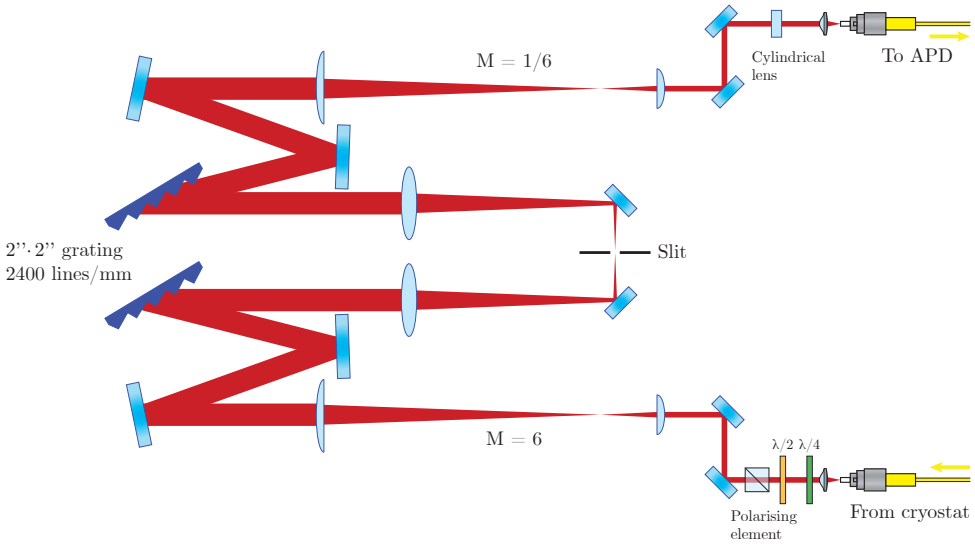


Figure 9.2: Double-monochromator for signal field separation. Two monochromators are placed in series selecting the same colour. The slit in between the mirrored set-ups is used to block unwanted frequencies in the Fourier plane. Whereas the resolution of this set-up is not superior to a single monochromator, stray light is suppressed more efficiently as the targeted frequency is selected twice. The design is inspired by the Czerny-Turner configuration [411]. Lenses are used instead of curved mirrors in order to reduce astigmatism. Before the filtered field is coupled to a fibre again, the difference in divergence between the optical axes is corrected by a cylindrical lens.

Under these conditions, a memory interaction in an ensemble of SiV^- centres may be realised. Signal and control field are sent into the diamond at the same time. In a phase-insensitive but phase-preserving interaction, the signal field is absorbed and transferred into the spin wave as a storage state. After a temporal delay comparable to the estimated ground state coherence time, a second control pulse, identical to the first one, is sent into the diamond retrieving the stored signal field. The control field is suppressed taking advantage of its cross-linear polarisation to the signal field. Furthermore, control and retrieved signal field are separated by the double-monochromator described above. The remaining field will be detected and temporally resolved by the nanowire detector.

Albeit phase-sensitive seeded FWM is suppressed, spontaneous Raman scattering by the control field coupling unintentionally to the lower ground state $|1\rangle$ generates phase-insensitive FWM so that noise uncorrelated to the signal field will be generated. This coupling cannot be suppressed by selection rules in an ensemble of SiV^- centres of all spatial orientations. Therefore, in the following section, different methods of noise suppression are presented.

9.2 Noise suppression

In past experiments of Raman memories in caesium (Cs) vapour (see Subsection 2.2.6), noise was generated by spontaneous Raman scattering and FWM. The strong control field couples unintentionally to the wrong ground state generating a Stokes field or anti-Stokes field according to the specific memory configuration. As opposed to phase-sensitive seeded FWM as described in Subsection 7.3.4, the phase of the Stokes field adapts automatically for maximum Stokes field generation [406].

The amount of noise can be measured by exercising the full memory sequence (read-in and read-out) without the application of a signal field. The intensity read out at the signal frequency is the noise added by spontaneous FWM.

To avoid noise generation, the FWM process needs to be inhibited. This is possible by removing the scattered Stokes field from the closed FWM contour. Several approaches have been developed to do so. For example, rubidium (Rb) vapour offers a double-Λ system with an excited state splitting in the visible regime. In [412] two-photon processes are explained for removing the Stokes field from the system. The energy is shelved in an otherwise non-participating energy level. Alternatively, the Stokes field can be absorbed

resonantly without the application of any additional fields. For this purpose, in SiV^-, the two-photon resonance of signal and control field has to be detuned from the upper excited state by $\Delta = 2 \cdot \delta_g$ as shown in Fig. 9.3. In consequence, the spontaneously generated Stokes field is on resonance with transition A ($|1\rangle - |4\rangle$) and is absorbed as soon as it is created. As the ensemble has been prepared into state $|1\rangle$ by resonant optical pumping, the Stokes field is strongly absorbed by the medium with a high OD. No FWM process can be established and, therefore, no noise is generated. This type of noise-free Raman memory is often unofficially referred to as the "Magic-Λ" memory. The same effect of absorption can be achieved with a two-photon transition red-detuned from the upper excited state by $\Delta = -(\delta_e - 2 \cdot \delta_g)$. In this case, the Stokes field is resonant to transition C ($|1\rangle - |3\rangle$).

In future experiments with an ensemble of SiV^- centres in all possible orientations, this method should allow noise suppression even though cross-linear polarisation selection rules for the optical Raman transitions are nonexistent.

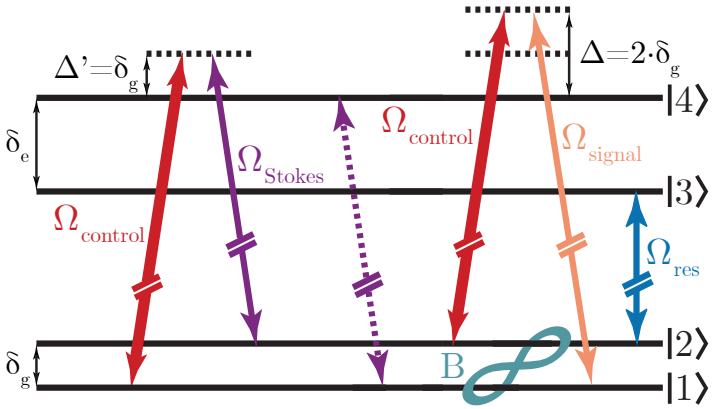


Figure 9.3: Magic-Λ scheme: Signal and control field are blue-detuned from the upper excited state by twice the ground state splitting, $\Delta = 2 \cdot \delta_g$. Therefore, the control field, coupling to ground state $|1\rangle$, generates a Stokes field on a virtual level with a detuning of $\Delta' = \delta_g$ from the excited state $|4\rangle$. The established Stokes field is in resonance with transition A between states $|1\rangle$ and $|4\rangle$ (dashed arrow). It is absorbed by the medium and cannot contribute to the FWM process. Hence, the generation of noise is strongly suppressed.

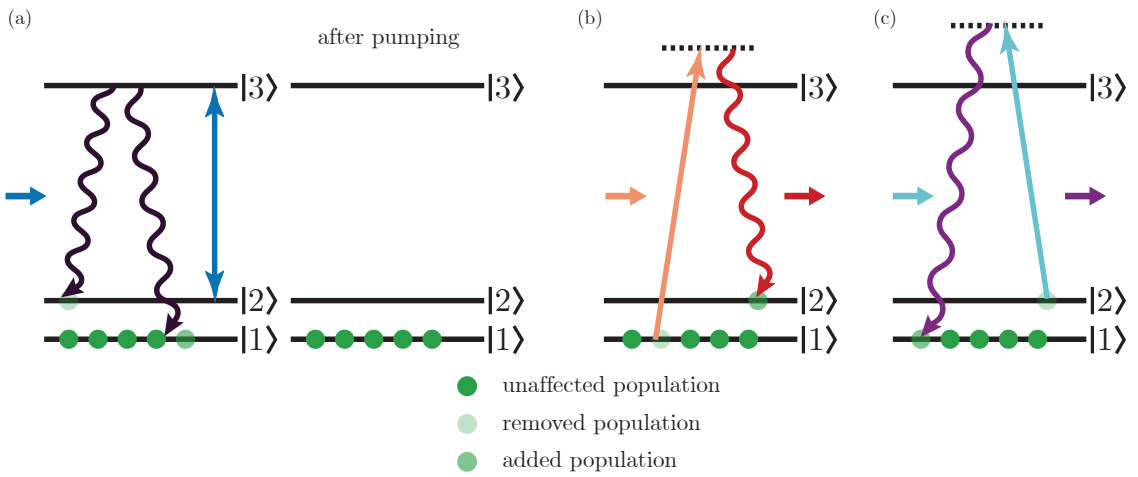


Figure 9.4: DLCZ-memory in a three-level system. Optical fields entering (exiting) the ensemble are indicated by horizontal small arrows in the colour of the respective field on the right (left) side of each level scheme. Fluorescence (a) and scattered ((b), (c)) fields are indicated as sinusoidal arrows, applied laser fields by straight arrows. Different colours are assigned to different wavelengths. Fluorescence from the excited state $|3\rangle$ is given in black. (a) Preparation of the ensemble. A resonant pump field is applied transferring population from state $|2\rangle$ to $|1\rangle$. (b) A laser field blue-detuned to state $|3\rangle$ is scattered in the ensemble. A photon is emitted if population is transferred to the storage state $|2\rangle$. (c) The stored state is read out applying a laser field coupling to state $|2\rangle$, triggering the emission of a photon.

9.3 DLCZ memory

As a preliminary step to a Raman memory, Raman scattering in ensembles of SiV^- centres may be observed. Assuming Raman scattering blue-detuned from transition A, population will be transferred from state $|1\rangle$ to $|2\rangle$ creating a Duan-Lukin-Cirac-Zoller (DLCZ) memory[129], as shown in Fig. 9.4. A successful storage process, i.e. population transfer, is confirmed when a photon at the Stokes frequency is detected. Applying a readout field coupling to the storage state, the information is retrieved and the stored field can be detected at the anti-Stokes frequency. Even though no preexisting signal field is stored in this memory scheme and the field read-out is of variable frequency, not necessarily identical to any other field sent into or scattered by the system, it is possible to measure the ground state coherence time with this experimentally less complex and simplified scheme (in comparison

to a full Raman memory protocol).

At this point, experiments at the single photon level are conceivable. Periodically poled potassium titanyl phosphate (PPKTP) waveguides pumped at 388 nm offer single photons at 737 nm generated by a spontaneous parametric down-conversion (SPDC) process.

9.4 Nonlinear interaction

Apart from quantum memory schemes, integrated devices with strong light-matter interactions are also desirable for single-photon nonlinearities enabling single-photon switches[413,414] or single photon phase gates[112,114,415].

As mentioned in the introduction (see Section 1.3), strong cross-phase modulation is possible within a double-Λ medium[114]. The SiV^- centre with its four-level structure (see Subsection 3.2.6) could provide ideal conditions for photon-photon cross-phase modulation by means of FWM. In Subsection 7.3.4 phase-sensitive FWM has already been demonstrated and although phase shifts have not been measured within the context of this thesis, simulations (see Fig. 7.14 in Subsection 7.4.2) show phase shifts of both signal and Stokes fields, which have to be determined in future experiments. However, as in other nonlinear schemes based on the Kerr-effect (see Section 1.3), strong phase shifts are accompanied by phase-dependent loss or gain which leads to a reduced fidelity on the single photon level[114].

In this context, colour centres in diamond would enable strong light-matter interaction in a compact and scalable system.

9.5 Further inversion symmetric defects in diamond

The experiments presented in this thesis form the foundation for similar work using other defects in diamond, such as germanium vacancy (GeV^-)[416–418], tin vacancy (SnV^-)[419,420] or nickel vacancy (NiV)[421] ensembles. These colour centres may combine the outstanding spectral properties already seen in SiV^- with even larger ground state splittings due to enhanced spin-spin and spin-orbit interactions[419].

While larger implanted atoms lead to a stronger deformation and disturbance of the diamond lattice, it seems that the ratio of the inhomogeneous broadening to the ground state splitting, $\Delta_{\mathrm{inh}}/\delta_g$, stays constant and may even be further reduced using CVD techniques diminishing strain in the diamond lattice. Apart from this ratio, Table 9.1 compares basic properties of Group-IV colour centres, including the wavelength of the ZPL, the ground and excited orbital state splitting and the measured inhomogeneous broadening at cryogenic temperatures. All centres of this group show an inversion symmetric D_{3d} symmetry. A detailed theoretical comparison of the magneto-optical properties of Group-IV colour centres can be found in [422]. While the frequency of the ZPL of Group-IV colour centres can be predicted reliably with deviations of less than 10% by first-principles density functional theory calculations[423], the mismatch between theoretically predicted and measured ground state splittings at 4 Kelvin is significant (factor of three)[423]. The most current development is the investigation of the lead vacancy centre (PbV^-)[423]. Still, the orbital excited state splitting of PbV^- could not be measured yet due to limitations of the set-up[423]. However, a large mismatch to the theoretical value given in Table 9.1 can be expected.

For memory applications, an increased ground state splitting not only enables larger memory bandwidths, but also facilitates to freeze out phonons reducing the phonon mediated ground state decay. To reach long spin coherence times, temperatures can be chosen such that $k_B T \ll \hbar\delta_g$ (see equation (3.7)). For example, in SnV^-, due to the large ground state splitting, phonon-mediated transitions are strongly suppressed, so that long spin coherence times in the millisecond regime are expected at cryogenic temperatures close to 4 K [419].

Apart from these Group-IV vacancy colour centres, other groups of colour centres as mentioned in Chapter 3.2 may be of interest. One of those are nickel vacancy centres and nickel related complexes with a multitude of charge states and configurations within the diamond lattice [421,424,425]. Future efforts must include to develop reproducible techniques to fabricate ensembles and single centres with a narrow inhomogeneous broadening and to determine the centres' symmetry group, quantum efficiency, DWF, orbital state splittings, as well as their life and coherence times.

Albeit the SiV^- centre has served in this thesis as a model system for proof-of-principle experiments and has developed to a well-known colour centre in diamond within recent years, one of the centres mentioned in this chapter might be more suitable for quantum memories and their applications. However, these are still in an early phase of investigation.

Colour centre	Symmetry group	λ_{ZPL} [nm]	δ_g [GHz]	δ_e [GHz]	Δ_{inh} [GHz]	$\Delta_{\mathrm{inh}}/\delta_g$
SiV^- [328]	D_{3d}	737	48 @ 5 K	257 @ 5 K	10 @ 5 K	0.208
GeV^- [416,426]	D_{3d}	602	169 @ 10 K	1112 @ 10 K	24-97 @ 10 K	0.142-0.574
SnV^- [419]	D_{3d}	619	850 @ 4 K	3000 @ 4 K	155 @ 4 K	0.182
PbV^- [422,423]	D_{3d}	520	2000 @ 4 K 6142 *	70605 *	376 @ 4 K †	0.188

Table 9.1: Characteristics of Group-IV colour centres. λ_{ZPL}: ZPL wavelength, δ_g: Ground state splitting, δ_e: Excited state splitting, Δ_{inh}: Inhomogeneous broadening. $\star$: theoretical prediction, †: arithmetic mean.

Bibliography

[1] Hecht, E. *Optics* (Pearson Education Limited, Harlow, England, 2017), 5th edn.

[2] Loudon, R. *The Quantum Theory of Light* (Oxford University Press, Oxford, 2000), 3rd edn.

[3] Einstein, A., Podolsky, B. & Rosen, N. Can quantum-mechanical description of physical reality be considered complete? *Physical Review* **47**, 777–780 (1935).

[4] Bell, J. S. The Einstein Podolsky Rosen Paradox and Local HiddenVariables Theories. *Physics* **1**, 195–200 (1964).

[5] O'Brien, J. L., Furusawa, A. & Vučković, J. Photonic quantum technologies. *Nature Photonics* **3**, 687–695 (2009).

[6] Kok, P. Photonic quantum information processing. *Contemporary Physics* **57**, 526–544 (2016).

[7] Dumke, R. *et al.* Roadmap on quantum optical systems. *Journal of Optics* **18**, 093001 (2016).

[8] Acín, A. *et al.* The quantum technologies roadmap : a European community view. *New Journal of Physics* **20**, 080201 (2018).

[9] Flamini, F., Spagnolo, N. & Sciarrino, F. Photonic quantum information processing: a review (2018). `arXiv:1803.02790`.

[10] Nielsen, M. A. & Chuang, I. L. *Quantum Computation and Quantum Information* (Cambridge University Press, Cambridge, 2010), 10th anniversary edn.

[11] Manousakis, E. *Practical Quantum Mechanics: Modern Tools and Applications* (Oxford University Press, Oxford, 2015).

[12] Berry, D. W., Lvovsky, A. I. & Sanders, B. C. Interconvertibility of single-rail optical qubits. *Optics Letters* **31**, 107–109 (2006).

[13] Kok, P., Munro, W. J., Nemoto, K., Ralph, T. C., Dowling, J. P. & Milburn, G. J. Linear optical quantum computing with photonic qubits. *Reviews of Modern Physics* **79**, 135–174 (2007).

[14] Humphreys, P. C. *et al.* Linear optical quantum computing in a single spatial mode. *Physical Review Letters* **111**, 150501 (2013).

[15] A. G. Fisher, K., England, D. G., MacLean, J. P. W., Bustard, P. J., Heshami, K., Resch, K. J. & Sussman, B. J. Storage of polarization-entangled THz-bandwidth photons in a diamond quantum memory. *Physical Review A* **96**, 012324 (2017).

[16] Lukens, J. M. & Lougovski, P. Frequency-encoded photonic qubits for scalable quantum information processing. *Optica* **4**, 8–16 (2016).

[17] Brecht, B., Reddy, D. V., Silberhorn, C. & Raymer, M. G. Photon temporal modes: A complete framework for quantum information science. *Physical Review X* **5**, 041017 (2015).

[18] Kupchak, C., Bustard, P. J., Heshami, K., Erskine, J., Spanner, M., England, D. G. & Sussman, B. J. Time-bin-to-polarization conversion of ultrafast photonic qubits. *Physical Review A* **96**, 053812 (2017).

[19] Donohue, J. M., Agnew, M., Lavoie, J. & Resch, K. J. Coherent ultrafast measurement of time-bin encoded photons. *Physical Review Letters* **111**, 1–5 (2013).

[20] Donohue, J. M., Lavoie, J. & Resch, K. J. Ultrafast time-division demultiplexing of polarization-entangled photons. *Physical Review Letters* **113**, 163602 (2014).

[21] Cirac, J. I., Zoller, P., Kimble, H. J. & Mabuchi, H. Quantum State Transfer and Entanglement Distribution among Distant Nodes in a Quantum Network. *Physical Review Letters* **78**, 3221–3224 (1997).

[22] Duan, L. M. & Kimble, H. J. Scalable photonic quantum computation through cavity-assisted interactions. *Physical Review Letters* **92**, 127902 (2004).

[23] Specht, H. P., Nölleke, C., Reiserer, A., Uphoff, M., Figueroa, E., Ritter, S. & Rempe, G. A single-atom quantum memory. *Nature* **473**, 190–193 (2011).

[24] Simon, J., Tanji, H., Thompson, J. K. & Vuletić, V. Interfacing collective atomic excitations and single photons. *Physical Review Letters* **98**, 183601 (2007).

[25] Afzelius, M. & Simon, C. Impedance-matched cavity quantum memory. *Physical Review A* **82**, 022310 (2010).

[26] Bao, X. H. *et al.* Efficient and long-lived quantum memory with cold atoms inside a ring cavity. *Nature Physics* **8**, 517–521 (2012).

[27] Sabooni, M., Tornibue Kometa, S., Thuresson, A., Kröll, S. & Rippe, L. Cavity-enhanced storage - Preparing for high-efficiency quantum memories. *New Journal of Physics* **15**, 035025 (2013).

[28] Sparkes, B. M. *et al.* Gradient echo memory in an ultra-high optical depth cold atomic ensemble. *New Journal of Physics* **15**, 085027 (2013).

[29] Chen, Y. H., Lee, M. J., Wang, I. C., Du, S., Chen, Y. F., Chen, Y. C. & Yu, I. A. Coherent optical memory with high storage efficiency and large fractional delay. *Physical Review Letters* **110**, 083601 (2013).

[30] Cho, Y. W. *et al.* Highly efficient optical quantum memory with long coherence time in cold atoms. *Optica* **3**, 100–107 (2016).

[31] Michelberger, P. S. *et al.* Interfacing GHz-bandwidth heralded single photons with a room-temperature Raman quantum memory. *New Journal of Physics* **17**, 043006 (2015).

[32] Kaczmarek, K. T. *et al.* Ultrahigh and persistent optical depths of caesium in Kagom\'e-type hollow-core photonic crystal fibres. *Optics Letters* **40**, 5582–5585 (2015).

[33] Finkelstein, R., Poem, E., Michel, O., Lahad, O. & Firstenberg, O. Fast, noise-free memory for photon synchronization at room temperature. *Science Advances* **4**, eaap8598 (2018).

[34] Babinec, T. M., Choy, J. T., Smith, K. J. M., Khan, M. & Lončar, M. Design and focused ion beam fabrication of single crystal diamond nanobeam cavities. *Journal of Vacuum Science & Technology B, Nanotechnology and Microelectronics: Materials, Processing, Measurement, and Phenomena* **29**, 010601 (2011).

[35] Bayn, I. *et al.* Processing of photonic crystal nanocavity for quantum information in diamond. *Diamond and Related Materials* **20**, 937–943 (2011).

[36] Riedrich-Möller, J. *et al.* One-and two-dimensional photonic crystal microcavities in single crystal diamond. *Nature Nanotechnology* **7**, 69–74 (2012).

[37] Budker, D. & Romalis, M. V. Optical Magnetometry. *Nature Physics* **3**, 227–234 (2007).

[38] Taylor, J. M. *et al.* High-sensitivity diamond magnetometer with nanoscale resolution. *Nature Physics* **4**, 810–816 (2008).

[39] Acosta, V. M. *et al.* Diamonds with a high density of nitrogen-vacancy centers for magnetometry applications. *Physical Review B - Condensed Matter and Materials Physics* **80**, 115202 (2009).

[40] Balasubramanian, G. *et al.* Ultralong spin coherence time in isotopically engineered diamond. *Nature Materials* **8**, 383–387 (2009).

[41] Dolde, F. *et al.* Electric-field sensing using single diamond spins. *Nat Phys* **7**, 459–463 (2011).

[42] Acosta, V. M., Jensen, K., Santori, C., Budker, D. & Beausoleil, R. G. Electromagnetically induced transparency in a diamond spin ensemble enables all-optical electromagnetic field sensing. *Physical Review Letters* **110**, 213605 (2013).

[43] Neumann, P. *et al.* High-precision nanoscale temperature sensing using single defects in diamond. *Nano Letters* **13**, 2738–2742 (2013).

[44] Toyli, D. M., de las Casas, C. F., Christle, D. J., Dobrovitski, V. V. & Awschalom, D. D. Fluorescence thermometry enhanced by the quantum coherence of single spins in diamond. *Proceedings of the National Academy of Sciences* **110**, 8417–8421 (2013).

[45] Clevenson, H., Trusheim, M. E., Teale, C., Schröder, T., Braje, D. & Englund, D. Broadband magnetometry and temperature sensing with a light-trapping diamond waveguide. *Nature Physics* **11**, 393–397 (2015).

[46] Appel, J., Windpassinger, P. J., Oblak, D., Hoff, U. B., Kjaergaard, N. & Polzik, E. S. Mesoscopic atomic entanglement for precision measurements beyond the standard quantum limit. *Proceedings of the National Academy of Sciences of the United States of America* **106**, 10960–10965 (2009).

[47] Chou, C. W., Hume, D. B., Koelemeij, J. C., Wineland, D. J. & Rosenband, T. Frequency comparison of two high-accuracy Al+ optical clocks. *Physical Review Letters* **104**, 070802 (2010).

[48] Dudin, Y. O., Li, L. & Kuzmich, A. Light storage on the time scale of a minute. *Physical Review A - Atomic, Molecular, and Optical Physics* **87**, 031801(R) (2013).

[49] Bloom, B. J. *et al.* An optical lattice clock with accuracy and stability at the 10^{-18} level. *Nature* **506**, 71–75 (2014).

[50] Giovannetti, V., Lloyd, S. & MacCone, L. Advances in quantum metrology. *Nature Photonics* **5**, 222–229 (2011).

[51] Zhou, J. W. *et al.* Quantum information processing and metrology with color centers in diamonds. *Frontiers of Physics* **9**, 587–597 (2014).

[52] Williamson, L. A., Chen, Y.-H. & Longdell, J. J. Magneto-Optic Modulator with Unit Quantum Efficiency. *Physical Review Letters* **113**, 203601 (2014).

[53] Blum, S., O'Brien, C., Lauk, N., Bushev, P., Fleischhauer, M. & Morigi, G. Interfacing microwave qubits and optical photons via spin ensembles. *Physical Review A - Atomic, Molecular, and Optical Physics* **91**, 033834 (2015).

[54] Li, Q., Bao, Y., Thuresson, A., Nilsson, A. N., Rippe, L. & Kröll, S. Slow-light-based optical frequency shifter. *Physical Review A* **93**, 043832 (2016).

[55] Bustard, P. J., England, D. G., Heshami, K., Kupchak, C. & Sussman, B. J. Quantum frequency conversion with ultra-broadband tuning in a Raman memory. *Physical Review A* **95**, 053816 (2017).

[56] Chang, D. E., Vuletić, V. & Lukin, M. D. Quantum nonlinear optics - Photon by photon. *Nature Photonics* **8**, 685–694 (2014).

[57] Distante, E., Farrera, P., Padrón-Brito, A., Paredes-Barato, D., Heinze, G. & De Riedmatten, H. Storing single photons emitted by a quantum memory on a highly excited Rydberg state. *Nature Communications* **8**, 14072 (2017).

[58] Pittman, T. B., Jacobs, B. C. & Franson, J. D. Single photons on pseudodemand from stored parametric down-conversion. *Physical Review A - Atomic, Molecular, and Optical Physics* **66**, 042303 (2002).

[59] Chen, S., Chen, Y. A., Strassel, T., Yuan, Z. S., Zhao, B., Schmiedmayer, J. & Pan, J. W. Deterministic and storable single-photon source based on a quantum memory. *Physical Review Letters* **97**, 173004 (2006).

[60] Simon, C. *et al.* Quantum memories. A review based on the European integrated project "Qubit Applications (QAP)". *European Physical Journal D* **58**, 1–22 (2010).

[61] Mower, J. & Englund, D. Efficient generation of single and entangled photons on a silicon photonic integrated chip. *Physical Review A* **84**, 052326 (2011).

[62] Jennewein, T., Barbieri, M. & White, A. G. Single-photon device requirements for operating linear optics quantum computing outside the post-selection basis. *Journal of Modern Optics* **58**, 276–287 (2011).

[63] Christ, A. & Silberhorn, C. Limits on the deterministic creation of pure single-photon states using parametric down-conversion. *Physical Review A - Atomic, Molecular, and Optical Physics* **85**, 023829 (2012).

[64] Takeuchi, S. 2014 Recent progress in single-photon and entangled-photon generation and applications. *Japanese Journal of Applied Physics* **53**, 030101 (2014).

[65] Laiho, K., Cassemiro, K. N. & Silberhorn, C. Producing high fidelity single photons with optimal brightness via waveguided parametric down-conversion. *Optics express* **17**, 22823–37 (2009).

[66] Raussendorf, R. & Briegel, H. J. A one-way quantum computer. *Physical Review Letters* **86**, 5188 (2001).

[67] Raussendorf, R., Browne, D. E. & Briegel, H. J. Measurement-based quantum computation on cluster states. *Physical Review A - Atomic, Molecular, and Optical Physics* **68**, 022312 (2003).

[68] Browne, D. E. & Rudolph, T. Resource-efficient linear optical quantum computation. *Physical Review Letters* **95**, 010501 (2005).

[69] Bodiya, T. P. & Duan, L. M. Scalable generation of graph-state entanglement through realistic linear optics. *Physical Review Letters* **97**, 143601 (2006).

[70] Humphreys, P. C., Kolthammer, W. S., Nunn, J., Barbieri, M., Datta, A. & Walmsley, I. A. Continuous-variable quantum computing in optical time-frequency modes using quantum memories. *Physical Review Letters* **113**, 130502 (2014).

[71] Heshami, K., England, D. G., Humphreys, P. C., Bustard, P. J., Acosta, V. M., Nunn, J. & Sussman, B. J. Quantum memories: emerging applications and recent advances. *Journal of Modern Optics* **63**, 2005–2028 (2016).

[72] Yao, X. C. *et al.* Observation of eight-photon entanglement. *Nature Photonics* **6**, 225–228 (2012).

[73] Migdall, A. L., Branning, D. & Castelletto, S. Tailoring single-photon and multiphoton probabilities of a single-photon on-demand source. *Physical Review A - Atomic, Molecular, and Optical Physics* **66**, 053805 (2002).

[74] Ma, X. S., Zotter, S., Kofler, J., Jennewein, T. & Zeilinger, A. Experimental generation of single photons via active multiplexing. *Physical Review A - Atomic, Molecular, and Optical Physics* **83**, 043814 (2011).

[75] Nunn, J. *et al.* Enhancing multiphoton rates with quantum memories. *Physical Review Letters* **110**, 133601 (2013).

[76] Pang, X.-L. *et al.* A Hybrid Quantum Memory Enabled Network at Room Temperature (2018). arXiv:1803.07122.

[77] Bennett, C. H. & DiVincenzo, D. P. Quantum Information and Computation. *Nature* **404**, 247–255 (2000).

[78] Deutsch, D. Quantum theory, the church–turing principle and the universal quantum computer. *Proceedings of the Royal Society of London A: Mathematical, Physical and Engineering Sciences* **400**, 97–117 (1985).

[79] Shor, P. Algorithms for quantum computation: discrete logarithms and factoring. In *Proceedings, 35th Annual Symposium on Foundations of Computer Science* (IEEE Press, Los Alamitos, CA, 1994).

[80] Shor, P. W. Polynomial-Time Algorithms for Prime Factorization and Discrete Logarithms on a Quantum Computer. *SIAM Journal on Computing* **26**, 1484–1509 (1995).

[81] Grover, L. K. A fast quantum mechanical algorithm for database search. In *Proceedings of the twenty-eighth annual ACM symposium on Theory of computing - STOC '96*, 212–219 (1996).

[82] Grover, L. K. Quantum mechanics helps in searching for a needle in a haystack. *Physical Review Letters* **79**, 325–328 (1997).

[83] Feynman, R. P. Simulating physics with computers. *International Journal of Theoretical Physics* **21**, 467–488 (1982).

[84] Lloyd, S. Universal Quantum Simulators. *Science* **273**, 1073–1078 (1996).

[85] Wineland, D. J. *et al.* Quantum Information Processing with Trapped Ions. *Philosophical Transactions of the Royal Society A* **361**, 1349–1361 (2003).

[86] Blatt, R. & Wineland, D. Entangled states of trapped atomic ions. *Nature* **453**, 1008–1015 (2008).

[87] Roos, C. Quantum Information Processing with Trapped Ions. In Quint, W. & Vogel, M. (eds.) *Fundamental Physics in Particle Traps*, vol. 256, chap. 8, 253–291 (Springer Berlin Heidelberg, Berlin, Heidelberg, 2014).

[88] Imamoglu, A., Awschalom, D. D., Burkard, G., DiVincenzo, D. P., Loss, D., Sherwin, M. & Small, A. Quantum information processing using quantum dot spins and cavity QED. *Physical Review Letters* **83**, 4204–4207 (1999).

[89] Press, D., Ladd, T. D., Zhang, B. & Yamamoto, Y. Complete quantum control of a single quantum dot spin using ultrafast optical pulses. *Nature* **456**, 218–221 (2008).

[90] Vandersypen, L. M. K., Steffen, M., Breyta, G., Yannoni, C. S., Sherwood, M. H. & Chuang, I. L. Experimental realization of Shor's quantum factoring algorithm using nuclear magnetic resonance. *Nature* **414**, 883–887 (2001).

[91] Suter, D. & Mahesh, T. S. Spins as qubits: Quantum information processing by nuclear magnetic resonance. *Journal of Chemical Physics* **128**, 052206 (2008).

[92] Nakamura, Y., Pashkin, Y. A. & Tsai, J. S. Coherent control of macroscopic quantum states in a single-Cooper-pair box. *Nature* **398**, 786–788 (1999).

[93] Makhlin, Y., Schön, G. & Shnirman, A. Josephson-junction qubits with controlled couplings. *Nature* **398**, 305–307 (1999).

[94] Wendin, G. Quantum information processing with superconducting circuits: a review. *Reports on Progress in Physics* **80**, 106001 (2017).

[95] Wrachtrup, J. & Jelezko, F. Processing quantum information in diamond. *Journal of Physics Condensed Matter* **18**, S807 (2006).

[96] Stoneham, A. M., Harker, A. H. & Morley, G. W. Could one make a diamond-based quantum computer? *Journal of Physics: Condensed Matter* **21**, 364222 (2009).

[97] Ladd, T. D., Jelezko, F., Laflamme, R., Nakamura, Y., Monroe, C. & O'Brien, J. L. Quantum computers. *Nature* **464**, 45–53 (2010).

[98] Togan, E. *et al.* Quantum entanglement between an optical photon and a solid-state spin qubit. *Nature* **466**, 730–734 (2010).

[99] Weber, J. R., Koehl, W. F., Varley, J. B., Janotti, A., Buckley, B. B., Van de Walle, C. G. & Awschalom, D. D. Quantum computing with defects. *Proceedings of the National Academy of Sciences* **107**, 8513–8518 (2010).

[100] Liu, G.-Q. & Pan, X.-Y. Quantum information processing with nitrogenvacancy centers in diamond. *Chinese Physics B* **27**, 020304 (2018).

[101] Imoto, N., Haus, H. A. & Yamamoto, Y. Quantum nondemolition measurement of the photon number via the optical Kerr effect. *Physical Review A* **32**, 2287–2292 (1985).

[102] Milburn, G. J. Quantum optical Fredkin gate. *Physical Review Letters* **62**, 2124–2127 (1989).

[103] Chuang, I. L. & Yamamoto, Y. Simple quantum computer. *Physical Review A* **52**, 3489–3496 (1995).

[104] Kerr, J. XL. A new relation between electricity and light: Dielectrified media birefringent. *The London, Edinburgh, and Dublin Philosophical Magazine and Journal of Science* **50**, 337–348 (1875).

[105] Kerr, J. LIV. A new relation between electricity and light: Dielectrified media birefringent (Second paper). *The London, Edinburgh, and Dublin Philosophical Magazine and Journal of Science* **50**, 446–458 (1875).

[106] Boyd, R. W. *Nonlinear Optics* (Academic Press, Amsterdam, Boston, Heidelberg, London, New York, Oxford, Paris, San Diego, San Francisco, Singapore, Sydney, Tokyo, 2008), 3rd edn.

[107] Kok, P., Lee, H. & Dowling, J. P. Single-photon quantum-nondemolition detectors constructed with linear optics and projective measurements. *Physical Review A - Atomic, Molecular, and Optical Physics* **66**, 063814 (2002).

[108] Fleischhauer, M., Imamoglu, A. & Marangos, J. P. Electromagnetically induced transparency: Optics in coherent media. *Reviews of Modern Physics* **77**, 633–673 (2005).

[109] Saffman, M., Walker, T. G. & Mø lmer, K. Quantum information with Rydberg atoms. *Reviews of Modern Physics* **82**, 2313–2363 (2010).

[110] Gorshkov, A. V., Otterbach, J., Fleischhauer, M., Pohl, T. & Lukin, M. D. Photon-photon interactions via Rydberg blockade. *Physical Review Letters* **107**, 133602 (2011).

[111] Firstenberg, O., Peyronel, T., Liang, Q. Y., Gorshkov, A. V., Lukin, M. D. & Vuletić, V. Attractive photons in a quantum nonlinear medium. *Nature* **502**, 71–75 (2013).

[112] Tiarks, D., Schmidt, S., Rempe, G. & Dürr, S. Optical phase shift created with a single-photon pulse. *Science Advances* **2**, e1600036 (2016).

[113] Shapiro, J. H. Single-photon Kerr nonlinearities do not help quantum computation. *Physical Review A - Atomic, Molecular, and Optical Physics* **73**, 062305 (2006).

[114] Liu, Z.-Y. *et al.* Large cross-phase modulations at the few-photon level. *Phys. Rev. Lett.* **117**, 203601 (2016).

[115] Knill, E., Laflamme, R. & Milburn, G. J. A scheme for efficient quantum computation with linear optics. *Nature* **409**, 46–52 (2001).

[116] Li, Y., Humphreys, P. C., Mendoza, G. J. & Benjamin, S. C. Resource costs for fault-tolerant linear optical quantum computing. *Physical Review X* **5**, 041007 (2015).

[117] Sangouard, N., Simon, C., De Riedmatten, H. & Gisin, N. Quantum repeaters based on atomic ensembles and linear optics. *Reviews of Modern Physics* **83**, 33–80 (2011).

[118] Gisin, N., Ribordy, G., Tittel, W. & Zbinden, H. Quantum cryptography. *Reviews of Modern Physics* **74**, 145–195 (2002).

[119] Sasaki, M. Quantum networks: where should we be heading? *Quantum Science and Technology* **2**, 020501 (2017).

[120] Kimble, H. J. The quantum internet. *Nature* **453**, 1023–1030 (2008).

[121] Bennett, C. H. & Brassard, G. Quantum cryptography: Public key distribution and coin tossing. *Theoretical Computer Science* **560**, 7–11 (2014).

[122] Ekert, A. K. Quantum cryptography based on Bells theorem. *Physical Review Letters* **67**, 661–663 (1991).

[123] Corning Incorporated. Corning® SMF-28® Optical Fiber. Tech. Rep., Corning Incorporated, Corning, NY, USA (2002).

[124] Crisp, J. & Elliott, B. *Introduction to Fiber Optics* (Elsevier Science, Oxford, 2005), 3rd edn.

[125] Wootters, W. K. & Zurek, W. H. A single quantum cannot be cloned. *Nature* **299**, 802–803 (1982).

[126] Briegel, H. J., Dür, W., Cirac, J. I. & Zoller, P. Quantum repeaters: The role of imperfect local operations in quantum communication. *Physical Review Letters* **81**, 5932–5935 (1998).

[127] Zukowski, M., Zeilinger, A., Horne, M. A. & Ekert, A. K. "Event-ready-detectors" Bell experiment via entanglement swapping. *Physical Review Letters* **71**, 4287–4290 (1993).

[128] Bussières, F., Sangouard, N., Afzelius, M., De Riedmatten, H., Simon, C. & Tittel, W. Prospective applications of optical quantum memories. *Journal of Modern Optics* **60**, 1519–1537 (2013).

[129] Duan, L. M., Lukin, M. D., Cirac, J. I. & Zoller, P. Long-distance quantum communication with atomic ensembles and linear optics. *Nature* **414**, 413–418 (2001).

[130] J. Nunn. Viewpoint: A Solid Footing for a Quantum Repeater. *Physics* **10**, 55 (2017).

[131] Bose, S., Knight, P. L., Plenio, M. B. & Vedral, V. Proposal for teleportation of an atomic state via cavity decay. *Physical Review Letters* **83**, 5158–5161 (1999).

[132] Cabrillo, C., Cirac, J. I., García-Fernández, P. & Zoller, P. Creation of entangled states of distant atoms by interference. *Physical Review A - Atomic, Molecular, and Optical Physics* **59**, 1025–1033 (1999).

[133] Simon, C., De Riedmatten, H., Afzelius, M., Sangouard, N., Zbinden, H. & Gisin, N. Quantum repeaters with photon pair sources and multimode memories. *Physical Review Letters* **98**, 190503 (2007).

[134] Sangouard, N., Simon, C., Miná, J., Zbinden, H., De Riedmatten, H. & Gisin, N. Long-distance entanglement distribution with single-photon sources. *Physical Review A - Atomic, Molecular, and Optical Physics* **76**, 050301(R) (2007).

[135] Hammerer, K., Sø rensen, A. S. & Polzik, E. S. Quantum interface between light and atomic ensembles. *Reviews of Modern Physics* **82**, 1041–1093 (2010).

[136] Jozsa, R. Fidelity for mixed quantum states. *Journal of Modern Optics* **41**, 2315–2323 (1994).

[137] Massar, S. & Popescu, S. Optimal extraction of information from finite quantum ensembles. *Physical Review Letters* **74**, 1259–1263 (1995).

[138] Braunstein, S. L., Fuchs, C. A. & Kimble, H. J. Criteria for Continuous-Variable Quantum Teleportation. *Journal of Modern Optics* **47**, 267–268 (1999).

[139] Hammerer, K., Wolf, M. M., Polzik, E. S. & Cirac, J. I. Quantum benchmark for storage and transmission of coherent states. *Physical Review Letters* **94**, 150503 (2005).

[140] Nunn, J., Reim, K., Lee, K. C., Lorenz, V. O., Sussman, B. J., Walmsley, I. A. & Jaksch, D. Multimode memories in atomic ensembles. *Physical Review Letters* **101**, 260502 (2008).

[141] Zaske, S. *et al.* Visible-to-telecom quantum frequency conversion of light from a single quantum emitter. *Physical Review Letters* **109**, 147404 (2012).

[142] Lvovsky, A. I., Sanders, B. C. & Tittel, W. Optical quantum memory. *Nature Photonics* **3**, 706–714 (2009).

[143] Kaneda, F. *et al.* Time-multiplexed heralded single-photon source. *Optica* **2**, 121010 (2015).

[144] Kaneda, F., Xu, F., Chapman, J. & Kwiat, P. G. Quantum-memory-assisted multi-photon generation for efficient quantum information processing. *Optica* **4**, 091034 (2017).

[145] Hahn, E. Spin Echoes. *Physical Review* **80**, 580–594 (1950).

[146] Kurnit, N. A., Abella, I. D. & Hartmann, S. R. Observation of a photon echo. *Physical Review Letters* **13**, 567–568 (1964).

[147] Mossberg, T. W. Time-domain frequency-selective optical data storage. *Optics Letters* **7**, 77 (1982).

[148] Azadeh, M., Sjaarda Cornish, C., Babbitt, W. R. & Tsang, L. Efficient photon echoes in optically thick media. *Physical Review A - Atomic, Molecular, and Optical Physics* **57**, 4662 (1998).

[149] Sjaarda Cornish, C., Babbitt, W. R. & Tsang, L. Demonstration of highly efficient photon echoes. *Optics letters* **25**, 1276 (2000).

[150] Ruggiero, J., Le Gouët, J. L., Simon, C. & Chanelière, T. Why the two-pulse photon echo is not a good quantum memory protocol. *Physical Review A - Atomic, Molecular, and Optical Physics* **79**, 053851 (2009).

[151] Moiseev, S. A. & Kröll, S. Complete reconstruction of the quantum state of a single-photon wave packet absorbed by a doppler-broadened transition. *Physical Review Letters* **87**, 173601 (2001).

[152] Nilsson, M. & Kröll, S. Solid state quantum memory using complete absorption and re-emission of photons by tailored and externally controlled inhomogeneous absorption profiles. *Optics Communications* **247**, 393–403 (2005).

[153] Kraus, B., Tittel, W., Gisin, N., Nilsson, M., Kröll, S. & Cirac, J. I. Quantum memory for nonstationary light fields based on controlled reversible inhomogeneous broadening. *Physical Review A - Atomic, Molecular, and Optical Physics* **73**, 020302(R) (2006).

[154] Alexander, A. L., Longdell, J. J., Sellars, M. J. & Manson, N. B. Photon echoes produced by switching electric fields. *Physical Review Letters* **96**, 043602 (2006).

[155] Hétet, G., Longdell, J. J., Alexander, A. L., Lam, P. K. & Sellars, M. J. Electro-optic quantum memory for light using two-level atoms. *Physical Review Letters* **100**, 023601 (2008).

[156] Tittel, W., Afzelius, M., Chanelire, T., Cone, R., Krll, S., Moiseev, S. & Sellars, M. Photon-echo quantum memory in solid state systems. *Laser & Photonics Reviews* **4**, 244–267 (2010).

[157] Lauritzen, B., Minář, J., De Riedmatten, H., Afzelius, M., Sangouard, N., Simon, C. & Gisin, N. Telecommunication-wavelength solid-state memory at the single photon level. *Physical Review Letters* **104**, 080502 (2010).

[158] Moerner, W. & Bjorklund, G. *Persistent spectral hole-burning : Science and applications* (Springer-Verlag, Berlin; London, 1988).

[159] Zeeman, P. On the influence of magnetism on the nature of the light emitted by a substance. *The London, Edinburgh, and Dublin Philosophical Magazine and Journal of Science* **43**, 226–239 (1897).

[160] Zeeman, P. Doublets and triplets in the spectrum produced by external magnetic forces. *The London, Edinburgh, and Dublin Philosophical Magazine and Journal of Science* **44**, 255–259 (1897).

[161] Zeeman, P. The Effect of Magnetisation on the Nature of Light Emitted by a Substance. *Nature* **55**, 347 (1897).

[162] Stark, J. Beobachtungen über den Effekt des elektrischen Feldes auf Spektrallinien. I. Quereffekt. *Annalen der Physik* **43**, 965–983 (1914).

[163] Hétet, G., Longdell, J. J., Sellars, M. J., Lam, P. K. & Buchler, B. C. Multimodal properties and dynamics of gradient echo quantum memory. *Physical Review Letters* **101**, 203601 (2008).

[164] Sangouard, N., Simon, C., Afzelius, M. & Gisin, N. Analysis of a quantum memory for photons based on controlled reversible inhomogeneous broadening. *Physical Review A - Atomic, Molecular, and Optical Physics* **75**, 032327 (2007).

[165] De Riedmatten, H., Afzelius, M., Staudt, M. U., Simon, C. & Gisin, N. A solid-state light-matter interface at the single-photon level. *Nature* **456**, 773–777 (2008).

[166] Afzelius, M., Simon, C., De Riedmatten, H. & Gisin, N. Multimode quantum memory based on atomic frequency combs. *Physical Review A - Atomic, Molecular, and Optical Physics* **79**, 052329 (2009).

[167] Afzelius, M. *et al.* Demonstration of atomic frequency comb memory for light with spin-wave storage. *Physical Review Letters* **104**, 040503 (2010).

[168] Dicke, R. H. Coherence in Spontaneous Radiation Processes. *Physical Review* **93**, 99–110 (1954).

[169] Nunn, J., Walmsley, I. A., Raymer, M. G., Surmacz, K., Waldermann, F. C., Wang, Z. & Jaksch, D. Mapping broadband single-photon wave packets into an atomic memory. *Phys. Rev. A* **75**, 011401 (2007).

[170] Gorshkov, A. V., André, A., Fleischhauer, M., Sørensen, A. S. & Lukin, M. D. Universal approach to optimal photon storage in atomic media. *Phys. Rev. Lett.* **98**, 123601 (2007).

[171] Sinclair, N. *et al.* Spectral multiplexing for scalable quantum photonics using an atomic frequency comb quantum memory and feed-forward control. *Physical Review Letters* **113**, 053603 (2014).

[172] Harris, S. E., Field, J. E. & Imamoğlu, A. Nonlinear Optical Processes Using Electromagnetically Induced Transparency. *Physical Review Letters* **64**, 1107–1110 (1990).

[173] Autler, S. H. & Townes, C. H. Stark Effect in Rapidly Varying Fields. *Physical Review* **100**, 703–722 (1955).

[174] Cohen-Tannoudji, C. N. The autler-townes effect revisited. In Chiao, R. Y. (ed.) *Amazing Light: A Volume Dedicated To Charles Hard Townes On His 80th Birthday*, 109–123 (Springer New York, New York, NY, 1996).

[175] Harris, S. E., Field, J. E. & Kasapi, A. Dispersive properties of electromagnetically induced transparency. *Physical Review A* **46**, 29–32 (1992).

[176] Vestergaard Hau, L., Harris, S. E., Dutton, Z. & Behroozi, C. H. Light speed reduction to 17˜metres per second in an ultracold atomic gas. *Nature* **397**, 594–598 (1999).

[177] Fleischhauer, M. & Lukin, M. D. Dark-state polaritons in electromagnetically induced transparency. *Physical Review Letters* **84**, 5094–5097 (2000).

[178] Phillips, D. F., Fleischhauer, A., Mair, A., Walsworth, R. L. & Lukin, M. D. Storage of light in atomic vapor. *Physical Review Letters* **86**, 783–786 (2001).

[179] Beil, F., Klein, J., Nikoghosyan, G. & Halfmann, T. Electromagnetically induced transparency and retrieval of light pulses in a Λ-type and a V-type level scheme in Pr3+:Y2SiO5. *Journal of Physics B: Atomic, Molecular and Optical Physics* **41**, 074001 (2008).

[180] Heinze, G., Hubrich, C. & Halfmann, T. Stopped light and image storage by electromagnetically induced transparency up to the regime of one minute. *Physical Review Letters* **111**, 033601 (2013).

[181] Schraft, D., Hain, M., Lorenz, N. & Halfmann, T. Stopped Light at High Storage Efficiency in a Pr3+: Y2SiO5 Crystal. *Physical Review Letters* **116**, 073602 (2016).

[182] Saglamyurek, E., Hrushevskyi, T., Rastogi, A., Heshami, K. & LeBlanc, L. J. Coherent storage and manipulation of broadband photons via dynamically controlled Autler-Townes splitting (2017). arXiv:1710.08902.

[183] Smekal, A. Zur Quantentheorie der Dispersion. *Naturwissenschaften* **11**, 873 (1923).

[184] Raman, C. V. A new radiation. *Indian Journal of Physics* **2**, 387–398 (1928).

[185] Landsberg, G. & Mandelstam, L. Über die Lichtzerstreuung in Kristallen. *Zeitschrift für Physik* **50**, 769–780 (1928).

[186] Kozhekin, A. E., Molmer, K. & Polzik, E. Quantum Memory for Light. *Physical Review A* **62**, 033809 (2000).

[187] Gorshkov, A. V., André, A., Lukin, M. D. & Sø rensen, A. S. Photon storage in Λ-type optically dense atomic media. I. Cavity model. *Physical Review A* **76**, 033804 (2007).

[188] Gorshkov, A. V., André, A., Lukin, M. D. & Sø rensen, A. S. Photon storage in Λ-type optically dense atomic media. II. Free-space model. *Physical Review A* **76**, 033805 (2007).

[189] Nunn, J. *Quantum memory in atomic ensembles*. DPhil thesis, University of Oxford (2008).

[190] Reim, K. F. *et al.* Multipulse addressing of a Raman quantum memory: Configurable beam splitting and efficient readout. *Physical Review Letters* **108**, 263602 (2012).

[191] Reim, K. F. *et al.* Towards high-speed optical quantum memories. *Nature Photonics* **4**, 218–221 (2010).

[192] Camacho, R. M., Vudyasetu, P. K. & Howell, J. C. Four-wave-mixing stopped light in hot atomic rubidium vapour. *Nature Photonics* **3**, 103–106 (2009).

[193] England, D. G. *et al.* High-fidelity polarization storage in a gigahertz bandwidth quantum memory. *Journal of Physics B: Atomic, Molecular and Optical Physics* **45**, 124008 (2012).

[194] Sprague, M. R. *et al.* Efficient optical pumping and high optical depth in a hollow-core photonic-crystal fibre for a broadband quantum memory. *New Journal of Physics* **15**, 055013 (2013).

[195] Thomas, S. E. *et al.* High efficiency Raman memory by suppressing radiation trapping. *New Journal of Physics* **19**, 063034 (2017).

[196] Bustard, P. J., England, D. G., Heshami, K., Kupchak, C. & Sussman, B. J. Reducing noise in a Raman quantum memory. *Optics Letters* **41**, 5055–5058 (2016).

[197] Vurgaftman, I. & Bashkansky, M. Suppressing four-wave mixing in warm-atomic-vapor quantum memory. *Physical Review A - Atomic, Molecular, and Optical Physics* **87**, 063836 (2013).

[198] England, D. G., Bustard, P. J., Nunn, J., Lausten, R. & Sussman, B. J. From photons to phonons and back: A THz optical memory in diamond. *Physical Review Letters* **111**, 243601 (2013).

[199] Bustard, P. J., Lausten, R., England, D. G. & Sussman, B. J. Toward quantum processing in molecules: A THz-bandwidth coherent memory for light. *Physical Review Letters* **111**, 083901 (2013).

[200] Solin, S. A. & Ramdas, A. K. Raman spectrum of diamond. *Physical Review B* **1**, 1687–1698 (1970).

[201] Lee, K. C. *et al.* Macroscopic non-classical states and terahertz quantum processing in room-temperature diamond. *Nature Photonics* **6**, 41–44 (2012).

[202] England, D. G., A.G. Fisher, K., Maclean, J. P. W., Bustard, P. J., Lausten, R., Resch, K. J. & Sussman, B. J. Storage and retrieval of THZ-bandwidth single photons using a room-temperature diamond quantum memory. *Physical Review Letters* **114**, 053602 (2015).

[203] Saunders, D. J. *et al.* Cavity-Enhanced Room-Temperature Broadband Raman Memory. *Physical Review Letters* **116**, 090501 (2016).

[204] Nunn, J. *et al.* Theory of noise suppression in Λ -type quantum memories by means of a cavity. *Physical Review A* **96**, 012338 (2017).

[205] Kaczmarek, K. T. *et al.* High-speed noise-free optical quantum memory. *Phys. Rev. A* **97**, 042316 (2018).

[206] Miyazaki, T. *et al.* Atomistic mechanism of perfect alignment of nitrogen-vacancy centers in diamond. *Applied Physics Letters* **105**, 261601 (2014).

[207] Michl, J. *et al.* Perfect alignment and preferential orientation of nitrogen-vacancy centers during chemical vapor deposition diamond growth on (111) surfaces. *Applied Physics Letters* **104**, 102407 (2014).

[208] Lesik, M. *et al.* Perfect preferential orientation of nitrogen-vacancy defects in a synthetic diamond sample. *Applied Physics Letters* **104**, 113107 (2014).

[209] Lemonde, M.-A., Meesala, S., Sipahigil, A., Schuetz, M. J. A., Lukin, M. D., Loncar, M. & Rabl, P. Phonon Networks with Silicon-Vacancy Centers in Diamond Waveguides. *Physical Review Letters* **120**, 213603 (2018).

[210] Orieux, A. & Diamanti, E. Recent advances on integrated quantum communications. *Journal of Optics* **18**, 083002 (2016).

[211] Doherty, M. W., Manson, N. B., Delaney, P., Jelezko, F., Wrachtrup, J. & Hollenberg, L. C. L. The nitrogen-vacancy colour centre in diamond. *Physics Reports* **528**, 1–45 (2013).

[212] Wyckoff, R. W. G. *Crystal structures* (Interscience, London, 1963), 2nd edn.

[213] Kaboli, S. & Burnley, P. C. Direct observations of crystal defects in polycrystalline diamond. *Materials Characterization* **142**, 154–161 (2018).

[214] Wooddell, C. E. Method of Comparing the Hardness of Electric Furnace Products and Natural Abrasives. *Journal of The Electrochemical Society* **68**, 111–130 (1935).

[215] Mildren, R. P. Intrinsic Optical Properties of Diamond. In Mildren, R. P. & Rabeau, J. (eds.) *Optical Engineering in Diamond*, chap. 1, 1–34 (John Wiley & Sons, Incorporated, 2013), 1st edn.

[216] Asmussen, J. & Reinhard, D. K. (eds.) *Diamond Films Handbook* (Marcel Dekker, Inc., New York, Basel, 2002).

[217] Bundy, F. P., Hall, H. T., Strong, H. M. & Wentorf, R. H. Man-Made diamonds. *Nature* **176**, 51–55 (1955).

[218] Balmer, R. S. *et al.* Chemical vapour deposition synthetic diamond: Materials, technology and applications. *Journal of Physics Condensed Matter* **21**, 364221 (2009).

[219] Ridgway, R. R., Ballard, A. H. & Bailey, B. L. Hardness Values for Electrochemical Products. *Transactions of The Electrochemical Society* **63**, 369–393 (1933).

[220] Bhatnagar, M. & Baliga, B. J. Comparison of 6H-SiC, 3C-SiC, and Si for Power Devices. *IEEE Transactions on Electron Devices* **40**, 645–655 (1993).

[221] Park, C. H., Cheong, B.-h., Lee, K.-h. & Chang, K. J. Structural and electronic properties of cubic, 2H, 4H, and 6H SiC. *Physical Review B* **49**, 4485 (1994).

[222] Streetman, B. & Banerjee, S. *Solid state electronic devices* (Pearson, Boston, 2016).

[223] Radulaski, M. & Vuckovic, J. Quantum Photonics Incorporating Color Centers in Silicon Carbide and Diamond (2018). arXiv:1806.06955.

[224] Nagy, R. *et al.* Quantum Properties of Dichroic Silicon Vacancies in Silicon Carbide. *Physical Review Applied* **9**, 034022 (2018).

[225] Simmons, S. *et al.* Entanglement in a solid-state spin ensemble. *Nature* **470**, 69–72 (2011).

[226] Saeedi, K. *et al.* Room-Temperature Quantum Bit Storage Exceeding 39 Minutes Using Ionized Donors in Silicon-28. *Science* **342**, 830–833 (2013).

[227] Morse, K. J. *et al.* A photonic platform for donor spin qubits in silicon. *Science Advances* **3**, e1700930 (2017).

[228] Walker, J. Optical absorption and luminescence in diamond. *Reports on Progress in Physics* **42**, 1605 (1979).

[229] Zaitsev, A. Vibronic spectra of impurity-related optical centers in diamond. *Physical Review B - Condensed Matter and Materials Physics* **61**, 12909–12922 (2000).

[230] Zaitsev, A. M. *Optical Properties of Diamond: A Data Handbook* (Springer, Berlin Heidelberg, 2001).

[231] Magyar, A., Hu, W., Shanley, T., Flatté, M. E., Hu, E. & Aharonovich, I. Synthesis of luminescent europium defects in diamond. *Nature Communications* **5**, 3523 (2014).

[232] Sandstrom, R. *et al.* Optical properties of implanted Xe color centers in diamond. *Optics Communications* **411**, 182–185 (2018).

[233] Mita, Y. Change of absorption spectra in type-Ib diamond with heavy neutron irradiation. *Physical Review B - Condensed Matter and Materials Physics* **53**, 11360–11364 (1996).

[234] Martin, J., Wannemacher, R., Teichert, J., Bischoff, L. & Köhler, B. Generation and detection of fluorescent color centers in diamond with submicron resolution. *Applied Physics Letters* **75**, 3096 (1999).

[235] Kalish, R. *et al.* Nitrogen doping of diamond by ion implantation. *Diamond and Related Materials* **6**, 516–520 (1997).

[236] Meijer, J. *et al.* Generation of single color centers by focused nitrogen implantation. *Applied Physics Letters* **87**, 261909 (2005).

[237] Wang, C., Kurtsiefer, C., Weinfurter, H. & Burchard, B. Single photon emission from SiV centres in diamond produced by ion implantation. *Journal of Physics B: Atomic, Molecular and Optical Physics* **39**, 37–41 (2006).

[238] Neu, E. *et al.* Narrowband fluorescent nanodiamonds produced from chemical vapor deposition films. *Applied Physics Letters* **98**, 243107 (2011).

[239] Neu, E., Steinmetz, D., Riedrich-Möller, J., Gsell, S., Fischer, M., Schreck, M. & Becher, C. Single photon emission from silicon-vacancy colour centres in chemical vapour deposition nano-diamonds on iridium. *New Journal of Physics* **13**, 025012 (2011).

[240] Neu, E. *et al.* Low-temperature investigations of single silicon vacancy colour centres in diamond. *New Journal of Physics* **15**, 043005 (2013).

[241] Chen, Y. C. *et al.* Laser writing of coherent colour centres in diamond. *Nature Photonics* **11**, 77–80 (2017).

[242] Chen, Y.-C. *et al.* Laser writing of individual atomic defects in a crystal with near-unity yield (2018). arXiv:1807.04028.

[243] Franck, J. & Dymond, E. G. Elementary processes of photochemical reactions. *Trans. Faraday Soc.* **21**, 536–542 (1926).

[244] Condon, E. A theory of intensity distribution in band systems. *Phys. Rev.* **28**, 1182–1201 (1926).

[245] Condon, E. U. Nuclear motions associated with electron transitions in diatomic molecules. *Phys. Rev.* **32**, 858–872 (1928).

[246] Kakkar, R. *Atomic and Molecular Spectroscopy : Basic Concepts and Applications* (Cambridge University Press, 2015).

[247] Pieper, J. & Freiberg, A. Electron-Phonon and Exciton-Phonon Coupling in Light Harvesting, Insights from Line-Narrowing Spectroscopies. In Golbeck, J. & van der Est, A. (eds.) *The Biophysics of Photosynthesis*, chap. 2, 45–77 (Springer Science+Business Media, New York, 2014).

[248] Jahnke, K. D. *et al.* Electron-phonon processes of the silicon-vacancy centre in diamond. *New Journal of Physics* **17**, 043011 (2015).

[249] Petersen, L. *High-resolution spectroscopy of praseodymium ions in a solid matrix - Towards single-ion detection sensitivity.* Doctoral thesis, Eidgenössische Technische Hochschule ETH Zürich (2011).

[250] Tamm, I. Über die Quantentheorie der molekularen Lichtzerstreuung in festen Körpern. *Zeitschrift für Physik* **60**, 345–363 (1930).

[251] Vasil'ev, N. S. & Gorelik, V. S. Properties of optical and acoustic phonons in diamond crystals. *Bulletin of the Lebedev Physics Institute* **38**, 255–262 (2011).

[252] Peckham, G. The Phonon Dispersion Relation for Diamond. *Solid State Communications* **5**, 311–313 (1967).

[253] Bose, S. N. Plancks Gesetz und Lichtquantenhypothese. *Zeitschrift für Physik* **26**, 178–181 (1924).

[254] Jahn, H. A. & Teller, E. Stability of Polyatomic Molecules in Degenerate Electronic States. I. Orbital Degeneracy. *Proceedings of the Royal Society of London A: Mathematical and Physical Sciences* **161**, 220–235 (1937).

[255] Fu, K. M. C., Santori, C., Barclay, P. E., Rogers, L. J., Manson, N. B. & Beausoleil, R. G. Observation of the dynamic Jahn-Teller effect in the excited states of nitrogen-vacancy centers in diamond. *Physical Review Letters* **103**, 256404 (2009).

[256] Ham, F. S. Dynamical Jahn-Teller effect in paramagnetic resonance spectra: Orbital reduction factors and partial quenching of spin-orbit interaction. *Physical Review* **138**, 1727 – 1740 (1965).

[257] Goldman, M. L. *et al.* Phonon-induced population dynamics and intersystem crossing in nitrogen-vacancy centers. *Physical Review Letters* **114**, 145502 (2015).

[258] Gomis-Bresco, J. *et al.* A one-dimensional optomechanical crystal with a complete phononic band gap. *Nature Communications* **5**, 4452 (2014).

[259] Safavi-Naeini, A. H., Hill, J. T., Meenehan, S., Chan, J., Gröblacher, S. & Painter, O. Two-dimensional phononic-photonic band gap optomechanical crystal cavity. *Physical Review Letters* **112**, 153603 (2014).

[260] Meesala, S. *et al.* Strain engineering of the silicon-vacancy center in diamond. *Physical Review B* **97**, 205444 (2018).

[261] Sohn, Y. I. *et al.* Controlling the coherence of a diamond spin qubit through its strain environment. *Nature Communications* **9**, 17–22 (2018).

[262] Davies, G. & Hamer, M. F. Optical Studies of the 1.945 eV Vibronic Band in Diamond. *Proceedings of the Royal Society of London A: Mathematical, Physical and Engineering Sciences* **348**, 285–298 (1976).

[263] Hauf, M. V. *et al.* Chemical control of the charge state of nitrogen-vacancy centers in diamond. *Physical Review B - Condensed Matter and Materials Physics* **83**, 081304(R) (2011).

[264] Haque, A. & Sumaiya, S. An Overview on the Formation and Processing of Nitrogen-Vacancy Photonic Centers in Diamond by Ion Implantation. *Journal of Manufacturing and Materials Processing* **1**, 6 (2017).

[265] Gruber, A. Scanning Confocal Optical Microscopy and Magnetic Resonance on Single Defect Centers. *Science* **276**, 2012–2014 (1997).

[266] Doherty, M. W., Manson, N. B., Delaney, P. & Hollenberg, L. C. L. The negatively charged nitrogen-vacancy centre in diamond: The electronic solution. *New Journal of Physics* **13**, 025019 (2011).

[267] Maze, J. R., Gali, A., Togan, E., Chu, Y., Trifonov, A., Kaxiras, E. & Lukin, M. D. Properties of nitrogen-vacancy centers in diamond: The group theoretic approach. *New Journal of Physics* **13**, 025025 (2011).

[268] Alléaume, R. *et al.* Experimental open-air quantum key distribution with a single-photon source. *New Journal of Physics* **6**, 92 (2004).

[269] Rabl, P., Cappellaro, P., Dutt, M. V. G., Jiang, L., Maze, J. R. & Lukin, M. D. Strong magnetic coupling between an electronic spin qubit and a mechanical resonator. *Physical Review B - Condensed Matter and Materials Physics* **79**, 041302(R) (2009).

[270] Neumann, P. *et al.* Scalable quantum register based on coupled electron spins in a room temperature solid. *Nature Physics* **6**, 249–253 (2010).

[271] Gali, A. Theory of the neutral nitrogen-vacancy center in diamond and its application to the realization of a qubit. *Physical Review B - Condensed Matter and Materials Physics* **79**, 235210 (2009).

[272] Cornwell, J. F. *Group theory in physics: an introduction* (Academic Press, San Diego, 1997).

[273] Dresselhaus, M. S., Dresselhaus, G. & Jorio, A. *Group Theory - Application to the Physics of Condensed Matter* (Springer, Berlin Heidelberg, 2008).

[274] Powell, R. *Symmetry, Group Theory, and the Physical Properties of Crystals* (Springer New York, New York, NY, 2010), 1st edn.

[275] Hepp, C. *Electronic Structure of the Silicon Vacancy Color Center in Diamond.* Dissertation, Universität des Saarlandes (2014).

[276] Goldman, M. L. *et al.* State-selective intersystem crossing in nitrogen-vacancy centers. *Physical Review B - Condensed Matter and Materials Physics* **91**, 165201 (2015).

[277] Felton, S., Edmonds, A. M., Newton, M. E., Martineau, P. M., Fisher, D. & Twitchen, D. J. Electron paramagnetic resonance studies of the neutral nitrogen vacancy in diamond. *Physical Review B - Condensed Matter and Materials Physics* **77**, 081201(R) (2008).

[278] Buckley, B. B., Fuchs, G. D., Bassett, L. C. & Awschalom, D. D. Spin-Light Coherence for Single-Spin Measurement and Control in Diamond. *Science* **330**, 1212–1215 (2010).

[279] Steiner, M., Neumann, P., Beck, J., Jelezko, F. & Wrachtrup, J. Universal enhancement of the optical readout fidelity of single electron spins at nitrogen-vacancy centers in diamond. *Physical Review B - Condensed Matter and Materials Physics* **81**, 035205 (2010).

[280] Neumann, P. *et al.* Single - Shot Readout of a Single Nuclear Spin. *Science* **329**, 542–5444 (2010).

[281] Gupta, A., Hacquebard, L. & Childress, L. Efficient signal processing for time-resolved fluorescence detection of nitrogen-vacancy spins in diamond. *Journal of the Optical Society of America B* **33**, B28–B34 (2016).

[282] Beveratos, A., Brouri, R., Gacoin, T., Poizat, J. P. & Grangier, P. Nonclassical radiation from diamond nanocrystals. *Physical Review A - Atomic, Molecular, and Optical Physics* **64**, 061802(R) (2001).

[283] Takahashi, S., Hanson, R., Van Tol, J., Sherwin, M. S. & Awschalom, D. D. Quenching spin decoherence in diamond through spin bath polarization. *Physical Review Letters* **101**, 047601 (2008).

[284] Redman, D. A., Brown, S., Sands, R. H. & Rand, S. C. Spin dynamics and electronic states of N-V center in diamond by EPR and Four-Wave_Mixing spectroscopy. *Physical Review Letters* **64**, 3420–3423 (1991).

[285] Meiboom, S. & Gill, D. Modified spin-echo method for measuring nuclear relaxation times. *Review of Scientific Instruments* **29**, 688–691 (1958).

[286] de Lange, G., Wang, Z. H., Ristè, D., Dobrovitski, V. V. & Hanson, R. Universal Dynamical Decoupling of a Single Solid-State Spin from a Spin Bath. *Science* **330**, 60–64 (2010).

[287] Pham, L. M. *et al.* Enhanced solid-state multispin metrology using dynamical decoupling. *Physical Review B - Condensed Matter and Materials Physics* **86**, 045214 (2012).

[288] Bar-Gill, N., Pham, L. M., Jarmola, A., Budker, D. & Walsworth, R. L. Solid-state electronic spin coherence time approaching one second. *Nature Communications* **4**, 1743–1746 (2013).

[289] Farfurnik, D. *et al.* Optimizing a dynamical decoupling protocol for solid-state electronic spin ensembles in diamond. *Physical Review B - Condensed Matter and Materials Physics* **92**, 060301(R) (2015).

[290] Rondin, L., Tetienne, J. P., Hingant, T., Roch, J. F., Maletinsky, P. & Jacques, V. Magnetometry with nitrogen-vacancy defects in diamond. *Reports on Progress in Physics* **77**, 056503 (2014).

[291] Schirhagl, R., Chang, K., Loretz, M. & Degen, C. L. Nitrogen-Vacancy Centers in Diamond: Nanoscale Sensors for Physics and Biology. *Annual Review of Physical Chemistry* **65**, 83–105 (2014).

[292] Childress, L. & Hanson, R. Diamond NV centers for quantum computing and quantum networks. *MRS Bulletin* **38**, 134–138 (2013).

[293] Hensen, B. *et al.* Loophole-free Bell inequality violation using electron spins separated by 1.3 kilometres. *Nature* **526**, 682–686 (2015).

[294] Klatzow, J. *et al.* Experimental demonstration of quantum effects in the operation of microscopic heat engines. *Physical Review Letters* **112**, 110601 (2019).

[295] Jeske, J. *et al.* Stimulated emission from nitrogen-vacancy centres in diamond. *Nature Communications* **8**, 14000 (2017).

[296] Breeze, J. D., Salvadori, E., Sathian, J., Alford, N. M. N. & Kay, C. W. Continuous-wave room-temperature diamond maser. *Nature* **555**, 493–496 (2018).

[297] Heshami, K., Santori, C., Khanaliloo, B., Healey, C., Acosta, V. M., Barclay, P. E. & Simon, C. Raman quantum memory based on an ensemble of nitrogen-vacancy centers coupled to a microcavity. *Physical Review A* **89**, 040301(R) (2014).

[298] Aharonovich, I., Castelletto, S., Simpson, D. A., Su, C. H., Greentree, A. D. & Prawer, S. Diamond-based single-photon emitters. *Reports on Progress in Physics* **74**, 076501 (2011).

[299] Beha, K., Batalov, A., Manson, N. B., Bratschitsch, R. & Leitenstorfer, A. Optimum photoluminescence excitation and recharging cycle of single nitrogen-vacancy centers in ultrapure diamond. *Physical Review Letters* **109**, 097404 (2012).

[300] Aslam, N., Waldherr, G., Neumann, P., Jelezko, F. & Wrachtrup, J. Photo-induced ionization dynamics of the nitrogen vacancy defect in diamond investigated by single-shot charge state detection. *New Journal of Physics* **15**, 013064 (2013).

[301] Siyushev, P., Pinto, H., Vörös, M., Gali, A., Jelezko, F. & Wrachtrup, J. Optically controlled switching of the charge state of a single nitrogen-vacancy center in diamond at cryogenic temperatures. *Physical Review Letters* **110**, 167402 (2013).

[302] Hacquebard, L. & Childress, L. Charge-state dynamics during excitation and depletion of the nitrogen-vacancy center in diamond. *Physical Review A* **97**, 063408 (2018).

[303] Shen, Y., Sweeney, T. M. & Wang, H. Zero-phonon linewidth of single nitrogen vacancy centers in diamond nanocrystals. *Physical Review B - Condensed Matter and Materials Physics* **77**, 033201 (2008).

[304] Fu, K. M. C., Santori, C., Barclay, P. E. & Beausoleil, R. G. Conversion of neutral nitrogen-vacancy centers to negatively charged nitrogen-vacancy centers through selective oxidation. *Applied Physics Letters* **96**, 121907 (2010).

[305] Wolters, J., Sadzak, N., Schell, A. W., Schröder, T. & Benson, O. Measurement of the ultrafast spectral diffusion of the optical transition of nitrogen vacancy centers in nano-size diamond using correlation interferometry. *Physical Review Letters* **110**, 027401 (2013).

[306] Davies, G. Dynamic Jahn-Teller distortions at trigonal optical centres in diamond. *Journal of Physics C: Solid State Physics* **12**, 2551–2566 (1979).

[307] Manson, N. B., Beha, K., Batalov, A., Rogers, L. J., Doherty, M. W., Bratschitsch, R. & Leitenstorfer, A. Assignment of the NV^0 575-nm zero-phonon line in diamond to a ^2E-$^2A_2$ transition. *Physical Review B - Condensed Matter and Materials Physics* **87**, 155209 (2013).

[308] Mizuochi, N. *et al.* Electrically driven single-photon source at room temperature in diamond. *Nature Photonics* **6**, 299–303 (2012).

[309] Liaugaudas, G., Davies, G., Suhling, K., Khan, R. U. A. & Evans, D. J. F. Luminescence lifetimes of neutral nitrogen-vacancy centres in synthetic diamond containing nitrogen. *Journal of Physics: Condensed Matter* **24**, 435503 (2012).

[310] Goss, J., Jones, R., Breuer, S., Briddon, P. & Öberg, S. The Twelve-Line 1.682 eV Luminescence Center in Diamond and the Vacancy-Silicon Complex. *Physical Review Letters* **77**, 3041–3044 (1996).

[311] Gali, A. & Maze, J. R. Ab initio study of the split silicon-vacancy defect in diamond: Electronic structure and related properties. *Phys. Rev. B* **88**, 235205 (2013).

[312] Sipahigil, A. *et al.* Indistinguishable photons from separated silicon-vacancy centers in diamond. *Physical Review Letters* **113**, 113602 (2014).

[313] Hepp, C. *et al.* Electronic structure of the silicon vacancy color center in diamond. *Physical Review Letters* **112**, 036405 (2014).

[314] Sternschulte, H., Thonke, K., Sauer, R., Münzinger, P. C. & Michler, P. 1.681-eV luminescence center in chemical-vapor-deposited homoepitaxial diamond films. *Physical Review B* **50**, 14554–14560 (1994).

[315] Poem, E. *et al.* Broadband noise-free optical quantum memory with neutral nitrogen-vacancy centers in diamond. *Physical Review B* **91**, 205108 (2015).

[316] Suzuki, T., Singh, R., Bayer, M., Ludwig, A., Wieck, A. D. & Cundiff, S. T. Coherent Control of the Exciton-Biexciton System in an InAs Self-Assembled Quantum Dot Ensemble. *Physical Review Letters* **117**, 157402 (2016).

[317] Sun, Y. C. Rare Earth Materials in Optical Storage and Data Processing Applications. In Liu, G. & Jacquier, B. (eds.) *Spectroscopic Properties of Rare Earths in Optical Materials*, 379 – 429 (Tsinghua University Press and Springer-Verlag, Berlin Heidelberg, 2005).

[318] Ahlefeldt, R. L., Hush, M. R. & Sellars, M. J. Ultranarrow Optical Inhomogeneous Linewidth in a Stoichiometric Rare-Earth Crystal. *Physical Review Letters* **117**, 250504 (2016).

[319] Sipahigil, A. *et al.* Supplemental Material: Indistinguishable photons from separated silicon-vacancy centers in diamond. *Physical Review Letters* **113**, 113602 (2014).

[320] Dudin, Y. O. & Kuzmich, A. Strongly Interacting Rydberg Excitations of a Cold Atomic Gas. *Science* **336**, 887–889 (2012).

[321] Lukin, M. D. Colloquium: Trapping and manipulating photon states in atomic ensembles. *Reviews of Modern Physics* **75**, 457–472 (2003).

[322] Edmonds, A. M., Newton, M. E., Martineau, P. M., Twitchen, D. J. & Williams, S. D. Electron paramagnetic resonance studies of silicon-related defects in diamond. *Physical Review B - Condensed Matter and Materials Physics* **77**, 245205 (2008).

[323] Edmonds, A. M., Newton, M. E., Martineau, P. M., Twitchen, D. J. & Williams, S. D. Erratum: Electron paramagnetic resonance studies of silicon-related defects in diamond (Physical Review B (2008) 77 (245205)). *Physical Review B - Condensed Matter and Materials Physics* **82**, 249901(E) (2010).

[324] D'Haenens-Johansson, U. F. *et al.* EPR of a defect in CVD diamond involving both silicon and hydrogen that shows preferential alignment. *Physical Review B - Condensed Matter and Materials Physics* **82**, 155205 (2010).

[325] D'Haenens-Johansson, U. F. S. *et al.* Optical properties of the neutral silicon split-vacancy center in diamond. *Physical Review B - Condensed Matter and Materials Physics* **84**, 245208 (2011).

[326] Green, B. L. *et al.* Neutral Silicon-Vacancy Center in Diamond: Spin Polarization and Lifetimes. *Physical Review Letters* **119**, 096402 (2017).

[327] Green, B. L. *et al.* Electronic structure of the neutral silicon-vacancy center in diamond (2018). arXiv:1804.09141.

[328] Arend, C., Becker, J. N., Sternschulte, H., Steinmüller-Nethl, D. & Becher, C. Photoluminescence excitation and spectral hole burning spectroscopy of silicon vacancy centers in diamond. *Physical Review B - Condensed Matter and Materials Physics* **94**, 045203 (2016).

[329] Rogers, L. J. *et al.* Multiple intrinsically identical single-photon emitters in the solid state. *Nature Communications* **5**, 4739 (2014).

[330] Neu, E., Steinmetz, D., Riedrich-Möller, J., Gsell, S., Fischer, M., Schreck, M. & Becher, C. Single photon emission from silicon-vacancy colour centres in chemical vapour deposition nano-diamonds on iridium. *New Journal of Physics* **13**, 025012 (2011).

[331] Neu, E., Fischer, M., Gsell, S., Schreck, M. & Becher, C. Fluorescence and polarization spectroscopy of single silicon vacancy centers in heteroepitaxial nanodiamonds on iridium. *Physical Review B - Condensed Matter and Materials Physics* **84**, 205211 (2011).

[332] Becker, J. N. & Becher, C. Coherence properties and quantum control of silicon vacancy color centers in diamond. *Physica Status Solidi (a)* **214**, 1700586 (2017).

[333] Riedrich-Möller, J. *et al.* Controlled coupling of a single silicon-vacancy center to a photonic crystal cavity in single crystal diamond. *Nano Letters* **14**, 5281–5287 (2014).

[334] Sipahigil, A. *et al.* An integrated diamond nanophotonics platform for quantum-optical networks. *Science* **354**, 847–850 (2016).

[335] Wang, C., Kurtsiefer, C., Weinfurter, H. & Burchard, B. Single photon emission from SiV centres in diamond produced by ion implantation. *Journal of Physics B: Atomic, Molecular and Optical Physics* **39**, 37–41 (2006).

[336] Benedikter, J. *et al.* Cavity-Enhanced Single-Photon Source Based on the Silicon-Vacancy Center in Diamond. *Physical Review Applied* **7**, 024031 (2017).

[337] Rogers, L. J. *et al.* Electronic structure of the negatively charged silicon-vacancy center in diamond. *Physical Review B - Condensed Matter and Materials Physics* **89**, 235101 (2014).

[338] Rogers, L. J. *et al.* All-optical initialization, readout, and coherent preparation of single silicon-vacancy spins in diamond. *Physical Review Letters* **113**, 263602 (2014).

[339] Pingault, B. *et al.* All-Optical Formation of Coherent Dark States of Silicon-Vacancy Spins in Diamond. *Phys. Rev. Lett.* **113**, 263601 (2014).

[340] Pingault, B. *et al.* Coherent control of the silicon-vacancy spin in diamond. *Nature Communications* **8**, 15579 (2017).

[341] Kutter, C., Moll, H. P., Van Tol, J., Zuckermann, H., Maan, J. C. & Wyder, P. Electron-spin echoes at 604 GHz using far infrared lasers. *Physical Review Letters* **74**, 2925–2928 (1995).

[342] Becker, J. N. *et al.* All-Optical Control of the Silicon-Vacancy Spin in Diamond at Millikelvin Temperatures. *Physical Review Letters* **120**, 053603 (2018).

[343] Becker, J. N., Görlitz, J., Arend, C., Markham, M. & Becher, C. Ultrafast all-optical coherent control of single silicon vacancy colour centres in diamond. *Nature Communications* **7**, 13512 (2016).

[344] Zhou, Y., Rasmita, A., Li, K., Xiong, Q., Aharonovich, I. & Gao, W.-B. Coherent control of a strongly driven silicon vacancy optical transition in diamond. *Nature Communications* **8**, 14451 (2016).

[345] Zhang, J. L. *et al.* Complete Coherent Control of Silicon-Vacancies in Diamond Nanopillars Containing Single Defect Centers. *Conference on Lasers and Electro-Optics* **4**, 1317–1321 (2017).

[346] Sukachev, D. D., Sipahigil, A., Nguyen, C. T., Bhaskar, M. K., Evans, R. E., Jelezko, F. & Lukin, M. D. Silicon-Vacancy Spin Qubit in Diamond: A Quantum Memory Exceeding 10 ms with Single-Shot State Readout. *Physical Review Letters* **119**, 223602 (2017).

[347] Happer, W. Optical Pumping. *Reviews of Modern Physics* **44**, 169–250 (1972).

[348] Le Bellac, M. *A Short Introduction to Quantum Information and Quantum Computation* (Cambridge University Press, 2006).

[349] Breuer, H.-P. & Petruccione, F. *The theory of open quantum systems* (Oxford: Clarendon, 2007).

[350] Nunn, J. Quantum Optics - Graduate Class Script (2014).

[351] Ramsey, N. F. A molecular beam resonance method with separated oscillating fields. *Physical Review* **78**, 695–699 (1950).

[352] Press, D. *et al.* Ultrafast optical spin echo in a single quantum dot. *Nature Photonics* **4**, 367–370 (2010).

[353] Gaubatz, U., Rudecki, P., Schiemann, S. & Bergmann, K. Population transfer between molecular vibrational levels by stimulated Raman scattering with partially overlapping laser fields. A new concept and experimental results. *The Journal of Chemical Physics* **92**, 5363–5376 (1990).

[354] Vitanov, N. V., Rangelov, A. A., Shore, B. W. & Bergmann, K. Stimulated Raman adiabatic passage in physics, chemistry, and beyond. *Reviews of Modern Physics* **89**, 015006 (2017).

[355] Bergmann, K., Theuer, H. & Shore, B. W. Coherent population transfer among quantum states of atoms and molecules. *Rev. Mod. Phys.* **70**, 1003–1023 (1998).

[356] Rabi, I. I., Ramsey, N. F. & Schwinger, J. Use of rotating coordinates in magnetic resonance problems. *Reviews of Modern Physics* **26**, 167–171 (1954).

[357] Fox, M. *Quantum Optics: An Introduction (Oxford master series in physics; 15)* (Oxford University Press, Oxford ; New York, 2006).

[358] Fewell, M., Shore, B. & Bergmann, K. Coherent Population Transfer among Three States : Full Algebraic Solutions and the Relevance of Non Adiabatic Processes to Transfer by Delayed Pulses. *Australian Journal of Physics* **50**, 281–308 (1997).

[359] Messiah, A. *Quantum Mechanics* (North-Holland, Amsterdam, 1961).

[360] Kuklinski, J. R., Gaubatz, U., Hioe, F. T. & Bergmann, K. Adiabatic population transfer in a three-level system driven by delayed laser pulses. *Physical Review A* **40**, 6741 (1989).

[361] Shore, B. W. *Manipulating Quantum Structures using Laser Pulses* (Cambridge University Press, Cambridge, 2011).

[362] Klein, J., Beil, F. & Halfmann, T. Robust population transfer by stimulated raman adiabatic passage in a Pr^{3+}:Y_2SiO_5 crystal. *Physical Review Letters* **99**, 113003 (2007).

[363] Grigoryan, G. G., Nikoghosyan, G. V., Halfmann, T., Pashayan-Leroy, Y. T., Leroy, C. & Guérin, S. Theory of the bright-state stimulated raman adiabatic passage. *Physical Review A - Atomic, Molecular, and Optical Physics* **80**, 033402 (2009).

[364] Vitanov, N. V. & Stenholm, S. Analytic properties and effective two-level problems in stimulated Raman adiabatic passage. *Physical Review A - Atomic, Molecular, and Optical Physics* **55**, 648–660 (1997).

[365] Cvijetic, M. & Djordjevic, I. B. *Advanced Optical Communications Systems and Networks* (Artech House, Boston, 2013).

[366] New, G. *Introduction to Nonlinear Optics* (Cambridge University Press, Cambridge ; New York, 2011).

[367] Mukherjee, N. & Zare, R. N. Stark-induced adiabatic Raman passage for preparing polarized molecules. *The Journal of Chemical Physics* **135**, 024201 (2011).

[368] Perreault, W. E., Mukherjee, N. & Zare, R. N. Preparation of a selected high vibrational energy level of isolated molecules. *The Journal of Chemical Physics* **145**, 154203 (2016).

[369] Bassett, L. C., Heremans, F. J., Christle, D. J., Yale, C. G., Burkard, G., Buckley, B. B. & Awschalom, D. D. Ultrafast optical control of orbital and spin dynamics in a solid-state defect. *Science* **345**, 6202 (2014).

[370] Acosta, V. M. *et al.* Dynamic stabilization of the optical resonances of single nitrogen-vacancy centers in diamond. *Physical Review Letters* **108**, 206401 (2012).

[371] Batalov, A. *et al.* Low Temperature Studies of the Excited-State Structure of Negatively Charged Nitrogen-Vacancy Color Centers in Diamond. *Physical Review Letters* **102**, 195506 (2009).

[372] Jobez, P., Usmani, I., Timoney, N., Laplane, C., Gisin, N. & Afzelius, M. Cavity-enhanced storage in an optical spin-wave memory. *New Journal of Physics* **16**, 083005 (2014).

[373] Putz, S. *et al.* Spectral hole burning and its application in microwave photonics. *Nature Photonics* **11**, 36–39 (2017).

[374] Tamarat, P. *et al.* Spin-flip and spin-conserving optical transitions of the nitrogen-vacancy centre in diamond. *New Journal of Physics* **10**, 045004 (2008).

[375] Tamarat, P. *et al.* Stark shift control of single optical centers in diamond. *Physical Review Letters* **97**, 083002 (2006).

[376] Tamm, I. E. *Fundamentals of the Theory of Electricity* (Mir Publishers, Moscow, 1979), english translation edn.

[377] Reim, K. F., Michelberger, P., Lee, K. C., Nunn, J., Langford, N. K. & Walmsley, I. A. Single-photon-level quantum memory at room temperature. *Physical Review Letters* **107**, 053603 (2011).

[378] Peter, F. Über Brechungsindizes und Absorptionskonstanten des Diamanten zwischen 644 und 226 mμ. *Zeitschrift für Physik* **15**, 358–368 (1923).

[379] Sprague, M. R. *et al.* Broadband single-photon-level memory in a hollow-core photonic crystal fibre. *Nature Photonics* **8**, 287–291 (2014).

[380] Vandersypen, L. M. K. & Chuang, I. L. NMR techniques for quantum control and computation. *Reviews of Modern Physics of Modern Physics* **76**, 1037–1069 (2004).

[381] Baaquie, B. E. *The Theoretical Foundations of Quantum Mechanics* (Springer, New York, 2013).

[382] Mourou, G., Stancampiano, C. V., Antonetti, A. & Orszag, A. Picosecond microwave pulses generated with a subpicosecond laser-driven semiconductor switch. *Applied Physics Letters* **39**, 295–296 (1981).

[383] Press, D., Ladd, T. D., Zhang, B. & Yamamoto, Y. Complete quantum control of a single quantum dot spin using ultrafast optical pulses. *Nature* **456**, 218–221 (2008).

[384] Lin, C. K., Wang, Y. H., Chang, H. C., Hayashi, M. & Lin, S. H. One- and two-photon absorption properties of diamond nitrogen-vacancy defect centers: A theoretical study. *Journal of Chemical Physics* **129**, 124714 (2008).

[385] Hornstra, J. Dislocation in the diamond lattice. *Journal of Physics and Chemistry of Solids* **5**, 129–141 (1958).

[386] Zhu, W., Badzian, A. R. & Messier, R. Structural imperfections in cvd diamond films. *Journal of Materials Research* **4**, 659663 (1989).

[387] Yang, N., Zong, W., Li, Z. & Sun, T. The dependency of diamond lapping surface morphology on crystal orientation. *The International Journal of Advanced Manufacturing Technology* **77**, 1029–1034 (2015).

[388] Spring, J. B. *Single photon generation and quantum computing with integrated photonics*. Ph.D. thesis, Oriel College, University of Oxford, United Kingdom (2014).

[389] McMaster, W. H. Polarization and the Stokes Parameters. *American Journal of Physics* **22**, 351 (1954).

[390] Hell, S. W. & Wichmann, J. Breaking the diffraction resolution limit by stimulated emission: stimulated-emission-depletion fluorescence microscopy. *Optics Letters* **19**, 780–782 (1994).

[391] Klar, T. A. & Hell, S. W. Subdiffraction resolution in far-field fluorescence microscopy. *Optics Letters* **24**, 954–956 (1999).

[392] Hepp, C. *Electronic Structure of the Silicon Vacancy Color Center in Diamond*. Ph.D. thesis, Universität des Saarlandes (2014).

[393] Dietrich, A., Jahnke, K. D., Binder, J. M., Teraji, T., Isoya, J., Rogers, L. J. & Jelezko, F. Isotopically varying spectral features of silicon-vacancy in diamond. *New Journal of Physics* **16**, 113019 (2014).

[394] Weinzetl, C., Görlitz, J., Becker, J. N., Walmsley, I. A., Poem, E., Nunn, J. & Becher, C. Coherent control and wave mixing in an ensemble of silicon-vacancy centers in diamond. *Phys. Rev. Lett.* **122**, 063601 (2019).

[395] Nunn, J. *et al.* Theory of noise suppression in Λ-type quantum memories by means of a cavity. *Phys. Rev. A* **96**, 012338 (2017).

[396] Belsley, M., Smithey, D. T., Wedding, K. & Raymer, M. G. Observation of extreme sensitivity to induced molecular coherence in stimulated Raman scattering. *Physical Review A* **48**, 1514–1525 (1993).

[397] Kosachiov, D. V., Matisov, B. G. & Rozhdestvensky, Y. V. Coherent phenomena in multilevel systems with closed interaction contour. *Journal of Physics B: Atomic, Molecular and Optical Physics* **25**, 2473–2488 (1999).

[398] Lugani, J. *et al.* Phase-sensitive amplification via coherent population oscillations in metastable helium at room temperature. *Opt. Lett.* **41**, 4731–4734 (2016).

[399] Neveu, P., Banerjee, C., Lugani, J., Bretenaker, F., Brion, E. & Goldfarb, F. Phase Sensitive Amplification Enabled by Coherent Population Trapping. *New Journal of Physics* **20**, 083043 (2018).

[400] Shahrokhshahi, R., Sagona-Stophel, S., Jordaan, B., Namazi, M. & Figueroa, E. Room temperature conditional π-phase shifts mediated by simultaneously propagating single-photon level pulses (2018). arXiv:1803.07012.

[401] Runge, C. Ueber die numerische Auflösung von Differentialgleichungen. *Mathematische Annalen* **46**, 167–178 (1895).

[402] Kutta, W. Beitrag zur näherungsweisen Integration totaler Differentialgleichungen. *Zeitschrift für Mathematik und Physik* **46**, 435–453 (1901).

[403] Heister, T. & Rebholz, L. G. *Scientific Computing : For Scientists and Engineers* (De Gruyter Textbook, Berlin/Boston, 2015).

[404] Trefethen, L. N. Chebyshev Differentiation Matrices. In *Spectral Methods in MATLAB*, chap. 6 (Society for Industrial and Applied Mathematics (SIAM), Oxford University, Oxford, England, 2000).

[405] Trefethen, L. N. Polynomial Interpolation and Clustered Grids. In *Spectral Methods in MATLAB*, chap. 5 (Society for Industrial and Applied Mathematics (SIAM), Oxford University, Oxford, England, 2000).

[406] Wu, C. B., Raymer, M. G., Wang, Y. Y. & Benabid, F. Quantum theory of phase correlations in optical frequency combs generated by stimulated Raman scattering. *Physical Review A* **82**, 053834 (2010).

[407] Lü, B., Burkett, W. H. & Xiao, M. Nondegenerate four-wave mixing in a double-Λ system under the influence of coherent population trapping. *Optics Letters* **23**, 804–806 (1998).

[408] Wang, S., Ducreay, D. G., Pina, R., Yan, M. & Zhu, Y. Coherent population trapping and four-wave mixing via dark states in a Doppler-broadened open Rb system. *Physical Review A - Atomic, Molecular, and Optical Physics* **61**, 033805 (2000).

[409] Hemmer, P. R., Katz, D. P., Donoghue, J., Shahriar, M. S., Kumar, P. & Cronin-Golomb, M. Efficient low-intensity optical phase conjugation based on coherent population trapping in sodium. *Opt. Lett.* **20**, 982–984 (1995).

[410] Wang, D. *et al.* Strong Coherent Light Amplification with Double Electromagnetically Induced Transparency Coherences. *Scientific Reports* **7**, 5796 (2017).

[411] Czerny, M. & Turner, A. F. Über den Astigmatismus bei Spiegelspektrometern. *Zeitschrift für Physik* **61**, 792–797 (1930).

[412] Prajapati, N., Romanov, G. & Novikova, I. Suppression of four-wave mixing in hot rubidium vapor using ladder scheme raman absorption. *J. Opt. Soc. Am. B* **34**, 1994–1999 (2017).

[413] Harris, S. E. & Yamamoto, Y. Photon switching by quantum interference. *Phys. Rev. Lett.* **81**, 3611–3614 (1998).

[414] Kang, H., Hernandez, G., Zhang, J. & Zhu, Y. Phase-controlled light switching at low light levels. *Physical Review A - Atomic, Molecular, and Optical Physics* **73**, 011802(R) (2006).

[415] Beck, K. M., Hosseini, M., Duan, Y. & Vuletić, V. Large conditional single-photon cross-phase modulation. *Proceedings of the National Academy of Sciences of the United States of America* **113**, 9740–9744 (2016).

[416] Iwasaki, T. *et al.* Germanium-Vacancy Single Color Centers in Diamond. *Scientific Reports* **5**, 12882 (2015).

[417] Ralchenko, V. G. *et al.* Observation of the Ge-vacancy color center in microcrystalline diamond films. *Bulletin of the Lebedev Physics Institute* **42**, 165–168 (2015).

[418] Siyushev, P. *et al.* Optical and microwave control of germanium-vacancy center spins in diamond. *Physical Review B* **96**, 081201(R) (2017).

[419] Iwasaki, T., Miyamoto, Y., Taniguchi, T., Siyushev, P., Metsch, M. H., Jelezko, F. & Hatano, M. Tin-Vacancy Quantum Emitters in Diamond. *Physical Review Letters* **119**, 253601 (2017).

[420] Tchernij, S. D. *et al.* Single-Photon-Emitting Optical Centers in Diamond Fabricated upon Sn Implantation. *ACS Photonics* **4**, 2580–2586 (2017).

[421] Larico, R., Justo, J. F., Machado, W. V. M. & Assali, L. V. C. Electronic properties and hyperfine fields of nickel-related complexes in diamond. *Physical Review B - Condensed Matter and Materials Physics* **79**, 115202 (2009).

[422] Thiering, G. & Gali, A. *Ab initio* magneto-optical spectrum of Group-IV – Vacancy color centers in diamond. *Physical Review X* 021063 (2018).

[423] Trusheim, M. E. *et al.* Lead-Related Quantum Emitters in Diamond (2018). arXiv:1805.12202.

[424] Iakoubovskii, K. Ni-vacancy defect in diamond detected by electron spin resonance. *Physical Review B - Condensed Matter and Materials Physics* **70**, 205211 (2004).

[425] Londero, E., Bourgeois, E., Nesladek, M. & Gali, A. Identification of nickel-vacancy defects by combining experimental and ab initio simulated photocurrent spectra. *Physical Review B* **97**, 241202 (2018).

[426] Ekimov, E. A. *et al.* Germaniumvacancy color center in isotopically enriched diamonds synthesized at high pressures. *JETP Letters* **102**, 701–706 (2015).

[427] Iachello, F. *Lie Algebras and Applications* (Springer, Berlin, Heidelberg, 2006).

[428] Axline, C. J. *Building Blocks for Modular Circuit QED Quantum Computing Building Blocks for Modular Circuit QED Quantum Computing.* D.Phil. Thesis, Yale University (2018).

[429] Kumar, K. S., Vepsäläinen, A., Danilin, S. & Paraoanu, G. S. Stimulated Raman adiabatic passage in a three-level superconducting circuit. *Nature Communications* **7**, 10628 (2016).

[430] Abdumalikov, A. A., Astafiev, O., Zagoskin, A. M., Pashkin, Y. A., Nakamura, Y. & Tsai, J. S. Electromagnetically induced transparency on a single artificial atom. *Physical Review Letters* **104**, 193601 (2010).

Appendix A

Optical pumping - Solutions to the rate equations

Full algebraic solution to the coupled linear first-order differential equations ((4.1) - (4.3)) for the description of optical pumping in a three-level Λ-system as shown in Fig. A.1:

$$N_1(t) = \frac{A_1}{D}(N_1(0)+N_2(0)+N_3(0)) - \frac{B_1}{D}\left(\cosh\left(\frac{E}{2}t\right) + \frac{C_1}{B_1 E}\sinh\left(\frac{E}{2}t\right)\right)e^{-\frac{1}{2}Ft}, \quad \text{(A.1)}$$

$$N_2(t) = \frac{A_2}{D}(N_1(0)+N_2(0)+N_3(0)) - \frac{B_2}{D}\left(\cosh\left(\frac{E}{2}t\right) - \frac{C_2}{B_2 E}\sinh\left(\frac{E}{2}t\right)\right)e^{-\frac{1}{2}Ft}, \quad \text{(A.2)}$$

$$N_3(t) = \frac{A_3}{D}(N_1(0)+N_2(0)+N_3(0)) + \frac{B_3}{D}\left(\cosh\left(\frac{E}{2}t\right) - \frac{C_3}{B_3 E}\sinh\left(\frac{E}{2}t\right)\right)e^{-\frac{1}{2}Ft}, \quad \text{(A.3)}$$

with an initial population distribution of $N_1(0)$, $N_2(0)$ and $N_3(0)$, and where

$$A_1 = \Gamma_{21}(\Gamma_{31}+\Gamma_{32}+R) + \Gamma_{31}R, \quad \text{(A.4)}$$

$$A_2 = \Gamma_{12}(\Gamma_{31}+\Gamma_{32}+R), \quad \text{(A.5)}$$

$$A_3 = \Gamma_{12}R, \quad \text{(A.6)}$$

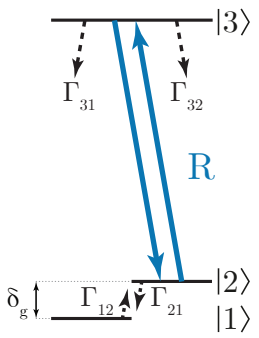


Figure A.1: Optical pumping in a three-level Λ-system with a ground state splitting of δ_g. A coherent laser field is applied resonantly to transition $|2\rangle - |3\rangle$ generating rates of stimulated absorption ($|2\rangle \rightarrow |3\rangle$) and stimulated emission ($|2\rangle \leftarrow |3\rangle$) of equal amount R. Decay rates Γ_{ij} from state $|i\rangle$ to state $|j\rangle$ are indicated as dashed arrows. Figure identical to Fig. 4.1 (a).

$$\begin{aligned} B_1 =& (-\Gamma_{12}\Gamma_{31} - 2\Gamma_{12}R)\, N_1(0) \\ &+ \Gamma_{12}\Gamma_{32}\,(-N_1(0) + N_2(0) + N_3(0)) \\ &+ (\Gamma_{21}\Gamma_{31} + \Gamma_{21}R + \Gamma_{31}R)\,(N_2(0) + N_3(0)), \end{aligned} \tag{A.7}$$

$$\begin{aligned} B_2 =& (\Gamma_{12}\Gamma_{31} + \Gamma_{12}\Gamma_{32})\,(N_1(0) + N_3(0)) \\ &- (\Gamma_{21}\Gamma_{31} + \Gamma_{21}\Gamma_{32} + \Gamma_{21}R + \Gamma_{31}R)\, N_2(0) \\ &+ \Gamma_{12}R\,(N_1(0) - N_2(0) + N_3(0)), \end{aligned} \tag{A.8}$$

$$\begin{aligned} B_3 =& (\Gamma_{12}\Gamma_{31} + \Gamma_{12}\Gamma_{32} + \Gamma_{21}\Gamma_{31} + \Gamma_{21}\Gamma_{32} + \Gamma_{21}R + \Gamma_{31}R)\, N_3(0) \\ &- \Gamma_{12}R\,(N_1(0) + N_2(0) - N_3(0)), \end{aligned} \tag{A.9}$$

$$
\begin{aligned}
C_1 =&(\Gamma_{12}^2\Gamma_{31} - \Gamma_{12}\Gamma_{32}^2 + \Gamma_{12}^2\Gamma_{32} - 4\Gamma_{12}R^2 + 2\Gamma_{12}^2R - 4\Gamma_{12}\Gamma_{32}R)\, N_1(0) \\
&- \Gamma_{12}\Gamma_{31}^2\,(N_1(0) + 2N_3(0)) \\
&+ (\Gamma_{21}\Gamma_{31}^2 - \Gamma_{21}^2\Gamma_{31} - \Gamma_{21}^2\Gamma_{32} - \Gamma_{21}^2R + \Gamma_{31}^2R)\,(N_2(0) - N_3(0)) \\
&+ (\Gamma_{21}\Gamma_{32}^2 + 2\Gamma_{21}R^2 + 2\Gamma_{31}R^2 + 2\Gamma_{21}\Gamma_{31}R + 3\Gamma_{21}\Gamma_{32}R + \Gamma_{31}\Gamma_{32}R)\,(N_2(0) + N_3(0)) \\
&+ (\Gamma_{12}\Gamma_{21}\Gamma_{31} + \Gamma_{12}\Gamma_{21}\Gamma_{32} - 2\Gamma_{12}\Gamma_{31}\Gamma_{32})\,(N_1(0) - N_2(0) + N_3(0)) \\
&+ \Gamma_{12}\Gamma_{21}R\,(-3N_2(0) + N_3(0)) + \Gamma_{12}\Gamma_{31}R\,(-2N_1(0) + N_2(0) - 3N_3(0)),
\end{aligned}
\tag{A.10}
$$

$$
\begin{aligned}
C_2 =&-2\Gamma_{12}\Gamma_{31}\Gamma_{32}\,N_1(0) + (-\Gamma_{21}^2\Gamma_{31} - \Gamma_{21}^2\Gamma_{32} - \Gamma_{21}^2R + \Gamma_{31}^2R)\,N_2(0) \\
&+ (2\Gamma_{21}R^2 + 2\Gamma_{31}R^2 + 2\Gamma_{21}\Gamma_{31}R)\,N_3(0) \\
&+ (\Gamma_{12}^2\Gamma_{31} - \Gamma_{12}\Gamma_{32}^2 + \Gamma_{12}^2\Gamma_{32})\,(N_1(0) - N_3(0)) \\
&- \Gamma_{12}\Gamma_{31}R\,(N_1(0) + N_3(0)) + 2\Gamma_{21}\Gamma_{31}\Gamma_{32}\,(N_2(0) + N_3(0)) \\
&+ (\Gamma_{21}\Gamma_{32}^2 + \Gamma_{31}\Gamma_{32}R)\,(N_2(0) + 2N_3(0)) + \Gamma_{21}\Gamma_{32}R\,(N_2(0) + 4N_3(0)) \\
&+ \Gamma_{12}\Gamma_{31}^2\,(-N_1(0) + N_2(0) - N_3(0)) - 2\Gamma_{12}R^2\,(N_1(0) + N_2(0) - N_3(0)) \\
&+ \Gamma_{12}^2R\,(3N_1(0) + N_2(0) - N_3(0)) + (\Gamma_{12}\Gamma_{21}\Gamma_{31} + \Gamma_{12}\Gamma_{21}\Gamma_{32})\,(N_1(0) - N_2(0) - N_3(0)) \\
&+ \Gamma_{12}\Gamma_{21}R\,(N_1(0) - 2N_2(0) - N_3(0)) + \Gamma_{12}\Gamma_{32}R\,(-3N_1(0) - N_2(0) + 3N_3(0)),
\end{aligned}
\tag{A.11}
$$

$$
\begin{aligned}
C_3 = (&\Gamma_{12}\Gamma_{31}^2 - \Gamma_{12}^2\Gamma_{31} + \Gamma_{12}\Gamma_{32}^2 - \Gamma_{12}^2\Gamma_{32} + \Gamma_{21}\Gamma_{31}^2 - \Gamma_{21}^2\Gamma_{31} + \Gamma_{21}\Gamma_{32}^2 \\
&- \Gamma_{21}^2\Gamma_{32} - \Gamma_{21}^2 R + \Gamma_{31}^2 R - 2\Gamma_{12}\Gamma_{21}\Gamma_{31} - 2\Gamma_{12}\Gamma_{21}\Gamma_{32} + 2\Gamma_{12}\Gamma_{31}\Gamma_{32} \\
&+ 2\Gamma_{21}\Gamma_{31}\Gamma_{32} + \Gamma_{31}\Gamma_{32}R)\, N_3(0) \\
&- 2(\Gamma_{21}R^2 + \Gamma_{31}R^2 + \Gamma_{21}\Gamma_{31}R)\, N_2(0) + 2\Gamma_{12}R^2\,(N_1(0) - N_2(0) + N_3(0)) \\
&+ \Gamma_{12}^2 R\,(N_1(0) + N_2(0) - N_3(0)) + \Gamma_{12}\Gamma_{21}R\,(N_1(0) + N_2(0) - 2N_3(0)) \\
&+ \Gamma_{12}\Gamma_{31}R\,(N_1(0) - N_2(0) + 2N_3(0)) + \Gamma_{12}\Gamma_{32}R\,(N_1(0) - N_2(0) + 3N_3(0)) \\
&+ \Gamma_{21}\Gamma_{32}R\,(-2N_2(0) + N_3(0)),
\end{aligned}
\tag{A.12}
$$

$$
D = \Gamma_{12}(\Gamma_{31} + \Gamma_{32} + 2R) + \Gamma_{21}(\Gamma_{31} + \Gamma_{32} + R) + \Gamma_{31}R, \tag{A.13}
$$

$$
\begin{aligned}
E = (&\Gamma_{12}(\Gamma_{12} + 2\Gamma_{21} - 2\Gamma_{31} - 2\Gamma_{32} - 4R) \\
&+ \Gamma_{21}(\Gamma_{21} - 2\Gamma_{31} - 2\Gamma_{32}) + \Gamma_{31}(\Gamma_{31} + 2\Gamma_{32}) \\
&+ \Gamma_{32}(\Gamma_{32} + 4R) + 4R^2)^{\frac{1}{2}},
\end{aligned}
\tag{A.14}
$$

$$
F = \Gamma_{12} + \Gamma_{21} + \Gamma_{31} + \Gamma_{32} + 2R. \tag{A.15}
$$

Appendix B

Optical Bloch equations for four-level systems

B.1 Hamiltonian of a four-level system with four interacting electromagnetic fields in rotating wave approximation

In the following, the interaction of four electromagnetic fields with an atomic-like system with fixed energy levels is described with classical fields and quantised energy levels.

The Hamiltonian $\mathcal{H}$ of the light-atom system can be separated into the Hamiltonian of the undisturbed four-level system $\mathcal{H}_0$ and the Hamiltonian of the system-field interaction $\mathcal{I}$,

$$\mathcal{H} = \mathcal{H}_0 + \mathcal{I}. \tag{B.1}$$

The Hamiltonian of the system $\mathcal{H}_0$ is given by the energies of its eigenstates as

$$\begin{aligned}\mathcal{H}_0 &= \hbar\omega_1 |1\rangle\langle 1| + \hbar\omega_2 |2\rangle\langle 2| + \hbar\omega_3 |3\rangle\langle 3| + \hbar\omega_4 |4\rangle\langle 4| \\ &= \sum_{i=1}^{4} \hbar\omega_i |i\rangle\langle i| = \sum_{i=1}^{4} E_i |i\rangle\langle i| \,. \end{aligned} \tag{B.2}$$

Here, $|i\rangle$ are the energy states of the system, which are used as eigenstates of the Hamiltonian. By this definition, the Hamiltonian of the system in matrix representation is diagonal with the state energies $E_i = \hbar\omega_i$ as eigenvalues, where $\hbar$ is the reduced Planck constant and ω_i the angular frequency attributed to the energy level $|i\rangle$, with $\omega_1 < \omega_2 < \omega_3 < \omega_4$ ($\omega_i < \omega_{i+1}$).

The interaction Hamiltonian $\mathcal{I}$ describes the interaction of the four different classical electromagnetic fields with the atomic system, each addressing one specific transition between the energy states only. The auxiliary field (A) couples to the optical transition between the states $|1\rangle$ and $|3\rangle$. The pump field (P) couples to the states $|2\rangle$ and $|3\rangle$, the signal field (S) couples to the states $|1\rangle$ and $|4\rangle$, and the control field (C) couples to the states $|2\rangle$ and $|4\rangle$. The transition $|1\rangle \leftrightarrow |2\rangle$ and $|3\rangle \leftrightarrow |4\rangle$ are assumed to be forbidden. All forbidden and allowed transitions are depicted in Fig. B.1. Unwanted couplings are excluded from further considerations. In Table B.1, all fields, the coupled states, as well as the dipole moments of the transitions are given. Therefore, the interaction Hamiltonian is composed of four

		Coupled states		
Field name	Abbreviation	lower	upper	Dipole moment
Signal	S	$\|1\rangle$	$\|4\rangle$	d_α
Control	C	$\|2\rangle$	$\|4\rangle$	d_β
Auxilary	A	$\|1\rangle$	$\|3\rangle$	d_γ
Pump	P	$\|2\rangle$	$\|3\rangle$	d_δ

Table B.1: Four-level system: Definition of fields and transitions.

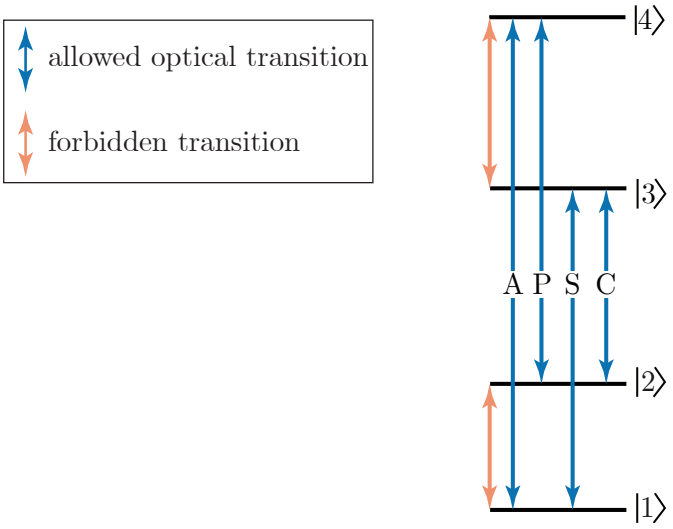


Figure B.1: Four-level system with four applied electromagnetic fields.

elements:

$$\mathcal{I} = \mathcal{I}_A + \mathcal{I}_P + \mathcal{I}_S + \mathcal{I}_C. \tag{B.3}$$

In dipole-approximation these interaction Hamiltonians can be written as

$$\mathcal{I}_S = -\vec{d}_\alpha \vec{E}_S = -\frac{1}{2}\vec{d}_\alpha \left(\vec{E}_{0,S} e^{-i\omega_S t} + \vec{E}^*_{0,S} e^{i\omega_S t}\right), \tag{B.4}$$

$$\mathcal{I}_C = -\vec{d}_\beta \vec{E}_C = -\frac{1}{2}\vec{d}_\beta \left(\vec{E}_{0,C} e^{-i\omega_C t} + \vec{E}^*_{0,C} e^{i\omega_C t}\right), \tag{B.5}$$

$$\mathcal{I}_A = -\vec{d}_\gamma \vec{E}_A = -\frac{1}{2}\vec{d}_\gamma \left(\vec{E}_{0,A} e^{-i\omega_A t} + \vec{E}^*_{0,A} e^{i\omega_A t}\right), \tag{B.6}$$

$$\mathcal{I}_P = -\vec{d}_\delta \vec{E}_P = -\frac{1}{2}\vec{d}_\delta \left(\vec{E}_{0,P} e^{-i\omega_P t} + \vec{E}^*_{0,P} e^{i\omega_P t}\right), \tag{B.7}$$

with $\vec{E}_{0,X}$, the time-independent amplitude of the electric field $\vec{E}_X$, and

$$\vec{d}_\alpha = \vec{d}_{41}\,|4\rangle\langle 1| + \vec{d}^{\,*}_{41}\,|1\rangle\langle 4|\,, \tag{B.8}$$

$$\vec{d}_\beta = \vec{d}_{42}\,|4\rangle\langle 2| + \vec{d}^{\,*}_{42}\,|2\rangle\langle 4|\,, \tag{B.9}$$

$$\vec{d}_\gamma = \vec{d}_{31}\,|3\rangle\langle 1| + \vec{d}^{\,*}_{31}\,|1\rangle\langle 3|\,, \tag{B.10}$$

$$\vec{d}_\delta = \vec{d}_{32}\,|3\rangle\langle 2| + \vec{d}^{\,*}_{32}\,|2\rangle\langle 3|\,, \tag{B.11}$$

where $\vec{d}_{nm}$ is the electric dipole moment

$$\vec{d}_{nm} = \begin{cases} 0 & \text{for } n = m \text{ due to negative parity} \\ & \text{of the atomic dipole operator (for } \vec{r} \to -\vec{r}\text{)}\,[189], \\ \langle n|\,\vec{d}\,|m\rangle & \text{for } n \neq m \text{ mediating an electric interaction} \\ & \text{between the energy states } |n\rangle \text{ and } |m\rangle. \end{cases} \tag{B.12}$$

The asterisk indicates the complex conjugate of the dipole moment. The total electric dipole moment of the atomic system, $\vec{d}$, is the sum of all dipole moments of the allowed transitions,

$$\vec{d} = \vec{d}_\alpha + \vec{d}_\beta + \vec{d}_\gamma + \vec{d}_\delta. \tag{B.13}$$

Substituting equations (B.8) - (B.11) into equations (B.4) - (B.7), the interaction Hamiltoni-

ans are given by:

$$\mathcal{I}_S = -\frac{1}{2}\left(\vec{d}_{41}\left|4\right\rangle\!\left\langle 1\right| + \vec{d}^{*}_{41}\left|1\right\rangle\!\left\langle 4\right|\right)\left(\vec{E}_{0,S}e^{-i\omega_S t} + \vec{E}^{*}_{0,S}e^{i\omega_S t}\right), \tag{B.14}$$

$$\mathcal{I}_C = -\frac{1}{2}\left(\vec{d}_{42}\left|4\right\rangle\!\left\langle 2\right| + \vec{d}^{*}_{42}\left|2\right\rangle\!\left\langle 4\right|\right)\left(\vec{E}_{0,C}e^{-i\omega_C t} + \vec{E}^{*}_{0,C}e^{i\omega_C t}\right), \tag{B.15}$$

$$\mathcal{I}_A = -\frac{1}{2}\left(\vec{d}_{31}\left|3\right\rangle\!\left\langle 1\right| + \vec{d}^{*}_{31}\left|1\right\rangle\!\left\langle 3\right|\right)\left(\vec{E}_{0,A}e^{-i\omega_A t} + \vec{E}^{*}_{0,A}e^{i\omega_A t}\right), \tag{B.16}$$

$$\mathcal{I}_P = -\frac{1}{2}\left(\vec{d}_{32}\left|3\right\rangle\!\left\langle 2\right| + \vec{d}^{*}_{32}\left|2\right\rangle\!\left\langle 3\right|\right)\left(\vec{E}_{0,P}e^{-i\omega_P t} + \vec{E}^{*}_{0,P}e^{i\omega_P t}\right). \tag{B.17}$$

These equations can be simplified defining the Rabi frequencies as:

$$\begin{aligned}
\Omega_X &= -\frac{\vec{d}_{ij}\vec{E}_{0,X}}{\hbar}, \qquad \bar{\Omega}_X = -\frac{\vec{d}_{ij}\vec{E}^{*}_{0,X}}{\hbar} \text{ (counter rotating)},\\
\Omega^{*}_X &= -\frac{\vec{d}^{*}_{ij}\vec{E}^{*}_{0,X}}{\hbar}, \qquad \bar{\Omega}^{*}_X = -\frac{\vec{d}^{*}_{ij}\vec{E}_{0,X}}{\hbar} \text{ (counter rotating)},
\end{aligned} \tag{B.18}$$

for a triplet $\{X, i, j\}$, where X defines the optical field, i the upper and j the lower energy state. This definition is valid for the triplets $\{S, 4, 1\}$, $\{C, 4, 2\}$, $\{A, 3, 1\}$, and $\{P, 3, 2\}$. Using definition (B.18) for equations (B.14) - (B.17), it is possible to write in a general form:

$$\mathcal{I}_X = \frac{\hbar}{2}\left\{\left(e^{-i\omega_X t}\Omega_X + e^{i\omega_X t}\bar{\Omega}_X\right)\left|i\right\rangle\!\left\langle j\right| + \left(e^{-i\omega_X t}\bar{\Omega}^{*}_X + e^{i\omega_X t}\Omega^{*}_X\right)\left|j\right\rangle\!\left\langle i\right|\right\}. \tag{B.19}$$

This equation can be simplified eliminating fast rotating terms using the rotating wave approximation (RWA). For reasons of simplicity, the RWA is demonstrated for one of the four applied fields only but can be applied equivalently to all other fields. For the demonstration, the interaction Hamiltonian

$$\mathcal{I}_P = \frac{\hbar}{2}\left\{\left(e^{-i\omega_P t}\Omega_P + e^{i\omega_P t}\bar{\Omega}_P\right)\left|3\right\rangle\!\left\langle 2\right| + \left(e^{-i\omega_P t}\bar{\Omega}^{*}_P + e^{i\omega_P t}\Omega^{*}_P\right)\left|2\right\rangle\!\left\langle 3\right|\right\} \tag{B.20}$$

of the pump field is used. For the RWA it is advantageous to change into the interaction picture (IP). The IP describes the same physics and temporal evolution of the system as the Schrödinger picture (SP) but simplifies the description of field-atom interactions. For the transformation between the IP and SP the following rules apply:

State Vectors:

$$|\psi_{IP}(t)\rangle = e^{\frac{i}{\hbar}\mathcal{H}_0 t}\,|\psi_{SP}(t)\rangle \qquad \Longleftrightarrow\ |\psi_{SP}(t)\rangle = e^{-\frac{i}{\hbar}\mathcal{H}_0 t}\,|\psi_{IP}(t)\rangle \tag{B.21}$$

Operators:

$$\begin{aligned}\mathcal{H}_{IP}(t) &= e^{\frac{i}{\hbar}\mathcal{H}_0 t}\mathcal{H}_{SP}e^{-\frac{i}{\hbar}\mathcal{H}_0 t} \qquad &\Longleftrightarrow \mathcal{H}_{SP} &= e^{-\frac{i}{\hbar}\mathcal{H}_0 t}\mathcal{H}_{IP}(t)\,e^{\frac{i}{\hbar}\mathcal{H}_0 t}\\ &= U\mathcal{H}_{SP}U^{\dagger} &&= U^{\dagger}\mathcal{H}_{IP}(t)\,U\end{aligned} \tag{B.22}$$

$$\text{with} \qquad U = e^{\frac{i}{\hbar}\mathcal{H}_0 t} = \sum_{j=1}^{4} e^{i\omega_j t}\,|j\rangle\langle j|\,. \tag{B.23}$$

$\mathcal{H}_0$ is the time-independent Hamiltonian describing the unperturbed four-level system already introduced above (see equation (B.2)). The time-independent Hamiltonian is the same in the SP as in the IP, as this operator commutes with itself leading to $\mathcal{H}_{0,SP} = \mathcal{H}_{0,IP}$ using equation (B.22). For equation (B.23) it is used that for square matrices A [427],

$$e^{\lambda A} = \sum_{n=1}^{\inf} \frac{(\lambda A)^n}{n!} = \sum_{n=1}^{\inf} \frac{\lambda^n}{n!} A^n. \tag{B.24}$$

Now, the interaction Hamiltonian $\mathcal{I}_P$ can be transformed into the IP:

$$\begin{aligned}
\mathcal{I}_{IP,P}(t) &= U\mathcal{I}_P U^\dagger \\
&= \frac{\hbar}{2}\left\{\left(\Omega_P e^{i(\omega_3-\omega_2-\omega_P)t} + \bar{\Omega}_P e^{i(\omega_3-\omega_2+\omega_P)t}\right)|3\rangle\langle 2| \right. \\
&\quad \left. + \left(\bar{\Omega}_P^* e^{-i(\omega_3-\omega_2+\omega_P)t} + \Omega_P^* e^{-i(\omega_3-\omega_2-\omega_P)t}\right)|2\rangle\langle 3|\right\} \\
&= \frac{\hbar}{2}\left\{\left(\Omega_P e^{i\delta_P t} + \bar{\Omega}_P e^{i(\delta_P+2\omega_P)t}\right)|3\rangle\langle 2| \right. \\
&\quad \left. + \left(\bar{\Omega}_P^* e^{-i(\delta_P+2\omega_P)t} + \Omega_P^* e^{-i\delta_P t}\right)|2\rangle\langle 3|\right\}, \qquad \text{(B.25)}
\end{aligned}$$

$$\text{where} \qquad \delta_P = \omega_3 - \omega_2 - \omega_P \ll \delta_P + 2\omega_P. \qquad \text{(B.26)}$$

Slowly (δ_P) and fast ($\delta_P + 2\omega_P$) rotating fields are found in the interaction. Fast rotating terms can be set to 0 as they average out to no effect over typical time scales τ of the system's evolution, where τ can be approximated to

$$\tau \approx \frac{2\pi}{\omega_3 - \omega_2} = \frac{2\pi}{\omega_P + \delta_P} \approx \frac{2\pi}{\omega_P}. \qquad \text{(B.27)}$$

Hence, the interaction Hamiltonian of field P in RWA is

$$\mathcal{I}_{IP,P}(t) = \frac{\hbar}{2}\left\{\Omega_P e^{i\delta_P t}|3\rangle\langle 2| + \Omega_P^* e^{-i\delta_P t}|2\rangle\langle 3|\right\}. \qquad \text{(B.28)}$$

The backtransformation into the Schrödinger picture, in which only state vectors are

time-dependent, leads to:

$$\begin{aligned}\mathcal{I}_P &= U^\dagger \mathcal{I}_{IP,P}\,(t)\,U \\ &= \frac{\hbar}{2}\left\{\Omega_P e^{-i\omega_P t}\,|3\rangle\langle 2| + \Omega_P^* e^{i\omega_P t}\,|2\rangle\langle 3|\right\}. \end{aligned} \tag{B.29}$$

Equivalently, the rest of the interaction Hamiltonians $\mathcal{I}_X$ are:

$$\mathcal{I}_S = \frac{\hbar}{2}\left\{\Omega_S e^{-i\omega_S t}\,|4\rangle\langle 1| + \Omega_S^* e^{i\omega_S t}\,|1\rangle\langle 4|\right\}, \tag{B.30}$$

$$\mathcal{I}_C = \frac{\hbar}{2}\left\{\Omega_C e^{-i\omega_C t}\,|4\rangle\langle 2| + \Omega_C^* e^{i\omega_C t}\,|2\rangle\langle 4|\right\}, \tag{B.31}$$

$$\mathcal{I}_A = \frac{\hbar}{2}\left\{\Omega_A e^{-i\omega_A t}\,|3\rangle\langle 1| + \Omega_A^* e^{i\omega_A t}\,|1\rangle\langle 3|\right\}. \tag{B.32}$$

Therefore, the complete Hamiltonian (see equations (B.1) and (B.3)) can be written as

$$\mathcal{H} = \frac{\hbar}{2}\begin{pmatrix} 2\omega_1 & 0 & \Omega_A^* e^{i\omega_A t} & \Omega_S^* e^{i\omega_S t} \\ 0 & 2\omega_2 & \Omega_P^* e^{i\omega_P t} & \Omega_C^* e^{i\omega_C t} \\ \Omega_A e^{-i\omega_A t} & \Omega_P e^{-i\omega_P t} & 2\omega_3 & 0 \\ \Omega_S e^{-i\omega_S t} & \Omega_C e^{-i\omega_C t} & 0 & 2\omega_4 \end{pmatrix}. \tag{B.33}$$

This Hamiltonian needs to be transformed into a multi-rotating frame, in which high frequencies are replaced by frequency differences. While describing the same physics the changes in the rotating frame are much slower and can be simulated more efficiently. The new Hamiltonian $\mathcal{H}'$ is generated by a time-dependent unitary transformation following [428]

$$\mathcal{H}' = U\mathcal{H}U^\dagger + i\hbar\frac{dU}{dt}U^\dagger. \tag{B.34}$$

The ansatz for the time-dependent unitary transformation U with a maximum degree of freedom can be chosen as

$$U = \sum_{j=1}^{4} e^{i(a_j\omega_1+b_j\omega_2+c_j\omega_3+d_j\omega_4+e_j\omega_A+f_j\omega_P+g_j\omega_S+h_j\omega_C)t} \left|j\right\rangle\!\left\langle j\right| \tag{B.35}$$

$$= \sum_{j=1}^{4} e^{i\mathbb{C}_j t} \left|j\right\rangle\!\left\langle j\right|, \tag{B.36}$$

$$\text{where} \qquad \mathbb{C}_j = a_j\omega_1 + b_j\omega_2 + c_j\omega_3 + d_j\omega_4 + e_j\omega_A + f_j\omega_P + g_j\omega_S + h_j\omega_C. \tag{B.37}$$

The transformation results in the new Hamiltonian of the general form of

$$\mathcal{H}' = \frac{\hbar}{2}\begin{pmatrix} 2\left(\omega_1 - \mathbb{C}_1\right) & 0 & \Omega_A^* e^{i(\omega_A+\mathbb{C}_1-\mathbb{C}_3)t} & \Omega_S^* e^{i(\omega_S+\mathbb{C}_1-\mathbb{C}_4)t} \\ 0 & 2\left(\omega_2 - \mathbb{C}_2\right) & \Omega_P^* e^{i(\omega_P+\mathbb{C}_2-\mathbb{C}_3)t} & \Omega_C^* e^{i(\omega_C+\mathbb{C}_2-\mathbb{C}_4)t} \\ \Omega_A e^{-i(\omega_A+\mathbb{C}_1-\mathbb{C}_3)t} & \Omega_P e^{-i(\omega_P+\mathbb{C}_2-\mathbb{C}_3)t} & 2\left(\omega_3 - \mathbb{C}_3\right) & 0 \\ \Omega_S e^{-i(\omega_S+\mathbb{C}_1-\mathbb{C}_4)t} & \Omega_C e^{-i(\omega_C+\mathbb{C}_2-\mathbb{C}_4)t} & 0 & 2\left(\omega_4 - \mathbb{C}_4\right) \end{pmatrix}. \tag{B.38}$$

Choosing the time-dependent unitary matrix as

$$U = e^{i(\omega_4-\omega_S)t} \left|1\right\rangle\!\left\langle 1\right| + e^{i(\omega_4-\omega_C)t} \left|2\right\rangle\!\left\langle 2\right| + e^{i\omega_3 t} \left|3\right\rangle\!\left\langle 3\right| + e^{i\omega_4 t} \left|4\right\rangle\!\left\langle 4\right| \tag{B.39}$$

$$= e^{i(\omega_1-\delta_S)t} \left|1\right\rangle\!\left\langle 1\right| + e^{i(\omega_2-\delta_C)t} \left|2\right\rangle\!\left\langle 2\right| + e^{i\omega_3 t} \left|3\right\rangle\!\left\langle 3\right| + e^{i\omega_4 t} \left|4\right\rangle\!\left\langle 4\right|, \tag{B.40}$$

the Hamiltonian simplifies to

$$\mathcal{H}' = \frac{\hbar}{2}\begin{pmatrix} 2\delta_S & 0 & \Omega_A^* e^{i(\delta_A-\delta_S)t} & \Omega_S^* \\ 0 & 2\delta_C & \Omega_P^* e^{i(\delta_P-\delta_C)t} & \Omega_C^* \\ \Omega_A e^{-i(\delta_A-\delta_S)t} & \Omega_P e^{-i(\delta_P-\delta_C)t} & 0 & 0 \\ \Omega_S & \Omega_C & 0 & 0 \end{pmatrix}. \tag{B.41}$$

Coefficients for the transformation were chosen, so that

$$\omega_S + \mathbb{C}_1 - \mathbb{C}_4 = 0, \tag{B.42}$$

$$\omega_C + \mathbb{C}_2 - \mathbb{C}_4 = 0, \tag{B.43}$$

$$\omega_3 - \mathbb{C}_3 = 0, \tag{B.44}$$

$$\omega_4 - \mathbb{C}_4 = 0, \tag{B.45}$$

and that $\omega_1 - \mathbb{C}_1$ and $\omega_2 - \mathbb{C}_2$ can be expressed as a linear combination of the detunings

$$\delta_A = \omega_A - (\omega_3 - \omega_1), \tag{B.46}$$

$$\delta_P = \omega_P - (\omega_3 - \omega_2), \tag{B.47}$$

$$\delta_S = \omega_S - (\omega_4 - \omega_1) \tag{B.48}$$

$$\text{and} \quad \delta_C = \omega_C - (\omega_4 - \omega_2). \tag{B.49}$$

B.2 Temporal evolution of a quantum system: The master equation in Lindblad form

In the SP the temporal evolution of a system can also be described using the density operator ρ. While the description of the temporal evolution of the quantum system with state vectors by the time-dependent Schrödinger equation[349] is possible, for open systems and mixed states the usage of the density operator is more appropriate to describe the temporal evolution and the coherence between two states of the quantum system. For a state, where the state vector $|\Phi\rangle$ is expressed in a complete basis of its eigenstates $|\phi_i\rangle$,

$$|\Phi\rangle = \sum_i c_i \, |\phi_i\rangle \, , \tag{B.50}$$

the density operator is called "pure" and has the following properties[381]:

$$\rho = |\Phi\rangle\langle\Phi| \qquad \text{Definition of the density operator for a pure state as projection operator} \tag{B.51}$$

$$\rho^2 = \rho \qquad \text{Idempotence} \tag{B.52}$$

$$\mathrm{tr}\,(\rho) = 1 \qquad \text{Conservation of state population} \tag{B.53}$$

$$\rho = \rho^\dagger \qquad \text{Hermiticity.} \tag{B.54}$$

In the case of a "mixed" state, where $\rho = \sum_{i=1}^{N} p_i \, |\psi_i\rangle\langle\psi_i|$ is the sum of orthonormal projection operators $|\psi_i\rangle\langle\psi_i|$ with probabilities p_i, the condition of idempotence (B.52) does not hold and $\mathrm{tr}\left(\rho^2\right) < 1$[381]. For "pure" and "mixed" states, the matrix representation in the

energy eigenstates of a four-level system, ρ is defined as

$$\rho = \begin{array}{c} \\ |1\rangle \\ |2\rangle \\ |3\rangle \\ |4\rangle \end{array} \begin{array}{c} \begin{array}{cccc} \langle 1| & \langle 2| & \langle 3| & \langle 4| \end{array} \\ \begin{pmatrix} \rho_{11} & \rho_{12} & \rho_{13} & \rho_{14} \\ \rho_{21} & \rho_{22} & \rho_{23} & \rho_{24} \\ \rho_{31} & \rho_{32} & \rho_{33} & \rho_{34} \\ \rho_{41} & \rho_{42} & \rho_{43} & \rho_{44} \end{pmatrix} \end{array}. \tag{B.55}$$

The temporal evolution of the density operator is governed by the master equation in Lindblad form[429]

$$\dot{\rho} = -\frac{i}{\hbar}\left[\mathcal{H}', \rho\right] + \mathcal{L}\left[\rho\right], \tag{B.56}$$

where $\mathcal{L}\left[\rho\right]$ is the Lindblad superoperator, which describes the decay between states as well as dephasing,[349]

$$\mathcal{L}\left[\rho\right] = \sum_{n,m=1}^{N^2} h_{n,m}\left(L_n \rho L_m^\dagger - \frac{1}{2}\left\{\rho, L_m^\dagger L_n\right\}\right) = \sum_{n,m=1}^{N^2} h_{n,m} X_{n,m}. \tag{B.57}$$

In order to calculate the Lindblad superoperator, the Lindblad operators $\{L_1 \dots L_{N^2}\}$ need to form an arbitrary linear basis $\mathbb{L}$ which spans the vector space of $N \times N$ matrices, where $N \times N$ is the dimension of the density matrix ρ. In the case of a four-level system the sum can be taken over the $N^2 = 4^2 = 16$ elements of the linear basis $\mathbb{L} = \{L_{ij} = |i\rangle\langle j|\,, \forall i, j \in \{1, 2, 3, 4\}\}$. $h_{n,m}$ is a $N^2 \times N^2$ coefficient matrix with all non-negative entries[349].

Choosing the two general basis matrices $L_n = L_{ab} = |a\rangle\langle b|$ and $L_m = L_{cd} = |c\rangle\langle d|$ with

the density operator ρ as defined in equation (B.55), the matrix $X_{n,m}$ can be written as:

$$X_{n,m} = \rho_{bd} \left|a\right\rangle\!\left\langle c\right| + \delta_{ac} \left(\rho_{1d} \left|1\right\rangle\!\left\langle b\right| + \rho_{2d} \left|2\right\rangle\!\left\langle b\right| + \rho_{3d} \left|3\right\rangle\!\left\langle b\right| + \rho_{4d} \left|4\right\rangle\!\left\langle b\right| \right.$$
$$\left. + \rho_{b1} \left|d\right\rangle\!\left\langle 1\right| + \rho_{b2} \left|d\right\rangle\!\left\langle 2\right| + \rho_{b3} \left|d\right\rangle\!\left\langle 3\right| + \rho_{b4} \left|d\right\rangle\!\left\langle 4\right| \right), \tag{B.58}$$

where δ_{ac} is a Dirac δ-function.

From an empirical point of view only terms can be preserved which describe changes of population and coherences due to changes in the population distributions (population decay and population dephasing), as well as decay of coherences over time (pure dephasing). All other terms expressing changes (increase and decrease) of coherence between two states influenced by the coherence between another couple of states, as well as changes in population due to coherence effects, are set to zero by an appropriate choice of the coefficient matrix h. This is possible by choosing $a = c$ and $b = d$. In consequence, in the basis $\mathbb{L}$, the coefficient matrix h reduces to a diagonal matrix $h = \mathrm{diag}\left(h_{11,11}, h_{12,12}, \ldots, h_{43,43}, h_{44,44}\right)$.

Furthermore, the Lindblad superoperator can be split into two parts,

$$\mathcal{L}\left[\rho\right] = \mathcal{P}\left[\rho\right] + \mathcal{D}\left[\rho\right]. \tag{B.59}$$

Population decay between states, as well as dephasing due to changes in population, is governed by $\mathcal{P}\left[\rho\right]$. $\mathcal{D}\left[\rho\right]$ describes pure dephasing, i.e. loss of coherence between the states of the four-level system. Dephasing of each individual state reduces the coherence between itself and all other states of the system. The two parts of the superoperator can be written

as

$$\mathcal{P}[\rho] = \sum_{\substack{i,j=1 \\ i\neq j}}^{4} \Gamma_{ij} \left(\rho_{ii} |i\rangle\langle i| - \frac{1}{2} \{\rho, |j\rangle\langle j|\} \right)$$
$$\text{and} \quad \mathcal{D}[\rho] = \sum_{i=1}^{4} \Gamma_{ii} \left(\rho_{ii} |i\rangle\langle i| - \frac{1}{2} \{\rho, |i\rangle\langle i|\} \right). \tag{B.60}$$

$\mathcal{P}[\rho]$ comprises all cases $L_n = L_m = |i\rangle\langle j|$ and $h_{ij,ij} = \Gamma_{ij}, \forall i, j \in \{1,2,3,4\}, i \neq j$. $\mathcal{D}[\rho]$ includes all cases where $L_n = L_m = |i\rangle\langle i|$ with $h_{ii,ii} = \Gamma_{ii}, \forall i \in \{1,2,3,4\}$. Following the properties of the coefficient matrix h, $\Gamma_{ij} \geq 0, \forall i, j \in \{1,2,3,4\}$. The full master equation in Lindblad form (see equation (B.56)) can be rewritten as

$$\dot{\rho} = -\frac{i}{\hbar} \left[\mathcal{H}', \rho\right] + \mathcal{P}[\rho] + \mathcal{D}[\rho]. \tag{B.61}$$

$\mathcal{P}[\rho]$ and $\mathcal{D}[\rho]$ can be restructured, so that the single matrix elements of ρ become apparent:

$$\mathcal{P}[\rho] = \sum_{\substack{i,j=1 \\ i\neq j}}^{4} \Gamma_{ij} \left(\rho_{ii} \left(|j\rangle\langle j| - |i\rangle\langle i|\right) - \frac{1}{2} \sum_{\substack{k=1 \\ k\neq i}}^{4} \left(\rho_{ik} |i\rangle\langle k| + \rho_{ki} |k\rangle\langle i|\right) \right),$$
$$\mathcal{D}[\rho] = -\frac{1}{2} \sum_{i=1}^{4} \Gamma_{ii} \left(\sum_{\substack{k=1 \\ k\neq i}}^{4} \left(\rho_{ik} |i\rangle\langle k| + \rho_{ki} |k\rangle\langle i|\right) \right), \tag{B.62}$$

which can be combined to the matrix elements

$$[\mathcal{P}+\mathcal{D}]_{ii} = \sum_{\substack{j=1 \\ j\neq i}}^{4} \left(\Gamma_{ji}\rho_{jj} - \Gamma_{ij}\rho_{ii}\right) \tag{B.63}$$

$$\text{and} \quad [\mathcal{P}+\mathcal{D}]_{ij} = -\frac{1}{2}\sum_{k=1}^{4} \left(\Gamma_{ik}+\Gamma_{jk}\right)\rho_{ij} = -\gamma_{ij}\rho_{ij}, \text{ for } i \neq j, \tag{B.64}$$

$$\text{with} \quad \gamma_{ij} = \frac{1}{2}\sum_{k=1}^{4} \left(\Gamma_{ik}+\Gamma_{jk}\right). \tag{B.65}$$

For the off-diagonal elements of the density operator ρ the coherence decay constants γ_{ij} between each state $|i\rangle$ and $|j\rangle$ satisfy the required hermitian condition $\gamma_{ij} = \gamma_{ji}^{*}$. Here, γ includes both pure and population dephasing.

In total, the Lindblad superoperator reads:

$$\begin{aligned}
\mathcal{L}[\rho] &= \sum_{i\neq j} C_{ij}\Gamma_i\rho_{ii}\left(|j\rangle\langle j| - |i\rangle\langle i|\right) - \sum_{i\neq j}\gamma_{ij}\rho_{ij}\,|i\rangle\langle j|\,, \text{ where } \sum_{i\neq j} C_{ij} = 1, \quad \forall i \\
&= \Gamma_1\rho_{11}\left(|2\rangle\langle 2| - |1\rangle\langle 1|\right) + \Gamma_2\rho_{22}\left(|1\rangle\langle 1| - |2\rangle\langle 2|\right) + C_{31}\Gamma_3\rho_{33}\left(|1\rangle\langle 1| - |3\rangle\langle 3|\right) \\
&\quad + C_{32}\Gamma_3\rho_{33}\left(|2\rangle\langle 2| - |3\rangle\langle 3|\right) + \Gamma_4\rho_{44}\left(|3\rangle\langle 3| - |4\rangle\langle 4|\right) - \sum_{i\neq j}\gamma_{ij}\rho_{ij}\,|i\rangle\langle j|\,,
\end{aligned} \tag{B.66}$$

with $C_{31} + C_{32} = 1$, and where Γ_i, $i \in \{1,2,3,4\}$, is the decay rate from state $|i\rangle$ as shown in Fig. B.2. γ_{ij} is the damping rate of the off-diagonal terms (dephasing) with $\gamma_{ij} = \gamma_{ji}$ [430].

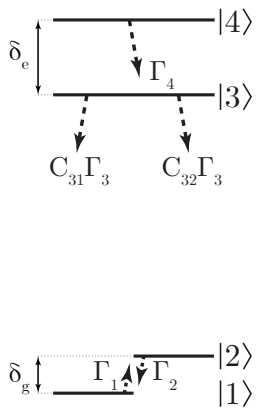


Figure B.2: Four-level system with decay rates Γ_i, $i \in \{1,2,3,4\}$, from state $|i\rangle$, ground state splitting δ_g, excited state splitting δ_e and $C_{31} + C_{32} = 1$.

B.3 Optical Bloch equations for a four-level system

In total, with the Lindblad superoperator determined and regarding equation (B.56), the four-level system interacting with four optical fields is described by a system of ten coupled differential equations, known as optical Bloch equations. The on-diagonal population terms are:

$$\dot{\rho}_{11} = -\frac{i}{2}\left\{\Omega_A^* e^{i(\delta_A-\delta_S)t}\rho_{31} + \Omega_S^*\rho_{41} - \Omega_A e^{-i(\delta_A-\delta_S)t}\rho_{13} - \Omega_S\rho_{14}\right\} - \Gamma_1\rho_{11} + \Gamma_2\rho_{22} + C_{31}\Gamma_3\rho_{33}, \tag{B.67}$$

$$\dot{\rho}_{22} = -\frac{i}{2}\left\{\Omega_P^* e^{i(\delta_P-\delta_C)t}\rho_{32} + \Omega_C^*\rho_{42} - \Omega_P e^{-i(\delta_P-\delta_C)t}\rho_{23} - \Omega_C\rho_{24}\right\} + \Gamma_1\rho_{11} - \Gamma_2\rho_{22} + C_{32}\Gamma_3\rho_{33}, \tag{B.68}$$

$$\dot{\rho}_{33} = -\frac{i}{2}\left\{\Omega_A e^{-i(\delta_A-\delta_S)t}\rho_{13} + \Omega_P e^{-i(\delta_P-\delta_C)t}\rho_{23} - \Omega_A^* e^{i(\delta_A-\delta_S)t}\rho_{31} - \Omega_P^* e^{i(\delta_P-\delta_C)t}\rho_{32}\right\} - \Gamma_3\rho_{33} + \Gamma_4\rho_{44}, \tag{B.69}$$

$$\dot{\rho}_{44} = -\frac{i}{2}\left\{\Omega_S\rho_{14} + \Omega_C\rho_{24} - \Omega_S^*\rho_{41} - \Omega_C^*\rho_{42}\right\} - \Gamma_4\rho_{44}. \tag{B.70}$$

The off-diagonal coherence terms are governed by:

$$\dot{\rho}_{12} = -\frac{i}{2}\left\{2\left(\delta_S - \delta_C\right)\rho_{12} + \Omega_A^* e^{i(\delta_A-\delta_S)t}\rho_{32} + \Omega_S^*\rho_{42} - \Omega_P e^{-i(\delta_P-\delta_C)t}\rho_{13} - \Omega_C\rho_{14}\right\}$$
$$- \gamma_{12}\rho_{12}, \tag{B.71}$$

$$\dot{\rho}_{13} = -\frac{i}{2}\left\{2\delta_S\rho_{13} + \Omega_A^* e^{i(\delta_A-\delta_S)t}\left(\rho_{33} - \rho_{11}\right) + \Omega_S^*\rho_{43} - \Omega_P^* e^{i(\delta_P-\delta_C)t}\rho_{12}\right\}$$
$$- \gamma_{13}\rho_{13}, \tag{B.72}$$

$$\dot{\rho}_{14} = -\frac{i}{2}\left\{2\delta_S\rho_{14} + \Omega_A^* e^{i(\delta_A-\delta_S)t}\rho_{34} + \Omega_S^*\left(\rho_{44} - \rho_{11}\right) - \Omega_C^*\rho_{12}\right\}$$
$$- \gamma_{14}\rho_{14}, \tag{B.73}$$

$$\dot{\rho}_{23} = -\frac{i}{2}\left\{2\delta_C\rho_{23} + \Omega_P^* e^{i(\delta_P-\delta_C)t}\left(\rho_{33} - \rho_{22}\right) + \Omega_C^*\rho_{43} - \Omega_A^* e^{i(\delta_A-\delta_S)t}\rho_{21}\right\}$$
$$- \gamma_{23}\rho_{23}, \tag{B.74}$$

$$\dot{\rho}_{24} = -\frac{i}{2}\left\{2\delta_C\rho_{24} + \Omega_P^* e^{i(\delta_P-\delta_C)t}\rho_{34} + \Omega_C^*\left(\rho_{44} - \rho_{22}\right) - \Omega_S^*\rho_{21}\right\}$$
$$- \gamma_{24}\rho_{24}, \tag{B.75}$$

$$\dot{\rho}_{34} = -\frac{i}{2}\left\{\Omega_A e^{-i(\delta_A-\delta_S)t}\rho_{14} + \Omega_P e^{-i(\delta_P-\delta_C)t}\rho_{24} - \Omega_S^*\rho_{31} - \Omega_C^*\rho_{32}\right\}$$
$$- \gamma_{34}\rho_{34}. \tag{B.76}$$